STUDIES ON STRUCTURE, LATTICE THERMAL EXPANSION AND OXIDE ION CONDUCTING PROPERTIES OF SOME RARE EARTH BASED ZIRCONATE PYROCHLORES

Thesis submitted to

The University of Kerala

for the award of the degree of

DOCTOR OF PHILOSOPHY

in

PHYSICS

under

THE FACULTY OF SCIENCE

by

RADHAKRISHNAN A N

DEPARTMENT OF ELECTRON MICROSCOPY

MATERIALS SCIENCE AND TECHNOLOGY DIVISION

NATIONAL INSTITUTE FOR INTERDISCIPLINARY SCIENCE AND TECHNOLOGY (CSIR)

THIRUVANANTHAPURAM

KERALA

2012

DECLARATION

I hereby declare that this thesis entitled **" STUDIES ON STRUCTURE, LATTICE THERMAL EXPANSION AND OXIDE ION CONDUCTING PROPERTIES OF SOME RARE EARTH BASED ZIRCONATE PYROCHLORES "** is an independent work carried out by me for the degree of Doctor of Philosophy in Physics of the University of Kerala under the guidance of **Dr. Peter Koshy**, Chief Scientist (Rtd.), National Institute for Interdisciplinary Science and Technology, Thiruvananthapuram and **Dr. P. Prabhakar Rao,** Senior Principal Scientist, National Institute for Interdisciplinary Science and Technology, Thiruvananthapuram and it has not been submitted anywhere else for any other degree.

Radhakrishnan A N

Thiruvananthapuram
July, 2012

NATIONAL INSTITUTE FOR INTERDISCIPLINARY SCIENCE AND TECHNOLOGY (NIIST)

Council of Scientific & Industrial Research (CSIR)
(Formerly Regional Research Laboratory)
Industrial Estate P.O., Thiruvananthapuram – 695 019
Kerala, INDIA

July 2012

CERTIFICATE

This is to certify that the thesis entitled "**STUDIES ON STRUCTURE, LATTICE THERMAL EXPANSION AND OXIDE ION CONDUCTING PROPERTIES OF SOME RARE EARTH BASED ZIRCONATE PYROCHLORES**" is an authentic record of the bonafide research work carried out by **Mr. Radhakrishnan A N** at the Materials Science and Technology Division of National Institute for Interdisciplinary Science and Technology (NIIST - CSIR), Thiruvananthapuram for the degree of Doctor of Philosophy in Physics of University of Kerala under our guidance and supervision.

Dr. Peter Koshy
(Guide)
Chief Scientist (Rtd.)
National Institute for Interdisciplinary
Science and Technology (NIIST - CSIR)
Thiruvananthapuram

Dr. P. Prabhakar Rao
(Co-Guide)
Senior Principal Scientist
National Institute for Interdisciplinary
Science and Technology (NIIST - CSIR)
Thiruvananthapuram

ACKNOWLEDGEMENTS

This thesis is the end of my journey in obtaining my Ph.D. I have not traveled in vacuum in this journey. This thesis would not have been possible without the guidance and help of several individuals who in one way or another contributed and extended their valuable assistance in the completion of my research work. I would like to thank all people who have helped and inspired me during my doctoral study.

First and foremost, I offer my sincerest gratitude to my supervisor, Dr. Peter Koshy for his guidance, understanding, patience, and most importantly, his friendship. This work would not have been possible without his guidance, support and encouragement. Dr. Peter Koshy has supported me not only by providing research guidance, but also academically and emotionally through the rough road to finish this thesis. I can say a proper thanks to him only by fulfilling his dreams about me.

I am deeply indebted to my co-guide, Dr. P. Prabhakar Rao, who has supported me throughout my research work with his patience and knowledge whilst allowing me the room to work in my own way. His wide knowledge and logical way of thinking have been of great value for me. His encouragement and personal guidance have provided a good basis for the present thesis. I express my sincere thanks to Dr. K. Ravindran Nair, Scientist (Rtd.), National Institute for Interdisciplinary Science and Technology, Thiruvananthapuram for the valuable guidance in the early stages of my research work.

I would like to convey my gratitude to Dr. Suresh Das Director, NIIST, Thiruvananthapuram and former directors Dr. T. K. Chandrashekar and Dr. B. C. Pai for

providing me all necessary infrastructural facilities as well as a congenial environment for doing my research work. I am grateful to the Council of Scientific and Industrial Research (CSIR), for the financial support provided to carry out this work.

My special thanks to Dr. K. G. K. Warrier for his support as the head of the division and for his positive comments on my research work, during my assessment presentations. My sincere thanks also goes to Dr. M. T. Sebastian and Dr. U. Syamaprasad for extending research facilities to me at various stages of my research work.

I am thankful to Mr. M. R. Chandran for helping me with all SEM related works and supporting me in many ways during my stay in the lab. I am indebted to Mr. M. R. Nair for the special care and support extended to me during my good as well as bad times. I am also thankful to Mr. V. Sreekantan, Smt. Lucy Paul and Mr. Shanoj for helping me in many ways. I express my sincere thanks to Mr. P. Guruswamy for XRD analysis and Dr. V. S. Prasad, Mr. Robert Philip, Mr. Naren and Mr. Kiran Mohan for TEM analysis.

My wholehearted gratitude to my colleagues: Mr. Sibi K. S, Ms. Deepa M., Ms. Sandhya Kumari L. , Ms. Jayasree V., Mr. S. K. Mahesh, Ms. S. Sumi, Ms. Sameera S., Ms. Mary Linsa K.S. , Mr. Nandagopal , Mr. Vaisakhan Thampi D.S., Ms. Linda Francis, Ms. Reshmi V.R., Ms. Vineetha James and Divya S. with whom I have spent many memorable occasions and who have been very helpful and supportive both in personal and academic. I am very thankful to all scientists, students and staff members of Materials Science and Technology Division for their help and support. I convey my special acknowledgments to Administrative section, Finance and Account section, Stores and Purchase Section, and

Library and Information section for extending me various services to facilitate my research program.

I express my deep love and thankfulness to all inmates of Vaisakh hostel: Sreekantan Nair (Tulasi Annan), Sibi K.S., Pratheesh V. Vair , Mahseh S.K., Jinu P.Y. , Shyam kishor, Hameed P., , Vipin M.G, Dhanesh V., Vaisakhan Thampi D.S., Milith Mathew Abraham, Anto Augstin, Lijosh Thomas, Rajeev Thomas, Jithin Prakash, Robinson C Jose, Jithesh and Arun Thomas. My special thanks to Anas, Akhil, Kiran Mohan, Prasanth, Arun Boby, Ajith, Syad, and to all my friends in NIIST.

I express my sincere gratitude to all my teachers and well-wishers of my college and school life. I convey special thanks to my friends: Sebin Paul Sebastian, Jerin Jose Kattoor, Anish K Tom, Sreeni P Gopal, Joseph Thomas and Martin V Mathew. I am deeply indebted to Remanan Chettan and his family for supporting me and my family at all times. Last but not least, my heart-felt thanks to my mother, father and brother for their unflinching love and support. Finally, I would express my whole hearted gratitude to all who contributed to the realization of this thesis and apologize for not mentioning all of them personally.

Radhakrishnan A N

CONTENTS

Chapter 2

Crystallography, Order-disorder Transformation, Lattice Thermal Expansion and Oxide Ion Conduction in Pyrochlore Oxides

Chapter 3

Experimental Methods & Characterization Techniques

Chapter 4

Order - disorder Phase Transformations in Ca–Y–Zr–Ta–O Pyrochlore Oxide System

Chapter 5

Influence of Disorder to Order Transition on Lattice Thermal Expansion and Oxide Ion Conductivity in $(Ca_xGd_{1-x})_2(Zr_{1-x}M_x)_2O_7$ Pyrochlore Solid Solutions

Chapter 6

Role of Bond Strength on Lattice Thermal Expansion and Oxide Ion Conductivity in Quaternary Pyrochlore Solid Solutions

Chapter 7

Lattice Thermal Expansion and Oxide Ion Conductivity in $M_2Zr2_{-x}Ce_xO_7$ (M = Gd, Y and x = 0.1, 0.2, 0.3, 0.4, 0.5) System

Chapter 8

Conclusions & Future Scope

LIST OF TABLES

LIST OF FIGURES

LIST OF ABBREVIATIONS

SOFC	Solid Oxide Fuel Cell
IT-SOFC	Intermediate Temperature Solid Oxide Fuel Cell
FIC	Fast Ion Conduction
NASA	National Aeronautics and Space Administration
FCV	Fuel Cell Vehicle
AFC	Alkaline Fuel Cell
PAFC	Phosphoric Acid Fuel Cell
MCFC	Molten Carbonate Fuel Cell
PEMFC	Proton Exchange Membrane Fuel Cell
DMFC	Direct Methanol Fuel Cell
RFC	Regenerative Fuel Cells
ZAFC	Zinc-Air Fuel Cell
YSZ	Yttria Stabilized Zirconia
SSZ	Scandia Stabilized Zirconia
LSM	Lanthanum Strontium Manganite
LSGM	Lanthanum Strontium Gallium Manganite
GDC	Gadolinium Doped Ceria
SDC	Samarium Doped Ceria
10GDC	10 mole % Gadolium Doped Ceria
LAMOX	$La_2Mo_2O_9$ based oxides
BIMEVOX	Metal doped $Bi_2VO_{5.5}$
BICUVOX-10	$Bi_2V_{0.9}Cu_{0.1}O_{5.35}$

XRD	X–Ray Diffraction
SEM	Scanning Electron Microscope
TEM	Transmission Electron Microscope
HRTEM	High Resolution Transmission Electron Microscope
SAED	Selected Area Electron Diffraction
IS	Impedance Spectroscopy
EIS	Electrochemical Impedance Spectroscopy
CVD	Chemical Vapour Deposition
PVA	Polyvinyl Alcohol
PEG	Polyethylene Glycol
PDF	Powder diffraction File
ICDD	International Centre for Diffraction Data
SE	Secondary Electron
CCD	Charge Coupled Device
FT	Fourier Transform
FFT	Fast Fourier Transform
CPE	Constant Phase Element
NIR	Near Infrared
FWHM	Full Width at Half Maximum
XANES	X-ray Absorption Near-Edge Spectroscopy

PREFACE

Oxide ion conductors are solid oxides that contain highly mobile oxide ions and they can be used as the electrolytes for Solid Oxide fuel Cells (SOFC). Commercially used electrolyte in SOFC is Yttria Stabilized Zirconia (YSZ) which is having an ionic conductivity of 10^{-1} S/cm at 1000 ^{o}C. But the high temperature operation causes problems such as chemical and thermal instabilities, electrode sintering problems, electrode-electrolyte interface reactions and ageing. The challenge is to design a ceramic mixed oxide that would allow operation of SOFC at intermediate temperature range (600 – 750 ^{o}C). The goal has not yet been achieved and new design concepts and discovery of new materials are needed. The ionic conductivity of ceramic oxides mainly depends on crystal structure as well as microstructure of the sample which in turn depends on the chemical composition, synthesis method and processing conditions. Pyrochlore, with general formula $A_2B_2O_7$, is a unique crystal structure with an inherent intrinsic oxygen vacancy which facilitates the motion of oxygen ions through the material and it can tolerate high level of doping and vacancies. Zirconate pyrochlores are reported to be more susceptible to order-disorder transformation which can enhance oxide ion conductivity to an appreciable extent. The main objectives of the present thesis are (i) synthesis and characterization of some zirconate pyrochlores to establish the correlation between structure, lattice thermal expansion and oxide ion conductivity and (ii) formulation of some design criteria for the development of solid electrolytes with high oxide ion conductivity and low thermal expansion coefficient.

A detailed introduction to oxide ion conduction in solids and solid oxide fuel cells is presented in the first chapter of the thesis. A general literature survey of oxide ion conducting solid electrolytes belonging to different crystal structures is presented and the chapter ends with the need for developing new electrolytes with high conductivity at intermediate temperatures. Chapter two is an introduction to crystallography of pyrochlore type oxides and order-disorder transformations in pyrochlore oxides. A brief literature review of lattice thermal expansion and oxide ion conduction in zirconate pyrochlores is presented and the chapter is concluded with the objective of the present work. The third chapter includes a brief discussion on ceramic processing by conventional solid state route and different characterization techniques used in the present study.

Chapter four of the thesis describes the order-disorder transformations in a quaternary pyrochlore oxide system, Ca – Y – Zr – Ta – O studied by powder X-ray diffraction (XRD) method, transmission electron microscope (TEM) and FT NIR Raman spectroscopic techniques. Lattice thermal expansion was measured by high temperature XRD and oxide ion conductivity was measured by impedance analyser and the results were correlated with structural properties. The effect of simultaneous substitutions of Ca at A site and Nb or Ta at B site on lattice thermal expansion and oxide ion conducting properties in pyrochlore type solid solutions: $(Ca_xGd_{1-x})_2(Zr_{1-x}M_x)_2O_7$ (x = 0.1, 0.2, 0.3, 0.4, 0.5 and M = Nb or Ta) studied by powder X-ray diffraction (XRD) method, FT NIR Raman spectroscopic techniques, transmission electron microscopy and impedance spectroscopy is detailed in chapter 5.

Chapter six of the thesis describes the role of the bond strength on lattice thermal expansion and oxide ion conducting properties of quaternary pyrochlore type solid solutions, $CaGdZrNb_{1-x}Ta_xO_7$ (x = 0, 0.2, 0.4, 0.6, 0.8, 1) prepared by high temperature ceramic route. Structural, thermal and electrical characterization of the prepared samples clearly established the role of chemical bonding in deciding the conductivity of pyrochlore oxides and confirmed the predominance of 48*f* - 48*f* mechanism of oxide ion conduction in pyrochlore oxides. In chapter 7, the preparation and characterization of $M_2Zr_{2-x}Ce_xO_7$ (M = Gd, Y and x = 0.1, 0.2, 0.3, 0.4, 0.5) system is presented in detail. The equivalence of disordered pyrochlore and defect fluorite is established through Rietveld refinement and structural properties are correlated with lattice thermal expansion and ionic conductivity. $Gd_2Zr_{1.6}Ce_{0.4}O_7$ with an oxide ion conductivity of 4.49×10^{-3} S/cm is found to be the best among the prepared compounds which can be a promising candidate as solid electrolyte for IT-SOFC.

Chapter 8 of the thesis presents the conclusions drawn from the study of structural and electrical properties of zirconate pyrochlores which will help in the design of oxide ion conductors belonging to pyrochlore family of oxides. This chapter also contains the future scope of the present study including microstructural optimization by various preparation methods, further electrical characterization to establish the effect of oxygen partial pressure on ionic conductivity and testing of the prepared electrolyte using SOFC testing unit.

Chapter 1

Oxide Ion Conducting Electrolytes
&
Solid Oxide Fuel Cells

This chapter is an introduction to oxide ion conduction in solids and application of oxide ion conductors as electrolytes in solid oxide fuel cells. The chapter begins with the importance of material science in the modern world and introduces the methodology of material science research in developing functional materials. A detailed introduction to oxide ion conduction in solids is presented followed by a brief introduction to fuel cells. Basic operation and material requirements for Solid oxide fuel is discussed in brief giving importance to oxide ion conducting solid electrolytes. A general literature survey of oxide ion conducting solid electrolytes belonging to different crystal structures is presented and the chapter ends with the need for developing new electrolytes with high conductivity at intermediate temperatures (600 - 800 ºC).

1.1 Introduction

Oxide ion conduction is solids and application of oxide ion conductors as electrolytes in solid oxide fuel cells has been intensively studied over last few decades. In spite of this intensive search for new electrolytes, material scientists were not able to make a breakthrough in this field. This is mainly due to lack of knowledge on the relationship between chemical compositions, crystal structure and oxide ion conductivity in different types of compounds. The purpose of this thesis is to establish a correlation among chemical composition, crystal structure, lattice thermal expansion and oxide ion conduction in some rare earth based zirconate pyrochlores. Pyrochlore systems are chosen for investigation due to their special crystallographic features which allows oxide ion conduction through the lattice. Moreover, pyrochlore compounds are chemically and thermally stable in both oxidizing and reducing atmospheres. Zirconate pyrochlores are more susceptible to order-disorder transformation which can enhance oxide ion conductivity significantly. It is very apt to present the basic methodology of research in material science in developing functional materials, brief discussion of fast ion conductors, and necessary fundamentals to understand oxide ion conduction in solids and application of oxide ion conductors as solid electrolyte in solid oxide fuel cells. The general survey of electrolytes provided in the chapter gives the current status of research in the development of electrolytes for intermediate temperature fuel cells. Chapter 2 is dedicated for a detailed literature survey of crystallography, order-disorder transformation, lattice thermal expansion and oxide ion conduction in pyrochlore oxides, relevant to the present study.

1.2 The Materials World

Materials science is an interdisciplinary field involving the properties of matter and its applications to various areas of science and engineering. This scientific field investigates the relationship between the structure of materials at atomic or molecular scales and their macroscopic properties. It incorporates elements of applied physics and chemistry. The basis of materials science involves relating the desired properties and relative performance of a material in a certain application to the structure of the atoms and phases in that material through characterization. The major

determinants of the structure of a material and thus of its properties are its constituent chemical elements and the way in which it has been processed into its final form. These characteristics govern a material's microstructure and thus its properties.

There are essentially four elements in material science and engineering: (i) Processing/Synthesis (ii) Structure/Composition (iii) Properties and (iv) Performance/Application. In order to develop new materials and to increase the efficiency of the presently used materials, all the four elements need to be combined which gives materials science an interdisciplinary nature. Materials are traditionally classified into four categories according to their nature: (i) Metals and Alloys (ii) Ceramics (iii) Polymers and Organic materials and (iv) Composites. The modern trend is to classify materials into two categories: Structural materials and Functional materials. Structural materials, as the name indicates, are the materials used to build structures, bodies and components where mechanical properties of the materials are very important (Gao and Sammes 1999).

Functional materials are distinctly different from structural materials, and their physical and chemical properties are sensitive to a change in the environment such as temperature, pressure, electric field, magnetic field, optical wavelength, adsorbed gas molecules and the pH value. The functional materials utilize the native properties and functions of their own to achieve an intelligent action. Electroceramics is a technologically important class of functional materials that have electromechanical, electrochemical, electromagnetic, electro-optic or other electric responses. Different classes of electroceramics materials include dielectric materials, fast ion conductors, piezoelectric materials, magnetic materials and semiconductors. Over the last two decades, electroceramics have become established as one of the most important research areas in materials science both through improvements in basic knowledge and their significant technological impact.

1.3 Fast Ion Conductors

The group of solids in which either cations or anions move freely throughout the structure, acting as charge carriers is called fast ion conductors. These materials are also known as solid electrolytes or superionic conductors. Such materials often have rather special crystal structures in that there are open channels or layers through

which the mobile ions move. Migration of ions does not occur to an appreciable extent in most ionic and covalent solids and atoms tend to fixed at their lattice sites. Therefore fast ion conductors are insulators at room temperature and only at high temperature, where defect concentration becomes very large and atoms have lot of thermal energy, the ionic conductivity becomes appreciable (West 1984). Solid-state ionics is the study of solid electrolytes and their uses in devices like solid oxide fuel cells, gas sensors etc. Solid State ionics has been a very active field of science during the last four decades. However, the first observation of conductivity in solid electrolytes occurred more than 150 years ago (Takahashi 1995). Fast ionic conductors (FICs) are characterized by an almost liquid-like mobility of one of the constituent ionic species. The fast ionic conducting materials exhibit the following common features: (i) crystal bonding is ionic, (ii) electrical conductivity is high (10^{-1} - 10^{-4} S/cm), (iii) principle charge carriers are ions, (iv) the electronic conductivity is negligible and (v) low activation energies for ion migration. The study of FICs has become important due to their potential applications in solid state ionic devices like solid state batteries, fuel cells, sensors, analog memory devices, electro chromic displays, etc. (Chowdari 1992, Gool 1973, Hagenmuller and Gool 1978).

High solid state conductivity was first noted by the brilliant and perceptive English scientist Michael faraday. He reported in 1833 that Ag_2S conducts electricity via the movement of silver ions and observed fluoride ion conduction in hot PbF_2 (Mehrer 2007). The oxygen ion conductivity at high temperature was found in yttria stabilized zirconia (YSZ) in 1899 by Nernst (Nernst 1899, Singhal and Kendall 2003). Tubant and Lorentz have reported the superionic phase in α-AgI in 1913 (Ehrenreich and Turnbull 1987). This discovery stimulated a great interest in the ion conducting properties of solids. Later in 1932, Tubant reported high ionic conduction at high temperature in Ag_2Se (Tubant 1932). Until 1960, only stabilized zirconia and silver iodide (above 147 ºC) were known to have very high ionic conductivities. Since then, various kinds of cation and anion conductors exhibiting high ionic conductivity at ambient conditions and at high temperatures have been synthesized. Numerous cationic (Ag^+, Cu^{2+}, Li^+, Na^+, K^+ etc.), anionic (O^{2-}, F^-) and proton conductors have been reported. An excellent history of the development and a list of these materials are available in the text by Chandra (Chandra 1981).

The property of fast ion conduction (FIC) in solids is now well established, and it is found in diverse groups of compounds. Such materials can have important technological applications, extending and superseding those areas traditionally reserved for liquid electrolytes. A growing emphasis on energy conservation and alternative energy sources has led to a good deal of research, especially to find better materials for battery and fuel cell applications. These must be relatively inexpensive, easy to fabricate, have good mechanical strength, high chemical stability, and most importantly, show FIC at lower temperatures (McGeehin and Hooper 1977). Different types of FICs are being synthesized to meet the practical requirements. In addition, they are also fascinating for the physicists in understanding the conduction process. The most essential part in the investigation of ionic transport is the establishment of a relationship between ionic conductivity and local atomic structure.

1.4 Oxide Ion Conductors

Materials which conduct O^{2-} ions in solid state are called oxide ion conductors. Compounds which exhibit predominantly oxide ion conduction are found mainly among the oxides of quadrivalent cations which crystallize with fluorite structure such as CeO_2 or distorted fluorite structure such as ZrO_2 etc. For these oxides to exhibit high oxide ion conductivity, solid solutions must be formed with oxides of lower valent cations such as Ca^{2+}, Y^{3+}, or Sc^{3+}, within its solubility limits. The introduction of such cations into the lattice of ZrO_2, stabilizes the cubic fluorite structure and also leads to the formation of oxygen vacancies in order to maintain charge neutrality. The oxide ion conduction occurs through oxygen vacancies present in the lattice (Hagenmuller and Gool 1978).

1.4.1 Arrhenius Equation for Oxide Ion Conduction

The oxide ion conduction in solids can be treated just like electronic conduction even if the mechanisms of both type conductions are different. Oxide ions move diffusively from an occupied site to crystallographically equivalent vacancy site. Hence good oxide ion conductivity requires only partial occupancy of oxygen sites and an easy pathway for migration of oxide ions (Goodenough 2000).

In a crystal, the electronic and ionic conductivities are generally tensor quantities, relating the current density to the applied electric field in accordance with Ohm's law. In an isotropic medium such as a polycrystalline ceramic, the conductivity is a scalar, and Ohm's law (Cheng 1983) has the form for oxygen-vacancy conduction is given by:

$$\mathbf{j} = \boldsymbol{\sigma}\mathbf{E} = \mathbf{n_V N q v} \qquad (\mathbf{1.1})$$

where *N* is the number of normal sites per unit volume, q = 2e is the lattice charge of the oxygen vacancy moving with velocity v, and n_v is the fraction of sites that are vacant (Goodenough 2003). From the definition of charge-carrier mobility,

$$\boldsymbol{\mu} = \mathbf{v}/\mathbf{E} \qquad (\mathbf{1.2})$$

Then oxygen-vacancy conductivity is given by:

$$\boldsymbol{\sigma} = \mathbf{n_v N q \mu} \qquad (\mathbf{1.3})$$

Since during ionic conductivity, ions jump from one stable site to another, the process can be described by equations similar to those for diffusion. If both ionic conductivity and ionic diffusion occur by the same random-walk mechanism, a relationship between the self-diffusion coefficient and the ionic conductivity can be derived. If oxygen vacancies are present, oxide ions can jump from a normal site into a neighbouring vacancy and gradually move through the crystal. Movement of a diffusing ion into a vacant site corresponds to movement of the vacancy in the other direction. This process is therefore frequently referred to as vacancy diffusion. Diffusion coefficients are usually found to vary considerably with temperature since ionic diffusion is a thermally activated process in oxide ion conductors. This variation can often be expressed in terms of the Arrhenius equation:

$$\mathbf{D} = \mathbf{D_o} \exp(-\mathbf{E_a}/\mathbf{KT}) \qquad (\mathbf{1.4})$$

where D is the diffusion coefficient, D_o is a pre-exponential factor, K is the Boltzmann constant, T is the absolute temperature and E_a is the activation energy for diffusion (Tilley 2004). The Nernst-Einstein relationship between the ionic diffusion coefficient and the mobility is given by:

$$\boldsymbol{\mu} = \mathbf{qD}/\mathbf{KT} \qquad (\mathbf{1.5})$$

By using equation (4) and (5) in equation (3), the equation for ionic conductivity is given by:

$$\boldsymbol{\sigma = (A_o/T)\ \exp(-E_a/KT)} \qquad (\mathbf{1.6})$$

where A_o is a pre-exponential factor which is a constant (Bruce 1995). But for thermally activated conduction of oxide ions which is highly temperature dependent, the basic form of Arrhenius equation is given by:

$$\boldsymbol{\sigma = \sigma_o\ \exp(-E_a/KT)} \qquad (\mathbf{1.7})$$

where σ_o is the pre-exponential factor which depends on the defect concentration, ion jump distance, jump frequency, structural geometry of conduction path ways etc. (Bagotzky 1993). This equation can be used as basic tool for studying conductivity data of the oxide ion conductors and any non-Arrhenius behavior of the experimental data results from the temperature dependence of the exponential prefactor, σ_o (Petrowsky and Frech 2009).

1.4.2 Applications of Oxide Ion Conductors

Oxide ion conductors are technologically important materials, essential for applications such as oxygen sensors (Kumar *et al.* 2000, Moon and Tuller 1990) and pumps (Hibino *et al.* 1997, Naumovich *et al.* 1996), ceramic membranes for oxygen separation (Bouwmeester and Burggraaf 1996, Hashim *et al.* 2011) and partial oxidation of light hydrocarbons (Kharton *et al.* 2002, Shaula *et al.* 2003) and solid oxide fuel cells (Ishihara 2008, Tuller *et al.* 2000), where they act as electrolytes. In the present study, emphasis is given solely on the development of oxide ion conductor suitable for using as electrolyte in solid oxide fuel cells. Henceforth, basics of fuel cell operation, material requirements and current status of research in the field are highlighted in the latter part of this chapter.

1.5 Fuel cells

The history of the fuel cell began in the year 1839, when Sir William Grove discovered that it may be possible to generate electricity by reversing the electrolysis of water. Grove discovered that by arranging two platinum electrodes with one end of

each immersed in a container of sulfuric acid and the other ends separately sealed in containers of oxygen and hydrogen, a constant current would flow between the electrodes (Grove 1839). The sealed containers held water as well as the gases, and he noted that the water level rose in both tubes as the current flowed. Grove realized that by combining several sets of these electrodes in a series circuit, electricity can be generated by combining hydrogen and oxygen. He named this device as "gas voltaic battery "and it was the first fuel cell. Sir William Robert Grove is known as "Father of the Fuel Cell" (Grove 1842, Harper 2008).

The Swiss scientist Christian Friedrich Schönbein can be credited with discovering the underpinning principles behind the fuel cell's operation. There were two schools of thought: the "contact" theory and the "chemical" theory. The contact theory stated that physical contact between materials generated the electricity, while the chemical theory stated that it was chemical reactions which generated the electricity. A furious debate ensued in the scientific community, and Gove's correspondent Schönbein argued for the chemical theory (Harper 2008). In 1889, two researchers, Charles Langer and Ludwig Mond, coined the term "fuel cell" as they were trying to engineer the first practical fuel cell using air and coal gas (Mond and Langer 1889). Friedrich Wilhelm Ostwald a founder of the field of physical chemistry provided much of the theoretical understanding of how fuel cells operate. In 1893, he experimentally determined the interconnected roles of the various components of the fuel cell: electrodes, electrolyte, oxidizing and reducing agents, anions, and cations (Bagockii 2009, Spiegel 2008). While further attempts were made in the early 1900s to develop fuel cells that could convert coal or carbon into electricity, the advent of the internal combustion engine temporarily quashed any hopes of further development of the fledgling technology.

Francis Bacon developed the first successful fuel cell device in 1932, with a hydrogen-oxygen cell using alkaline electrolytes and nickel electrodes - inexpensive alternatives to the catalysts used by Mond and Langer (Blomen and Mugerwa 1993). Due to a substantial number of technical hurdles, it was not until 1959 that Bacon and company first demonstrated a practical five-kilowatt fuel cell system (Busby 2005). Also in the late 1950s, NASA began to build a compact electricity generator for use on space missions. NASA soon came to fund hundreds of research contracts involving

fuel cell technology (Chambers 2004). Fuel cells now have a proven role in the space program, after supplying electricity to several space missions .In more recent decades, a number of manufacturers - including major auto makers - and various federal agencies have supported ongoing research into the development of fuel cell technology for use in fuel cell vehicles (FCV) and other applications. Fuel cell energy is now expected to replace traditional power sources in coming years - from micro fuel cells to be used in cell phones to high-powered fuel cells for stock car racing.

1.5.1 Basics of Fuel cell Operation

A fuel cell is an electrochemical conversion device which converts chemical energy directly into electrical energy. It produces electricity from fuel on the anode side and an oxidant on the cathode side, which react in the presence of an electrolyte. The reactants flow into the cell, and the reaction products flow out of it, while the electrolyte remains within it. Fuel cells can operate virtually continuously as long as the necessary flows are maintained (Li 2006). Fuel cells are different from electrochemical cell batteries in that they consume reactant from an external source, which must be replenished -- a thermodynamically open system. By contrast batteries store electrical energy chemically and hence represent a thermodynamically closed system (Buydos 2007). The basic physical structure, or building block, of a fuel cell consists of an electrolyte layer in contact with an anode and a cathode on either side. A schematic representation of a unit cell with the reactant/product gases and the ion conduction flow directions through the cell are shown in the figure (E&G Services 2004). In a typical fuel cell, fuel is fed continuously to the anode and an oxidant, often oxygen from air, is fed continuously to the cathode. The electrochemical reactions take place at the electrodes to produce ionic conduction through the electrolyte, while driving a complementary electric current that performs work on the load (Vielstich *et al.* 2003). Fuel cells are classified according to the choice of electrolyte and fuel, which in turn determine the electrode reactions and the type of ions that carry the current across the electrolyte (E&G Services 2004).

- Alkaline Fuel Cell (AFC)
- Phosphoric Acid Fuel Cell (PAFC)
- Molten Carbonate Fuel Cell (MCFC)

- Solid Oxide Fuel Cell (SOFC)
- Proton Exchange Membrane Fuel Cell (PEMFC)
- Direct Methanol Fuel Cell (DMFC)
- Regenerative Fuel Cells (RFC)
- Zinc-Air Fuel Cell (ZAFC)

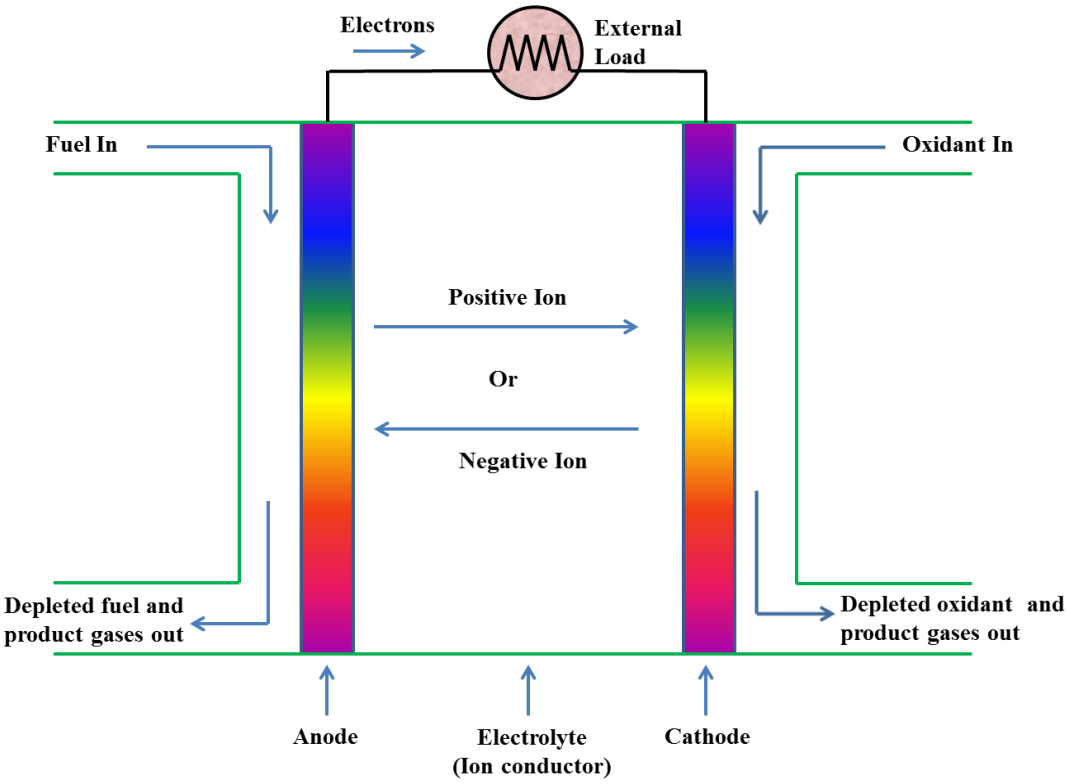

Fig. 1.1 Basic building block of a fuel cell

Fuel cells can achieve high efficiencies in energy conversion terms, especially where waste heat is utilized in co- generation systems. High power density allows fuel cells to be relatively compact source of electric power, beneficial in application with space constraints. Fuel cells, due to their nature of operation, are extremely quiet in operation and do not produce any noise pollution (Schmidt 2007). Fuel cell is one of the cleanest eco-friendly energy sources. They produce much smaller quantities of greenhouse gases and none of the air pollutants that create smog and cause health problems. If pure hydrogen is used as a fuel, fuel cells emit only heat and water as a byproduct (Rodríguez and Garcia 2007). However, in spite of the attractive system

efficiencies and environmental benefits associated with fuel-cell technology, it has proved difficult to develop the early scientific experiments into commercially viable industrial products. These problems have often been associated with the lack of appropriate materials or manufacturing routes that would enable the cost of electricity per kWh to compete with the existing technology (Steele 2001).

Applications of fuel cells include powering of vehicles, machines and satellites for telecommunications. Fuel cells have the potential to slip into every kind of electronic device. Fuel cells offer the possibility of laptops and cell phones with energy life measured in days or weeks, rather than hours. The fuel cell is scalable, which means it can go small enough to power medical devices that normally require battery replacement. Stationary Power Production and Backup- larger-scale fuel cells could allow every city to have its own power station, rather than a centralized power grid (Basu 2007, Srinivasan 2006). Co-generation, which is a technique of primary energy conservation, involves the generation of electricity and useful heat from a single fuel. The most important requirement in this technique is the ability to generate electricity and produce high-grade heat at low cost. Co-generation systems using fuel cells have high efficiency and lower emission of pollutants in comparison with other technologies. The high-temperature fuel cells are most suited for co-generation applications because they are able to produce high-temperature steam (Boyce 2002, Singhal and Dokiya 1999).

1.6 Solid Oxide Fuel Cells (SOFC)

Solid oxide fuel cells (SOFCs) are the most efficient devices yet invented for the conversion of chemical fuels directly into electrical power. Originally the basic ideas and materials were proposed by Nernst and his colleagues at the end of the nineteenth century. Nernst then made the breakthrough of observing various types of conduction in stabilized zirconia, that is zirconium oxide doped with several mole per cent of calcia, magnesia, yttria, etc. Nernst found that stabilized zirconia was an insulator at room temperature, conducted ions in red hot conditions, from 600 ºC to 1000 ºC and then became an electronic and ionic conductor at white heat, around 1500 ºC (Nernst 1899). Nernst's invention languished until the late 1930s when a fuel cell concept based on zirconium oxide was demonstrated at the laboratory scale by

Baur and Preis (Bagockii 2009). The empirical phase of the development of solid electrolyte fuel cells was overcome only after many general advances in research on solids. These included development of X-ray structure analysis, new knowledge on the ion conduction of solids from the measurements of transport numbers by Tubandt, the establishment of the theory of disorder in solids by Frenkel, Schottky, Wagner and Jost, and the development of isotope methods for the investigation of diffusion processes in solids (Singhal and Kendall 2003). Scientists at Westinghouse Electric Corporation (now Siemens Westinghouse) demonstrated for the first time the feasibility of extracting electricity from a device they called a "solid electrolyte fuel cell" in 1962 (Weissbart and Ruka 1962). Since then there has been an intense research and development effort to develop the alternative energy technology known as fuel cells. Now, as energy issues are at the forefront of current events, fuel cell technology is ripening and on the verge of being ready for large scale commercial implementation.

The Solid Oxide Fuel Cell (SOFC) is currently the highest-temperature fuel cell in development and can be operated over a wide temperature range from 600 – 1000 ºC allowing a number of fuels to be used. To operate at such high temperatures, the electrolyte is a thin, solid ceramic material (solid oxide) that is conductive to oxygen ions (O^{2-}). The operating efficiency in generating electricity is among the highest of the fuel cells at about 60% (Kalogirou 2009). Furthermore, the high operating temperature allows cogeneration applications to create high-pressure steam that can be used in many applications. Combining a high-temperature fuel cell with a turbine into a hybrid fuel cell further increases the overall efficiency of generating electricity with a potential of an efficiency of more than 70% (Bosch *et al.* 2006).

1.6.1 Working of SOFC

The basic unit cell of SOFC composed of four ceramic layers namely anode, electrolyte, cathode, and interconnect as shown in Fig. 1.2. Oxidant gas (usually the air) is supplied to the cathode, and the fuel is supplied to the anode. The ceramics used in SOFCs do not become electrically and ionically active until they reach very high temperature ranging from 600 ºC to 1000 ºC (Wood 2008). Reduction of oxygen

into oxygen ions occur at the cathode. These ions can then diffuse through the solid oxide electrolyte to the anode where they can electrochemically oxidize the fuel. In this reaction, two electrons are produced per oxide ion and water as byproduct in addition to heat. These electrons then flow through an external circuit from anode to cathode producing useful electric power. The cycle then repeats as those electrons enter the cathode material again. The basic reactions at electrodes are given as (Blomen and Mugerwa 1993, E&G Services 2004):

Anode Reaction: $2\ H_2 + 2\ O^{2-} \Rightarrow 2\ H_2O + 4\ e^-$

Cathode Reaction: $O_2 + 4\ e^- \Rightarrow 2\ O^{2-}$

Overall Cell Reaction: $2\ H_2 + O_2 \Rightarrow 2\ H_2O$

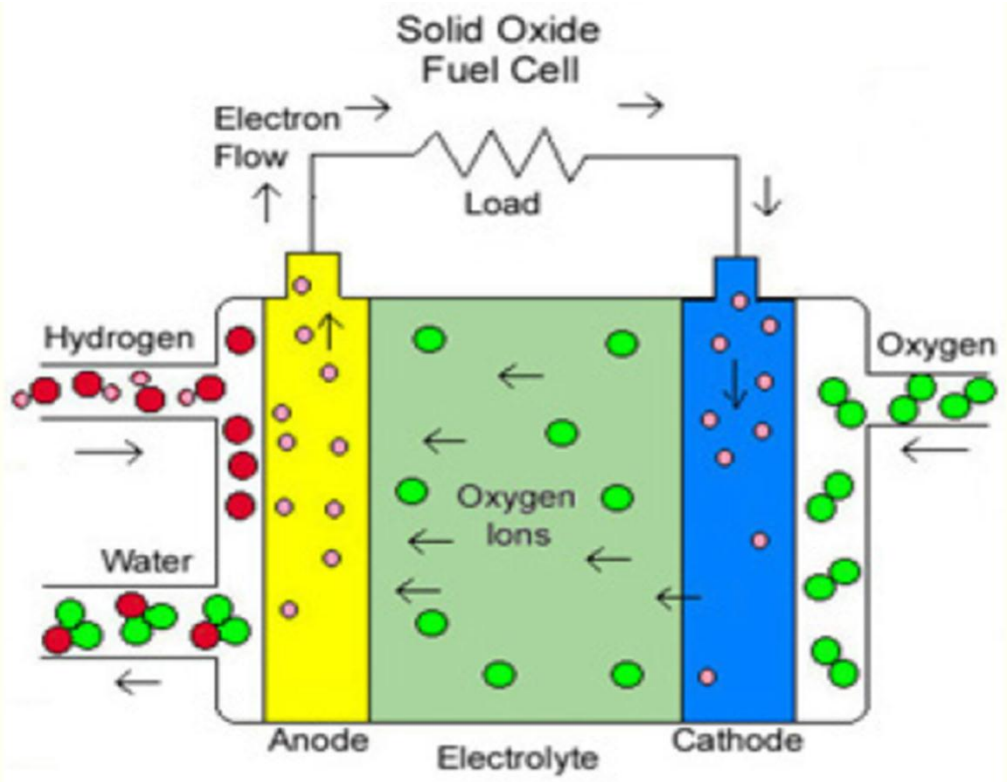

Fig. 1.2 Basic unit cell of a solid oxide fuel cell

The role of an anode in a solid oxide fuel cell is to provide the sites for the fuel gas to react with the oxide ions delivered by the electrolyte, within a structure which also facilitates the necessary charge neutralization by its electronic conductivity.

Anode layer must be very porous to allow the fuel to flow towards the electrolyte. Anode must be a mixed electronic and ionic conductor and should exhibit catalytic properties necessary for the kinetics of the fuel oxidation with the oxide ions coming through the solid electrolyte. Ionic conductivity allows the anode to spread the oxide ions across a broader region of anode/electrolyte interface, and electronic conductivity is necessary to convey the electrons resulting from the electrode reaction out into the external circuit. These functional considerations together with the operating environment of the anode are the key factors in the materials selection for the anode. The most common material used is a cermet made up of nickel mixed with the ceramic material that is used for the electrolyte in that particular cell, typically YSZ (yttria stabilized zirconia). The anode is commonly the thickest and strongest layer in each individual cell, because it has the smallest polarization losses, and is often the layer that provides the mechanical support (Singhal and Kendall 2003).

The electrolyte is a dense layer of oxygen ion conducting ceramic. Once the molecular oxygen has been converted to oxygen ions it must migrate through the electrolyte to the fuel side of the cell. In order for such migration to occur, the electrolyte must possess a high ionic conductivity and no electrical conductivity. It must be fully dense to prevent short circuiting of reacting gases through it and it should also be as thin as possible to minimize resistive losses in the cell. As with the other materials, it must be chemically, thermally, and structurally stable across a wide temperature range (Ong *et al.* 2000). YSZ has emerged as the most suitable electrolyte material. Yttria serves the dual purpose of stabilizing zirconia into the cubic structure at high temperatures and also providing oxygen vacancies at the rate of one vacancy per mole of dopant. A thin, dense film of electrolyte (approximately 40 microns thick) needs to be applied to the cathode substrate. A reliable way to apply the electrolyte is known as electrochemical vapor deposition which offers high purity and a high level of process control (Singhal 2000). Cerium oxide has also been considered as a possible electrolyte. Its advantage is that it has high ionic conductivity in air but can operate effectively at much lower temperatures below 700 ºC (Ralph *et al.* 2000).

The cathode, or air electrode, is a thin porous layer on the electrolyte where oxygen reduction takes place. Cathodes for solid oxide fuel cells have to possess

many properties including high electrical conductivity, high catalytic activity for oxygen reduction, and compatibility with other cell components (Singhal and Kendall 2003). Currently, lanthanum strontium manganite (LSM) is the cathode material of choice for commercial use because of its compatibility with doped zirconia electrolytes. Mechanically, it has similar coefficient of thermal expansion to YSZ and thus limits stresses built up during high temperature operation. Also, LSM has low levels of chemical reactivity with YSZ which extends the lifetime of the material (Kotomin *et al.* 2008).

Interconnect can be either a metallic or ceramic layer that sits between each individual cell. Its purpose is to connect each cell in series, so that the electricity each cell generates can be combined. Because interconnect is exposed to both the oxidizing and reducing side of the cell at high temperatures, it must be extremely stable. For this reason, ceramics have been more successful in the long term than metals as interconnect materials (Singhal and Kendall 2003). However, these ceramic interconnect materials are very expensive as compared to metals. Nickel- and steel-based alloys are becoming more promising as lower temperature (600 – 800 ºC) SOFCs are developed. The most common intermetallic materials used today are doped lanthanum chromites (Sammes *et al.* 2005).

1.6.2 Materials Selection and Processing

Although the operating concept of SOFCs is rather simple, the selection of materials for the individual components presents enormous challenges. Each material must have the electrical properties required to perform its function in the cell. There must be enough chemical and structural stability to endure fabrication and operation at high temperatures. The fuel cell needs to run at high temperatures in order to achieve sufficiently high current densities and power output Reactivity and inter diffusion between the components must be as low as possible (Kilner and Pena-Martinez 2011). The thermal expansion coefficients of the components must be as close to one another as possible in order to minimize thermal stresses which could lead to cracking and mechanical failure. The air side of the cell must operate in an oxidizing atmosphere and the fuel side must operate in a reducing atmosphere. The temperature and atmosphere requirements drive the materials selection for all the

other components. In order for SOFCs to reach their commercial potential, the materials and processing must also be cost-effective (Weissbart and Ruka 1962).

1.6.3 Advantages of SOFC

In general, all fuel cells are characterized as being low noise, low polluting, and highly fuel-efficient compared to conventional power sources. However, the SOFC has its own specific set of additional advantages over other types of fuel cells. SOFCs are the most efficient (fuel input to electricity output) fuel cell electricity generators currently being developed world-wide. SOFCs are flexible in the choice of fuel such as carbon-based fuels like natural gas. SOFC technology is most suited to applications in the distributed generation (ie, stationary power) market because its high conversion efficiency provides the greatest benefit when fuel costs are higher, due to long fuel delivery systems to customer premises. SOFCs have a modular and solid state construction and do not present any moving parts, thereby are quiet enough to be installed indoors. The high operating temperature of SOFCs produces high quality heat byproduct which can be used for co-generation, or for use in combined cycle applications (Brown *et al.* 1986). SOFCs do not contain noble metals that could be problematic in resource availability and price issue in high volume manufacture. SOFCs do not have problems with electrolyte management (liquid electrolytes, for example, which are corrosive and difficult to handle). SOFCs have extremely low emissions by eliminating the danger of carbon monoxide in exhaust gases, as any CO produced is converted to CO_2 at the high operating temperature. SOFCs have a potential long life expectancy of more than 40000–80000 h (Stambouli and Traversa 2002).

1.6.4 Intermediate Temperature Solid Oxide Fuel Cell (IT-SOFC)

SOFCs that operate in an intermediate temperature (IT) range, meaning between 600 ºC and 800 ºC, are named IT-SOFCs. Because of the high degradation rates and materials costs incurred at temperatures in excess of 900 ºC, it is economically more favorable to operate SOFCs at lower temperatures (Sammes, *et al.* 2005). The intermediate temperature solid oxide fuel cell combines the best available attributes of fuel cell technology development with intermediate temperature (600 -800 ºC) operation. Since ceramic components are used for electrodes and

electrolytes, carbon does not deposit on these ceramic materials. Therefore, this fuel cell may accept hydrocarbons and carbon monoxide in the fuel. Internal reforming is practical at temperatures above 650 ºC. The reduced temperature from the IT-SOFC allows stainless steel construction, which represents reduced manufacturing costs over more exotic metals (Moulson and Herbert 1992). The disadvantages of IT-SOFCs are that electrolyte conductivity and electrode kinetics drop significantly with lowered temperature. Present technology development is addressing these issues through thin-film electrolyte development and also a search for alternate materials. The push for high performance IT-SOFCs is currently the topic of much research and development (E&G Services 2004).

1.7 General Survey of Solid Oxide Electrolytes

Electrolyte is the heart of the fuel cell and ionic conductivity of the electrolyte is the major factor which affects total efficiency of the fuel cell. The general requirements for an electrolyte are high ionic conductivity, negligible electronic conductivity, stability in both oxidizing and reducing environments, good mechanical properties and long-term stability with respect to dopant segregation. In oxide ion conductors, the ionic transport mechanism is mediated by the presence of oxygen vacancies which depends on the crystal structure of the compounds (Goodenough 2003, Jacobson 2010). In this section, a general survey of conventional as well as new materials that have attracted interest for potential use in SOFCs as electrolytes will be presented.

1.7.1 Zirconia Based Solid Electrolytes

Zirconia (ZrO_2) exhibits three polymorphs. It has monoclinic structure at room temperature, changing to tetragonal above 1170 ºCand to the cubic fluorite structure above 2370 ºC. The addition of a trivalent dopant such as yttria stabilizes the tetragonal or cubic fluorite phase down to room temperature, leading to an increase in the oxide vacancy concentration (Singhal and Kendall 2003, Yashima *et al.* 1996). The maximum ionic conductivity in ZrO_2-based systems is observed when the concentration of acceptor-type dopant is close to the minimum necessary to completely stabilize the cubic fluorite-type phase. This concentration is called low

stabilization limit and the corresponding conductivity are, to a degree, dependent on the processing history and microstructural features (Etsell and Flengas 1970). In the ZrO_3-Y_2O_3 system, 2.5 mol % Y_2O_3 stabilizes the tetragonal and 8 mol % Y_2O_3 the cubic phase. The van Gool criterion stated that in order to promote high oxide ion conductivity the oxide ions on the various sites should have identical or very similar energy. This points towards structures with relatively high, possibly even cubic symmetry (Mogensen *et al.* 2004, Van Gool 1973). Hence zirconia stabilized into cubic fluorite phase exhibits higher ionic conductivity than low symmetry phases. The highest conductivity levels in $Zr_{1-x}Y_xO_{2-\delta}$ and $Zr_{1-x}Sc_xO_{2-\delta}$ ceramics are observed at x = 0.08 – 0.11 and x = 0.09 – 0.11 respectively where it stabilizes to cubic fluorite structure. Further additions decrease the ionic conductivity due to increasing association of the oxygen vacancies and dopant cations into complex defects of low mobility. It is commonly accepted that this tendency increases with increasing difference between the host and dopant cation radii (Kharton *et al.* 2004).

Yttria stabilized zirconia (YSZ) is the most widely used electrolyte for SOFCs and boasts good chemical and physical stability over a wide operating range of temperature and oxygen partial pressures, without suffering from electronic conductivity. Addition of 8 mol% of yttria i.e. $(ZrO2)_{0.92}(Y2O3)_{0.08}$ – 8YSZ leads to the highest oxide ion conductivity, although higher levels produce a better stabilized cubic phase (Brett *et al.* 2008). A range of dopant cations have been investigated including Y^{3+}, Eu^{3+}, Gd^{3+}, Yb^{3+}, Er^{3+}, Dy^{3+}, Sc^{3+} Ca^{2+} and Mg^{2+}. 8YSZ shows a conductivity of 0.14 S/cm at 1000 ºC and scandia stabilized zirconia (SSZ) gives the same conductivity at 780 ºC(Singhal and Kendall 2003). But scandia stabilized zirconia undergoes aging on long exposure to high temperatures and this kind of aging effect is very minimum in YSZ (Omar *et al.* 2011, Yamamoto *et al.* 1995). Dense YSZ thin film of few micron thicknesses can be easily fabricated by vapour deposition and tape casting methods. Hence in conventional SOFCs, YSZ is used as the electrolyte and are generally operated at 1000 ºC. With this high temperature SOFC stacks, stable power generation of several hundred kW has been already produced by Siemens Westinghouse Power Corporation (Srinivasan *et al.* 1999).

1.7.2 Lanthanum Gallate Based Electrolytes

Perovskite type ABO_3 phases derived from lanthanum gallate, $LaGaO_3$, possess a higher ionic conductivity than that of stabilized zirconia and are thus promising materials for electrochemical cells operating in the intermediate temperature range (Kim and Yoo 2001, Yasuda *et al.* 2000). Materials derived from lanthanum gallate have relatively low thermal expansion, similar to that of stabilized zirconia. High oxygen ionic conductivity in $LaGaO_3$ can be achieved by substituting lanthanum with alkaline earth elements and/or incorporating divalent metal cations, such as Mg^{2+}, into the gallium sublattice in order to increase the oxygen vacancy concentration. Following the principle of minimum lattice distortion giving maximum oxygen ion mobility, doping with Sr leads to a higher ionic conductivity in comparison with calcium or barium (Hayashi *et al.* 1999, Ishihara *et al.* 1994, Stevenson *et al.* 1997). For the $La_{1-x}Sr_xGa_{1-y}Mg_yO_{3-\delta}$ (LSGM) series, the maximum ionic transport is achieved at x = 0.10 – 0.20 and y = 0.15 – 0.20; further acceptor-type doping leads to progressive vacancy association processes. A decrease in conductivity is also observed on doping with a smaller radius A-site cation, or creating A-site deficiency (Ishihara *et al.* 1998). Many of the reported LSGM compositions exhibited ionic conductivity at 800 ºC higher or comparable to that of YSZ at 1000 ºC. The highest ionic conductivity of 0.17 S/cm at 800 ºC was achieved with $La_{0.8}Sr_{0.2}Ga_{0.8}Mg_{0.2}O_{3-\delta}$ which can be used as electrolyte in intermediate temperature fuel cells (Ishihara *et al.* 1995). Disadvantages of $LaGaO_3$-based materials include possible reduction and volatilization of gallium oxide, formation of stable secondary phases in the course of processing, the relatively high cost of gallium and significant reactivity with perovskite electrodes under oxidizing conditions as well as with metal anodes in reducing conditions (Djurado and Labeau 1998, Yamaji *et al.* 1999). Moreover, LSGM becomes a mixed conductor at high temperatures, limiting its usage as electrolyte in high temperature SOFCs. But LSGM can be used as a cathode material in high temperature SOFCs (Mogensen *et al.* 2009).

1.7.3 Ceria Based Electrolytes

The properties of solid electrolytes based on doped cerium dioxide belonging to fluorite type structure, have been considered in numerous reviews and survey

papers (Inaba and Tagawa 1996, Steele 2001). The main advantages of this group of oxygen ion conductors include a higher ionic conductivity than YSZ at lower temperatures and a lower cost in comparison with LSGM and its derivatives. Stabilized ceria is normally doped with gadolinia (GDC) or samaria (SDC) for the creation of the oxygen vacancies required to deliver high oxide ion conductivities (Eguchi *et al.* 1992, Mogensen *et al.* 2000). The optimum doping levels are in this case close to 10-11 % of rare earth oxide(Kharton *et al.* 2001). $Ce_{0.9}Gd_{0.1}O_{1.95}$ (10GDC) is the most extensively studied ceria based electrolyte and has a conductivity of 0.015 S/cm at 600 ºC (Kharton, *et al.* 2001).

The main drawback of stabilized ceria is the partial reduction of Ce^{4+} to Ce^{3+} under the high temperature and reducing conditions present in a fuel cell. The consequence of this chemical reaction is that there is a volume expansion of the lattice which can result in mechanical failure of the electrolyte and n-type electronic conductivity is introduced that reduces performance due to electronic leakage currents between the anode and cathode. The mechanism of reduction and mixed ionic electronic conduction of ceria based electrolytes has been studied and reviewed in depth (Mogensen, *et al.* 2000). However, the reduction of cerium has been shown to be almost negligible at temperatures below 600 ºC, and so the doped ceria is a suitable candidate for intermediate temperature fuel cells operating in the range 500 – 600 ºC.

1.7.4 Bismuth Oxide Based Electrolytes

High-temperature δ-Bi_2O_3 has the highest known oxide-ion conductivity of approximately 2.3 S/cm at 800 ºC due to its extremely open crystal structure. However, it is only stable in the narrow temperature interval between 730 ºC and its melting point at 804 ºC (Boivin and Mairesse 1998, Goodenough 2003). The δ-Bi_2O_3 phase has a fluorite-related structure with a random distribution of oxygen ions. At room temperature, the oxygen vacancies are ordered but on heating above 730 ºC, an order-disorder transition occurs and the conductivity increases by nearly three orders of magnitude (Jacobson 2010). δ-phase can be stabilized to lower temperatures by partial substitution for Bi though dopants lower the conductivity (Takahashi *et al.* 1972). The biggest problem with stabilized bismuth oxides for practical application is their instability with respect to reduction to bismuth metal under anode conditions

(Azad *et al.* 1994). In addition to that Bi_2O_3 based materials are thermodynamically instability in reducing atmospheres, volatilization of bismuth oxide at moderate temperatures, a high corrosion activity and low mechanical strength. Hence, the applicability of these oxides in electrochemical cells is considerably limited (Kharton, *et al.* 2004).

1.7.5 LAMOX Family of Electrolytes

$La_2Mo_2O_9$ (LAMOX) is an oxygen ion conductor first reported by Lacorre et al. in 2000 that shows an oxygen ion conductivity greater than that of YSZ (Lacorre *et al.* 2000). $La_2Mo_2O_9$ undergoes a structural phase transition from a non-conductive monoclinic α-form to the highly conductive cubic β-form at about 580 ºC similar to that observed in Bi_2O_3. The conductivity increases by almost two orders of magnitude and is 0.06 S/cm at 800 ºC. Because of the phase transition and the possible reducibility of molybdenum, a number of substitutions for both lanthanum and molybdenum have been made in order to suppress the phase transition and improve the stability in reducing environments for practical applications (Corbel *et al.* 2005, Georges *et al.* 2004). The main problem with LAMOX is its reactivity toward electrode materials. The vulnerability of $La_2Mo_2O_9$ against reduction under the hydrogen atmosphere has been significantly overcome by tungsten substitution, without much loss in oxide-ion conductivity. But the practical application of $La_2Mo_{2-y}WyO_9$ of materials is rather limited because of their high chemical reactivity and high thermal expansion coefficients (Jacobson 2010).

1.7.6 Brownmillerite Structured Electrolytes

Brownmillerite is a perovskite-related structure of general formula, $A_2B_2O_5$ which is interesting from the viewpoint of oxide ion conduction. This structure can be viewed as a perovskite with oxygen vacancies ordered along the [101] direction in alternate layers. Such vacancy ordering results in an increased unit cell relative to the perovskite and therefore high oxide ion conductivity is also expected in brownmillerites (Singhal and Kendall 2003). The parent compound, $Ba_2In_2O_5$, possesses mixed conductivity with dominant oxygen ionic transport in dry air and this phase then undergoes an order-disorder transition to a tetragonal perovskite above 925 ^oC that gives a drastic increase in its oxide ion conductivity. Substitution of

indium with higher-valence cations, such as Zr, Ce, Sn or Hf, makes it possible to stabilize the disordered cubic perovskite structure and thus to increase the ionic transport in the intermediate temperature range (Goodenough *et al.* 1990). The oxygen ion conductivity of the composition $(Ba_{0.3}Sr_{0.2}La_{0.5})InO_{2.75}$ is the best among brownmillerites, reaching a value of 0.12 S/cm at 800 ºC exceeding that of yttria-stabilized zirconia. Brownmillerites and related phases were shown to be highly sensitive to moisture and are good proton conductors at moderate temperatures. The limited number of investigated phases and the lack of precise structural data do not allow definitive conclusions to be drawn about the ability of these types of material to provide useful oxide electrolytes (Boivin and Mairesse 1998).

1.7.7 Apatite Structured Electrolytes

Rare-earth apatite materials have relatively high oxide ion conductivity at moderate temperatures as well as at low oxygen partial pressures (Kendrick *et al.* 2007, Slater *et al.* 2004) and have been proposed as alternative solid electrolyte materials following the initial work of Nakayama on the silicate-based systems (Nakayama *et al.* 1995). The compounds have the general formula $M_{10}(XO_4)_6O_3$, where M is a rare-earth or alkaline earth metal and X is P, Si, or Ge. These compounds exhibit hexagonal structure with two open channels which allows oxide ion migration through the lattice. Lanthanum silicate apatites exhibit the highest conductivities and show pure oxygen ion conductivities over a wide range of oxygen partial pressures. A number of studies of chemical substitutions aimed at optimizing the ionic conductivity have shown that the apatites can tolerate a wide range of dopants and that the conductivity depends on the degree of anion and cation non-stoichiometry and the chemical nature of the dopant (Jacobson 2010). The most interesting aspect of the apatite conductors is that, in contrast to the perovskite and fluorite based compounds, in which conduction proceeds via oxygen vacancies, the conductivity in apatite involves interstitial oxide-ions. $La_9Sr(SiO_4)_6O_{2.5}$ is the best among apatite compounds having an oxide ion conductivity of 1.2×10^{-3} S/cm at 500 ºC. In the context of applications, it should be noted that high-quality apatite ceramics are not easy to make and very high temperatures greater than 1600 ºC are required to obtain dense samples (Shaula *et al.* 2006).

1.7.8 Aurivillius Structured Electrolytes

Aurivillius is class of materials based upon a layered bismuth oxide/perovskite structure first reported by Aurivillius in 1949. Aurivillius phases are generally formulated as $Bi_2A_{n-1}B_nO_{3n+3}$ and consist of 'n' perovskite-like layers $(A_{n-1}B_nO_{3n+1})^{2-}$ sandwiched between bismuth-oxygen sheets $(Bi_2O_2)^{2+}$ (Kendall *et al.* 1996, Subbarao 1962). $Bi_2VO_{5.5}$ has an oxygen-deficient Aurivillius n = 1 structure and on heating, it undergoes two transitions, from a monoclinic α phase to an orthorhombic β phase at 450 ºC, and from the β phase to a tetragonal γ phase at 570 ºC. Abraham et al. found a high oxide-ion conductivity in the tetragonal γ phase and they subsequently stabilized the tetragonal, vacancy-disordered phase to room temperature by substituting other elements for vanadium (Abraham *et al.* 1988). These stabilized oxide-ion conductors were identified as BIMEVOX, where ME represents the substituted metal atom. Highest oxide-ion conductivities were obtained with BICUVOX-10, $Bi_2V_{0.9}Cu_{0.1}O_{5.35}$. At temperatures higher than about 500 ºC, BICUVOX begins to be reduced at oxygen partial pressures less than 10^{-2} atm, which introduces n-type electronic conduction. The practical use of BIMEVOX ceramics for electrochemical applications is complicated by high-chemical reactivity, low-mechanical strength, and a high-thermal-expansion coefficient (Goodenough 2003).

1.7.9 Pyrochlore Structured Electrolytes

Oxygen ion-conducting materials with pyrochlore structure have been studied since the 1960s (Etsell and Flengas 1970, Mori *et al.* 2003). The lattice of $A_2B_2O_7$ pyrochlore can be considered as an $(A,B)O_2$ fluorite-based structure with one vacant oxygen site per formula unit in which the cations and anion vacancies are both ordered. These unoccupied sites provide pathways for fast oxygen transport. At elevated temperatures, typically as high as 1650 – 2500 K, most pyrochlores disorder into fluorite polymorphs. High conductivity in pyrochlore type electrolytes are reported among doped gadolinium and yttrium, zirconates and titanates (Kharton, *et al.* 2004). A detailed description of pyrochlore structure and literature survey of pyrochlore electrolytes are presented in chapter 2.

1.7 Need for Developing New Electrolytes

Energy exploitation of fossil fuels is reaching its limits. Future alternatives must therefore be developed for long-term and environmental-friendly energy supply needed by a constantly growing world population. The generation of energy by clean, efficient and environmental-friendly means is now one of the major challenges for engineers and scientists. Fuel cells convert chemical energy of a fuel gas directly into electrical work, and are efficient and environmentally clean, since no combustion is required. Moreover, fuel cells have the potential for development to a sufficient size for applications for commercial electricity generation. Solid oxide fuel cell is one of the most efficient and environmental-friendly technologies available for generating power from hydrogen, natural gas, and other renewable fuels.

The performance of the oxide-ion electrolyte of a solid oxide fuel cell is critical to the development of an intermediate-temperature system. Although yttria-stabilized zirconia is the electrolyte used in SOFCs under commercial development and other candidate materials are now available, there remains a strong motivation to search for new, improved oxide-ion electrolytes. Reducing the operating temperature of SOFCs below 700 ºC is needed for a wide practical application of these devices. The use of IT-SOFC will reduce the cost as well as size of the fuel cell. The limitations of the currently using electrolytes and possibilities of newer applications highly demand the need for novel ceramic electrolytes having high ionic conductivity and low electronic conductivity at intermediate temperatures. But challenge for making an electrolyte for IT-SOFC has not yet been realized.

Chapter 2

Crystallography, Order-disorder Transformation, Lattice Thermal Expansion and Oxide Ion Conduction in Pyrochlore Oxides

This chapter is an introduction to crystallography of pyrochlore type oxides and order-disorder transformations in pyrochlore oxides. A brief literature review of lattice thermal expansion and oxide ion conduction in zirconate pyrochlores is presented and the chapter is concluded with the objective of the present work.

2.1 Introduction

Pyrochlore oxides are drawing a great deal of attention in many areas of materials science of technological interest because of their unique properties induced by the remarkable chemical and structural stability (Subramanian *et al.* 1983). Pyrochlores find applications in a surprising number of very different technologies, from the use as electrolyte in solid oxide fuel cells to advanced material for nuclear waste disposal. Pyrochlore oxides exhibit a large variation in electric properties from highly insulating through semiconducting to metallic behavior (Rao and Subba Rao 1970). Usefulness of pyrochlore-type oxides in various devices and other applications is due to their wide spectrum of properties such as electrical, magnetic, dielectric, optical and catalytic behavior. These properties are nominally controlled by the parameters such as ionic size, polarizability of the ions, electronic configuration and occasionally on the preparative conditions. The refractory nature of the pyrochlore oxides is also useful for some applications (Subramanian, *et al.* 1983). Intense research activity in the pyrochlore compounds dates back only to the early seventies. Synthesis, characterization and measurement of physical properties of the substituted stoichiometric and defect pyrochlores are areas receiving wide attention at the present time. A systematic and proper understanding of the chemistry and physics of pyrochlore oxides and related materials will enable us to fully realize their potentialities for practical applications.

2.2 Pyrochlore Structure

Among the ternary metallic oxides, compounds of the general formula, $A_2B_2O_6O'$ (A and B are metals), represent a family of phases isostructural to the mineral pyrochlore, $(Na,Ca)_2(Nb,Ta)_2O_6(F,OH)$. These compounds, among which about 150 in number are predominantly cubic and ionic in nature, lend themselves to a wide variety of chemical substitution at the A, B and O sites provided the ionic radius and charge neutrality criteria are satisfied. The crystal structure also tolerates vacancies at the A and O' sites to a certain extent. Depending upon the oxidation state of A and B cation, oxide pyrochlores can be generally classified as $A_2^{3+}B_2^{4+}O_7$ (3+, 4+) and $A_2^{2+}B_2^{5+}O_7$ (2+, 5+) types. The existence, field of stability, synthesis and physical properties of (3+, 4+) and (2+, 5+) pyrochlores have discussed in detail by

Subramanian et al (Subramanian, *et al.* 1983). Oxide pyrochlore and related phases have been studied by many workers over the past several years and there is available a considerable body of experimental data to allow correlations to be made with various crystal chemical properties.

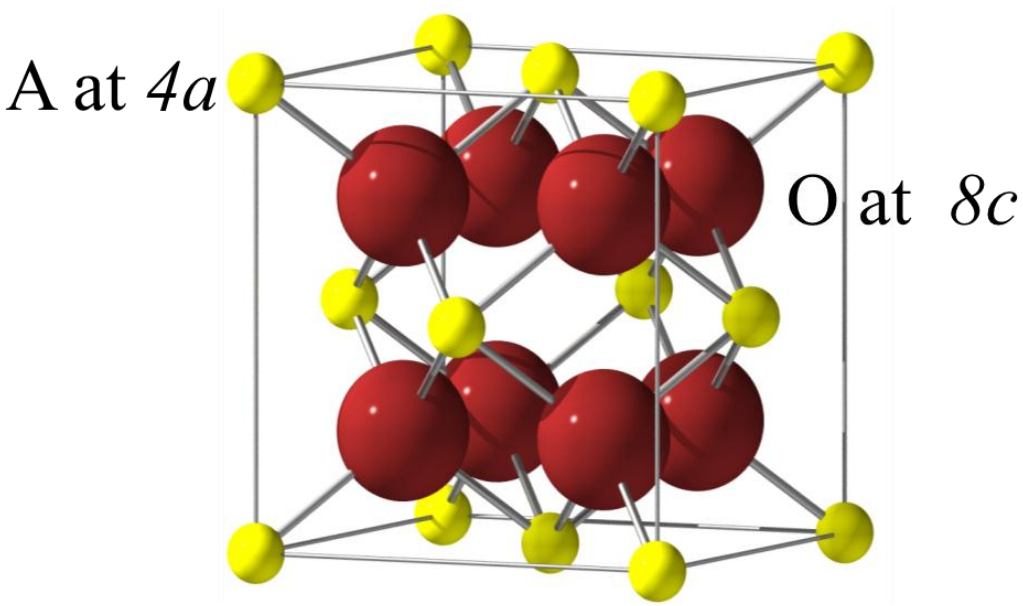

Fig. 2.1 Unit cell of the fluorite structure

The ordered pyrochlore with $A_2B_2O_6O'$ stoichiometry is a superstructure of the defect fluorite structure with exactly twice the lattice constant. Ideal fluorite is a simple crystal structure having a general formula AO_2 and the unit cell of fluorite structure is shown in Fig.2.1. The A^{4+} cation is eight coordinated with an fcc arrangement and O^{2-} anion occupying the tetrahedral holes within the cubic polyhedron. It belongs to the space group $Fm\bar{3}m$ (No.225) and its unit cell contains four formula units. The atoms occupying the following special positions in the unit cell: A^{4+} cation at *4a* and O^{2-} anion at *8c* sites. The lattice parameter of the fluorite structure is of the order of 5Å and oxygen ion occupying a definite position with position parameter, x = 0.375. But defect fluorite structure is anion deficient with a formula, $AO_{1.75}$ and one of the 8c sites is vacant (Stanek 2003).

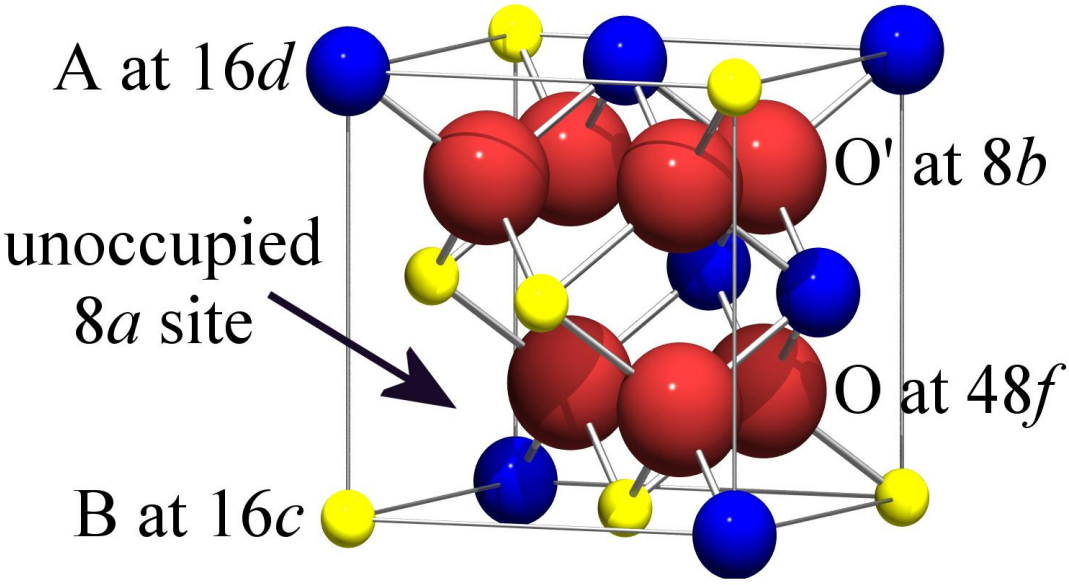

Fig. 2.2 One eighth of the unit cell of pyrochlore structure

The general formula of the oxide pyrochlores can be written as $A_2B_2O_6O'$ with four crystallographically non-equivalent kinds of atoms. The space group of the ideal pyrochlore structure is $Fd\bar{3}m$ and there are eight molecules per unit cell (Z = 8). A common way of describing the pyrochlore structure is by fixing its origin on the B site, with atomic position specified using Wyckoff notation. The cation sublattice is an alternate arrangement of A-site (16*d*) and B-site (16*c*) cations along <110> direction in an fcc lattice. The anion sublattice is comprised of three different oxygen sites, two of which are occupied (8*b*) and (48*f*), and the third site (8*a*) is vacant. Hence, the anion vacancies are ordered.

The pyrochlore structure is composed of two types of cation co-ordination polyhedron. The A cation (usually ~1 Å ionic radius) are eight coordinated and are located within scalenohedra (distorted cubes) that contain six equally spaced anions (O'-atoms) at a slightly shorter distance from the central cations. The smaller B cations (~0.6 Å ionic radius) are six coordinated and are located within trigonal antiprisms with all the six anions at equal distances from the central cations. All anion sites are tetrahedrally coordinated with 8*b* site surrounded by four *A* cations and 48*f* site surrounded by two *A* and two *B* cations that are slightly displaced from the center of the tetrahedral site toward the unoccupied 8*a* site. The magnitude of the

displacement is represented by the positional parameter *x* of oxygen at the 48*f* site, which is 0.375 for the ideal fluorite structure. Oxygen *x*-parameter is the only internal variable in the pyrochlore structure and it depends on the choice of the origin. The shape of BO_6 and AO_8 polyhedra depends on x-parameter. The lattice parameters are of the order of 10 Å and x- parameter is found to vary from 0.3125 to 0.375.

Many of the pyrochlore oxides known in the literature are of the (3+,4+) type and is due to the fact that a large number of A^{3+} and B^{4+} cations have suitable ionic radius for the formation of pyrochlore structure. The A^{3+} ion can be a rare earth, Sc,Y, Bi,T1 or In whereas B^{4+} can be a transition metal or any of the group IV elements. The formation and stability of the oxide pyrochlores are governed by the ionic radius ratio (r_A/r_B) and the oxygen *x*-parameter. The ionic radii are taken from Shannon's radius table for A cation at eight co-ordination and B cation at six co-ordination. Pyrochlores can form for r_A/r_B = l.46 to 1.80 at one atmosphere and extended up to 2.3 for high pressure synthesis. Charge neutrality considerations indicate that it must be possible to replace the A cation or B cation or both in the pyrochlore, by mixed cations of suitable ionic radii. In addition to the RR criteria, difference in charge, electronic configuration and polarizability of the cations play a part in stabilizing the cubic pyrochlore structure (Subramanian, *et al.* 1983).

2.3 Order-disorder Transformations in Pyrochlore Oxides

All compounds with the pyrochlore stoichiometry ($A_2B_2O_7$) but do not actually form in the cubic pyrochlore structure. There are at least two variants, one is the disordered fluorite ($[AB]_2O_7$) which tends to form in the large B cation, small A cation region and the other forms a monoclinic structure which tends to form in the large A cation, small B cation region of the compositional space. Pyrochlore to defect fluorite transformation is an order-disorder transformation resulting from the disorder in both cation and anion sublattices in the pyrochlore structure (Stanek 2003).

The order-disorder transition from the pyrochlore to defect fluorite structure type may be induced by ion-irradiation (Hess *et al.* 2002, Lian *et al.* 2001), compositional changes (Moon and Tuller 1988, Wuensch *et al.* 2000), pressure (Sanjay Kumar *et al.* 2008, Zhang *et al.* 2006) and thermal treatment (Wuensch and

Eberman 2000). The specific chemistries of the A- and B-site cations, as well as anion ordering on the 48*f* and 8*b* sites, constrain the stability of the ordered pyrochlore structure. The ionic radii of the A and B site cations are typically in the ranges of $r_{A\,=}$ 0.087 – 0.151 nm; r_B = 0.040 – 0.078 nm, respectively. The relative ionic radii or the ionic radius ratio, r_A/r_B , and the 48*f* oxygen positional parameter *x* determine the phase stability of pyrochlore. At normal pressure, the ordered pyrochlore structure can form for r_A/r_B = 1.46 to 1.78 and usually, smaller values of r_A/r_B below 1.46 favor the formation of disordered fluorite type structure (Zhang *et al.* 2007). 48*f* oxygen *x*-parameter increases with increase in disorder and reaches its upper limit, 0.375 when the structure is completely transformed to defect fluorite (Chakoumakos 1984).

Progressive disorder takes place in pyrochlore solid solutions as average radii of A and B cations become more similar. As the structure starts disordering, the distinction between A and B cation slowly disappears and as the disorder progress, both 16*d* and 16*c* Wyckoff positions get occupied randomly by A and B cations. The pyrochlore structure transforms to defect fluorite at complete disorder. A defect pyrochlore phase exists between a completely ordered pyrochlore phase and completely disorder defect fluorite phase during the structural transformation driven by compositional adjustments. Analogously, for a given radius ratio of A and B cations, there exists a temperature above which defect fluorite structure is preferred over ordered pyrochlore phase (Heremans *et al.* 1995). A few pyrochlore materials have been observed to disorder at a very high temperature, e.g. 2300 ºC for $Nd_2Zr_2O_7$, 2200 ºC for $Sm_2Zr_2O_7$ and 1530 ºC for $Gd_2Zr_2O_7$ (Meilicke and Halle 1995, Michel *et al.* 1974). The transition temperature decreases rapidly as r_A/r_B approaches the lower limit of the pyrochlore stability field. The high temperature of the transformation has probably prevented observation of the transition in a greater number of pyrochlores.

Atomistic simulations based on energy minimization techniques have been used to evaluate the energetics of the disordering process. All combinations of A-site cations (Lu^{3+} to La^{3+}) and B-site cations (Ti^{4+} to Ce^{4+}) were simulated, and the results were plotted on contour maps of the cation anti-site and anion Frenkel defect energies. The calculations are generally consistent with the radius ratio criteria for the observed compositions that form the pyrochlore structure at atmospheric pressure. Cation anti-site defect energies for pyrochlore are generally in the range of 3 to 6 eV, but these

may be lowered by approximately 1 eV by defect clustering (Minervini *et al.* 2000, Sickafus *et al.* 2000).

Synthesis of $Ln_2Ti_2O_7$ (Ln = Sm – Yb, and Y) pyrochlores were reported in the literature whereas pyrochlores with Ln = La, Pr, and Nd do not crystallize in the pyrochlore structure because the cation ionic radius ratio requirement is not satisfied (Ewing *et al.* 2004). The pyrochlore structure can form for the stannate series, $Ln_2Sn_2O_7$ (Ln = La – Lu, and Y). $Bi_2Sn_2O_7$ forms, but adopts a distorted pyrochlore structure at room temperature and transforms to ideal pyrochlore above 953 K (Kennedy *et al.* 1997). Zirconate pyrochlore compositions can be easily synthesized for $Ln_2Zr_2O_7$ (Ln = La–Gd). For Ln = Dy – Lu and Y, cubic zirconate pyrochlores are not stable because the cation ionic radius ratio limit precludes their formation; thus, these compositions form a disordered fluorite structure (Klee and Weitz 1969). Hafnate pyrochlores with compositions of $Ln_2Hf_2O_7$ (Ln = La – Tb) are easily formed and have an ordered pyrochlore structure. Similarly, for Ln = Dy – Lu and Y, these compositions have a disordered fluorite structure (Ewing, *et al.* 2004, Spiridinov *et al.* 1968). This is consistent with the results of Stanek and Grimes who used atomistic simulation calculations to determine the energetics of disordering in the series $A_2Hf_2O_7$ (Stanek and Grimes 2002).

Pyrochlore is unique among oxides in that simultaneous order-disorder processes must occur in the cation and anion arrays. However, the cation and anion disordering may occur to different degrees and at different temperatures. Using neutron diffraction and Rietveld analysis, Heremans *et al.* studied the chemically induced order–disorder transition in the $Y_2(Zr_xTi_{1-x})_2O_7$ system by analyzing the fractional occupancy of the interstitial 8*a* site and the effective scattering length for the A- and B-site cations, a measure of the extent of cation anti-site disorder. With the increasing concentrations of Zr at the B-site, the structure of the $Y_2(Zr_xTi_{1-x})_2O_7$ solid solution progressively changes to a defect-fluorite structure at x = 0.9. The anion disorder precedes the disordering of the cation lattice. The interstitial 8*a* site was filled immediately with the oxygen ions displaced from the nearest-neighbor anion site, the 48*f* oxygen, upon the addition of the larger Zr-cation. The occupancy of the interstitial 8*a* site increases linearly with Zr-content over the entire range of the solid solution. The onset of cation disorder occurred at x > 0.45 and was coupled with

disordering of anions at the 8*b* site. Complete mixing of all three cation species occurs abruptly in the compositional range x= 0.6 – 0.9. The positional parameter for 48*f* oxygen has been found to increase sharply to 0.375 for the ideal fluorite structure due to the occupancy of oxygen at the interstitial 8*a* site and the decreasing average ionic radius difference at the A and B-sites as the extent of cation mixing increases (Heremans, *et al.* 1995). Rietveld analysis of neutron diffraction or X-ray diffraction data is a powerful method for the investigation of order-disorder transformation in pyrochlore oxides.

X-ray diffraction studies are more sensitive to disorder in the cationic sublattice compared to anionic sublattice whereas Raman spectroscopy is primarily sensitive to oxygen-cation vibrations and is an excellent probe for local disorder. The Raman spectroscopic investigation has been found to provide unequivocal information to distinguish between a pyrochlore, disordered pyrochlore and a defect fluorite material, because these phases differ essentially with respect to local disorder around the A or B cations (Mandal *et al.* 2007). In cubic pyrochlores, $A_2B_2O(1)_6O(2)$, belonging to the space group $Fd\bar{3}m$ (no.227) with Z= 8, the site symmetry is D_{3d} for A and B cations, $C_{2\upsilon}$ for O(1) anions and T_d for O(2) anions (McCauley 1980). D_{3d}, $C_{2\upsilon}$, and T_d are Schoenfies notations used in spectroscopy for representing symmetry point groups. Factor group analysis based on above site symmetries predicted six Raman active modes (Rousseau *et al.* 1981) and the irreducible representations are given below.

$$\mathbf{\Gamma\ (Raman) = A_{1g} + E_g + 4F_{2g}} \qquad \mathbf{(2.1)}$$

A_{1g}, E_g, and F_{2g} are Mullikan symbols representing different vibrational modes of the molecule and '+' symbol here merely representing combination of Raman active vibrations. E_g mode can be assigned to B-O_6 bending vibrations and A_{1g} mode to O-B-O bending vibrations. F_{2g} modes represent a mixture of A-O and B-O bond stretching vibrations with bending vibrations.(Mandal *et al.* 2010, Vandenborre *et al.* 1983). In cubic fluorites, AO_2, belonging to space group $Fm\bar{3}m$ (no.225) with Z = 4, the site symmetry is O_h for the A cations and T_d for O anion. According to factor group analysis, the only Raman active mode of fluorite type

structure is F_{2g} (Keramidas and White 1973). But in defect fluorites, intensity for F_{2g} mode is observed to be very weak and appear as a broad peak.

Electron microscopy and electron diffraction are often used to solve structural details that X-ray diffraction method cannot resolve and provides indisputable information at molecular or atomic level. Selected area electron diffraction (SAED) and high-resolution transmission electron microscopy (HRTEM) can be used to elucidate disorder in pyrochlore oxides. The Bragg reflection in SAED pattern can be indexed to determine its structure and presence of diffuse scattering spots indicates perturbations in the basic unit cell. High resolution lattice image can be used to accurately determine the lattice spacing and the corresponding planes which are the fingerprints of crystal structure (Arévalo-López and Alario-Franco 2007, Williams and Carter 1996). Pyrochlore phase exhibits the classical pattern of sharp and distinct pyrochlore superlattice diffraction intensities with somewhat stronger fluorite sub cell intensities. Disorder in the pyrochlore lattice is characterized by weak superlattice reflections and transformation to defect fluorite is indicated by the annihilation of superlattice reflections (Whittle *et al.* 2009).

Pyrochlore oxides are one of the most promising candidate materials as ionic and electronic conductors. Their structure and electronic properties depend on the disordering of cations and anions. Hence the study of order-disorder transformation in pyrochlores is essential for developing oxide ion conductors and tuning their properties to make them suitable for using as an electrolyte in SOFC system.

2.4 Lattice Thermal Expansion in Pyrochlore Oxides

The macroscopic thermodynamic properties like lattice thermal expansion are determined by microscopic crystal structure and atomic vibrations, and these are determined by the nature of bonding between the atoms. The modeling of the structure, dynamics, and various thermodynamic properties is done either by the first-principles quantum mechanical methods (Martin 2004) or by the semi-empirical methods (Chaplot *et al.* 2010) largely based on models of interatomic interactions. But these methods are computationally far more intensive and therefore, its application to complex structures is somewhat limited. On the experimental side, a

variety of microscopic and macroscopic techniques are in use, out of which high temperature X-ray diffraction technique is the most accurate method for the determination of lattice thermal expansion coefficient.

Nearly all applications of oxide ion conductors involve high temperature operation and thus it is integral to investigate the thermal expansion behavior of these materials at high temperature which can affect the thermal compatibility with other components in the device. Kutty et al. have measured the linear thermal expansion coefficients (TEC) of a series of rare-earth zirconate pyrochlores $Ln_2Zr_2O_7$ (Ln = La, Nd, Sm, Eu, Gd), which fall in the range of 8-11 × 10^{-6} K^{-1} within the temperature range 298 - 1500 K, and came to a conclusion that the TEC value increases with decreasing ionic radius, that is, it increases from $La_2Zr_2O_7$ to $Gd_2Zr_2O_7$ (Kutty *et al.* 1994). Schelling et al. have summarized the TEC values of $La_2Zr_2O_7$, $Sm_2Zr_2O_7$, and $Gd_2Zr_2O_7$ to be 9.1 × 10^{-6}, 10.8 × 10^{-6}, and 11.6 × 10^{-6} K^{-1} (293 - 1273 K), respectively (Schelling *et al.* 2004). The effect of A site dopants on thermo physical properties of in zirconate pyrochlore were investigated by a Shimamura et.al and found that the thermal expansion becomes smaller with increasing ionic radius of A cation and increasing crystal binding energy (Shimamura *et al.* 2007). But the effect of substitution at B site as well as simultaneous substitution at A and B sites upon thermal expansion behavior of zirconate pyrochlores are not available in the literature and this aspect is taken into account in the present work.

2.5 Oxide Ion Conduction in Zirconate Pyrochlores

Fast ion conduction in pyrochlore oxides has been extensively studied by both experimental and computational methods. The pyrochlore structured oxides have high ionic conductivity due to the presence of ‘vacancies’ which are intrinsic structural features of these materials. The pyrochlore structure has a number of empty interstitial sites which would be viewed as oxygen vacancies in the defect fluorite structure. There are two crystallographic sites (48*f*, 8*b*) for oxygen ions in ordered pyrochlores. Oxygen ions located at 48*f* sites can be exchanged with empty interstitial 8a sites at high temperature as observed from neutron diffraction studies. This exchange creates anion Frenkel defects consisting of an oxygen interstitial-vacancy pair. All of the oxygen sites have other oxygen sites as second nearest neighbours. It is therefore

reasonable to suppose that these are the sites between which oxygen vacancy hopping will occur. The second nearest neighbours of the 8*b* ions and 8*a* sites are always 48*f* oxygen ions, but not forming a continuous network by which diffusion could proceed. The 48*f* sites, on the other hand, have 8*b*, 8*a* and 48*f* sites as second nearest neighbours and forms a continuous chain of oxygen second nearest neighbours along which oxygen vacancy-hopping diffusion could take place. This is the major oxide ion conduction mechanism in pyrochlore oxides (Moon and Tuller 1988, van Dijk *et al.* 1985).

The small energy difference between and 'fluorite' phases, especially for those materials which lie close to the edge of the stability field, means that structural disorder occurs easily. Among the 4d transition elements, zirconium forms the (3+, 4+) pyrochlores with trivalent rare earth elements. The compounds $Ln_2Zr_2O_7$ (Ln = La - Gd) can easily be prepared and have a cubic pyrochlore structure. These are stable at ordinary temperature, but at high temperature (>1500 ºC), an order-disorder transition, pyrochlore - defect fluorite structure, occurs and the transition temperature depends on the lanthanide ion (Michel *et al.* 1976). Similar to $Ln_2Ti_2O_7$ phases, $Ln_2Zr_2O_7$ compounds (d^o- system) are also expected to be electronic insulators. However, oxide ion conductivity is possible at high temperature and evidence for this has been reported for Ln = Sm, Nd and Gd (Shinozaki *et al.* 1979, Subramanian, *et al.* 1983). Apart from these rare earth zirconates, $Y_2Zr_2O_7$ also form disordered pyrochlore phase and transform to defect fluorite above 1500 ºC.

The order-disorder transformation in a pyrochlore-type structure is quite interesting due to the occurrence of order-disorder transformation in both the anion and the cation arrangements. Modified pyrochlore oxides are of great interest in solid electrolytes due to their high oxide ion conductivity, which makes them suitable for applications in SOFC (Wuensch, *et al.* 2000). Rare-earth zirconates have been of considerable interest as potential electrolytes for intermediate temperature SOFC due to their high ionic conductivity at relatively low temperatures. The electrical conductivity of the pyrochlore phase $Sm_2Zr_2O_7$ was comparable to those of good oxide ion conductors in low temperature region. It has been found that electrical conductivity of pyrochlore-type materials is obviously higher than that of defective

fluorite-type materials for doped $Sm_2Zr_2O_7$ ceramics in the temperature range of 723–1073 K (Liu *et al.* 2009).

The most extensive research on pyrochlore oxide electrolytes has been conducted by Tuller's group from Cambridge, MA (Kramer and Tuller 1995, Tuller 1997). They focused their investigations on $Gd_2Ti_2O_7$ and $Gd_2Zr_2O_7$ based conductors in particular. The $Gd_2(Ti_{1-x}Zr_x)_2O_7$ solid solution is of a great interest because the $x = 0$ member is an ionic insulator whereas the $x = 1$ end member is a very good oxide ion conductor. As a consequence, the x value enables one to control the σ_o/σ_e ratio over several orders of magnitude. Doping of the A site with Ca^{2+} in $Gd_2Ti_2O_7$ has been performed by Tuller et al. and the conductivity at 1000 ºC quickly increased from 10^{-4} S cm^{-1} for pure $Gd_2Ti_2O_7$ up to 5 x 10^{-2} S cm^{-1} for samples doped with 10 mol % of Ca^{2+} (Tuller 1997).This value exceeds the conductivity of $Gd_2Zr_2O_7$ and is within a factor of 2 of that for yttria-stabilized zirconia. But As usually observed, the activation energy decreases as the ionic conductivity increases; it varies from 0.94 eV for $Gd_2Ti_2O_7$ down to 0.63 eV for the 10 % doped sample. At higher dopant concentration, the conductivity quickly decreases. Conductivity measurements as a function of p(O2) indicate a significant dependence of the ionic and electronic relative contributions on the calcium dopant concentration. All samples exhibit n-type conductivity at low p(O2), ionic conductivity at intermediate p(O2), and p-type conductivity at high p(O2). The most striking feature is the rapid extension of the ionic domain as the Ca^{2+} ratio increases. These studies showed that doped pyrochlore may exhibit conductivity values with the same order of magnitude as stabilized zirconia. But the electronic conductivity present in titanate pyrochlores limits their application as electrolytes in SOFCs. On other hand, zirconate pyrochlores exhibit properties like high chemical stability, pure oxide ion conductivity and low lattice thermal expansion which makes them potential candidate to use them as solid electrolyte in SOFCs.

2.6 Objective of the Present Study

Solid oxide fuel cells (SOFCs) have attracted much attention because of their potential of providing an efficient, environmentally benign, and fuel-flexible power generation system for both small power units and for large scale power plants.

However, conventional SOFCs with yttria-stabilized zirconia (YSZ) electrolyte require high operation temperature (800 – 1000 ºC), which presents material degradation problems, as well as other technological complications and economic obstacles. Therefore, numerous efforts have been made to lower the operating temperature of SOFCs. The discovery of new electrolytes for IT-SOFCs is a grand challenge for the SOFC community.

The special crystallography of the pyrochlore type structure enables one to do a large number of chemical substitutions at different crystallographic sites and tailor the properties of such compounds so that can be used as functional materials for a good number of applications. Pyrochlore is a unique crystal structure with an inherent intrinsic oxygen vacancy which facilitates the motion of oxygen ions through the material and it can tolerate high level of doping and vacancies. Many zirconate pyrochlores which undergo order-disorder transformation to defect fluorite structure were investigated in the last few decades with a vision of making them into solid electrolytes used in intermediate temperature fuel cells. But the design of an oxide ion conductor in pyrochlore structure with low thermal expansion and high oxide ion conductivity is still at its 'stone age' due to the lack of basic understanding of correlationship between structure, lattice thermal expansion and oxide ion conductivity in pyrochlore oxides. In this context, it is quite interesting to study the structure-property correlationship in pyrochlore oxides with the following objectives:

- Control of disorder in pyrochlore oxides with the substitution of suitable elements at A and B sites.
- Correlation of lattice thermal expansion with structural parameters and disorder in pyrochlore oxides.
- Correlation of oxide ion conductivity with disorder in pyrochlore oxides.
- Role of bond strength in deciding lattice thermal expansion and oxide ion conductivity in pyrochlore oxides.
- Formulation of some design criteria for the development of solid oxide electrolytes with high conductivity and low thermal expansion coefficient.

Zirconates pyrochlores are selected for investigation due to their high chemical stability at high temperatures and the possibility of controlling the disorder with suitable doping. Zirconate pyrochlores are more susceptible to undergo order-disorder structural transformation due to the bigger size of Zr^{4+} cation. In the present study, zirconate pyrochlores with simultaneous substitution at A and B sites as well as substitution only at B site, were prepared by solid state route and characterized by powder X-ray diffraction, Rietveld analysis, Raman spectroscopy, Transmission electron microscopy, high temperature XRD, Scanning electron microscopy and Impedance spectroscopy.

Chapter 3

Experimental Methods
&
Characterization Techniques

Within the context of materials science, the genesis of a creative idea, first and foremost, requires a knowledge bank of all classes of solids and how to make them. The preparation methods and processing conditions play a crucial role in the development of materials with a definite structure and microstructure exhibiting useful properties. The first part of this chapter includes a brief discussion on ceramic processing by conventional solid state route. The role of characterization techniques in materials science is to bridge the gap between the materials synthesis and the materials performance. A brief note on different characterization techniques used in the present study is also included in this chapter.

3.1 Introduction

Man's skill in processing functional ceramics dates back many millennia, preceding the introduction of more formable and less brittle materials, viz. metals that have since received more economic, technological and scientific attention due to their deserved engineering importance. Ceramic materials, with their multiplicity of elemental combinations and structural arrangements, produce a multitude of unique properties, which are still being uncovered. Today, advanced ceramics are finding potential applications ranging from advanced heat engines to communication and energy transmission and they are emerging as the leading class of materials needed to implement many advanced technologies.

There are a wide variety of ceramic materials that have electromechanical, electrochemical, electromagnetic, electro-optic or other electric responses termed generally as electro ceramic materials. Ceramic oxides form a large group of electro ceramic materials with wide spectrum of properties and can be used in ferroelectric, piezoelectric, superconductor, thermoelectric, dielectric, magnetic, linear and nonlinear electro-optic devices. Some ceramic oxides have electronic or oxide ion conducting properties and can be used as electrodes or electrolytes in SOFCs since these oxides have good mechanical, thermal and chemical stability. But all these properties depend on crystal structure and microstructure of the ceramic compound which in turn depends on the processing methods and conditions. This structure - property correlationship can be established by structural as well as electrical characterization of the samples. Hence the research in the field of electro ceramics involves synthesis of compounds by suitable methods, characterization of prepared samples by different techniques, data analysis and interpretation to establish a structure – property correlationship. The structural as well as electrical properties are optimized by varying the processing conditions like sintering temperature, rate of heating, particle size of the precursor powders etc. This chapter presents a brief introduction to preparation of ceramic oxides by solid state reaction method and characterization techniques like X-ray powder diffraction (XRD), Raman Spectroscopy, Transmission Electron Microscopy (TEM), Scanning Electron Microscopy (SEM) and Impedance Spectroscopy (IS).

3.2 Synthesis of Ceramic Oxides

Ceramics can be fabricated from suitable starting materials into solid product with the desired shape such as a film, fiber, or monolith and with the desired microstructure by a variety of methods, some of which have their origins in early civilization. The main fabrication methods can be classified into three groups, depending on whether the starting materials involve a gaseous phase, a liquid phase, or a solid phase. Gaseous phase reactions includes processes like chemical vapour deposition (CVD) and liquid phase reactions includes soft chemical routes like sol-gel synthesis, citrate routes, polymer pyrolysis etc. But ceramic oxides are mostly synthesized by solid phase reactions from component oxides in powder form which are insoluble in most of the solvents and cannot be easily vaporized. Solid phase sythesis involves the production of the desired body from an assemblage of finely divided solids (i.e., powders) by the action of heat. It gives rise to the two most widely used methods for the fabrication of ceramics: melt casting and solid state reaction route. These two fabrication routes have their origins in the earliest civilizations.

Melt casting involves melting a batch of raw materials (commonly in the form of powders), followed by forming into shape by one of several methods, including casting, rolling, pressing, blowing, and spinning. For ceramics that crystallize relatively easily, solidification of the melt is accompanied by rapid nucleation and growth of grains. The main disadvantage of this method is the uncontrolled grain growth that leads to the production of ceramics with undesirable properties. Another problem is that many ceramics have high melting points (e.g., ZrO_2 with a melting point of 2600 ºC) or decompose prior to melting (e.g., Si_3N_4), so that obtaining a melt is rather difficult. The melt casting method is therefore limited to the fabrication of glasses (Rahaman 2003).

3.3 Solid State Reaction Route

Solid state reaction route, also called conventional ceramic route is the most widely used method for the production of polycrystalline ceramics and is the direct reaction, in solid state, of a mixture of solid starting materials in solid state. Solids do not usually react together at room temperature over normal time scales and it is necessary to heat them to much higher temperatures in order for the reaction to occur at an appreciable rate. This shows that both thermodynamic and kinetic factors are

important in solid state reactions. Thermodynamic considerations shows that whether or not a particular reaction should occur by considering the changes in the free energy that are involved and kinetic factors determine the rate at which this reaction occurs.

In solid state reaction route, the fabrication process starts from a mass of powder obtained from commercial sources. The characteristics of the starting materials (in powder form) which influence the subsequent processing of the ceramic are the size, size distribution, shape, degree of agglomeration, chemical composition, and purity. The factors on which the feasibility and rate of a solid state reaction include, reaction conditions, structural properties of the reactants, surface area of the solids, their reactivity and the thermodynamic free energy change associated with the reaction The structural difference between reactants and products often makes solid state reactions difficult since a large amount of structural reorganization is involved in forming the product. During reactions, bonds must be broken and reformed and atoms migrate over considerable distances. But ions are trapped on their appropriate lattice sites and it is difficult for them to jump out and diffuse through the crystal. At high temperatures, ions diffuse across the interface to form a product layer which will subsequently grow even if the diffusion rate becomes slow. For the completeness of the reaction and to form a good microstructure, prolonged heat treatment or repeated heat treatment is required at sufficiently high temperature below the melting point of the material. The different steps involved in the solid state reaction for the synthesis of complex ceramic oxides for technical applications are depicted in the flowchart shown in Fig. 3.1.

3.3.1 Selection and Weighing of Starting Materials

The characteristics of the starting materials have a remarkable effect on subsequent processing, such as consolidation of the powder into a green body and firing to produce the desired microstructure. For the synthesis of electro ceramic materials, highly purified (99.99 %) powders of starting materials (usually oxides or carbonates) with uniform particle size are selected depending upon the composition. Stoichiometric amounts of the constituent oxides are calculated based on the chemical formula of the final product. Raw materials are weighed accordingly using an electronic balance with accuracy up to four decimal places. A preheating of reactant

materials is sometimes required to remove any moisture content to ensure correct stoichiometry in weighing.

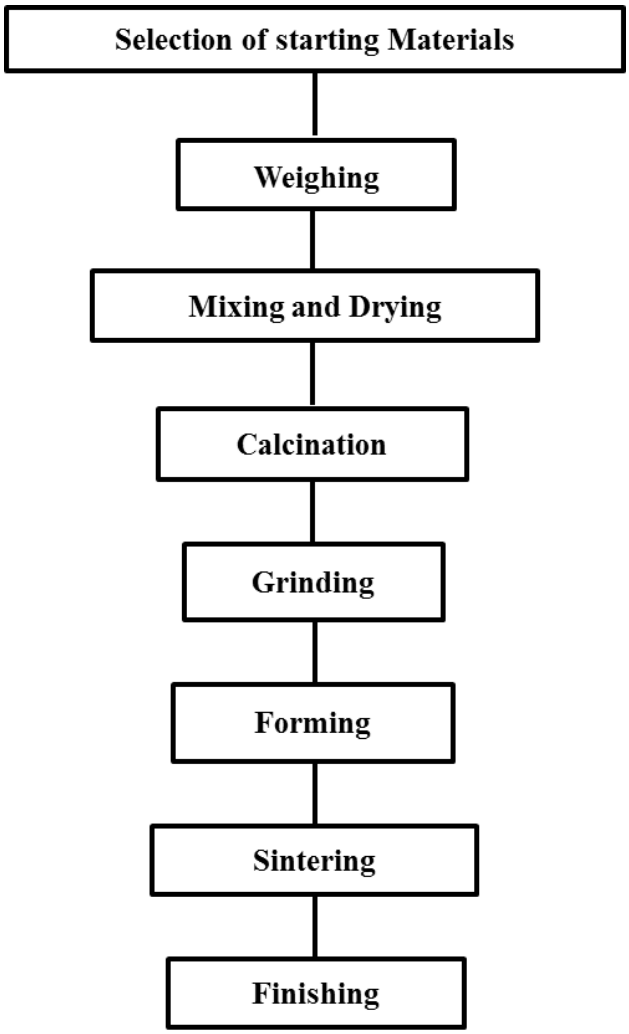

Fig. 3.1 Flowchart showing different steps in solid state reaction route

3.3.2 Mixing and drying

After the reactants have been weighed out in the required amounts, they are mixed together. For manual mixing of small quantities, usually an agate mortar and pestle are employed. Sufficient amount of some volatile organic liquid- preferably acetone or alcohol is added to the mixture to aid homogenization. During the process of grinding and mixing, the organic liquid gradually volatilizes and has usually evaporated completely after 10 to 15 minutes. For quantities much larger than ~20 gm, mechanical mixing is usually adopted using a ball mill and the process may take several hours. After mixing the powder is kept in a hot air oven at 100 ºC for 30

minutes. The process of mixing and drying is repeated at least three times so as to get a homogeneous, finely powdered mixture. For solid state diffusion mechanism, the growth of the reaction product in powder system occurs at the contact points. The homogeneity of mixing is one of the most important factors which decide the ability of a process to produce homogeneous, single phase powder. The size and distribution of the reactant particles are important factors for deciding the degree of homogeneity. A homogeneous mixture has great influence on the diffusion distances and the number of contacts between the reactant particles. The presence of agglomerates results in porosity of the final product. Therefore, it is necessary to mix the reactants to a high level and to powder them repeatedly. During mixing process these agglomerates get broken and defects are introduced into the grains which enhance the diffusion mechanism (Rahaman 2003).

3.3.3 Calcination

Calcination is a thermal treatment process applied to a mixture of solid materials in order to bring about a thermal decomposition, phase transition, or a chemical reaction to form a product with the removal of volatile or gaseous fractions. The calcination process normally takes place at temperatures below the melting point of the product materials. The purpose of calcination is to promote sufficient interaction between constituents to a material which upon compaction and sintering forms the desired final product. Though the final phases of interest may not be completely formed, the calcination yields a consistent product.

3.3.4 Grinding

The process in which small particles are produced by reducing the size of larger ones by mechanical forces is usually referred to as comminution. It involves operations such as crushing, grinding, and milling. Grinding prepares the reacted material for ceramic forming by changing its physical characteristics like particle size, size distribution etc. whereas milling sometimes causes chemical reaction (mechanochemical reaction). The grinding process has an effective role in deciding the degree of homogeneity. Generally grinding to somewhere around 1 to 10 μm is advisable since grinding the solid material to very fine powder (<1 μm) can lead to the formation of agglomerates which result in non-uniform packing. Agate mortar with pestle is used for grinding the calcined powder.

3.3.5 Ceramic Forming

Ceramic forming involves consolidation and molding of ceramic powders to produce a cohesive body of the desired size and shape. Dry powders can be simultaneously compacted and shaped by pressing in a rigid die or flexible mold. Pressing is the most widely used forming process in ceramics manufacturing. Powder pressing involves three general stages including: (1) filling the die or mold; (2) compacting and shaping the powder; and (3) extracting the pressed part from the die. Pressing defects can be minimized by using granulated powders and appropriate additives, and by controlling the pressing pressure, pressurization rate, and depressurization rate used in forming.

Binders are typically long chain polymers that serve the primary function of providing strength to the green body by forming bridges between the particles. The addition of binder imparts sufficient strength and elastic properties which helps in the handling and shaping of ceramic powders. The commonly used polymer binders are PVA (Polyvinyl Alcohol), PEG (Polyethylene Glycol) etc. Binder selection depends on the ceramic powder, the size of the part, how it is formed, and the green density and strength required. Binder concentration is determined by these variables and the particle size, size distribution, and surface area of the ceramic powder. The polymeric dispersions and organic binders provide the pressed ceramic powders with optimal properties from the point of view of thickening abilities and mechanical strength of pressed samples. The binder concentration for different types of processes is different and for dry processing it is about 3 – 5 mole %. During heating, these binder materials will burn out since they have low boiling point.

Die compaction of powders is a process which involves filling a die with powder, compression of the powder using rigid punches to form a dense compact, and ejection from the die. Compaction of powder has a vital role in usual ceramic fabrication processes. The packing structure of the green body basically influences the microstructural development during sintering and consequently determines the properties of sintered ceramics. A large number of ceramics are formed by uniaxial dry pressing because of its high productivity and suitability for automation. The calcined powder undergoes a limited sintering and hence it is again grounded thoroughly. The resulting powder is mixed well with suitable binder of appropriate

amount. This mixture is then again ground using mortar and pestle. This thoroughly mixed powder is transferred to a suitable die and is subjected to compaction by slow uniaxial dry pressing to ensure the escape of entrapped air. Uniaxial pressing involves the compaction of powder into a rigid die by applying pressure in a single axial direction through a rigid punch or piston. Cylindrical pellets of 10 mm diameter and 2–3 mm thicknesses are prepared to maintain the aspect ratio so that the pressure distribution is more or less uniform in the powder compacts. A pressure of 150 - 250 MPa is applied for ceramic forming.

3.3.6 Solid State Sintering

Powder compacts are made dense by heat treatments at temperatures where mass transport can occur to eliminate the voids between the powder particles. Densification is driven by the free energy decrease associated with the powder's surface area and differential surface curvature causes mass to fill the contact region between touching particles. This heat treatment process for producing dense ceramics is called sintering. In solid state sintering, the powder compact is heated at a temperature below the melting point of the material. Here the particles are bonded together spontaneously without the formation of the liquid phase. The sinterability of the powder compact depends on the chemistry of the powder material, particle size, agglomeration, and the pressure applies during the compaction. The variables of solid state sintering process are sintering temperature, duration, and heating and cooling rates. During solid sintering process, the porosity decreases leading to high density and strength whereas grain size increases. The green body shrinks during sintering and the shrinkage depends upon the processing parameters. Microstructures that control properties are primarily developed during densification and post-densification heat treatments can be used to develop specific microstructures to optimize a specific property. But, in all cases, the average microstructure and heterogeneities within the microstructure are a direct consequence of all processing stages starting with the chemistry and characteristics of the powder (Binner 1990).

3.3.7 Finishing

Finishing is the final step of ceramic fabrication which is required to meet dimensional tolerance, achieve improved surface finish and to remove surface flaws.

This can be achieved through polishing of the surface using emery paper. Final finishing can be done with diamond paste and polishing cloth.

3.4 Characterization Techniques

The correlation of physical and chemical properties with structural characteristics and preparation conditions are of crucial importance for the development optimization of new materials for technological applications. Characterization refers to the use of external techniques to probe into the internal structure and properties of a material. Characterization methods includes to those that provide information about composition, structure, and defects and that yield information primarily related to materials properties, such as thermal, electrical, and mechanical properties. Characterization techniques can be loosely classified into five different categories: diffraction methods, chemical analysis, microscopy, thermal analysis and spectroscopic methods. A brief description of characterization methods used for the investigation of structural and electrical properties of oxide ion conductors is presented in the latter part of this chapter.

3.4.1 Powder X-ray Diffraction Technique

X-ray powder diffraction is a non-destructive technique widely applied for the characterization of crystalline materials. X-rays are electromagnetic radiation found between gamma-rays and the ultraviolet in the electromagnetic spectrum with wavelength ranging from 0.1 – 100 Å, typically similar to the interatomic distances in a crystal. This is convenient as it allows crystal structures to diffract X-rays. . The discovery of X-rays in 1895 enabled scientists to probe crystalline structure at the atomic level. X-ray diffraction has been in use in two main areas, for the fingerprint characterization of crystalline materials and the determination of their structure. Each crystalline solid has its unique characteristic X-ray powder pattern which may be used as a "fingerprint" for its identification. Once the material has been identified, X-ray crystallography may be used to determine its structure, i.e. how the atoms pack together in the crystalline state and what the interatomic distance and angle are etc. X-ray diffraction is one of the most important characterization tools used in solid state chemistry and materials science.

X-rays primarily interact with electrons in atoms. When x-ray photons collide with electrons, some photons from the incident beam will be deflected away from the

direction where they originally travel. If the wavelength of these scattered x-rays did not change (meaning that x-ray photons did not lose any energy), the process is called elastic scattering in that only momentum has been transferred in the scattering process. These are the x-rays that we measure in diffraction experiments, as the scattered x-rays carry information about the electron distribution in materials. Diffracted waves from different atoms can interfere with each other and the resultant intensity distribution is strongly modulated by this interaction. If the atoms are arranged in a periodic fashion, as in crystals, the diffracted waves will consist of sharp interference maxima (peaks) with the same symmetry as in the distribution of atoms. Measuring the diffraction pattern therefore allows us to deduce the distribution of atoms in a material.

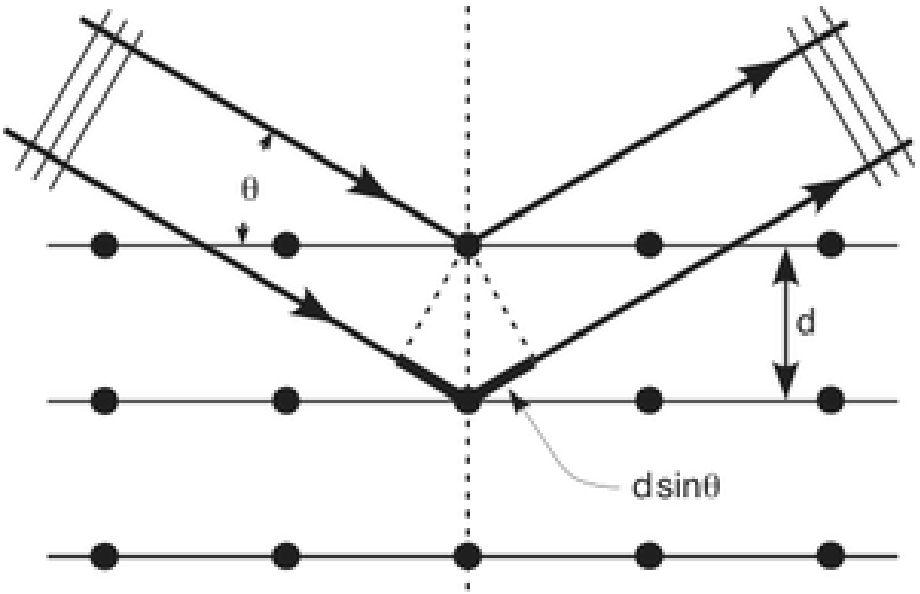

Fig. 3.2 Diffraction of X-rays by crystallographic planes of atoms

The peaks in an X-ray diffraction pattern are directly related to the atomic distances. Let us consider an incident X-ray beam interacting with the atoms arranged in a periodic manner as shown in the Fig. 3.2. The atoms, can be viewed as forming different sets of planes in the crystal and for a given set of lattice planes, the condition for a diffraction (peak) to occur can be simply written as

$$\mathbf{2dsin\theta = n\lambda} \qquad (\mathbf{3.1})$$

which is known as the Bragg's law, after W.L. Bragg, who first proposed it. In the equation, d is the interplanar distance, θ is the angle of diffraction, n is the order of diffraction and λ is the wavelength of the incident X-rays. The Bragg's Law is one of most important laws used for interpreting X-ray diffraction data.

X-ray diffractometers consist of three basic elements: an X-ray tube, a sample holder, and an X-ray detector. X-rays are generated in a cathode ray tube by heating a filament to produce electrons, accelerating the electrons toward a target by applying a voltage, and bombarding the target material with electrons. When electrons have sufficient energy to dislodge inner shell electrons of the target material, characteristic X-ray spectra are produced. These spectra consist of several components, the most common being K_α and K_β. K_α consists, in part, of $K_{\alpha1}$ and $K_{\alpha2}$. $K_{\alpha1}$ has a slightly shorter wavelength and twice the intensity as $K_{\alpha2}$. The specific wavelengths are characteristic of the target material (Cu, Fe, Mo, Cr). Filtering, by foils or crystal monochromators, is required to produce monochromatic X-rays needed for diffraction. $K_{\alpha1}$ and $K_{\alpha2}$ are sufficiently close in wavelength such that a weighted average of the two is used. Copper is the most common target material for single-crystal diffraction, with Cu K_α radiation = 1.5418 Å. These X-rays are collimated and directed onto the sample. As the sample and detector are rotated, the intensity of the reflected X-rays is recorded. When the geometry of the incident X-rays impinging the sample satisfies the Bragg Equation, constructive interference occurs and a peak in intensity occurs. A detector records and processes this X-ray signal and converts the signal to a count rate which is then output to a device such as a printer or computer monitor.

The d-spacing of each peak is then obtained by solution of the Bragg equation for the appropriate value of λ. Once all d spacings have been determined, automated search/match routines compare the *d*-values of the unknown to those of known materials. Because each material has a unique set of d-spacings, matching these d-spacings provides an identification of the unknown sample. Files of d- spacings for several thousands of inorganic compounds are available from the International Centre for Diffraction Data (ICDD) as the Powder Diffraction File (PDF).

Rietveld analysis is one of the best techniques that have been developed for refining crystal structures from powder diffraction data. The method takes a trial

structure, calculates a powder diffraction profile and compares it to the measured profile. The trial structure is modified by changing various refineable parameters, including lattice parameters, atomic positions, thermal parameters, site occupancies, peak shape parameters, etc. until a best-fit match is obtained with the measured pattern. Rietveld structure refinement is a method for estimating the intensities of Bragg peaks in a powder diffraction pattern within the constraints imposed by a crystallographic space group. The entire diffraction profile is calculated (model) and compared with the observed step profile point by point and the parameters of the model are then adjusted using the Least-Square method.

The structural model involves three categories of parameters: crystallographic parameters describing size of the unit cell, space group, atomic positions, thermal parameters and occupancy, instrumental parameters describing the optics and set up of the diffractometer and profile parameters describing the shape of the Bragg peaks. It is a crucial feature of the Rietveld method that no effort is made in advance to allocate observed intensity to particular Bragg reflections or to resolve overlapped reflections. Consequently a good starting model is required. Rietveld method is not a structure solution method. It is a structure refinement method. The intensity at each point i, in the pattern is calculated from the structural model using the equation

$$\mathbf{y_{ci} = \sum_K L_K |F_K|^2 \varphi(2\theta_i - 2\theta_K) P_K A + y_{bi}} \qquad (3.2)$$

where 's' is the scale factor, K represents Miller indices h, k, l for a Bragg reflection, L_K contains the Lorentz, polarization and multiplicity factors, φ is the reflection profile function, P_K is the preferred orientation function, A is the absorption factor, F_K is the structure factor for K^{th} Bragg reflection, y_{ci} is the calculated intensity at i^{th} step and y_{bi} is the background intensity at i^{th} step. The quantity minimized in least square fit is the residual, S_y:

$$\mathbf{S_y = \sum_i w_i (y_i - y_{ci})^2} \qquad (3.3)$$

where w_i is a weight factor, y_i is the observed intensity at the i^{th} step and sum is over all the data points.

The Rietveld refinement process will adjust the refineable parameters until the residual is minimized and a best fit is obtained. The goodness of fit can be judged

from a set of parameters obtained after the refinement called residual parameters or R-values like R- structure factor (R_F), R-Bragg factor (R_B), R- pattern (R_P) and R-weighted pattern (R_{wp}). Goodness of fit factor (S), Chi-square (χ^2) and Durbin-Watson statistic (d) are also indicators of goodness of fit obtained by Rietveld method.

3.4.2 Raman Spectroscopy

Raman spectroscopy is a spectroscopic technique used in condensed matter physics and chemistry to study vibrational, rotational, and other low-frequency modes in a system. It relies on inelastic scattering, or Raman scattering of monochromatic light, usually from a laser in the visible, near infrared, or near ultraviolet range. The laser light interacts with phonons or other excitations in the system, resulting in the energy of the laser photons being shifted up or down. The shift in energy gives information about the phonon modes in the system. Although both IR absorption and Raman spectroscopy measure the vibrational spectra of materials, the physical processes are different, the selection rules that determine which of the vibrational modes are excited are different, and the two spectroscopies must be considered to be complementary. Both, however, these are characterization probes that are sensitive to the details of atomic arrangement and chemical bonding.

The Raman effect occurs when light impinges upon a molecule and interacts with the electron cloud and the bonds of that molecule. For the spontaneous Raman effect, a photon excites the molecule from the ground state to a virtual energy state. When the molecule relaxes it emits a photon and it returns to a different rotational or vibrational state. The difference in energy between the original state and this new state leads to a shift in the emitted photon's frequency away from the excitation wavelength. If the final vibrational state of the molecule is more energetic than the initial state, then the emitted photon will be shifted to a lower frequency in order for the total energy of the system to remain conserved. This shift in frequency is designated as a Stokes shift. If the final vibrational state is less energetic than the initial state, then the emitted photon will be shifted to a higher frequency, and this is designated as an Anti-Stokes shift.

A change in the molecular polarization potential or amount of deformation of the electron cloud with respect to the vibrational coordinate is required for a molecule

to exhibit a Raman effect. The amount of the polarizability change will determine the Raman scattering intensity. The pattern of shifted frequencies is determined by the rotational and vibrational states of the sample. Raman spectroscopy is primarily a structural characterization tool. The spectrum is more sensitive to the lengths, strengths, and arrangement of bonds in a material than it is to the chemical composition. The Raman spectrum of crystals likewise responds more to details of defects and disorder than to trace impurities and related chemical imperfections.

Raman spectra of molecules and crystals are composed of a pattern of relatively sharp lines. The wavenumber scale for most vibrations extends from 50 cm^{-1} to about 1800 cm^{-1} with some molecular vibrations extending to 3500 cm^{-1} Line widths are on the order of 1-5 cm^{-1}. The Raman spectrum thus has a fairly high density of information and can be used as a fingerprint for the identification of unknown materials by direct comparison of the spectrum of the unknown with spectra in a reference catalog. Raman spectroscopy is sensitive to ordering arrangements of crystal structures and the effect depends on the type of order. Ordering atoms onto specific lattice sites in the parent structure often forms derivative structures having different space groups. The new symmetry leads to relaxed selection rules, which in turn lead to new Raman lines or to the splitting of the lines of the parent structure. Group theoretical calculations allow a good prediction of expected spectral behavior for possible ordering schemes, and Raman (IR) spectra can be used select the correct model. Raman spectra of solid solutions, crystals with lattice defects, and systems having other types of structural disorder usually exhibit a pronounced line broadening in comparison with ordered structures. Structural defects, such as lattice vacancies, produce line broadening with little temperature dependence.

3.4.3 Scanning Electron Microscopy

Electron microscopes are scientific instruments that use a beam of energetic electrons to examine objects on a very fine scale. Electron microscopes were developed due to the limitations of Light Microscopes which are limited by the physics of light**.** The scanning electron microscope (SEM) uses a focused beam of high-energy electrons to generate a variety of signals at the surface of solid specimens. The signals that derive from electron-sample interactions reveal information about the sample including external morphology (texture), chemical

composition, and crystalline structure and orientation of materials making up the sample. In most applications, data are collected over a selected area of the surface of the sample, and a two dimensional image is generated that displays spatial variations in these properties. Areas ranging from approximately 1 cm to 5 microns in width can be imaged in a scanning mode using conventional SEM techniques (magnification ranging from 20X to approximately 30,000X, spatial resolution of 50 nm to 100 nm).

A Scanning Electron Microscope is composed of an electronic optic column, sample chamber, a vacuum system, detectors to catch all the signals that the sample gives out and video screen to examine the pictures. Electron gun produces an electron beam and the beam is accelerated by the high voltage (up to 30 KV) created between the wire and the anode. It is then focused on the sample surface by electromagnetic lenses. When the beam touches the surface of the sample, it produces interactions and these interactions are each collected by the right detector, and are then converted into an electric signal. The video screen is used to examine the sample synchronically with the electron beam of the optic column.

The principle images produced in the SEM are of three types: secondary electron images, backscattered electron images, and elemental X-ray maps. Secondary and backscattered electrons are conventionally separated according to their energies. They are produced by different mechanisms. When a high-energy primary electron interacts with an atom, it undergoes either inelastic scattering with atomic electrons or elastic scattering with the atomic nucleus. In an inelastic collision with an electron, some amount of energy is transferred to the other electron. If the energy transfer is very small, the emitted electron will probably not have enough energy to exit the surface. If the energy transferred exceeds the work function of the material, the emitted electron can exit the solid. When the energy of the emitted electron is less than about 50 eV**,** by convention it is referred to as a secondary electron (SE). Most of the emitted secondary electrons are produced within the first few nm of the surface. These secondary electrons are detected, processed and imaged. For normal morphological as well as microstructural studies secondary electron image more useful.

The use of the SEM requires very little in regard to sample preparation, provided that the specimen is vacuum compatible. Non-conductive solid specimens

should be coated with a layer of conductive material, except when observed with Variable Vacuum or Environmental SEM. Such coatings are made on the surface of non-conductive samples using gold or palladium (Goldstein *et al.* 1981).

3.4.4 Transmission Electron Microscopy

Transmission electron microscope (TEM) is a scientific instrument that uses electrons instead of light to scrutinize objects at very fine resolutions. They were developed in the 1930s when scientists realized that electrons can be used instead of light to "magnify" objects or specimens under study. TEMs provided a means to go beyond the magnification and resolution limits of light microscopes, allowing for magnification of up to 100,000X and resolutions in the nanometer range owing to the small de Broglie wavelength of electrons. In Transmission electron microscope a beam of electrons is transmitted through an ultra-thin specimen, interacting with the specimen as it passes through. An image is formed from the interaction of the electrons transmitted through the specimen and the image is magnified and focused onto an imaging device, such as a fluorescent screen, or detected by a CCD camera.

A great advantage of the transmission electron microscope is in the capability to observe, by adjusting the electron lenses, both electron microscope images (information in real space) and diffraction patterns (information in reciprocal space) for the same region of the specimen. Selected area electron diffraction (SAED), is a crystallographic experimental technique that can be performed inside a transmission electron microscope. When a thin crystalline specimen is subjected to a parallel beam of high-energy electrons, the electrons typically have energy of 100 - 400 KeV, the electrons pass through the sample easily. If electrons are treated as waves and since the wavelength of high-energy electrons is a few thousandths of a nanometer, and the spacing between atoms in a solid are about a hundred times larger, the atoms act as a diffraction grating to the electrons. Therefore some fraction of electrons will be diffracted to particular angles, determined by the crystal structure of the sample, while others continue to pass through the sample without deflection. The selected area diffraction pattern will be a series of spots and each spot corresponding to a satisfied diffraction condition of the sample's crystal structure. For polycrystalline materials a set of diffractions rings are usually observed corresponding to a family of crystallographic planes (Williams and Carter 1996).

3.4.5 Impedance Spectroscopy

Impedance spectroscopy (IS) is a general term that subsumes the small-signal measurement of the linear electrical response of a material of interest (including electrode effects) and the subsequent analysis of the response to yield useful information about the physicochemical properties of the system. Analysis is generally carried out in the frequency domain, although measurements are sometimes made in the time domain and then Fourier transformed to the frequency domain. Electrochemical impedance spectroscopy (EIS) involves measurements and analysis of materials in which ionic conduction strongly predominates. Examples of such materials are solid and liquid electrolytes, fused salts, ionically conducting glasses and polymers, and nonstoichiometric ionically bonded single crystals, where conduction can involve motion of ion vacancies and interstitials. EIS is also valuable in the study of fuel cells, rechargeable batteries, and corrosion (Macdonald 1992).

Generally, the electric conduction properties of the complex polycrystalline ceramics are due to intra-grain, inter-grain and electrode effects. The motion of charges could take place by charge displacement, dipole reorientation, space charge formation, hopping and other mechanisms. In order to understand the electrical properties of a given sample, the ceramic grain, the grain boundary and the electrode contributions must be separated. The inter-grain boundaries in ceramics are defective regions as well as the place of segregated impurities or dopants. Accordingly, it is expected that from the electrical point of view, the grain bulk and the grain boundary regions have different dielectric and conductive properties. In addition, the ceramic region in contact with electrodes might be "modified" with respect to the inner part of the bulk: different Fermi levels of the two materials in contact give rise to Schottky barriers, imperfect conductivity of the electrodes create a screening region changing the potential distribution in their neighborhood and metallic ions might diffuse into the ceramic creating a doped interface regions. In any of these situations, the dielectric and conductive properties at the contact electrode-ceramics might be different with respect to the rest of material. The complex impedance analysis has proved as a very powerful tool for separating these contributions (Mitoseriu *et al.* 2008).

Electrical measurements to evaluate the electrochemical behavior of electrolyte materials are usually made with cells having two identical electrodes applied to the faces of a sample in the form of a circular cylinder or rectangular parallelepiped. The most common and standard procedure of EIS is to measure impedance by applying a single-frequency voltage or current to the interface and measuring the phase shift and amplitude, or real and imaginary parts, of the resulting current at that frequency using either analog circuit or fast Fourier transform (FFT) analysis of the response. Commercial instruments are available which measure the impedance as a function of frequency automatically in the frequency ranges of about 1 mHz to 1 MHz and are easily interfaced to laboratory microcomputers. Any intrinsic property that influences the conductivity of an electrode–materials system, or an external stimulus, can be studied by IS. The parameters derived from an IS spectrum fall generally into two categories: (a) those pertinent only to the material itself, such as conductivity, dielectric constant, motilities of charges and (b) those pertinent to an electrode–material interface, such as adsorption–reaction rate constants, capacitance of the interface region, and diffusion coefficient of neutral species in the electrode itself (Barsoukov and Macdonald 2005).

EIS data for electrochemical cells such as fuel cells are most often represented in Nyquist plots. Nyquist plot depicts the imaginary impedance, which is indicative of the capacitive and inductive character of the cell, versus the real impedance of the cell. This kind of graphical representation is also known as a Cole–Cole plot or a complex impedance plane plot. Cole-Cole plots have the advantage that activation-controlled processes with distinct time-constants show up as unique impedance arcs and the shape of the curve provides insight into possible mechanism or governing phenomena (Orazem and Tribollet 2008). Equivalent circuit modeling of EIS data is used to extract physically meaningful properties of the electrochemical system by modeling the impedance data in terms of an electrical circuit composed of ideal resistors (R), capacitors (C), and inductors (L). Since real systems do not necessarily behave ideally with processes that occur distributed in time and space, specialized circuit elements such as the generalized constant phase element (CPE), Warburg element (ZW) etc. can be used for equivalent circuit modeling (Barsoukov and Macdonald 2005).

Chapter 4

Order - disorder Phase Transformations in Ca–Y–Zr–Ta–O Pyrochlore Oxide System

Order-disorder transformations in a quaternary pyrochlore oxide system, Ca – Y – Zr – Ta – O were studied by powder X-ray diffraction (XRD) method, transmission electron microscope (TEM) and FT NIR Raman spectroscopic techniques. The solid solutions in different ratios: 4:1, 2:1, 1:1, 1:2, 1:4, 1:6 of $CaTaO_{3.5}$ and $YZrO_{3.5}$ were prepared by the conventional high temperature ceramic route. The XRD results and Rietveld analysis revealed that the crystal structure changed from an ordered pyrochlore structure to a disordered defect fluorite structure as the ratios of the solid solutions of $CaTaO_{3.5}$ and $YZrO_{3.5}$ were changed from 4:1 to 1:4. This structural transformation in the present system is attributed to the lowering of the average cation radius ratio, r_A/r_B as a result of progressive and simultaneous substitution of larger cation Ca^{2+} with Y^{3+} at A sites and smaller cation Ta^{5+} with Zr^{4+} at B sites. Raman spectroscopy and TEM analysis corroborated the XRD results. Lattice thermal expansion was measured by high temperature XRD and oxide ion conductivity was measured by impedance analyzer and the results were correlated with structural properties.

A.N. Radhakrishnan, P. Prabhakar Rao, K.S. Sibi, M. Deepa and Peter Koshy, "Order–disorder phase transformations in quaternary pyrochlore oxide system: Investigated by X-ray diffraction, transmission electron microscopy and Raman spectroscopic techniques", ***Journal of Solid State Chemistry***, 2009, 82 (8), 2312-2318.

4.1 Introduction

Pyrochlore oxides of the general formula, $A_2B_2O_7$ (A and B are metals) have considerable importance in both basic science (Champion *et al.* 2001, García-Adeva and Huber 2002, Gardner *et al.* 1999, Hassan *et al.* 2003, Subramanian *et al.* 1998) and engineering (Begg *et al.* 2001, Lian *et al.* 2002, Lutique *et al.* 2003, Lutique *et al.* 2003) and become a point of attraction for researchers, especially in material science. This is because pyrochlores lend themselves to a wide variety of substitution at the A and B sites provided the ionic radius ratio (r_A/r_B) and charge neutrality criteria are satisfied. The crystal structure can tolerate vacancies at A and O sites to an extent allowing cation and anion migration. These compounds exhibit a wide variety of physical properties such as semiconducting properties, dielectric properties, ionic conductivity etc. (Subramanian, *et al.* 1983). Many vacancy containing pyrochlores possess good oxide ion conductivity and can be considered as a potential candidate as solid electrolytes for solid oxide fuel cell (SOFC) applications (Moon and Tuller 1988).

The order-disorder transformation in a pyrochlore structure is of immense interest because this is the only oxide in which order-disorder transformations occur in both the anion and cation arrangements. It has been reported earlier that disorder can be introduced into the structure by ion-irradiation (Hess *et al.* 2002, Lian *et al.* 2003, Lian *et al.* 2004, Lian, *et al.* 2001, Wang *et al.* 1999), compositional changes (which lead to lower the difference in the ratio of the ionic size of the cations at the A sites to that at B sites) (Wuensch, *et al.* 2000), pressure (Zhang, *et al.* 2006) and thermal treatment (Wuensch and Eberman 2000). Disorder in pyrochlore oxides are of great interest in the area of solid oxide electrolytes because they exhibit high oxide ion conductivity which makes them suitable for applications in SOFCs (Wuensch, *et al.* 2000). It is drawn from earlier investigations that one of the key parameters influencing structural disorder in $A_2B_2O_7$ pyrochlores is the cation radius ratio, r_A/r_B. As r_B approaches r_A, disorder in both the cations and anions sublattices increases ultimately resulting complete disorder characteristic of the defect fluorite structure as in the case of $Y_2(Ti_yZr_{1-y})_2O_7$ (Liu *et al.* 2004) and $Gd_2(Ti_yZr_{1-y})_2O_7$ when Zr content is high (Moon and Tuller 1988). These types of disorder may lack stability of the

phase for repeated thermal cycles. Apart from the cation ionic radius ratio (r_A/r_B) considerations, the investigations on $Y_2(Sn_xTi_{1-x})_2O_7$ and $Gd_2(Sn_xTi_{1-x})_2O_7$ solid solutions indicated that the crystal chemistry of B site cations (e.g. chemical bonding) have an important effect on the order–disorder transformation and the degree of disorder in the pyrochlore (Ewing, *et al.* 2004).. In the present investigation, some quaternary pyrochlore type oxides in Ca – Y – Zr – Ta – O system were prepared in which pyrochlore (order) to defect fluorite (disorder) transformation is observed when the $YZrO_{3.5}$ phase is more than $CaTaO_{3.5}$ phase. This order disorder transformation is studied by powder X-ray diffraction, Raman spectroscopy and Transmission electron microscopy techniques. Lattice thermal expansion behavior of the prepared complex oxides were measured by high temperature XRD and oxide ion conducting properties were measured by impedance analyzer. The changes in microstructure, lattice thermal expansion and oxide ion conductivity that accompany order-disorder transformation were investigated to derive a structure-property correlationship.

4.2 Experimental

Solid solutions in different stoichiometric compositions: $Ca_{1.6}Y_{.4}Zr_{.4}Ta_{1.6}O_7$, $Ca_{1.33}Y_{.67}Zr_{.67}Ta_{1.33}O_7$, $CaYZrTaO_7$, $Ca_{.67}Y_{1.33}Zr_{1.33}Ta_{.67}O_7$, $Ca_{.4}Y_{1.6}Zr_{1.6}Ta_{.4}O_7$ and $Ca_{.29}Y_{1.71}Zr_{1.71}Ta_{.29}O_7$ in a Ca – Y – Zr – Ta – O system were prepared by the conventional ceramic route using the starting materials, $CaCO_3$, Y_2O_3, ZrO_2 and Ta_2O_5 (ACROS ORGANICS, 99.99%). For better understanding, these compounds can be treated as different ratios of Ca – Ta – O and Y – Zr – O system that is 4:1, 2:1, 1:1, 1:2, 1:4, 1:6. These are represented as C4YZT4, C2YZT2, CYZT, CY2Z2T, CY4Z4T and CY6Z6T respectively. (These nomenclatures are used in the discussion of the later part of the text.). The raw materials were weighed according to the stoichiometry of the samples and then mixed thoroughly in an agate mortar. Acetone was added to the powdered mixture for proper mixing. Then, the mixture was dried in an air oven at 100 ºC for 1 h. This procedure of mixing and subsequent drying was repeated thrice to get a homogeneous mixture. The powdered samples were calcined at 1300 ºC for 6 h. The calcined product was ground into a fine powder and then mixed with 2 wt. % solution of polyvinyl alcohol (PVA) as the organic binder for

strengthening and good compaction of the pellet. The dried powder was pressed into cylindrical pellets of 10 mm diameter and about 2 - 3 mm thickness using a hydraulic press. Pellets were initially heated to 600 ºC and kept for 30 minutes to completely remove the organic binder and then sintered at a temperature of 1600 ºC for 6 h. Powder X-ray diffraction patterns were recorded to identify the crystalline phase of the sintered samples using a Ni filtered Cu K_α radiation by a Philip's X'pert diffractometer (Step size = 0.067, Scanning time per step = 39.95 seconds, Divergence slit = 1^o, Receiving slit = 12.75 mm and exported by X'Pert software). The unit cell parameters were calculated by least square method and Rietveld analysis was also performed to refine the structure using X'pert plus software. The FT NIR Raman spectra of the powdered samples were recorded on a Bruker RFS100/S spectrometer using near infrared laser excitation (Nd: YAG, 1064 nm). Standard Ge detector cooled to liquid nitrogen temperature is used and it was set to scan over the range from 50 cm^{-1} – 1000 cm^{-1}. The resolution of the spectrometer is 4 cm^{-1}. The selected area electron diffraction (SAED) pattern and high resolution transmission electron microscopy (HRTEM) of the samples were carried out on a FEI TECNAI $30G^2$ S-TWIN transmission electron microscope (TEM) operating at 300 kV. The sintered samples were ground into very fine powder and a small amount of the powder is dispersed in acetone medium using ultrasonicator. The solution is drop casted on carbon coated copper grid using a micropipette and dried. For lattice thermal expansion studies, the XRD patterns of sintered samples were recorded from $2\theta = 10 – 90^o$, in the temperature range 298 – 1273 K on a PANalytical Philips X'pert Pro MPD XRD unit equipped with Anton Paar HTK attachment, at a regular interval of 200 K, in vacuum (~$1x10^{-4}$ mbar). SEM micrographs of the thermally etched samples were recorded using a scanning electron microscope (JEOL, JSM 5600 LV). For impedance spectroscopic studies, a high temperature curing silver paste was applied on polished flat faces of the pellet and electroded with long silver wires. The electroded pellets were cured in a tube furnace for half an hour at 600 ºC. Impedance measurements of the pellets were carried out from 400 ºC to 750 ºC in the frequency range 10 Hz to 1 MHz using a computer controlled Impedance Analyzer (Solartron, SI 1260). The complex impedance plots were made with the SMART software supplied by M/s Solartron Schlumberger, U.K.

4.3 Results and discussion

4.3.1 Powder X-ray Diffraction Studies

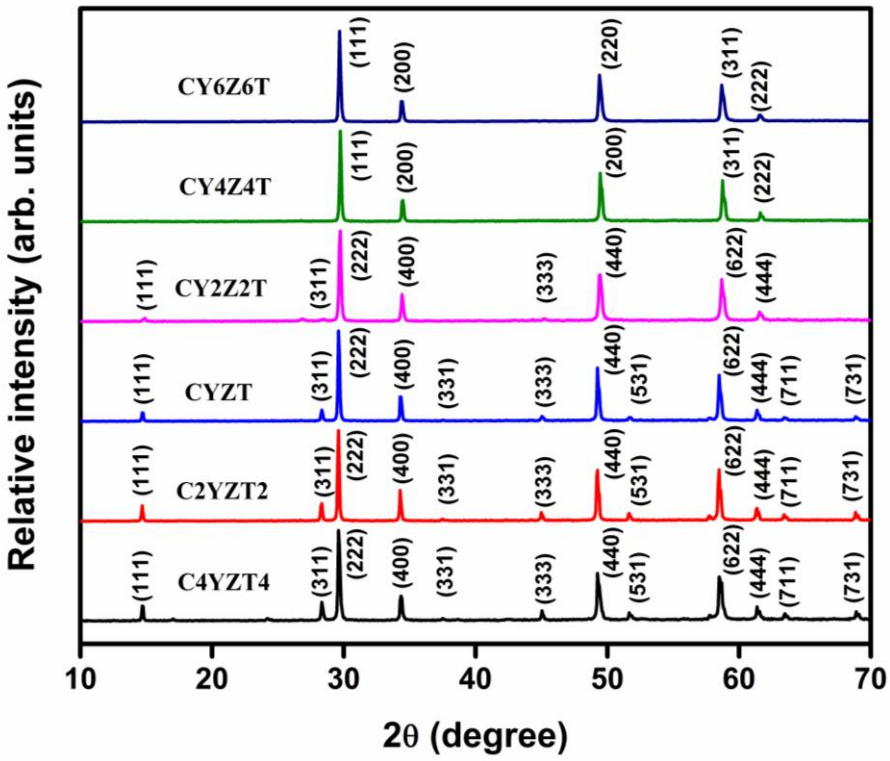

Fig 4.1 Powder X-ray diffraction patterns of various compositions in the Ca–Y–Zr–Ta–O system.

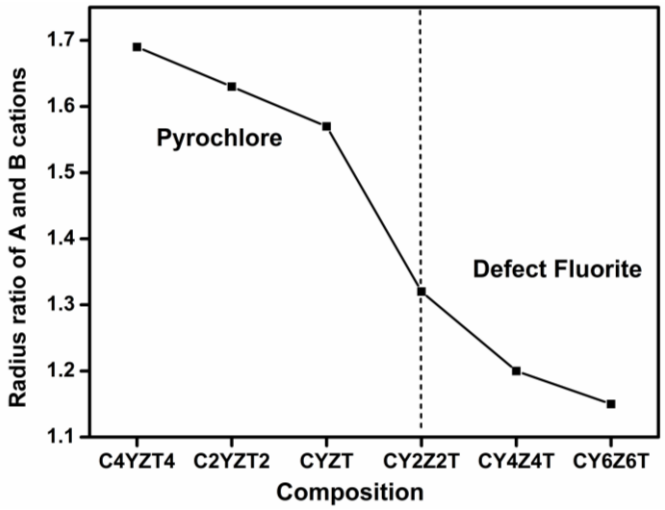

Fig. 4.2 Plot of radius ratio (r_A/r_B) as a function of various compositions in the Ca–Y–Zr–Ta–O system

Fig. 4.1 shows the powder XRD patterns obtained for various stoichiometries: C4YZT4, C2YZT2, CYZT, CY2Z2T, CY4Z4T and CY6Z6T in the Ca – Y – Zr – Ta – O system. The XRD patterns of C4YZT4, C2YZT2, CYZT and CY2Z2T are similar to the earlier reported cubic pyrochlore type oxides of the formula $A_2B_2O_7$ such as $(Ca_{2/3}Y_{1/3})_2(Ti_{1/3}Nb_{2/3})_2O_7$ (Nair *et al.* 2007) and $Bi_{1.5}ZnNb_{1.5-x}Ta_xO_7$ (Wang *et al.* 2007). All the reflections are indexed with respect to the cubic pyrochlore structure in the space group $Fd\bar{3}m$ (No. 227). The presence of super lattice reflections peaks like (111), (311), (331), (333), (531), (711) and (731) points to a doubling of the cubic-cell parameter, the characteristic peaks of the pyrochlore structure. It was further found that the intensity of the characteristic super-structure peaks systematically diminishes on going from C4YZT4 to CY2Z2T as the $YZrO_{3.5}$ phase is increased. On the other hand, the absence of these pyrochlore characteristic peaks in the XRD patterns of CY4Z4T and CY6Z6T confirm the disorder of the cations at the A and B sites. In general, the transformation from order to disorder in pyrochlore type oxides is attributed to the lowering of the ratio of the average ionic size at A site to that at B site (r_A/r_B). In the present system, this ratio varies from 1.69 to 1.46 as shown in Fig. 4.2 (The ionic radii of Ca^{2+} and Y^{3+}, in 8-fold coordination are 1.12 Å and 1.019 Å and that of Zr^{4+} and Ta^{5+} in 6-fold coordination are 0.72 Å and 0.64 Å respectively). Usually, structural disorder takes place in pyrochlore type compounds as the average cation radius ratio (r_A/r_B) approaches unity. However, structural disorder induced in the present system (CY4Z4T) for r_A/r_B =1.47 which is much higher than that observed in the transformation from the P-type to the F-type phase in the $Ln_2Zr_2O_7$ system (Yamamura *et al.* 2003). ($Y_2Zr_2O_7$ has a metastable pyrochlore structure having r_A/r_B, 1.41). Ordered pyrochlore is favoured when the radius ratio (r_A/r_B) of the cations lies within the range 1.46 - 1.78 (e.g. $La_2Zr_2O_7$, r_A/r_B = 1.61).Conversely, when the ratio is less than 1.46, a defect fluorite structure is favoured (e.g. $Y_2Zr_2O_7$, r_A/r_B = 1.42) (Whittle, *et al.* 2009). Although, the r_A/r_B value controls the formation of pyrochlore structure and its transformation to a disordered fluorite state, however, no significant order – disorder structural transition occurs in the solid solution for which there is strong covalent bonding, e.g., in the systems of $Y_2(Sn_xTi_{1-x})_2O_7$ and $Gd_2(Sn_xTi_{1-x})_2O_7$ for the same range of r_A/r_B values in the $RE_2(Zr, Ti)_2O_7$ solid solution. It is concluded from these results that other factors

such as the crystal chemistry of B site cations (e.g. chemical bonding and the extent of covalency) have an important effect on the order-disorder transformation and the degree of disorder in the pyrochlore (Ewing, *et al.* 2004). Therefore apart from cation radius ratio consideration, the structural transformation in the present system may be attributed to the crystal chemistry of the cations substituted at the A (Ca^{2+} for Y^{3+}) and B (Ta^{5+} for Zr^{4+}) sites.

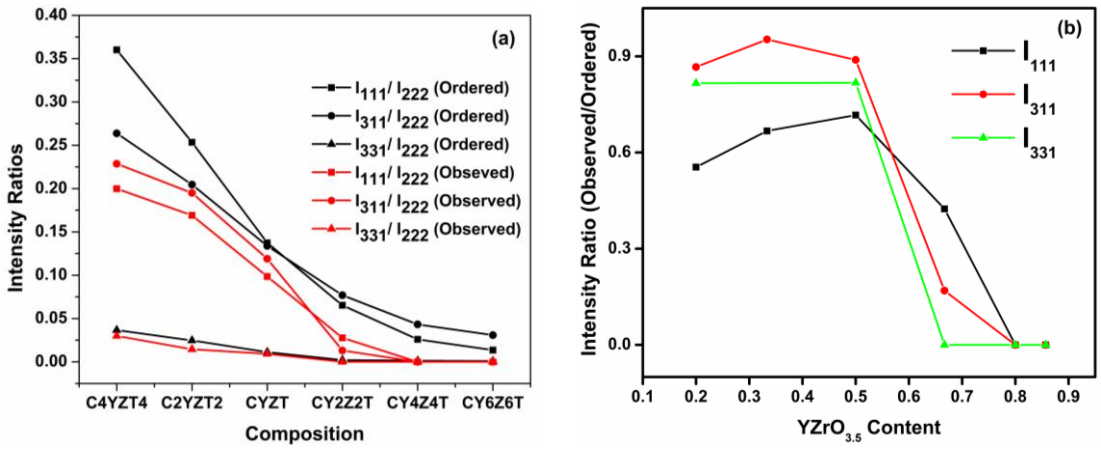

Fig 4.3 (a) Comparison of intensity ratios (I_{111}/I_{222}, I_{311}/I_{222} and I_{331}/I_{222}) of simulated ordered XRD patterns and observed patterns for different compositions in Ca–Y–Zr–Ta–O system and (b) I_{obs}/I_{cal} for (111), (311) and (331) reflections as a function of $YZrO_{3.5}$ content.

The intensity ratios of superlattice peaks like (111), (311) and (331) with (222) reflection of the simulated ordered patterns and the observed patterns are compared in a plot in Fig 4.3(a). It should be mentioned here that for fully ordered XRD pattern of $Ca_2Ta_2O_7$ and $Y_2Zr_2O_7$, the super structure peaks are very strong for $Ca_2Ta_2O_7$ due to large difference in scattering power of Ca and Ta, whereas the super structure peaks are very tiny for fully ordered $Y_2Zr_2O_7$ presumably due to the fact that Y^{3+} and Zr^{4+} are isoelectronic. It is very clear from the plot that the peak intensity ratio values for the observed patterns are smaller than that of the simulated ordered patterns. This indicates that the decrease in peak intensity ratio values is not presumably contributed entirely due to the small scattering power difference of Y and Zr due to their isoelectronic nature. (The intensity ratios were calculated after normalizing to the maximum intensity peak and the XRD patterns were recorded for all the samples under identical measuring conditions). Therefore, the extent of

structural disorder in the system is also contributing to the decrease in peak intensity ratios with increase of $YZrO_{3.5}$ content. To illustrate further, the ratios of the observed and calculated superlattice peaks of (1 1 1), (3 1 1) and (3 3 1) reflections (I_{obs}/I_{cal}) were plotted as a function of $YZrO_{3.5}$ content in Fig 4.3(b). As can be seen from the figure, the intensity ratios, $I_{111,}$ I_{311} and I_{331}, are seen to be more or less same for the compositions: C4YZT4, C2YZT2, CYZT and then decrease markedly at the phase boundary of pyrochlore and fluorite structure for the composition, CY2Z2T and finally the ratios become zero for CY4Z4T and CY6Z6T. Similar observations have been made in the study of the pyrochlore-fluorite phase transitions in $Ln_2Ti_2O_7$ (Ln = Tm - Lu) (Shlyakhtina *et al.* 2005). It has been observed that such structural disorder in pyrochlore type oxides displays remarkable change in ionic conductivity as in the case of $Gd_2(Ti_yZr_{1-y})_2O_7$ (Moon and Tuller 1988) and $Gd_{2-y}Nd_yZr_2O_7$ (Mandal *et al.* 2008). The increase in ionic conductivity is associated with cation anti-site disorder which has been verified by XRD (Moon and Tuller 1990). Furthermore, some pyrochlores undergo order – disorder transitions on substitutions of cations differing in valence state (Shlyakhtina *et al.* 2004). Here, in the present system, order – disorder transition is observed on going from Ca – Ta – O rich phase (Ca^{2+}/Ta^{5+} which have valence difference of 3) to Y – Zr – O rich phase (Y^{3+}/Zr^{4+} which have valence difference of 1). It also elucidates that the reduction in valence state between the cations occupying A and B sites might have contributed for the order – disorder phenomena observed in the present system in addition to the reasons cited above.

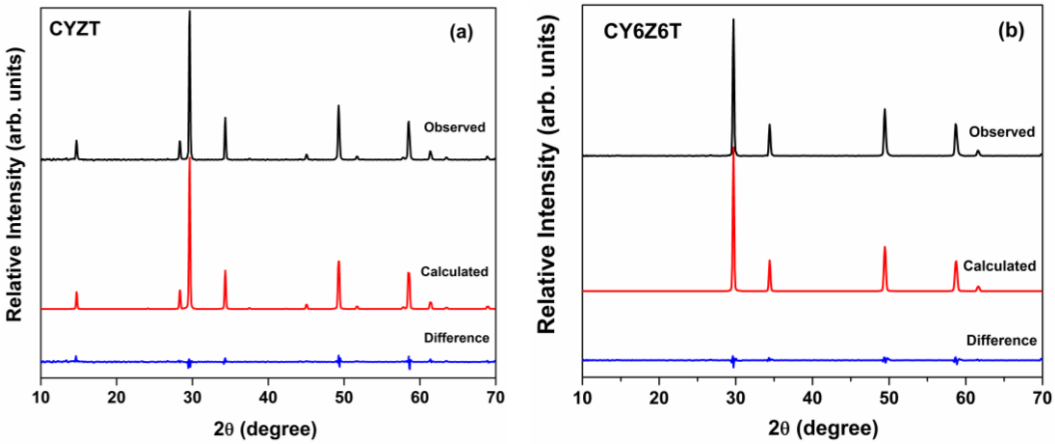

Fig 4.4 Observed calculated and difference XRD pattern profiles of (a) CYZT and (b) CY6Z6T.

Table 4.1 Refined lattice parameter and R-values for various compositions in the Ca–Y–Zr–- Ta–O system.

Composition	Crystal phase	Lattice constant (Å)	R_{exp} %	R_p %	R_{wp} %	GOF
CY6Z6T	Defect fluorite	10.4326(7)	5.06	6.61	9.97	3.87
CY4Z4T	Defect fluorite	10.4364(6)	11.95	1.26	17.28	2.09
CY2Z2T	Pyrochlore	10.4440(1)	9.83	3.77	18.62	3.58
CYZT	Pyrochlore	10.4652(8)	11.16	1.46	17.26	2.39
C2YZT2	Pyrochlore	10.4725(6)	9.78	4.20	17.53	3.21
C4YZT4	Pyrochlore	10.4730(5)	10.62	5.95	20.00	3.55

Rietveld analysis of the XRD data of all the compositions in the Ca – Y– Zr – Ta – O system was carried out in the space group $Fd\bar{3}m$ (No. 227). The profile was fitted using Pseudo-Voigt profile function. The refinement is in good agreement with the space group in all aspects, in which the A cations (A = Ca, Y) are at 16*d* sites (1/2, 1/2, 1/2) and the B ones (B = Zr, Ta) at 16*c* (0, 0, 0). There are two types of oxygen: one at the 48*f* sites (*x*, 1/8, 1/8) and the other at the 8*b* sites (3/8, 3/8, 3/8). The variable positional parameter (*x*) of the oxygen at 48*f* site determines the pyrochlore structure stability. Acceptable values for this oxygen coordinate are within the range 0.3125 – 0.375. The Rietveld analysis of the powder diffraction data of the samples C4YZT4, C2YZT2, and CYZT reveal that these three compositions belong to cubic pyrochlore system with space group $Fd\bar{3}m$ (No.227). Fig 4.4(a) shows observed, calculated and difference pattern of CYZT sample. The Rietveld refinement of CY2Z2T, CY4Z4T and CY6Z6T were performed by assuming the

disordering of cationic and anionic sublattices to different extent. The A cation and B cation sites in pyrochlore become indistinguishable when it is transforming to a defect fluorite structure. The pyrochlore structure (space group: $Fd\bar{3}m$) was used as the starting model, assuming the intermixing of the cations at A and B sites. The cation disordering is due to anti-site defect pair formation, accompanied by the generation of Frenkel defects in the anion sublattice which has a significant effect on the electrical properties of material (Panero *et al.* 2004). As a result of this disordering, the intensity of superlattice peaks gets decreased, but still belong to space group $Fd\bar{3}m$ (No.227). But in CY4Z4T and CY6Z6T cation disordering is maximum, led to structural transformation from pyrochlore to defect fluorite structure. Fig 4.4(b) shows observed, calculated and difference pattern of CY6Z6T sample. Table 4.1 shows refined lattice parameters and R- values for various stoichiometric compositions. The lattice constant of the solid solutions increased linearly with the increasing of $CaTaO_{3.5}$ as expected based on the ionic size consideration of the cations.

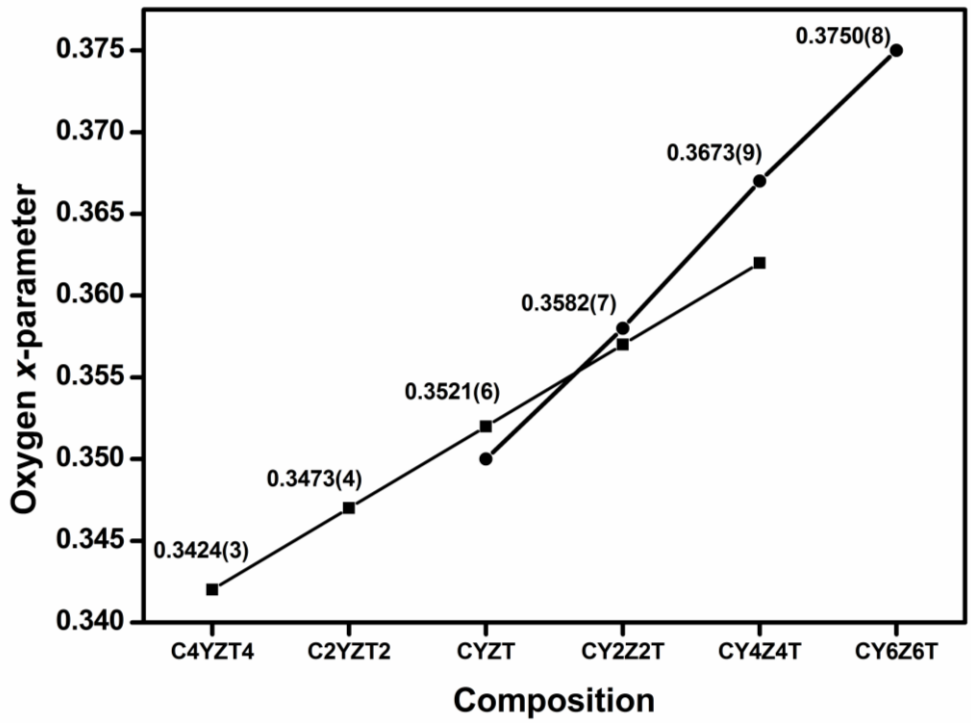

Fig 4.5 Variation of oxygen *x*-parameter as a function of different compositions in the Ca–Y–Zr–Ta–O system.

Fig 4.5 gives the variation of oxygen positional parameter, *x* as a function of different compositions. The structural stability of the compound is affected by the positional parameter (*x*) of the oxygen at *48f*. Considering an $A_2B_2O_7$ pyrochlore structure, varying this value changes the shape of the A-site and B-site polyhedra (Mandal, *et al.* 2007). For a value of 0.375 for this fractional coordinate, the A-site and B-site polyhedra are regular cubes and trigonally flattened octahedra, respectively. When the *x* coordinates decreases to 0.3125, the B-site becomes a regular octahedron and the cubic A-site distorts into a trigonal scalenohedron. The deviation of oxygen at 48*f* from the special position (*x*, 1/8, 1/8) with $x = 0.375$ is thus a sensitive measurement of the difference between a pyrochlore and a "defect fluorite" phase (Subramanian, *et al.* 1983). It has been observed after Rietveld analysis that with increase of $YZrO_{3.5}$ phase in the system, the positional parameter, *x* increases which in turn drives the system to transform from ordered pyrochlore to disordered pyrochlore and finally to defect fluorite.

4.3.2 Raman Spectroscopic Studies

Raman spectroscopic investigation provides information to distinguish between a defect-fluorite structure and the pyrochlore structure (Mandal *et al.* 2006). Based on the crystal structure and group theory analysis, there are only six Raman active modes for the pyrochlore structure.

$$\mathbf{\Gamma_{raman} = A_{1g} + E_g + 4F_{2g}} \qquad \mathbf{(4.1)}$$

A and B cations do not contribute to Raman active vibrations since they are located at the inversion centre and the six Raman active modes involve only the movement of oxygen atoms. One of the F_{2g} modes is caused by the 8*a* oxygen sub-lattice vibration and other modes are attributed to 48*f* oxygen sub-lattice vibrations. For ideal fluorite structure there is only one F_{2g} mode related to 8*c* site (Glerup *et al.* 2001). From experimental data, defect fluorite structure normally has weak Raman peaks (Mandal, *et al.* 2006). More Raman lines other than theoretically calculated, may appear in the Raman spectra of pyrochlores and fluorites due to various reasons as discussed by Glerup et al. (Glerup, *et al.* 2001).

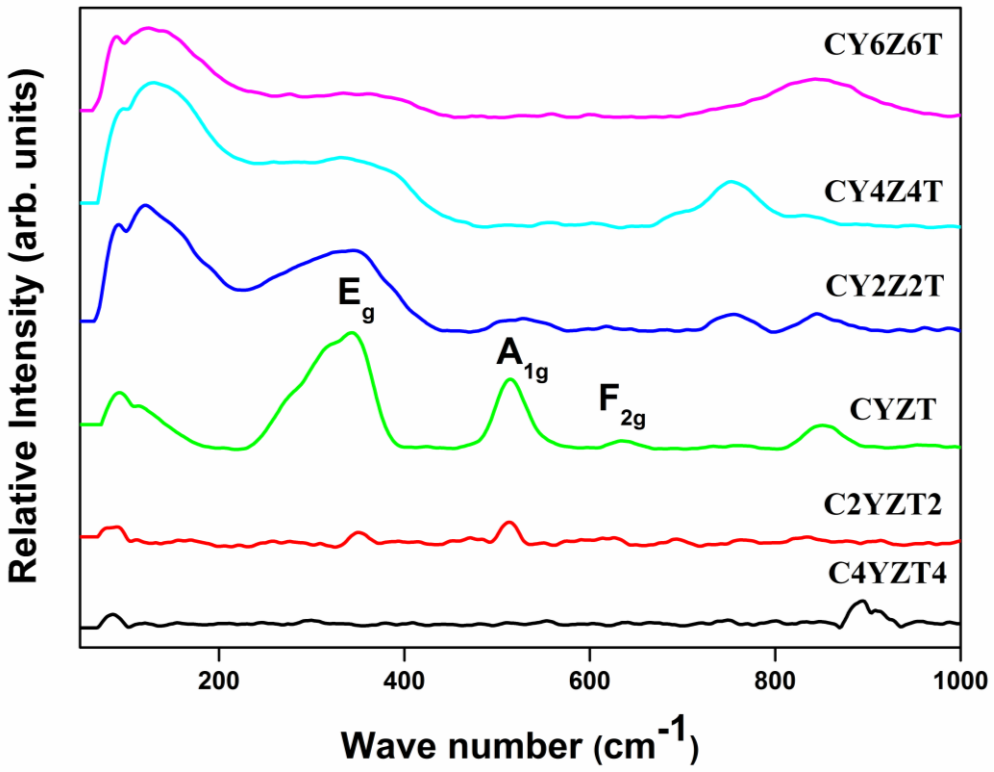

Fig 4.6 FT-NIR Raman spectra of the samples sintered at 1600°C for 6 h

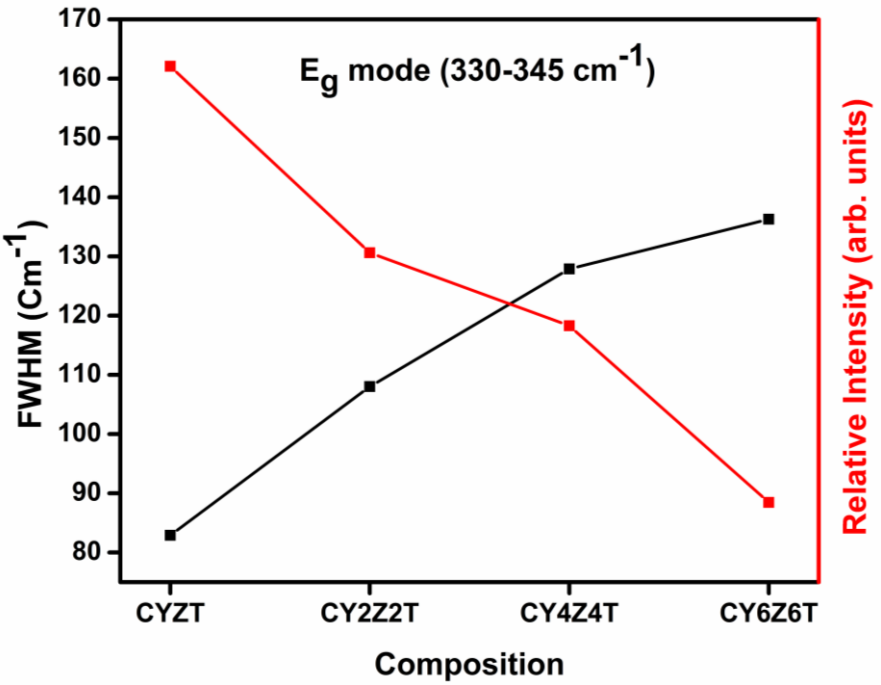

Fig 4.7 FWHM and relative intensity of E_g mode (330-345 cm^{-1}) for the compositions CYZT, CY2Z2T, CY4Z4T and CY6Z6T

The FT Raman spectra for different stoichiometries in Ca-Y-Zr-Ta-O system are shown in Fig 4.6. The Raman bands are broad as compared to that of well-ordered crystalline compounds, similar to that observed by Scheetz et al for pyrochlore zirconates (Scheetz and White 1979). The Raman spectra of CYZT shows major Raman modes of pyrochlores like A_{1g} at 514 cm^{-1}, E_g at 343 cm^{-1} and one F_{2g} band at 634 cm^{-1} with considerable intensity (Gupta *et al.* 2001). Other F_{2g} modes are too weak to be observable and additional peaks appeared around 100 cm^{-1} and 850 cm^{-1} may be due to local lattice modes arising due to distortion of the octahedra (Du and Yao 2004). But it is very difficult to take the Raman spectra of C4YZT4 and C2YZT2 samples because of their high fluorescence and as a result, the relative intensity of Raman peaks became very less or indistinguishable from the noise. Also it is already reported that as the content of Ta is increased at B site in $A_2B_2O_7$ pyrochlores, intensity of the Raman lines becomes weaker and weaker (Glerup, *et al.* 2001). Raman spectrum of CY2Z2T is almost similar to that of CYZT, but the intensity of the peaks became very low and peaks corresponding to local disordering become relatively intense. Small distortions of the atomic positions caused by B cation species in pyrochlore structure compounds affect the force constant of vibrational mode resulting small shift in vibrational frequency. Thus, the full width at half maximum (FWHM) of a vibrational mode provides a measure of the level of localized short range structural disorder in the materials (Mandal, *et al.* 2007). Typically, the FWHM of the vibrational mode, E_g (330 - 345 cm^{-1}) increases considerable with changing slope in the phase boundary combined with the decrease of Raman intensity for the progressive and simultaneous substitution of larger cation Ca^{2+} with Y^{3+} at A sites and smaller cation Ta^{5+} with Zr^{4+} at B sites as shown in Fig 4.7. This clearly confirms that pyrochlore structure is getting disordered as revealed through XRD analysis. Raman spectra of CY4Z4T and CY6Z6T show considerable difference from that of other samples and the broadening of the Raman bands is due to structural disorder (Mandal, *et al.* 2006). Raman peaks corresponding to A_{1g}, and E_g of pyrochlore becomes very less in intensity whereas peaks corresponding to local lattice modes become comparably intense. However, the F_{2g} mode usually observed at ~466 cm^{-1} for ideal fluorite structured oxides ThO_2, CeO_2, etc., was not observed by us (Mandal, *et al.* 2006). The extra bands observed around 760 cm^{-1} for CY4Z4T

and 840 cm^{-1} for CY6Z6T can be attributed to seven coordinated A cation in the defect fluorite structure (Du and Yao 2004, Gupta, *et al.* 2001). Therefore the structural transformation from ordered pyrochlore phase to more disordered fluorite phase can be confirmed from the Raman spectra.

4.3.3 Transmission Electron Microscopy Studies

Fig 4.8 shows the selected area electron diffraction patterns (SAED) recorded from C2YZT2 and CY6Z6T samples which can be indexed according to a pyrochlore unit cell and fluorite type unit cell respectively. SAED pattern of C2YZT2 shows highly ordered diffraction maxima with the appearance of weak superlattice diffraction spots in between the bright diffraction spots. The absence of weak super lattice diffraction spots in CY6Z6T SAED pattern distinguishes from the pyrochlore unit cell and the diffraction maxima arranged in a ring pattern is similar to that observed in a fluorite type SAED pattern of $Ce_2Zr_2O_7$ (Lian, *et al.* 2004). High resolution TEM images of CYZT and CY6Z6T are also shown in Fig 4.9. The lattice constant of the fluorite structure layer is one half that of the pyrochlore unit cell layer as shown by the difference of the (111) spacing. These results are in support of the XRD.

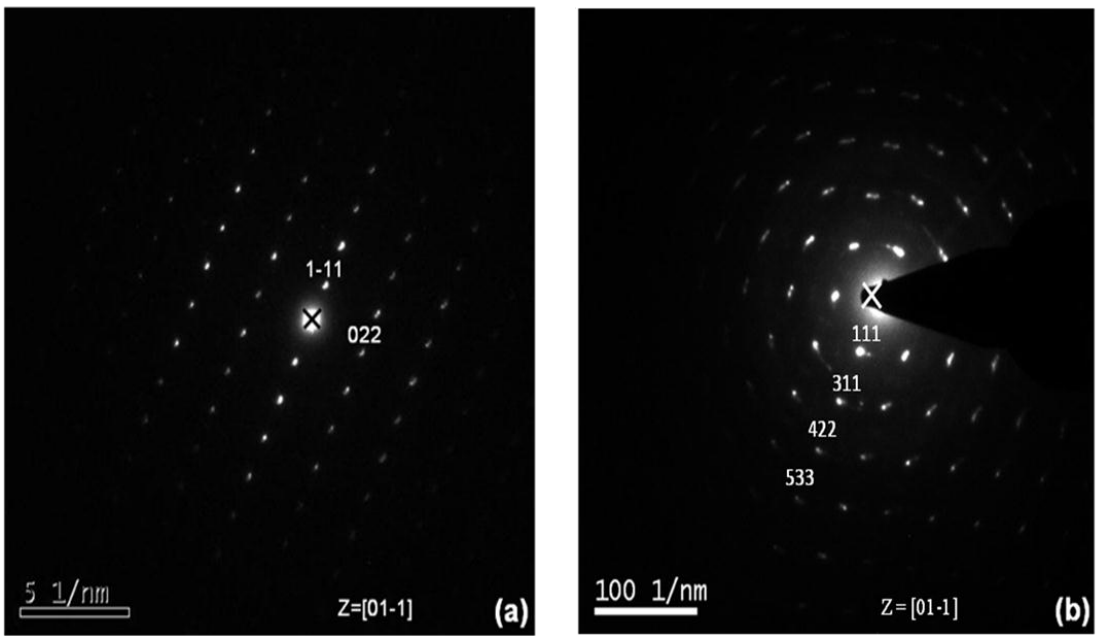

Fig 4.8 Selected Area Electron Diffraction (SAED) pattern of (a) C2YZT2 and (b) CY6Z6T.

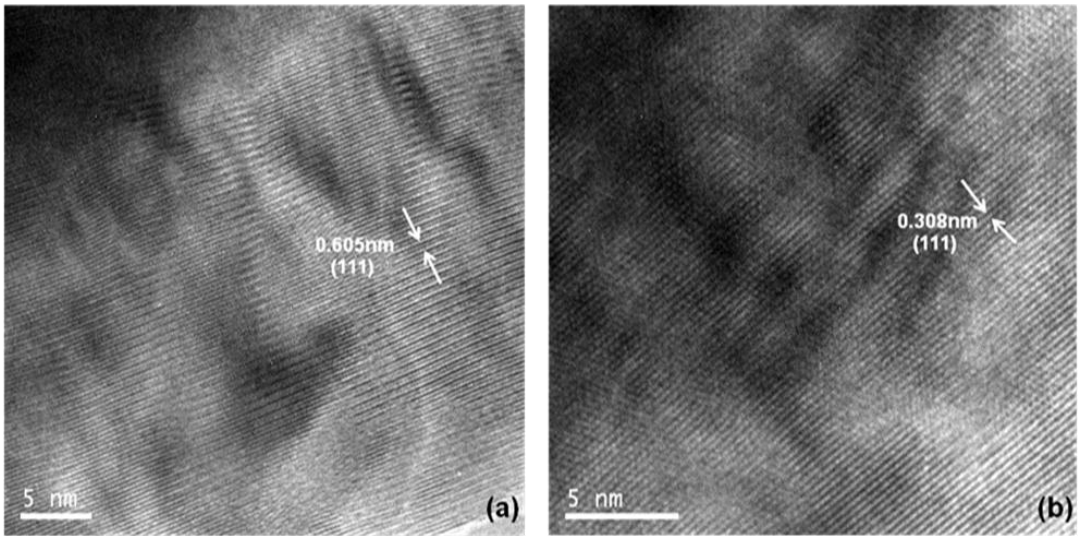

Fig 4.9 High resolution TEM images of (a) CYZT and (b) CY6Z6T

4.3.4 High Temperature XRD Studies

Lattice thermal expansion studies on different compositions in Ca-Y-Zr-Ta-O pyrochlore systems were carried out by high temperature XRD from room temperature to 1273 K. The HTXRD patterns do not show any phase transformation in the temperature range (298 – 1273 K) of the present investigation. The most intense peak in the XRD pattern, (222), of CYZT at different temperatures is shown in Fig 10(a). The shift of the peak towards the lower theta-side with increase in temperature implies an increase in the corresponding interplanar spacing, resulting in a lattice expansion. The overall lattice expansion can be characterized by the change in lattice constant as a function of temperature, as all the compounds belong to cubic crystal system. The lattice thermal expansion coefficient is best estimate of structural stability with temperature and can be easily determined using high temperature XRD. Lattice thermal expansion coefficient is calculated using the equation:

$$\alpha_a = \frac{1}{a_{298}} \left(\frac{da}{dT}\right) \quad K^{-1} \qquad (4.2)$$

The XRD patterns were fitted by Lebail fitting method using X'pert High Score Plus. For each sample, plots are made with lattice parameter as a function of absolute temperature. The slope of the graph is calculated by a linear fit of the graph and lattice thermal expansion coefficient is calculated using above equation. The variation of lattice parameter with temperature for CYZT and its linear fit is shown in

Fig 4.10(b). The variation of lattice thermal expansion coefficient with different compositions in the Ca-Y-Zr-Ta-O pyrochlore system is shown in Fig 4.11. It can be observed from the figure that lattice expansion coefficient increases with increase in $YZrO_{3.5}$ content in the pyrochlore regime and vice versa in the defect fluorite regime.

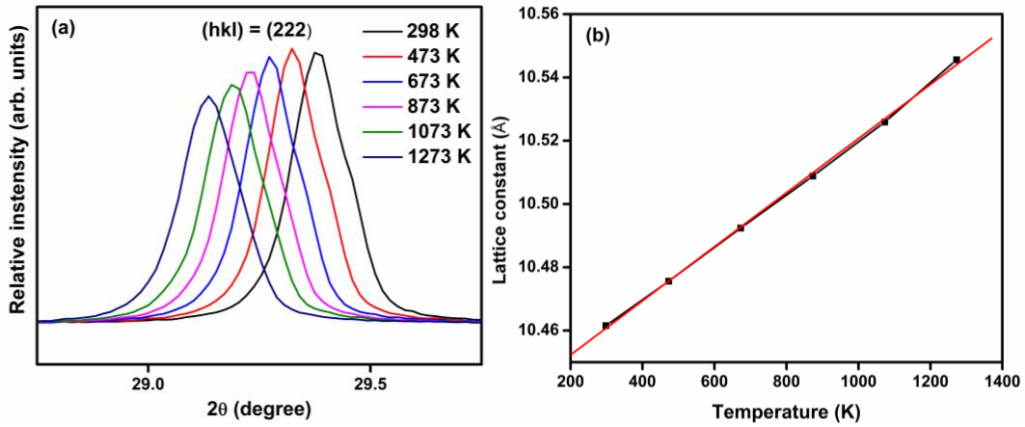

Fig 4.10 (a) High temperature XRD pattern showing only (222) peak of CYZT and (b) the corresponding lattice parameter vs. temperature plot (red line indicates the linear fit of the graph)

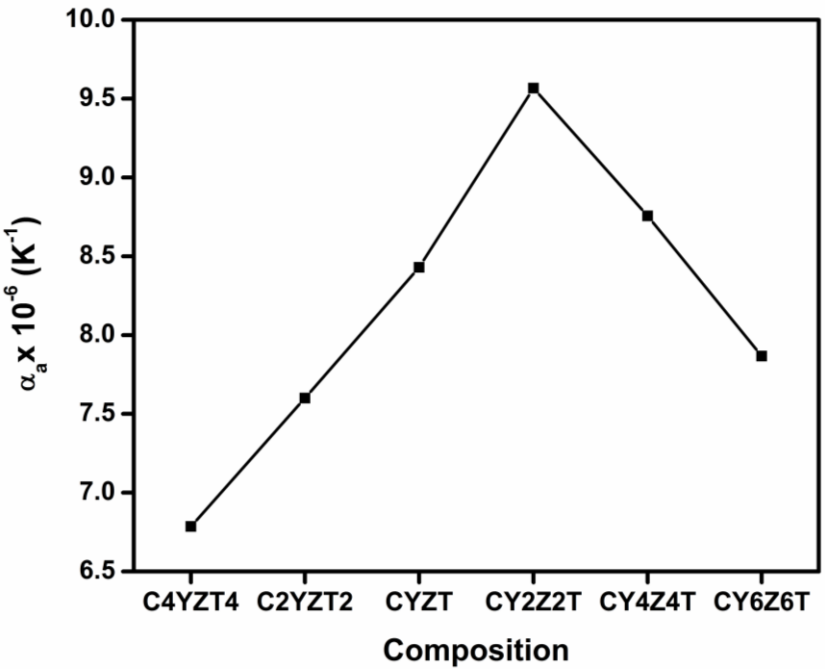

Fig 4.11 Variation of lattice thermal expansion coefficient with different compositions in Ca-Y-Zr-Ta-O system.

In the pyrochlore structured composition disorder increases with increases in $YZrO_{3.5}$ content and CY2Z2T adopts a defect pyrochlore structure. This disorder may be the reason for high thermal expansion of CY2Z2T and for pyrochlore compositions lattice expansion increases with increase in disorder. But with the transformation of the structure to defect fluorite, the lattice thermal expansion decreases with increases in $YZrO_{3.5}$ content as the coordination around all the four cations become identical, giving a good stability to the structure. The thermal expansion behavior of the compounds has a significant effect on oxide ion conductivity and will be discussed in the latter part of this chapter.

4.3.5 Scanning Electron Microscopy Studies

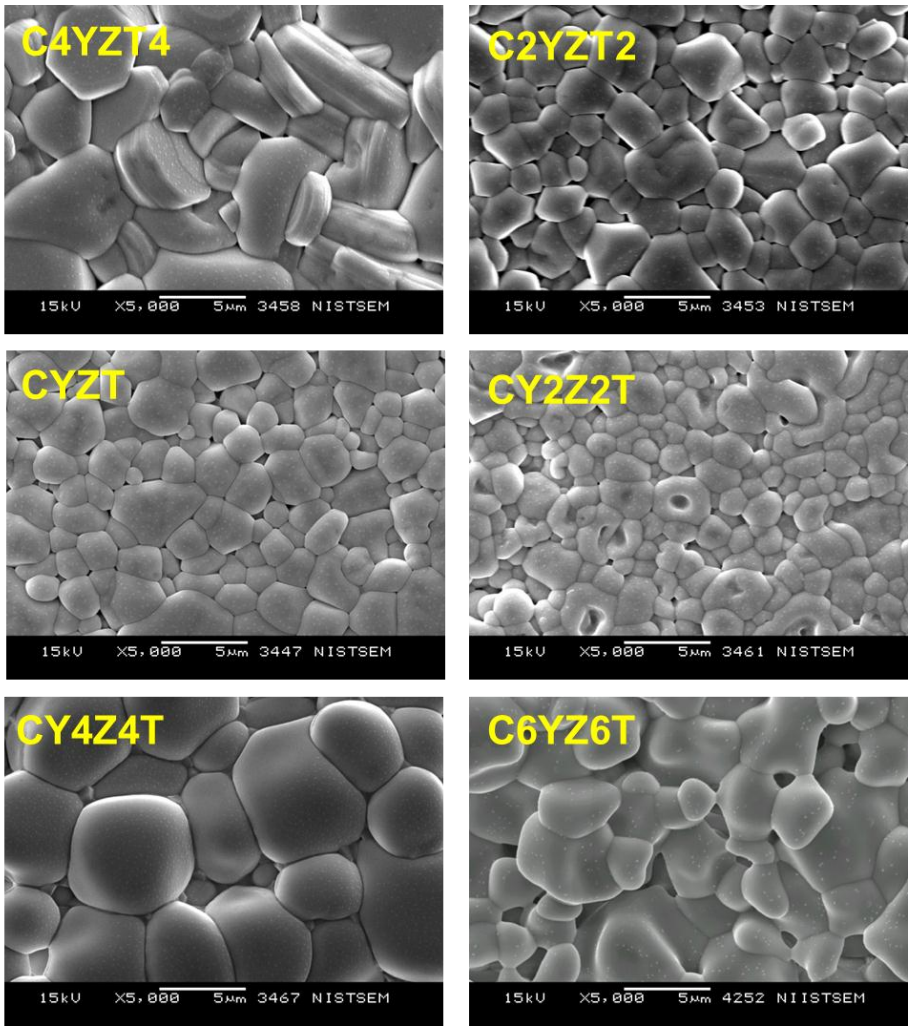

Fig 4.12 SEM micrographs of different compositions in Ca-Y-Zr-Ta-O system sintered at 1600ºC for 6 h.

Table 4.2 Average grain size calculated using linear intercept method and density data for different compositions in Ca-Y-Zr-Ta-O system sintered at 1600 ºC for 6 h.

Compound	Average grain size (μm)	Theoretical density (gm/cm^3)	Experimental density (gm/cm^3)	Relative density (%)
C4YZT4	3.93±0.37	6.2177	6.0043	96.57
C2YZT2	3.11±0.29	6.0925	5.8130	95.41
CYZT	2.38±0.17	5.9472	5.6436	94.90
CY2Z2T	1.91±0.14	5.8246	5.4140	92.95
CY4Z4T	5.01±0.45	5.7098	4.7731	83.60
CY6Z6T	3.56±0.39	5.6614	4.2606	75.26

Surface morphology of different compositions in Ca-Y-Zr-Ta-O system sintered at 1600 ºC is shown in Fig 11. A progressive change in the microstructure can be observed with an increase in the $YZrO_{3.5}$ content. All the pyrochlore structured compounds show well sintered grains, less porosity and perfect grain boundaries. But with the order-disorder transformation to defect fluorite, the porosity increases with increase in $YZrO_{3.5}$ content. Both CY4Z4T and CY6Z6T have less packing density of grains and high porosity at the same sintering temperature when compared to the pyrochlore structured compounds. Average grain sizes calculated from SEM images using linear intercept method along with theoretical, experimental and relative densities are given in Table 4.2. Average grain size decreases with increase in $YZrO_{3.5}$ content up to pyrochlore – fluorite phase boundary. A sudden jump in grain size is observed with structural transformation to fluorite and in the defect fluorite region, grain size decreases with increase in $YZrO_{3.5}$ content.

4.3.6 Impedance Spectroscopic Studies

Ac impedance spectroscopy was used for the total conductivity measurement of the sintered pellets in the temperature range 400 – 750 ºC. Variation of total conductivity with reciprocal of the absolute temperature for all compositions is shown in Fig 4.12. These compounds are electrical insulators with negligible electronic conduction since there are no free electrons available for conduction. Free electrons will be created only when any of the cation gets reduced to its lower

valence state at high temperature. But if such a reduction occurs, the lattice parameter will change significantly, resulting in a large thermal expansion coefficient. But lattice thermal expansion studies showed that there is no anomalous increase in lattice parameter in the temperature range 298 - 1273 K. Hence the conduction is predominantly ionic and follows Arrhenius behavior.

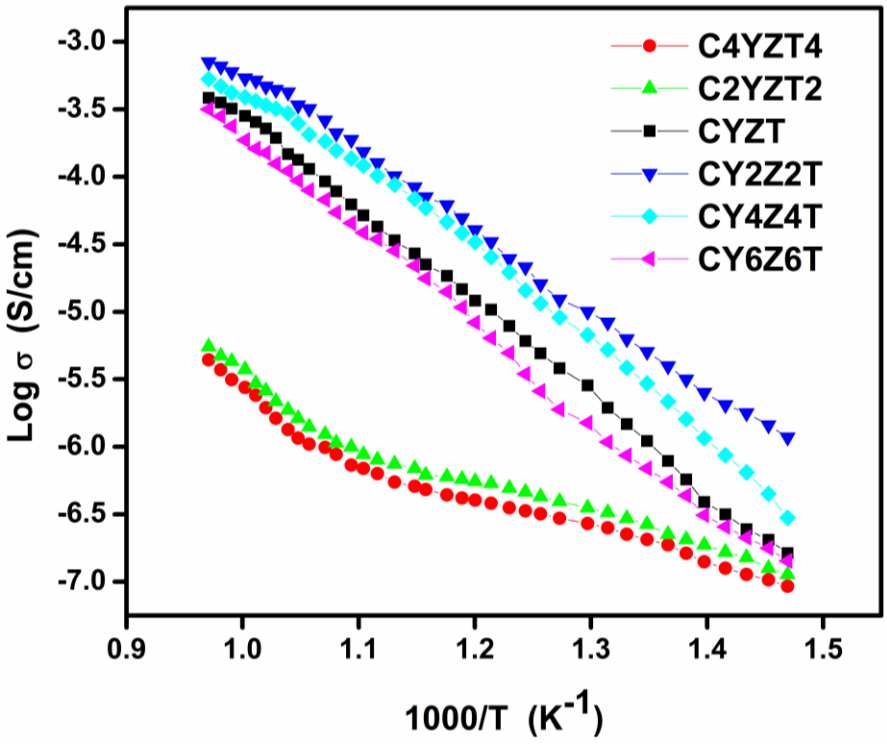

Fig 4.13 Arrhenius plot for all compositions in Ca-Y-Zr-Ta-O pyrochlore oxide system

It is obvious from the figure that total conductivity increases with increase in $YZrO_{3.5}$ content and reaches a maximum for CY2Z2T and there after it decreases significantly. Highly ordered pyrochlore compounds, C4YZT4 and C2YZT2, conductivity is very low due to the low mobility of the oxide ions through the highly ordered lattice. For CYZT the conductivity increases by a factor of around 100 and reaches a maximum for CY2Z2T. The high conductivity of CY2Z2T is due to its disordered pyrochlore structure which enable easy conduction path way for oxide ions due to the simultaneous disorder in both cation and anion sublattices. High density of pyrochlore compounds (evident from SEM micrographs) also contribute to the high conductivity. Microstructure has significant role in deciding ionic

conductivity of the samples and usually ionic conductivity decreases with decrease in grain size due to the significant increase of grain boundary area which acts as a blocking layer for oxide ions. But a reverse trend is observed and this may be due to that fact that disorder in the pyrochlore structure has dominant effect than microstructural properties like grain size provided the sintered sample is highly dense.

The structural transformation induced changes in both structural as well as microstructural parameters which in turn affects the electrical properties. For CY4Z4T, the conductivity is slightly less than that of CY2Z2T and this small change is due to the low density of the sintered pellet as evident from SEM micrographs. But conductivity further decreases significantly when the structural transformation is complete with CY6Z6T. This is because as the structure changes completely to defect fluorite, cations and anions now occupy definite crystallographic positions allowed by the space group $Fm\bar{3}m$. This may increase the path length between an oxide ion and nearest oxygen vacancy which in turn cause more hindrance to oxide ion diffusion. The poor density of the sintered pellet also reduces the conductivity significantly.

Since oxide ion conduction took place at high temperature, lattice thermal expansion plays an important role in enhancing ionic conductivity. If the lattice thermal expansion is high, oxide ion diffusion will be much easy since the average radius of the migration path increases with expansion of the unit cell and corresponding increase in interplanar distance. For pyrochlore compositions, thermal expansion increases with disorder and the oxide ion conductivity also follows the same trend. Both lattice thermal expansion and oxide ion conductivity values are maximum near the phase boundary of pyrochlore and defect fluorite structure. These results are very useful in tuning lattice thermal expansion and oxide ion conductivity by suitable dopants at A and B sites in pyrochlore oxides.

4.4 Conclusions

In summary, the present study determined the structural variation, Pyrochlore to Fluorite type in the solid solutions of different ratios: 4:1, 2:1, 1:1, 1:2, 1:4, 1:6 of

$CaTaO_{3.5}$ and $YZrO_{3.5}$. The pyrochlore phase stabilizes for the r_A/r_B in the range 1.69 - 1.57 and the defect fluorite phase for 1.47 – 1.45 values. The structural disorder induced in the present system for r_A/r_B = 1.47 as the ratios of the solid solutions of $CaTaO_{3.5}$ and $YZrO_{3.5}$ were changed from 4:1 to 1:4. This ratio, r_A/r_B is much higher than that observed in the transformation from the pyrochlore-type to the fluorite-type phase in the $Ln_2Zr_2O_7$ system. Therefore apart from cation radius ratio consideration, the structural transformation in the present system may be attributed to the crystal chemistry of the cations substituted at the A (Ca^{2+} for Y^{3+}) and B (Ta^{5+} for Zr^{4+}) sites. It is found that structural transformation in pyrochlore type oxides induced remarkable changes in thermal as well as electrical properties. Lattice thermal expansion increases with increase in $YZrO_{3.5}$ content and reaches a maximum value near the phase boundary of pyrochlore and fluorite structures. Oxide ion conductivity also follows the same trend and this in turn proves that lattice thermal expansion and oxide ion conductivity are correlated.

Chapter 5

Influence of Disorder to Order Transition on Lattice Thermal Expansion and Oxide Ion Conductivity in $(Ca_xGd_{1-x})_2(Zr_{1-x}M_x)_2O_7$ Pyrochlore Solid Solutions

The effect of simultaneous substitutions of Ca at A site and Nb or Ta at B site in pyrochlore type solid solutions: $(Ca_xGd_{1-x})_2(Zr_{1-x}M_x)_2O_7$ (x = 0.1, 0.2, 0.3, 0.4, 0.5 and M = Nb or Ta) were studied by powder X-ray diffraction (XRD) method, FT NIR Raman spectroscopic techniques and transmission electron microscopy. The XRD results and Rietveld analysis revealed that the defect fluorite structure of $Gd_2Zr_2O_7$ progressively changed to more ordered pyrochlore phase by the simultaneous substitutions at A and B sites. Raman spectroscopy reveals the progressive ordering in anion sublattice with simultaneous doping. High resolution images and selected area electron diffraction patterns obtained from TEM confirms the XRD and Raman spectroscopic results. High temperature XRD studies show that the lattice expansion coefficient in these pyrochlore oxides is of the order of 10^{-6} K^{-1}. Lattice thermal expansion coefficient increases with increase of disorder in pyrochlore oxides and hence the variation of thermal expansion coefficient with composition is also a good indicator of disordering in pyrochlore type oxides. The ionic conducting properties of the samples were characterized by impedance spectroscopy and it is found that Nb doped compositions show a considerable change in conductivity near the phase boundary of disordered pyrochlore and defect fluorite phases.

A.N. Radhakrishnan, P. Prabhakar Rao, K.S. Mary Linsa, M. Deepa and Peter Koshy, "Influence of disorder-to-order transition on lattice thermal expansion and oxide ion conductivity in (Ca*x*Gd1−*x*)2(Zr1−*x*M*x*)2O7 pyrochlore solid solutions", **Dalton Transactions**, 2011 , 40 (15), 3839-3848 .

5.1 Introduction

$Gd_2Zr_2O_7$ is one of the most studied pyrochlores because of the fact that its radius ratio r_{Gd3+}/r_{Zr4+} = 1.46 which is the phase boundary between pyrochlore type phase and fluorite type phase and hence the maximum disorder in cation and anion sublattices enhances high oxide ion conductivity(van Dijk *et al.* 1983). With reference to the phase diagram the ordered pyrochlore can be formed in a Gd_2O_3-ZrO_2 system with Gd content of 32-62 wt % at temperature below 1500 ºC. The pyrochlore to fluorite transition temperature for $Gd_2Zr_2O_7$ is about 1550 ºC (Wang *et al.* 2003). XANES spectroscopic studies of the phase transition in $Gd_2Zr_2O_7$ have been studied by Lee et al.(Lee *et al.* 2009) and reported that when $Gd_2Zr_2O_7$ in defect fluorite phase with Zr in seven coordination on average, transformed to ordered pyrochlore phase with Zr in six coordination, the Zr-O bond distance decreases. This implies that lower the coordination number stronger the bond because of shorter bond length of Zr-O bond. Based on O and Zr K- edge X-ray absorption spectra of $Gd_2Zr_2O_7$ in pyrochlore and fluorite phases, it is established that the crystal field splitting energy of Zr (4d) is larger in pyrochlore phase than that in fluorite phase indicating an increase in interaction between Zr and O atoms in pyrochlore phase. Purton et al.(Purton and Allan 2002) compared the calculated (static energy minimization using GULP code) and experimental lattice parameters and bond lengths for $Gd_2Zr_2O_7$ and $Gd_2Ti_2O_7$ and found that experimental values deviate considerably from calculated values except for Zr/Ti – O bond distance. The deviation is comparably high for $Gd_2Zr_2O_7$ and it may be due to the fact that lattice parameters and bond lengths are sensitive to intrinsic disorder in pyrochlores which is ignored in the energy minimization calculations. This clearly establishes the fact that study of disorder in pyrochlore is an important factor deciding its structural properties which in turn influences its electrical properties.

Different studies have shown that the most stable intrinsic defect in these compounds to be an oxygen Frenkel pair consisting of a vacant 48*f* position and an interstitial ion located at the 8*a* site(Pirzada *et al.* 2001, Wilde and Catlow 1998a, Wilde and Catlow 1998b). The oxygen ion conductivity in pyrochlore oxides depend essentially on the formation energy of these defects. This energy is substantially reduced by the presence of disordering in cation sublattice because cation disorder increases the similarity between non-equivalent oxygen sites and promotes Frenkel

defect formation(Wilde and Catlow 1998a). But the most disordered pyrochlores are not necessarily the best ionic conductors because of their high activation energies needed for migration. The optimal conductivity is observed in partially disordered materials (Díaz-Guillén *et al.* 2008, Pirzada, *et al.* 2001). Sickafus et.al. predicted using atomistic simulation that disordered pyrochlore type phases are more radiation resistant than ordered pyrochlore phases as disordered phases have more propensity to accommodate lattice disorder and are able to resist lattice instability in radiation environment (Sickafus, *et al.* 2000) and their hypothesis is supported by many additional experiments(Wang *et al.* 1999, Wang, *et al.* 1999). Many investigations have already been done with either A-site doping(Mandal, *et al.* 2008) or B-site doping (Moon and Tuller 1988) with different cations and its effect on structure and electrical properties. The effect of simultaneous doping has not been well studied in the context of order-disorder transformations and ionic conductivity. The presence of four cations with oxidation states ranging from 2+ to 5+ put difficulty in deconvoluting different factors deciding the extent of disorder in the pyrochlore oxides when both A and B sites are doped simultaneously. The study of disorder in quaternary type of pyrochlore is extremely useful in providing a basis for researches in technologically important fields like the development of solid electrolytes for intermediate temperature fuel cells and development of suitable host materials for nuclear waste disposal. The search for alternate, ecofriendly energy sources accelerated researches in the field of solid oxide fuel cells and the search for new electrolytes. Pyrochlores have good temperature stability and structure can tolerate a wide range of doping at A and B sites. If pyrochlore structure is tuned properly to enhance oxide ion conductivity, then it will be suitable candidate for using as an electrolyte in intermediate temperature fuel cells. Recently we have reported order-disorder transformation in a quaternary pyrochlore oxide system, $Ca_2Ta_2O_7 – Y_2Zr_2O_7$ characterized by powder X-ray diffraction, Raman spectroscopy and TEM studies(Radhakrishnan *et al.* 2009). In the present study, a series of pyrochlore type solid solutions, $(Ca_xGd_{1-x})_2(Zr_{1-x}M_x)_2O_7$ (x = 0.1, 0.2, 0.3, 0.4, 0.5 and M = Nb or Ta) were prepared and studied its structural as well as electrical properties. In addition to this, lattice thermal expansion studies on this system was done by high temperature

XRD measurements. The results on order-disorder transformation in the system are discussed in correlation with the thermal and electrical properties.

5.2 Experimental

$(Ca_xGd_{1-x})_2(Zr_{1-x}M_x)_2O_7$ (x = 0.1, 0.2, 0.3, 0.4, 0.5 and M = Nb or Ta**)** samples were prepared by the conventional ceramic route using the starting materials, $CaCO_3$, Gd_2O_3, ZrO_2, Nb_2O_5 and Ta_2O_5 (ACROS ORGANICS, 99.99%). Nb doped samples are named as CN10, CN20, CN30, CN40 and CN50 and Ta doped compounds as CT10, CT20, CT30, CT40 and CT50 with reference to mole percentage of doping. (This nomenclature is followed in the latter part of the text for easy understanding). The raw materials were weighed according to the stoichiometry of the samples and then mixed thoroughly in an agate mortar. Acetone was added to the powdered mixture for proper mixing. Then, the mixture was dried in an air oven at 100 ºC for 1 h. This procedure of mixing and subsequent drying was repeated thrice to get a homogeneous mixture. The powdered samples were calcined at 1300 ºC for 6 h, followed by a second calcination at 1400 ºC for 10 h.

The calcined product was ground into a fine powder and then mixed with 2 wt. % solution of polyvinyl alcohol (PVA) as the organic binder for strengthening and good compaction of the pellet. The dried powder was pressed into cylindrical pellets of 10 mm diameter and about 2 - 3 mm thickness using a hydraulic press. Pellets were initially heated to 600 ºC and kept for 30 minutes to completely remove the organic binder and the final sintering process was done in the temperature range 1500 – 1600 ºC for 10 h to optimize the density of the samples. All characterizations were performed upon the final sintered products. Powder X-ray diffraction patterns were recorded at room temperature to identify the crystalline phase of the sintered samples using a Ni filtered Cu K_α radiation ($K_{\alpha1}$ = 1.54060 Å, $K_{\alpha2}$ = 1.54443 Å, $K_{\alpha1}/K_{\alpha2}$ = 0.5) by a PANalytical Philips X'pert Pro MPD XRD diffractometer (Step size = 0.02, Scanning time per step = 20 seconds, Divergence slit = 0 .5^o, and exported by X'pert Pro software) with X'lerator detection technology. The unit cell parameters were calculated by least square method and Rietveld analysis was also performed to refine the structure using Fullprof-2010. For lattice thermal expansion studies, the XRD patterns of sintered samples were recorded from 2θ = 10 – 90^o, in

the temperature range 298 – 1273 K on a PANalytical Philips X'pert Pro MPD XRD unit equipped with Anton Paar HTK attachment, at a regular interval of 200 K, in vacuum (~$1x10^{-4}$ mbar). The FT NIR Raman spectra of the powdered samples were recorded on a Bruker RFS100/S spectrometer using near infrared laser excitation (Nd: YAG, 1064 nm). Standard Ge detector cooled to liquid nitrogen temperature is used and it was set to scan over the range from 50 - 1000 cm^{-1}. The resolution of the spectrometer is 4 cm^{-1}. For impedance spectroscopic studies, a high temperature curing silver paste was applied on polished flat faces of the pellet and electroded with long silver wires. The electroded pellets were cured in a tube furnace for 30 minutes at 600 ºC. Impedance measurements of the pellets were carried out from 300 ^oC to 750 ^oC in the frequency range 10 Hz to 1 MHz using a computer controlled Impedance Analyzer (Solartron, SI 1260) with Solartron 1296 Dielectric Interface. The complex impedance plots were made with the SMART software supplied by M/s Solartron Schlumberger, U.K. The selected area electron diffraction (SAED) pattern and high resolution electron microscopy (HREM) of the samples were taken using transmission electron microscope (TEM) TECNAI $30G^2$ S-TWIN (FEI, The Netherlands). A small amount of finely powdered sample is dispersed in acetone medium by ultra-sonication; drop casted on carbon coated copper grids and dried.

5.3 Results and discussion

5.3.1 Powder X-ray Diffraction Studies

The powder XRD patterns of the samples in the series $(Ca_xGd_{1-x})_2(Zr_{1-x}M_x)_2O_7$ (x = 0.1, 0.2, 0.3, 0.4, 0.5 and M = Nb or Ta**)** are shown in Fig 5. 1(a) and (b). All the XRD peaks are indexed according to pyrochlore type unit cell with $Fd\bar{3}m$ space group. As pyrochlore is a superstructure of fluorite–like array of atoms, its diffraction pattern consists of a set of strong intensities representatives of average fluorite structure plus an additional set of superstructure intensities. The superstructure intensities and the associated compliment structure contain all of the information on the ordering process responsible for the formation of the superstructure (Heremans, *et al.* 1995). All samples have high intensity peaks with even miller indices like (222), (400), (622) etc. representing average fluorite type unit cells. But superlattice peaks with odd miller indices like (111), (311), (331) etc. are very weak in intensity and

their intensity progressively increases with substitution of Ca and Nb/Ta in $Gd_2Zr_2O_7$. For Nb substituted compounds, superlattice peaks are very less intense compared to Ta substituted compounds. Both Ta and Nb have the same ionic radii (r = 0.64 Å), (Shannon 1976) but differ in X-ray scattering power. Scattering power of Nb is very

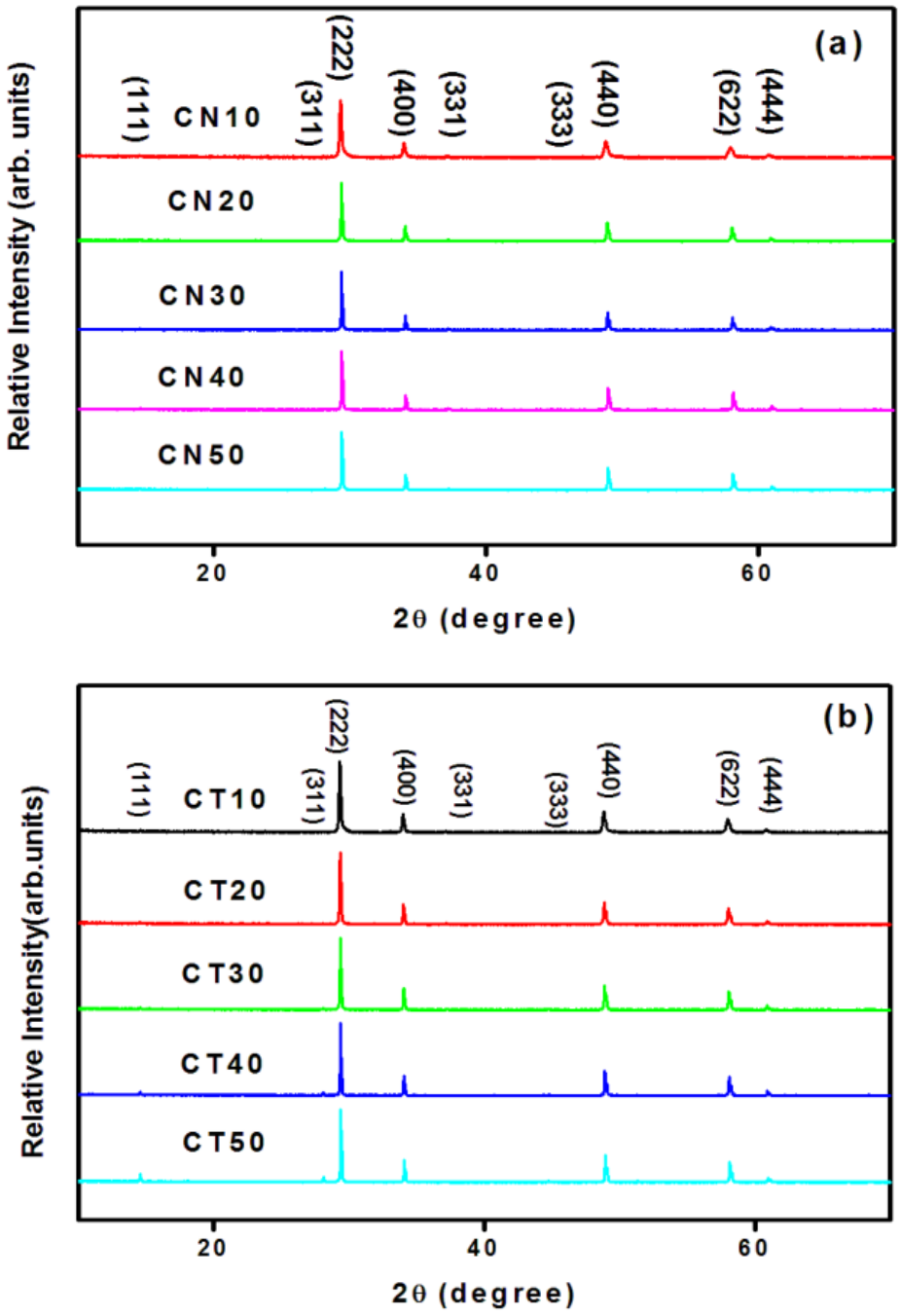

Fig 5.1 Powder X-ray diffraction patterns of (a) $(Ca_xGd_{1-x})_2(Zr_{1-x}Nb_x)_2O_7$ (b) $(Ca_xGd_{1-x})_2(Zr_{1-x}Ta_x)_2O_7$ samples

less compared to Ta which leads to a significant decrease in the intensity of superlattice peaks. This is evident from Fig 5.2 which shows the powder XRD patterns of $Ca_2Nb_2O_7$ and $Ca_2Ta_2O_7$ simulated using X'pert High Score Plus software. Progressive structural transformation into defect pyrochlore structure can also lead to decrease in intensity of the superlattice peaks. Hence it is very difficult to directly determine from XRD pattern whether the average structure of the compounds is defect pyrochlore or defect fluorite.

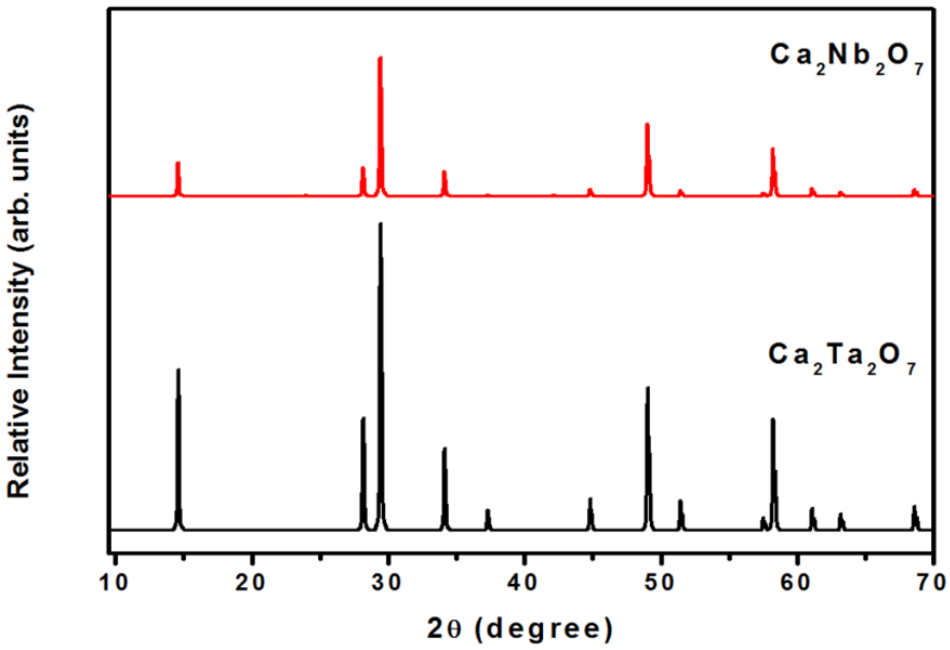

Fig 5.2 Powder XRD patterns of $Ca_2Nb_2O_7$ and $Ca_2Ta_2O_7$ simulated using X'pert High Score Plus software.

Rietveld refinement of XRD data is the best method to validate the crystal system and the space group in which the compound belongs. Structural analysis was done by using Rietveld refinement program Fullprof-2010. First of all scale factor and background parameters were fitted. Diffraction peak profile was fitted with pseudo-Voigt profile function and Caglioti profile parameters were refined. Absorption and extinction coefficients were not considered during refinement. Oxygen *x*-parameters were refined for all samples. Refinement of occupancy of cations and anion with stoichiometric constraints was not converged to a reasonable value during refinement because of the complexity due to the presence of four different cations distributed over two crystallographic sites.

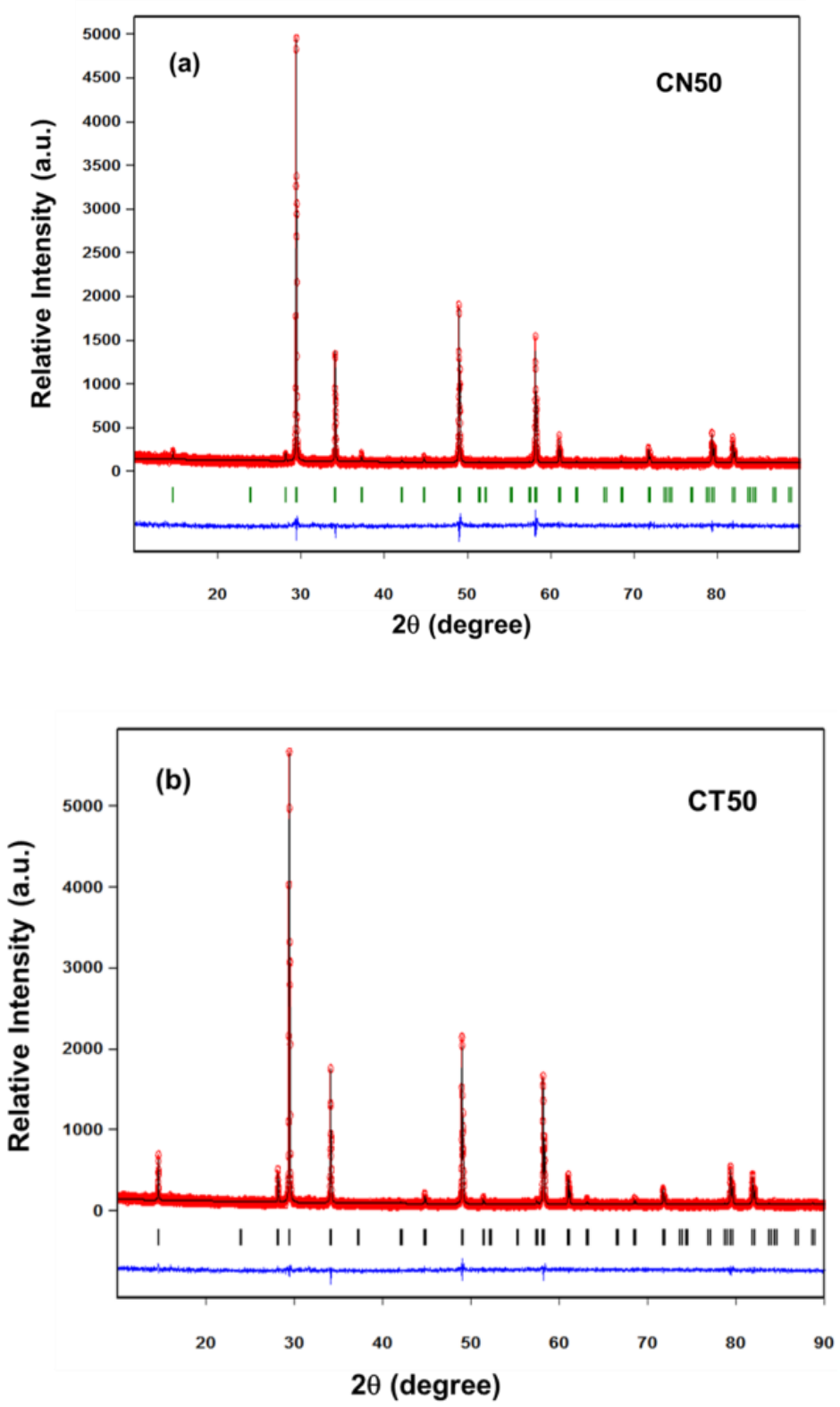

Fig 5.3 Observed calculated and difference patterns of (a) CN50 (b) CT50. The Rietveld refinement using Fullprof 2010 software was performed with X-ray diffraction patterns of the sintered products taken at room temperature.

Table 5.1 Rietveld refined parameters of $(Ca_xGd_{1-x})_2(Zr_{1-x}Nb_x)_2O_7$ (x = 0.1, 0.2, 0.3, 0.4, 0.5) samples

Sample	CN10	CN20	CN30	CN40	CN50
Phase	Defect Pyrochlore	Defect Pyrochlore	Defect Pyrochlore	Pyrochlore	Pyrochlore
Unit Cell	Cubic	Cubic	Cubic	Cubic	Cubic
Space Group	$Fd\bar{3}m$	$Fd\bar{3}m$	$Fd\bar{3}m$	$Fd\bar{3}m$	$Fd\bar{3}m$
Total number of independent reflections	43	43	43	43	43
Lattice constant (Å)	10.5510(3)	10.5345(6)	10.5253(5)	10.5188(6)	10.5117(4)
FWHM U	0.6506(7)	0.0362(5)	0.0243(8)	0.0123(5)	0.0295(6)
Parameters V	-0.2096(4)	-0.0109(3)	-0.0043(4)	-0.0025(7)	-0.0136(5)
W	0.0404(5)	0.0037(8)	0.0011(2)	0.0016(4)	0.0031(3)
Zero	-0.0007(2)	0.0378(5)	0.0217(6)	0.0175(3)	-0.0080(1)
Asymmetry parameters	-0.0793(8)	0.0252(5)	0.0200(1)	0.0001(7)	0.0027(6)
	-0.0442(6)	0.0022(3)	0.0017(4)	-0.0077(5)	-0.0071(5)
Oxygen x-parameter	0.3500(5)	0.3437(6)	0.3378(8)	0.3335(2)	0.3293(3)
Overall B-factor	0.8586(7)	0.8317(4)	0.5402(4)	0.2795(6)	0.2235(5)
R-Factors Rp (%)	8.45	7.70	7.75	7.79	8.86
Rwp (%)	11.10	9.79	9.94	10.10	10.60
Rexp (%)	8.18	8.28	8.41	8.63	8.82
χ^2	1.86	1.40	1.40	1.36	1.45
GOF	1.4	1.2	1.2	1.2	1.2

A few typical X-ray diffraction patterns after Rietveld refinement are given in Fig 5.3. The results of refinement are given in Table 5.1 and Table 5.2. Even a 10 mol% substitution leads to some amount of ordering in the lattice and average structure becomes pyrochlore with $Fd\bar{3}m$ space group. It has been found that lattice parameter decreases with the substitution of Ca^{2+} (1.12 Å) in place of Gd^{3+} (1.053 Å) at A-site and Nb^{5+} (0.64 Å) in place of Zr (0.72 Å) at B-site. This decrease in lattice parameter can be attributed to a significant decrease in ionic size at B site due to substitution compared to a small increase in ionic radius at A site. The decrease of

lattice parameter can also be attributed to progressive ordering of both anions and cations of the pyrochlore structure. It is also evident from the tables that 48*f* oxygen *x* parameter also decreases with doping concentration. This indicates that the ordering in the lattice increases with simultaneous substitution as *x* -parameter is a sensitive measure of disorder in anion sublattice. In a pyrochlore structure with origin (0, 0, 0) at B site, 48*f* oxygen *x* parameter lies within the range 0.309- 0.375.

Table 5.2 Rietveld refined parameters of $(Ca_xGd_{1-x})_2(Zr_{1-x}Ta_x)_2O_7$ (x = 0.1, 0.2, 0.3, 0.4, 0.5) samples

Sample	CT10	CT20	CT30	CT40	CT50
Phase	Defect Pyrochlore	Defect Pyrochlore	Defect Pyrochlore	Pyrochlore	Pyrochlore
Unit Cell	Cubic	Cubic	Cubic	Cubic	Cubic
Space Group	$Fd\bar{3}m$	$Fd\bar{3}m$	$Fd\bar{3}m$	$Fd\bar{3}m$	$Fd\bar{3}m$
Total number of independent reflections	43	43	43	43	43
Lattice constant (Å)	10.5451(6)	10.5350(7)	10.5310(3)	10.5257(6)	10.5177(4)
FWHM U	0.3598(2)	0.0253(5)	0.0315(8)	0.0194(7)	0.0197(3)
Parameters V	-0.1110(5)	0.0038(7)	-0.0072(4)	-0.0075(2)	-0.0084(6)
W	0.0220(9)	0.0011(8)	0.0015(8)	0.0017(6)	0.0020(7)
Zero	-0.0142(4)	-0.0147(5)	-0.0065(2)	-0.0087(3)	-0.0113(6)
Asymmetry	-0.0410(8)	0.0149(6)	0.0144(6)	0.0285(4)	0.0319(5)
parameters	-0.0282(3)	0.0015(4)	0.0013(2)	0.0047(1)	0.0024(3)
Oxygen x-parameter	0.3495(6)	0.3422(7)	0.3355(4)	0.3299(8)	0.3263(7)
Overall B-factor	0.7455(5)	0.6938(8)	0.2657(4)	0.6505(6)	0.6160(9)
R-Factors Rp (%)	9.00	8.50	8.69	8.75	8.71
Rwp (%)	11.60	10.80	11.10	11.30	11.40
Rexp(%)	8.63	8.86	8.97	9.07	9.18
χ^2	1.84	1.49	1.54	1.55	1.53
GOF	1.4	1.2	1.2	1.2	1.2

The theoretical calculation of unknown oxygen *x*-parameter can be accomplished by using inequalities developed by Nikiforov (Nikiforov 1972). These inequalities are reproduced below:

$$\frac{1}{2} - r_O\frac{\sqrt{2}}{a} \geq x \geq \frac{2r_O}{a} \quad \textbf{(5.1)}$$

$$\frac{3}{8} - \frac{1}{8}\left\{3\left[\frac{r_B+r_O}{r_A+r_O}\right]^2 - 2\right\}^{1/2} \geq x \geq \frac{3}{8} - \left\{\left[\frac{r_B+r_O}{a}\right]^2 - \frac{1}{32}\right\}^{1/2} \quad \textbf{(5.2)}$$

where r_A is the ionic radius of A cation, r_B is the ionic radius of B cation, r_O is the ionic radius of oxygen, and '*a'* is the lattice parameter. The values calculated using above inequalities are for origin at O' ion- site. The equation to convert these values to an origin at B site is given by:

$$x(\mathbf{B}) = \frac{5}{8} - x(\mathbf{O}') \quad \textbf{(5.3)}$$

Fig 5.4 shows the variation of calculated and observed *x*-parameter with composition for various pyrochlore type compounds. The calculated values are obtained by solving Nikiforov inequalities and then averaging the smaller of the two larger values and larger of the smaller values and then converted to values corresponding to origin at B site using equation (3). The ionic radii were those of Shannon (Shannon 1976). The observed values are obtained from powder XRD pattern through Rietveld analysis. Usually the observed values are slightly greater than the values calculated using Nikiforov equations. These are believed to be close enough to establish trends in pyrochlore stability field although they may not be totally accurate (McCauley 1980). But it is clear from the graph that as the doping concentration decreases, the variation of *x* parameter is very large and deviates much from the theoretical trend. This can be attributed to the fact that during our theoretical calculations using Nikiforov equations, the disorder in cation and anion array is not taken into consideration. As the doping concentration decreases, disorder in the lattice increases and x-parameter also increases rapidly than expected as it is very sensitive to disorder.

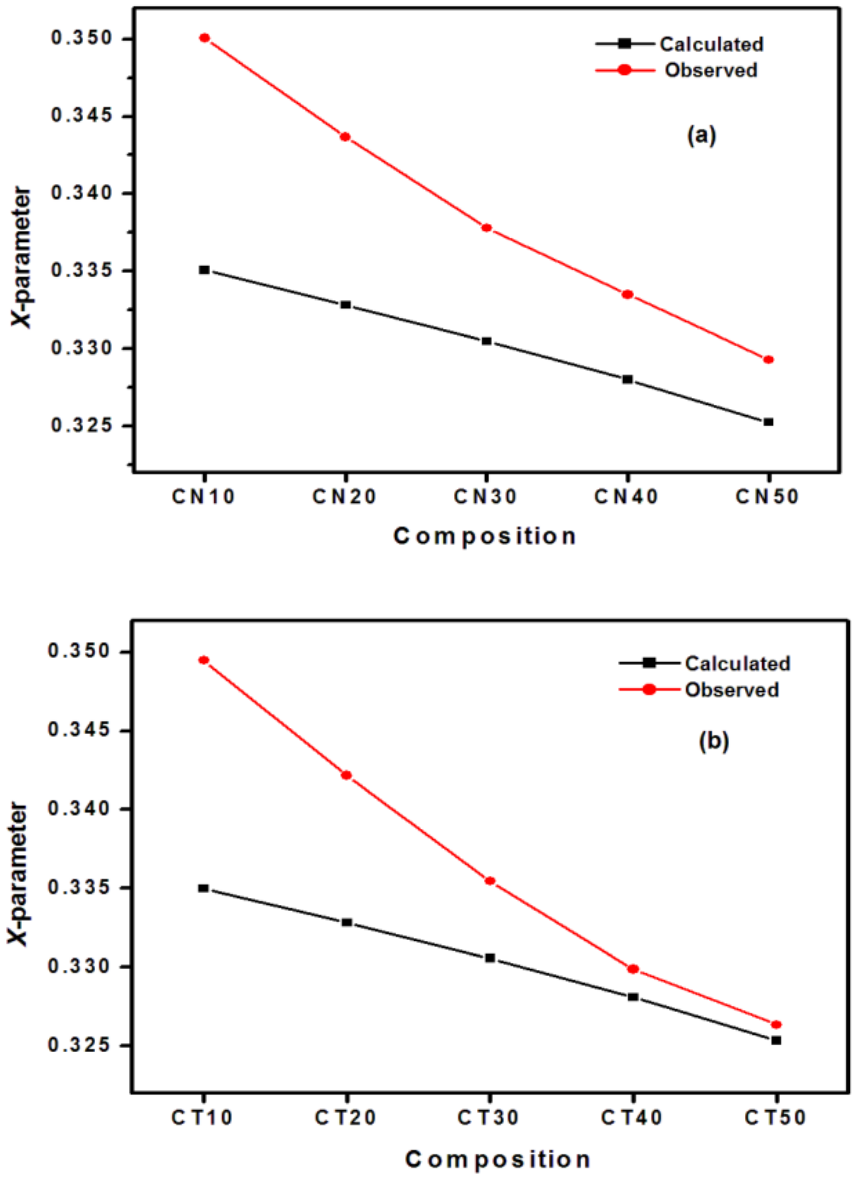

Fig 5.4 Calculated and observed *x*-parameter for (a) $(Ca_xGd_{1-x})_2(Zr_{1-x}Nb_x)_2O_7$ and (b) $(Ca_xGd_{1-x})_2(Zr_{1-x}Ta_x)_2O_7$ samples.

5.3.2 High Temperature XRD Studies

For high temperature applications of functional materials, the structural stability with temperature is a key factor to be investigated. The lattice thermal expansion coefficient is best estimate of structural stability with temperature and can be easily determined using high temperature XRD. Lattice thermal expansion coefficient is calculated using the equation:

$$\alpha_a = \frac{1}{a_{298}}\left(\frac{da}{dT}\right) \quad K^{-1} \tag{5.4}$$

The XRD patterns were recorded for each sample at different temperatures in the range 298 to 1273 K and the patterns are fitted by Lebail fitting method using X'pert High Score Plus. For each sample, plots are made with lattice parameter as a function of absolute temperature. The slope of the graph is calculated by a linear fit of the graph and lattice thermal expansion coefficient is calculated using equation (5.4).

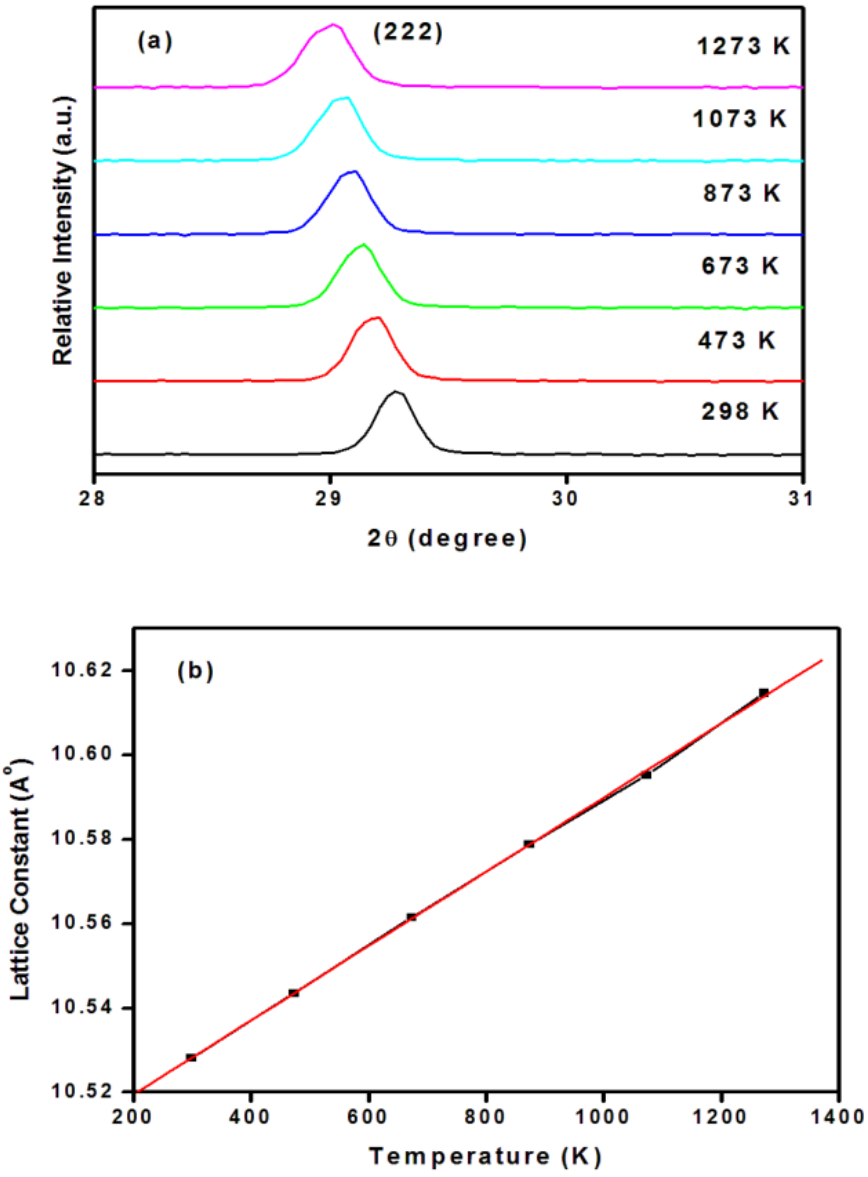

Fig 5.5 (a) High temperature XRD patterns of CT20 and (b) variation of lattice constant with temperature for CT20 (red line shows the linear fit of the data).

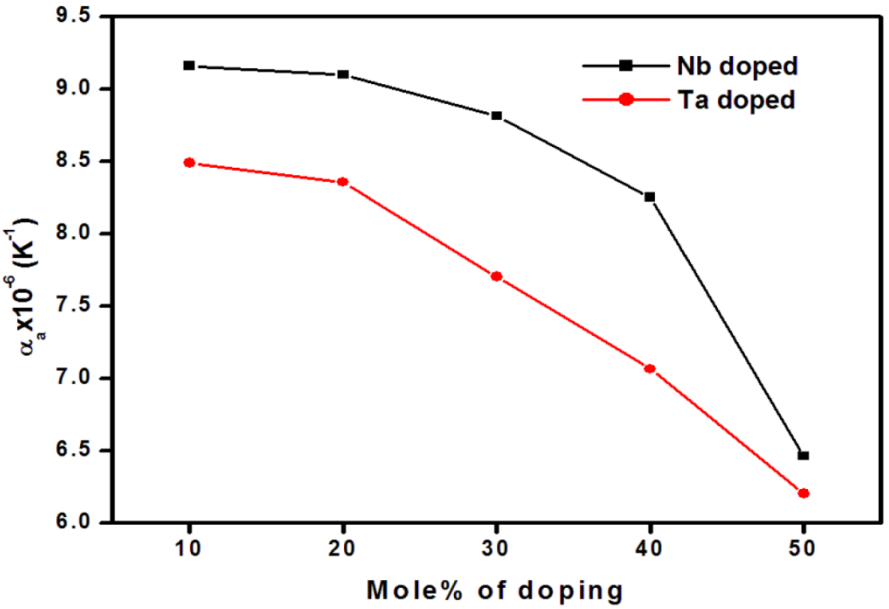

Fig 5.6 Variation of lattice thermal expansion coefficient with different compositions $(Ca_xGd_{1-x})_2(Zr_{1-x}M_x)_2O_7$ (M = Nb or Ta).

High temperature XRD patterns of CT20 at different temperatures and the corresponding lattice parameter vs. temperature plots are shown in Fig 5.5 (a) and (b). In high temperature XRD pattern, only (222) peak is shown and shift of the peak to the lower angle as temperature increases indicates the expansion of the lattice. The variation of lattice thermal expansion coefficient with different compositions, $(Ca_xGd_{1-x})_2(Zr_{1-x}Nb_x)_2O_7$ and $(Ca_xGd_{1-x})_2(Zr_{1-x}Ta_x)_2O_7$ (x = 0, 0.1, 0.2, 0.3, 0.4, 0.5) is shown in Fig 5.6. In pyrochlore type compositions, the thermal expansion coefficient decreases with increase in substitution of Ca and Ta. Shimura et al. reported that the thermal expansion of zirconate pyrochlores decreases with an increase in the ionic radius of A cation. The thermal expansion of zirconate pyrochlores depends on the Madelung binding energy and as Madelung binding energy increases, thermal expansion decreases(Kutty, *et al.* 1994, Shimamura, *et al.* 2007). The Madelung binding energy of zirconate pyrochlores depends on 48*f* oxygen *x* parameter and as *x* parameter decreases, Madelung energy increases(Pannetier 1973, Subramanian, *et al.* 1983). The experimental results of our

high temperature XRD studies were in good agreement with the above trend. The decrease in thermal expansion coefficient with increase in substitution can also be correlated with the ordering process with in the pyrochlore unit cell with substitution.

Pyrochlore structure can progressively disorder to defect fluorite phase through a defect pyrochlore region and during this transition the coordination of B cation also changes progressively from six to eight. B cation in pyrochlore is six coordinated with D_{3d} site symmetry and this can be treated as B cations occupy octahedral site with a tetrahedral distortion, which is induced by the vacant 8*a* site adjacent to BO_6 octahedron. During the phase transition to defect fluorite, the tetrahedral distortion decreases. Nachimuthu et al. (Nachimuthu *et al.* 2005) reported on the disorder in $Gd_2(Ti_{1-y}Zr_y)_2O_7$ investigated by Ti 2p and O 1s near-edge X-ray absorption fine structure spectroscopy and found that as Zr substitutes for Ti the tetrahedral distortion decreases and B cation coordination increases from 6 to 8. Lee et al. (Lee, *et al.* 2009) studied the local electronic structure of fluorite and pyrochlore polymorphs of $Gd_2Zr_2O_7$ by the Zr and O X-ray absorption near-edge spectroscopy (XANES). Zr K-edge absorption spectra of pyrochlore and fluorite phases of $Gd_2Zr_2O_7$ have two absorption peaks around 18030 eV and 18020 eV. But peak splitting width (ΔE) of the two peaks as well as intensity ratio (I_{18030}/I_{18020}) for pyrochlore phases are found to be higher than that in fluorite phases. Li et al. (Li *et al.* 1993) reported that ΔE increases with increase in the crystal symmetry of the system. As a consequence, centre of symmetry of Zr-O bonding is higher in pyrochlore phases than in defect fluorite phases. The full width at half maximum (FWHM) of the absorption is found to be sensitive to environment of Zr atoms and FWHM increases with increase in Zr-O bond length. FWHM absorption peak is found to be higher in defect fluorite phase due to high Zr-O bond length compared to pyrochlore phases. This means that lower the coordination number of Zr, higher the bond strength of Zr-O bond as it get shortened. It can be concluded that high bond strength of B-O bond and hence the low thermal expansion coefficient for ordered pyrochlore can be due to the lower coordination of B cations. In the present study, partially disordered pyrochlores shows high value of lattice thermal expansion coefficient compared to ordered pyrochlores and this may be due to increase in the coordination at B site. Hence the study of

variation of lattice thermal expansion coefficient using high temperature XRD is a useful method to find the extent of disorder present in the pyrochlore structure.

5.3.3 Raman Spectroscopic Studies

X-ray diffraction technique is more sensitive to disorder in cation sublattice compared to anion sublattice since the x-ray scattering power of oxygen is very less compared to rare earth as well as transition metal cations. But Raman spectroscopy is very sensitive to metal – oxygen vibrational modes rather than to metal – metal vibrational modes. Therefore, Raman spectroscopy is an excellent tool to analyze the extent of disorder in pyrochlores and hence to distinguish between pyrochlore type phases and defect fluorite type phases.(Glerup, *et al.* 2001) In cubic pyrochlores, $A_2B_2O(1)_6O(2)$, belonging to the space group $Fd\bar{3}m$ (no.227) with Z= 8, the site symmetry is D_{3d} for A and B cations, C_{2v} for O(1) anions and T_d for O(2) anions(McCauley 1980) (D_{3d}, C_{2v}, and T_d are Schoenfies notations used in spectroscopy for representing symmetry point groups). Factor group analysis based on above site symmetries predicted six Raman active modes(Rousseau, *et al.* 1981) and the irreducible representations are given below.

$$\Gamma \text{ (Raman)} = A_{1g} + E_g + 4F_{2g} \qquad (5.5)$$

A_{1g}, E_g, and F_{2g} are Mullikan symbols representing different vibrational modes of the molecule and '+' symbol here merely representing combination of Raman active vibrations. E_g mode can be assigned to B-O_6 bending vibrations and A_{1g} mode to O-B-O bending vibrations. F_{2g} modes represent a mixture of A-O and B-O bond stretching vibrations with bending vibrations (Mandal, *et al.* 2010, Vandenborre, *et al.* 1983)

In cubic fluorites, AO_2, belonging to space group $Fm\bar{3}m$ (no.225) with Z = 4, the site symmetry is O_h for the A cations and T_d for O anion. According to factor group analysis, the only Raman active mode of fluorite type structure is F_{2g} (Keramidas and White 1973). But in defect fluorites, intensity for F_{2g} mode is observed to be very weak and appear as a broad peak (Hess, *et al.* 2002).

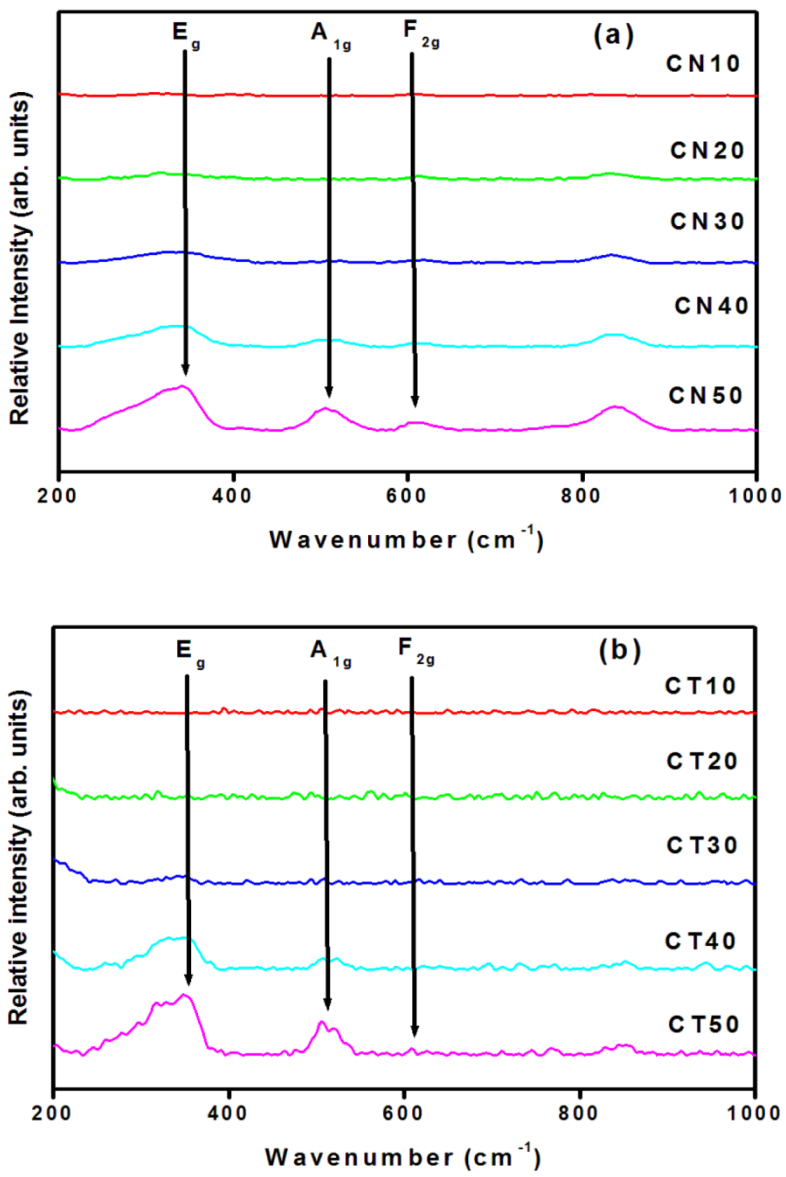

Fig 5.7 Fourier Transform Raman spectra of (a) $(Ca_xGd_{1-x})_2(Zr_{1-x}Nb_x)_2O_7$ (b) $(Ca_xGd_{1-x})_2(Zr_{1-x}Ta_x)_2O_7$ samples.

Fig 5.7 (a) and (b) show the Fourier Transform Raman spectra of Nb and Ta substituted compounds respectively. The Raman spectra of CN50 and CT50 show major Raman modes of pyrochlores like A_{1g} at ~514 cm^{-1}, E_g at ~348 cm^{-1} and one F_{2g} band at ~610 cm^{-1} with considerable intensity. The mode appears at ~830 cm^{-1} may be due to local disorder, vacancies and defects present in the pyrochlore lattice. The presence of vacancies and defects disrupts the translational periodicity of the lattice and consequently it relaxes the $k \approx 0$ selection rule (Mandal, *et al.* 2007). This may lead to the presence of additional modes, but of very less intensity in Raman spectra.

Other F_{2g} bands are very weak in intensity and indistinguishable from the background. All Raman modes observed are quite broad and as the doping concentration decreases broadness increases. It is also clear from the spectra that as the doping level decreases, there is a progressive decrease in intensity of A_{1g}, E_g and F_{2g} modes indicating a progressive disordering of anion sublattice. A quantitative analysis of extent of disordering is not appreciable because of the weak intensity of Raman peaks, but it confirms the results obtained from Rietveld analysis.

5.3.4 Transmission Electron Microscopy Studies

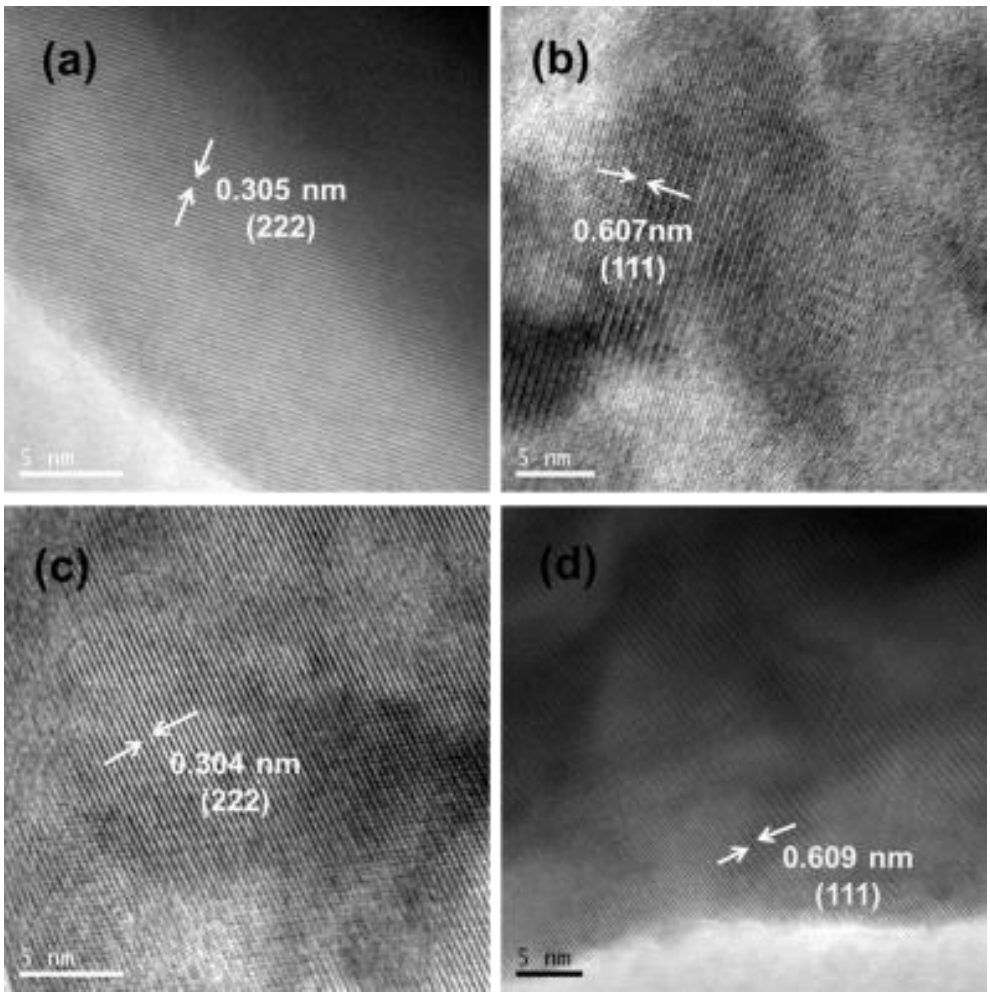

Fig 5.8 High resolution images of (a) CN10 (b) CN50 (c) CT10 and (d) CT50

Fig 5.8 shows the high resolution images of representative samples of both defect pyrochlore and ordered pyrochlore with Nb as well as Ta substituted compositions. In Fig 5.8 (a) and (c), (222) plane with its lattice spacing is marked and

the absence of superlattice plane (111) is a clear indication of disorder in the ideal pyrochlore structure. It is obvious from Fig 5.8 (b) and (d) that the (111) superlattice plane with (222) plane is clearly visible for ordered pyrochlore compositions. Fig 5.9 shows the SAED patterns of CN10 and CN50. SAED pattern appears to have many pyrochlore diffraction spots due the aggregation of two or more powder particles leading to the merging of two or more diffraction patterns. Also the particle size of the powder is in micro range as it is sintered at high temperature and is not completely electron transparent so that the diffraction spots are weak in intensity. The major set of reflections is indexed and is in good agreement with planes corresponding to pyrochlore structure. The superlattice plane, (111) is observed in both cases as weak reflection indicating that CN10 has not completely disordered to defect fluorite structure and this confirms the Rietveld refinement results.

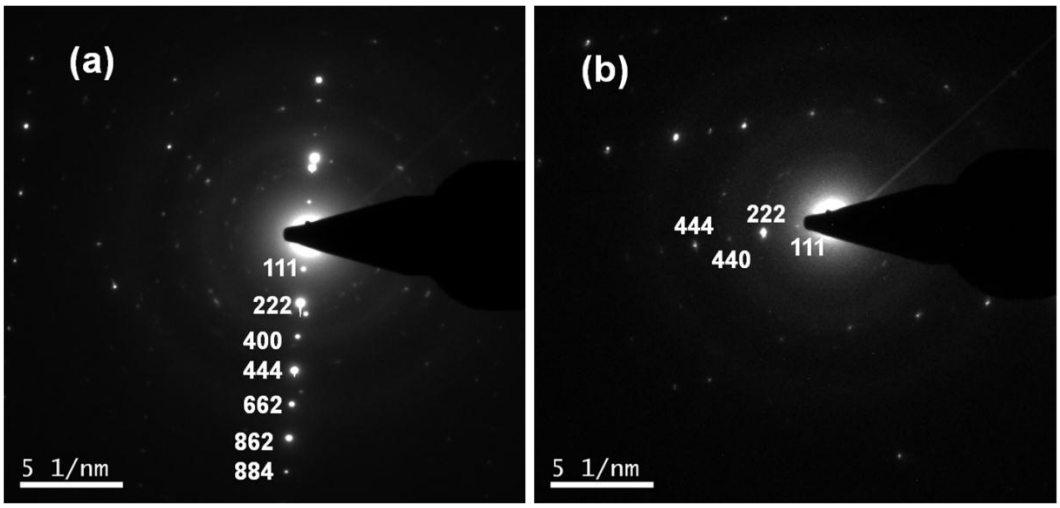

Fig 5.9 Selected area electron diffraction patterns of (a) CN10 and (b) CN50

5.3.5 Impedance Spectroscopic Studies

The temperature dependence of the total conductivity of $(Ca_xGd_{1-x})_2(Zr_{1-x}Nb_x)_2O_7$ and $(Ca_xGd_{1-x})_2(Zr_{1-x}Ta_x)_2O_7$ (x = 0.1, 0.2, 0.3, 0.4, 0.5) samples are respectively shown in Fig 5.10 (a) and (b). The conduction is predominantly ionic and found to follow Arrhenius behavior given by the equation:

$$\sigma(T) = \sigma_0 \exp(-E_a/K_BT) \quad (5.6)$$

where σ_0 is a pre-exponential factor, which is a measure of effective number of oxide mobile ions, E_a denotes the activation energy for conduction process, K_B is the Boltzmann constant, and T is the absolute temperature.

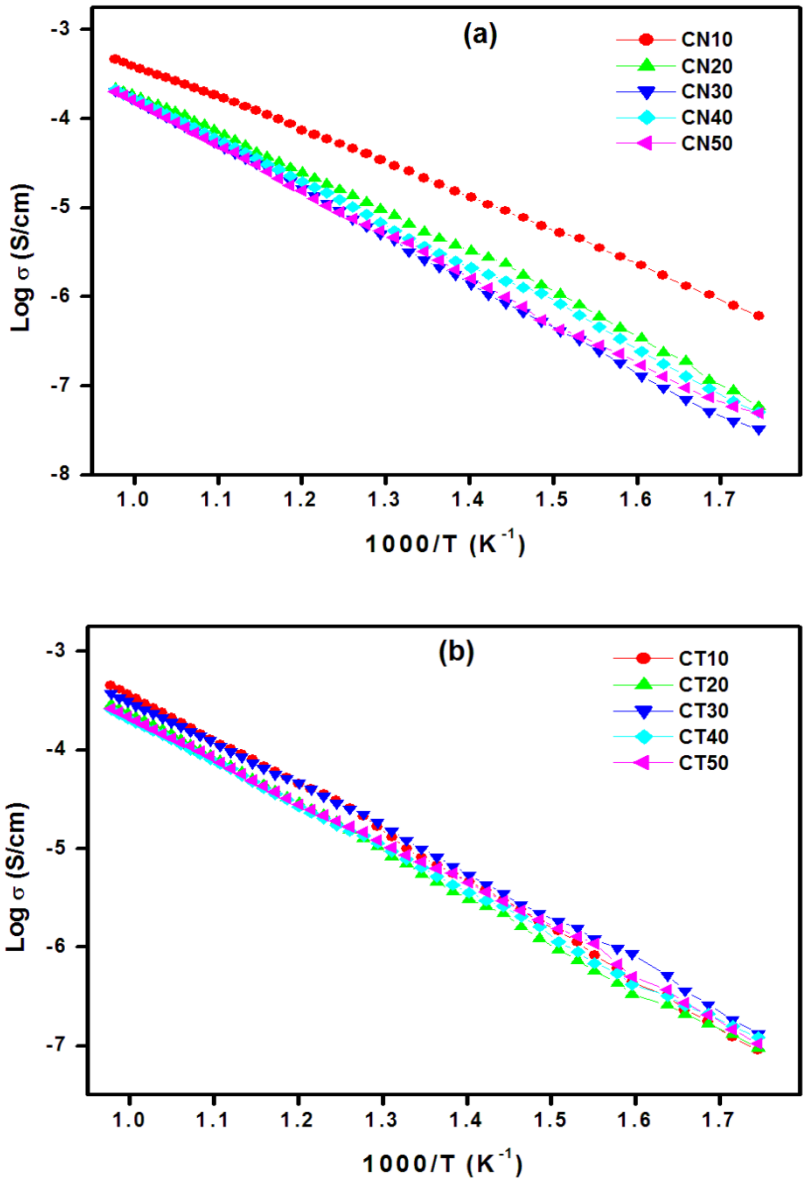

Fig 5.10 Temperature dependence of total conductivity of (a) $(Ca_xGd_{1-x})_2(Zr_{1-x}Nb_x)_2O_7$ (b) $(Ca_xGd_{1-x})_2(Zr_{1-x}Ta_x)_2O_7$ samples.

The intrinsic oxide ion conductivity is high for pure $Gd_2Zr_2O_7$ than compared to other pyrochlore in accordance with the results found in literature. (Burggraaf *et al.* 1981) As $Gd_2Zr_2O_7$ belong to defect fluorite structure with a completely disordered anion and cation array, it provides easy pathway for oxide ion to move through the

lattice. But with doping the disordered structure becomes more ordered and ionic conductivity decreases sharply. When the compounds gain sufficient pyrochlore ordering, the ionic conductivity remains almost a constant with variation in further doping. It can be noted from the figures that in Ta substituted compounds, ionic conductivity remains constant with doping and in Nb substituted compounds there is a jump in ionic conductivity at near the phase boundary between disordered pyrochlore and defect fluorite compounds. This is because substitution of Ta in place of Zr leads to more ordering in the lattice compared to Nb even though both of them have the same ionic radius. This is because bond strength is also a factor deciding structure stability and disorder. Ta – O bond strength is higher than that of Nb – O bond and it is evident from thermal expansion studies of the samples where Nb substituted compounds show higher values of thermal expansion coefficient compared to Ta substituted compounds. This can also be theoretically proved using Renormalization group method based on the ionization energy theory developed by Arulsamy (Arulsamy 2011).

Table 5.3 Activation energy calculated from Arrhenius plots of $(Ca_xGd_{1-x})_2(Zr_{1-x}M_x)_2O_7$ (M = Nb, Ta) samples

Sample	Activation Energy (Ea) in eV	Sample	Activation Energy (Ea) in eV
CN10	0.7446	**CT10**	0.9261
CN20	0.9078	**CT20**	0.9249
CN30	0.9137	**CT30**	0.9306
CN40	0.9230	**CT40**	0.9331
CN50	0.9295	**CT50**	0.9392

According to ionization energy theory, the phonon frequency of the solid increases exponentially with increase in ionization energy of the constituent ions. The increase in phonon frequency implies increasing rigidity of the system and therefore stronger bond. As the ionization energy of Ta is higher than that of Nb, Ta substituted compounds have higher bond strength than Nb substituted compounds. The activation energy is calculated for all samples from the slope of the corresponding Arrhenius plot and is shown in Table 5.3. Activation energy remains almost constant for all the

samples except CN10 which has higher conductivity compared to other compositions. The ionic conductivity as well as activation energy depends on extent of disorder in the lattice and bond strength.

5.4. Conclusions

Pyrochlore type solid solutions, $(Ca_xGd_{1-x})_2(Zr_{1-x}M_x)_2O_7$ (x = 0.1, 0.2, 0.3, 0.4, 0.5 and M = Nb or Ta) were prepared by high temperature solid state route and structural studies were made by powder X-ray diffraction (XRD) method, FT NIR Raman spectroscopic techniques and transmission electron microscopy (TEM). It is observed that with increase in doping a progressive ordering in the lattice from a defect pyrochlore to an ordered pyrochlore type structure indicated by increase in the intensity of superlattice peaks and decrease in the value of 48*f* oxygen *x*- parameter. This disorder to order transformation is confirmed from Rietveld analysis of powder XRD patterns and Raman spectroscopic analysis. The lattice thermal expansion coefficient for pyrochlore type compounds is of the order of 10^{-6} K^{-1} and found to decrease with decrease in 48*f* oxygen *x* parameter. Ordered pyrochlores are found to have more temperature stability as they have low value of lattice thermal expansion coefficient compared to disordered pyrochlore compositions. Hence variation thermal expansion coefficient with composition is also a good indicator of disordering in pyrochlore type oxides. From the impedance spectroscopic studies, it is found that not only structural disorder, but the bond strength also is a key parameter in deciding the conductivity of pyrochlore type solid solutions.

Chapter 6

Role of Bond Strength on Lattice Thermal Expansion and Oxide Ion Conductivity in Quaternary Pyrochlore Solid Solutions

Quaternary pyrochlore type solid solutions, $CaGdZrNb_{1-x}Ta_xO_7$ (x = 0, 0.2, 0.4, 0.6, 0.8, 1) were prepared by high temperature ceramic route. The pyrochlore phase of the compounds were confirmed by powder X-ray diffraction, Raman spectroscopy and transmission electron microscopy. The crystallographic parameters of the pyrochlore compounds were accurately determined by the Rietveld analysis of the powder diffraction data. The isovalent substitution of Ta in place of Nb at B site can reveal the effect of chemical bonding on lattice thermal expansion and oxide ion conductivity since both Nb and Ta have the same ionic radius (0.64 Å). Lattice thermal expansion coefficient of the samples were calculated from the high temperature XRD measurements and found that thermal expansion coefficient decreases with the substitution of Ta. Oxide ion conductivity measured by two probe method also shows the same trend with the substitution of Ta and this can be attributed to the high bond strength of Ta-O bond compared to that of Nb-O bond. Microstructural characterization using SEM proves that size of the grains has a small effect on oxide ion conductivity. Our studies establish the role of chemical bonding in deciding the conductivity of pyrochlore oxides and confirmed that 48*f* - 48*f* mechanism of oxide ion conduction is dominant in pyrochlore oxides.

A. N. Radhakrishnan, P. Prabhakar Rao, S. K. Mahesh, D. S. Vaisakhan Thampi and Peter Koshy, "Role of Bond Strength on the Lattice Thermal Expansion and Oxide Ion Conductivity in Quaternary Pyrochlore Solid Solutions", ***Inorganic Chemistry***, 2012, 51 (4), 2409–2419

6.1 Introduction

Oxides with pyrochlore structure have been the subject of a number of investigations in the last few decades and exhibits diverse properties such as semiconductivity, (Deepa *et al.* 2011, Rao *et al.* 2005) ionic conductivity,(Kharton, *et al.* 2004, Sibi *et al.* 2009) superconductivity,(Hiroi *et al.* 2007, Yoshimura *et al.* 2003) high radiation tolerance,(Sickafus, *et al.* 2000) dielectric properties (Sameera *et al.* 2011) and luminescence properties (Hirayama *et al.* 2008). Pyrochlore oxides have the general formula $A_2B_2O_7$ where A is the larger cation and B is the smaller one. Mostly A is a trivalent rare-earth ion, but can also be a mono, divalent cation, and B may be 3d, 4d or 5d transition element having an appropriate oxidation state required for charge balance to give rise to the composition $A_2B_2O_7$. Pyrochlore oxides lend themselves to a wide variety of chemical substitutions at the A, B and O sites and the crystal structure can tolerate vacancies at the A and O sites to a certain extent. This structure is closely related to fluorite and can be considered as an ordered, defect fluorite structured materials with anion vacancies (Erickson *et al.* 2002, Stanek *et al.* 2002). Owing to their unique structural characteristics, pyrochlore oxides show high chemical stability, high catalytic activity, high melting temperature, and excellent oxide ion conductivity. Oxide ion conducting pyrochlores find applications in solid oxide fuel cells as electrolytes (Kumar *et al.* 2008) and gas sensors (Shimizu and Maeda 1998).

Generally pyrochlores are of two major classes depending upon the combination of oxidation states namely (2+, 5+) pyrochlores and (3+, 4+) pyrochlores. Pyrochlore structure has only one parameter, the 48*f* oxygen *x* value, needs to be defined in the structure containing four different kinds of atoms, A (16*d*), B (16*c*), O (48*f*) and O' (8*b*). However, the 8- fold and 6-fold coordination polyhedra of oxygen around the A and B cations respectively in $A_2B_2O_7$ change shape with *x* and the entire structure can be viewed in several different ways. A comprehensive account of the crystal structure, field of stability, synthesis and physical properties of $A_2^{3+}B_2^{4+}O_7$ (3+,4+), $A_2^{2+}B_2^{5+}O_7$ (2+,5+) and various substituted pyrochlores is presented in review by Subramanian et.al (Subramanian, *et al.* 1983). Many of the pyrochlore oxides known in the literature are of the (3+,4+) type and is due to the fact that a large number of A^{3+} and B^{4+} cations have suitable ionic radius for the formation

of pyrochlore structure. The relative ionic radii or the ionic radius ratio, (RR = r_A/r_B) and the oxygen parameter govern the formation and stability of the (3+,4+) type oxide pyrochlores. Relatively fewer number of (2+, 5+) oxide pyrochlores are known in comparison to the large number of available (3+, 4+) pyrochlores. This is because there are fewer suitable A^{2+} and B^{5+} cations than the A^{3+} and B^{4+} cations. It is not possible to define the field of existence in terms of RR more accurately because of the absence of elements of closely related ionic radii similar to the rare earths in the (3+,4+) pyrochlores. However, the (2+, 5+) pyrochlores are unique in that the covalency, polarizability and electronegativity of the constituent ions give rise to a wide variety of interesting physical properties (Subramanian, *et al.* 1983).

Quaternary pyrochlore systems with the general formula, $A_1^{2+}A_2^{3+}B_1^{4+}B_2^{5+}O_7$, can be considered as a combination of two types of pyrochlores. But detailed phase diagram studies (Belyaev *et al.* 1978) established that the quaternary phases crystallizing with cubic pyrochlore structure are indeed well-defined stoichiometric phases and not solid solutions of two binary phases. The presence of multivalent cations can induce distortions in the structure which in turn affects the thermal and electrical properties of the compounds. Structure - property correlation studies provide a basic understanding required for designing new oxide ion conductors which can be used in Intermediate Temperature Solid Oxide Fuel Cells as electrolytes. Researches in the field of solid oxide fuel cells have recently gained more attention due to the great concerns over energy crisis and environmental pollution. Govindan Kutty et al. (Kutty, *et al.* 1994) reported a systematic study of thermal expansion coefficients of lanthanide pyrochlore zirconates and hafnates and found that thermal expansion coefficient decreases with an increase in the A cation radius. They have correlated thermal expansion behavior with oxygen *x* parameter, Madelung binding energy and finally to the bond strength. Extensive amount of experimental data is available in the literature on the relationship between oxide ion conductivity and structural disorder,(Wuensch, *et al.* 2000) mostly in (3+, 4+) pyrochlore oxides with substitutions either at A site (Diaz-Guillen *et al.* 2009) or B site (Takamura and Tuller 2000). We have recently reported the influence of disorder on structure, lattice thermal expansion and oxide ion conducting properties of $(Ca_xGd_{1-x})_2(Zr_{1-x}M_x)_2O_7$ (M = Nb or Ta) pyrochlore solid solutions.(Radhakrishnan *et al.* 2011) Disorder in

pyrochlore can enhance the oxide ion conductivity, but also led to high thermal expansion of the lattice. The influence of chemical bonding on lattice thermal expansion and oxide ion conductivity were not investigated in quaternary pyrochlores and such an investigation enables one now predict the ionic conductivity based on the elemental composition of a particular compound which is important in materials design for SOFC applications. In the present study, $CaGdZrNb_{1-x}Ta_xO_7$ (x = 0, 0.2, 0.4, 0.6, 0.8, 1) were prepared and characterized to establish the correlation among structure, lattice thermal expansion and oxide ion conductivity. The study is particularly focused on relating bond strength to lattice thermal expansion and oxide ion conductivity so that one can predict unambiguously the lattice expansion and oxide ion conductivity from the bond-strengths.

6.2 Experimental

$CaGdZrNb_{1-x}Ta_xO_7$ (x = 0, 0.2, 0.4, 0.6, 0.8, 1) samples were prepared by the conventional ceramic route using the starting materials: $CaCO_3$, Gd_2O_3, ZrO_2, Nb_2O_5 and Ta_2O_5 (SIGMA - ALDRICH, 99.99 %). The raw materials were weighed according to the stoichiometry of the samples and then mixed thoroughly in an agate mortar. Acetone was added to the powdered mixture for proper mixing. Then, the mixture was dried in an air oven at 100 ºC for 1 h. This procedure of mixing and subsequent drying was repeated thrice to get a homogeneous mixture. The powdered samples were calcined at 1300 ºC for 6 h, followed by a second calcination at 1400 ºC for 10 h.

Table 6.1 Theroretical, experimental and relative densities of $CaGdZrNb_{1-x}Ta_xO_7$ (x = 0.1, 0.2, 0.3, 0.4, 0.5) samples sintered at 1550 ºC for 36 h

Compound	Theoretical density (gm/cm^3)	Experimental density (gm/cm^3)	Relative density (%)
$CaGdZrNbO_7$	5.6384	5.4388	96.46
$CaGdZrNb_{0.8}Ta_{0.2}O_7$	5.8313	5.6109	96.22
$CaGdZrNb_{0.6}Ta_{0.4}O_7$	6.0424	5.8019	96.02
$CaGdZrNb_{0.4}Ta_{0.6}O_7$	6.2430	5.9758	95.72
$CaGdZrNb_{0.2}Ta_{0.8}O_7$	6.4463	6.1653	95.64
$CaGdZrTaO_7$	6.6484	6.3532	95.56

The calcined product was ground into a fine powder and then mixed with 2 wt. % solution of polyvinyl alcohol (PVA) as the organic binder for strengthening and good compaction of the pellet. The dried powder was pressed into cylindrical pellets of 10 mm diameter and about 2 - 3 mm thickness using a hydraulic press. Pellets were initially heated to 600 ºC and kept for 30 minutes to completely remove the organic binder and sintered for 36 h at 1550 ºC to optimize the density of the samples (Density data is given in Table 6.1). Powder X-ray diffraction patterns were recorded to identify the crystalline phase of the sintered samples using a Ni filtered Cu Kα radiation by a Philip's X'pert diffractometer (Step size = 0.02, Scanning time per step = 20 seconds, Divergence slit = 0.5°, and exported by X'pert Pro software). The unit cell parameters were calculated by least square method and Rietveld analysis was also performed to refine the structure using Fullprof-2010. For lattice thermal expansion studies, the XRD pattern of sample was recorded from $2\theta = 10 - 90°$, in the temperature range 293 – 1273 K on a Philips X'pert Pro XRD unit equipped with Anton Paar HTK attachment, at a regular interval of 200 K, in static air. The FT NIR Raman spectra of the powdered samples were recorded on a Bruker RFS100/S spectrometer using near infrared laser excitation (Nd: YAG, 1064 nm). Standard Ge detector cooled to liquid nitrogen temperature is used and it was set to scan over the range from 50 – 1000 cm^{-1}. The resolution of the spectrometer is 4 cm^{-1}. The selected area electron diffraction (SAED) pattern and high resolution transmission electron microscopy (HRTEM) of the samples were taken using transmission electron microscope (TEM) TECNAI 30G2 S-TWIN (FEI, The Netherlands). A small amount of finely powdered sample is dispersed in acetone medium by ultrasonication and drop casted on carbon coated copper grids and dried. The sintered pellets were polished and thermally etched near the sintering temperature for about 30 minutes. The grain microstructure on the surface of the thermally etched samples was recorded using a scanning electron microscope (JEOL, JSM 5600 LV). For impedance spectroscopic studies, a high temperature curing silver paste was applied on polished flat faces of the pellet and electroded with long silver wires. The electroded pellets were cured in a tube furnace for half an hour at 600 ºC. Impedance measurements of the pellets were carried out from 400 ºC to 750 ºC in the frequency range 10 Hz to 1 MHz using a computer controlled Impedance Analyzer (Solartron, SI 1260). The

complex impedance plots were made with the SMART software supplied by M/s Solartron Schlumberger, U.K.

6.3 Results and Discussion

6.3.1 Powder X-ray Diffraction Studies

Powder X-ray diffraction patterns of $CaGdZrNb_{1-x}Ta_xO_7$ (x = 0, 0.2, 0.4, 0.6, 0.8, 1) samples sintered at 1550 ºC are shown in Fig 6.1. Patterns can be well indexed with an ideal cubic pyrochlore structure belonging to $Fd\bar{3}m$ space group. Pyrochlore is a super structure of fluorite type unit cell which has a typical face centered cubic arrangement of cations with anions in the tetrahedral holes. Pyrochlore unit cell also has similar arrangements except the fact that there are two different kinds of cations and consequently two crystallographically non-equivalent anion sites (48*f* and 8*b*) and an anion vacancy (8*a*). Hence the X-ray diffraction pattern of a typical pyrochlore consists of a set of strong intensities representing average fluorite structure plus an additional set of superstructure intensities. The diffraction peaks corresponding to average fluorite structure in the pyrochlore satisfies the set of conditions:(Heremans, *et al.* 1995)

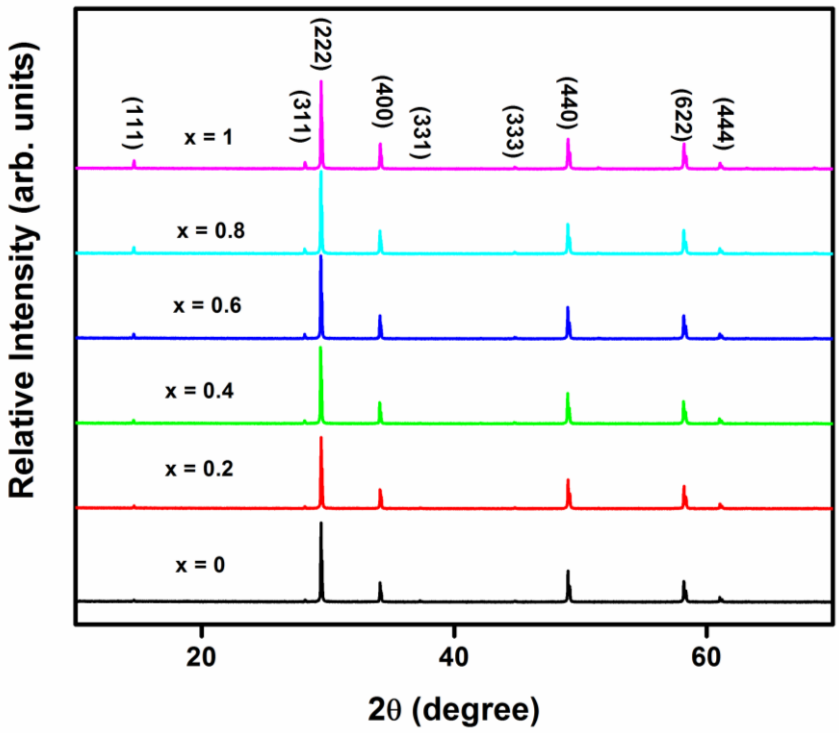

Fig 6.1 Powder X-ray diffraction patterns of $CaGdZrNb_{1-x}Ta_xO_7$ (x = 0.1, 0.2, 0.3, 0.4, 0.5) samples sintered at 1550 ºC

$$\begin{aligned} h + k &= 4n \\ k + l &= 4n \\ h + l &= 4n \end{aligned} \qquad \textbf{(6.1)}$$

where (hkl) is the Miller indices of the plane and n is an integer. These peaks receive more contribution from cation sublattice due to the high scattering power of electron rich rare earth elements and transition metals compared to that of oxygen atoms. Superlattice peaks in the diffraction pattern does not satisfy the conditions (6.1) and Miller indices (hkl) corresponding to these peaks are all odd. The super structure intensities depends on the difference in the scattering power between A and B cations, distortion of anion array, distribution of oxygen vacancies and oxygen *x* parameter (Heremans, *et al.* 1995). Superlattice peaks are observed to be less intense for $CaGdZrNbO_7$ and as the doping level of Ta increases, the superlattice peaks like (111) and (311) becomes more intense. This can be attributed to the fact that the presence of Ta leads to more ordering in the structure and reduces the distortion of the anion sublattice. This variation in intensity of superlattice peaks can also be due to the high X-ray scattering power of Ta compared to that of Nb.

Rietveld Analysis of powder XRD patters was performed using Full proof - 2010 software in order to quantify the structural changes within the unit cell due the progressive substitution of Ta in place of Nb. The initial structure model was based on ideal pyrochlore structure with $Fd\bar{3}m$ space group and occupancies are decided as per the stoichiometry of the compositions. First of all scale factor and background parameters were fitted. Diffraction peak profile was fitted with pseudo-Voigt profile function and Caglioti profile parameters were refined. Absorption and extinction coefficients were not considered during refinement. Lattice parameter and Oxygen *x* parameter were refined for all samples. The results of refinement are given in Table 6.2 and two typical X-ray diffraction patterns after Rietveld refinement are given in Fig 6.2. From the Rietveld analysis, it is found that substitution of Ta in place of Nb leads to a slight decrease in the lattice parameter as evident from composition vs. lattice parameter graph shown in Fig 6.3 along with composition vs. oxygen *x*-parameter graph. The variation of oxygen *x*- parameter also follows the same trend as that of lattice parameter. This is an interesting observation of lattice contraction with substitution of Ta even though the ionic radii of Nb and Ta are the same (0.64 Å)

when six coordinated. The decrease in the lattice parameter with the substitution of Ta may due to the fact that nuclear charge of the Ta is high compared to that of Nb which attracts the electron cloud around it, make the bond shorter. This makes the bond stronger and unit cell to shrink a little.

Table 6.2 Rietveld refined parameters of CaGdZrNb$_{1-x}$Ta$_x$ O$_7$ (*x* = 0.1, 0.2, 0.3, 0.4, 0.5) samples

Sample		**x = 0**	**x = 0.2**	**x = 0.4**	**x = 0.6**	**x = 0.8**	**x = 1**
Phase		Pyrochlore	Pyrochlore	Pyrochlore	Pyrochlore	Pyrochlore	Pyrochlore
Unit Cell		Cubic	Cubic	Cubic	Cubic	Cubic	Cubic
Space Group		$Fd\bar{3}m$	$Fd\bar{3}m$	$Fd\bar{3}m$	$Fd\bar{3}m$	$Fd\bar{3}m$	$Fd\bar{3}m$
Total number of independent reflections		43	43	43	43	43	43
Lattice constant (Å)		10.5139(6)	10.5134(7)	10.5130(2)	10.5125(6)	10.5122(2)	10.5118(5)
FWHM Parameters	**U**	0.0111(6)	0.0192(8)	0.0215(1)	0.0198(1)	0.0256(8)	0.0265(2)
	V	-0.0042(1)	-0.0103(2)	-0.0110(3)	-0.0092(5)	-0.0113(4)	-0.0116(8)
	W	0.0012(1)	0.00253(3)	0.0022(7)	0.0021(5)	0.0026(5)	0.0027(2)
Zero		0.0421(1)	0.0495(3)	0.0080(2)	0.0256(8)	0.0266(7)	0.0485(8)
Asymmetry parameters		-0.0015(7)	0.0319(1)	0.0292(7)	0.0292(8)	0.0453(9)	0.0606(2)
		0.0162(3)	0.0022(4)	-0.0033(5)	0.0077(5)	0.0080(2)	0.0137(4)
Oxygen x-parameter		0.3291(1)	0.3286(2)	0.3281(6)	0.3276(6)	0.3270(5)	0.3265(3)
Overall B-factor		0.2021(7)	0.1498(2)	0.2656(7)	0.1650(3)	0.1859(5)	0.2234(5)
R Factors	**Rp%**	6.74	6.84	6.60	6.61	6.38	6.52
	Rwp%	8.64	8.76	8.51	8.51	8.22	8.38
	Rexp%	6.85	6.98	6.96	6.87	6.77	6.78
	χ^2	1.59	1.58	1.50	1.54	1.47	1.53
	GOF	1.3	1.3	1.2	1.2	1.2	1.2

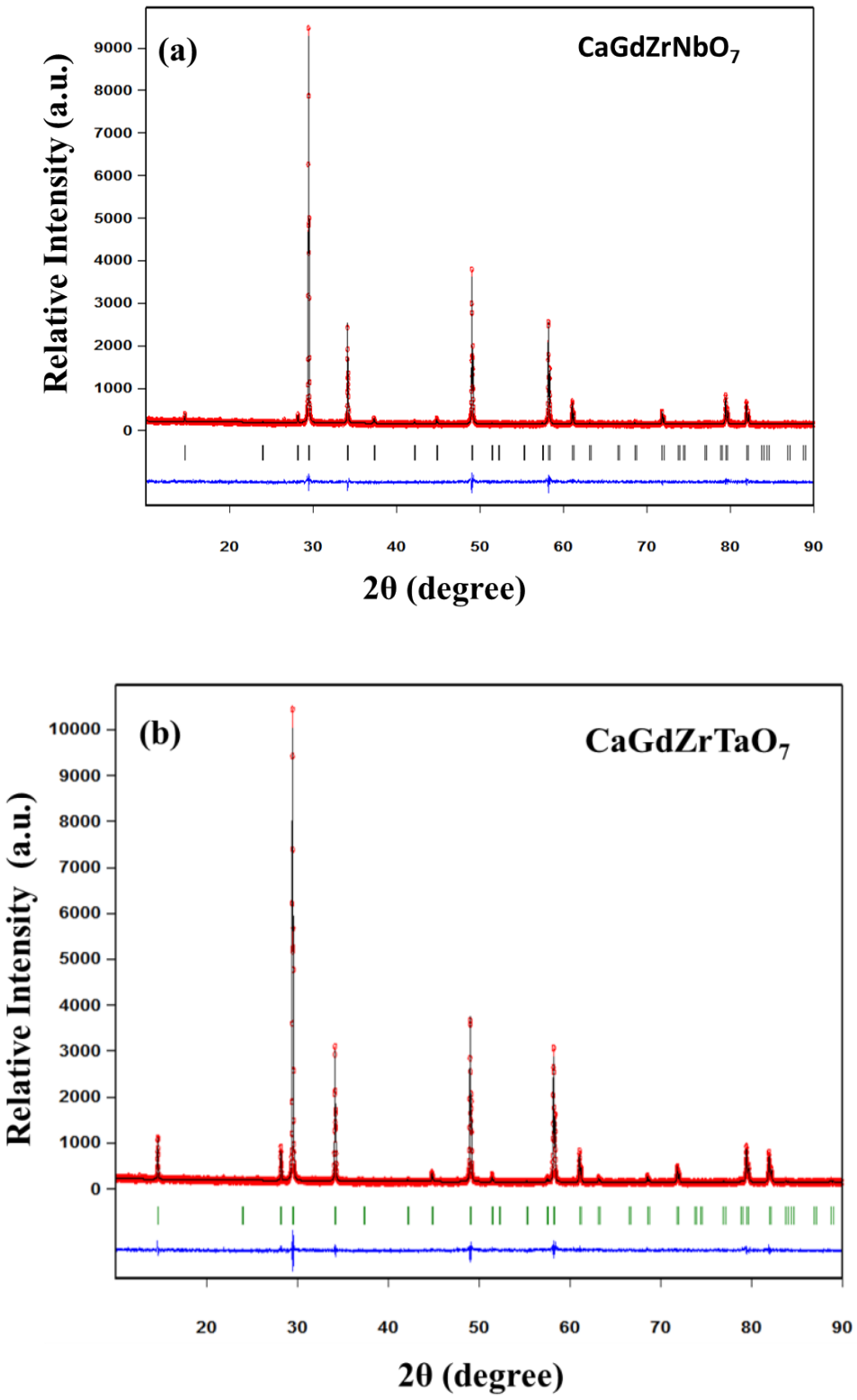

Fig 6.2 Observed , calculated and difference XRD profiles of (a) $CaGdZrNbO_7$ and (b) $CaGdZrTaO_7$ after Rietveld refinement

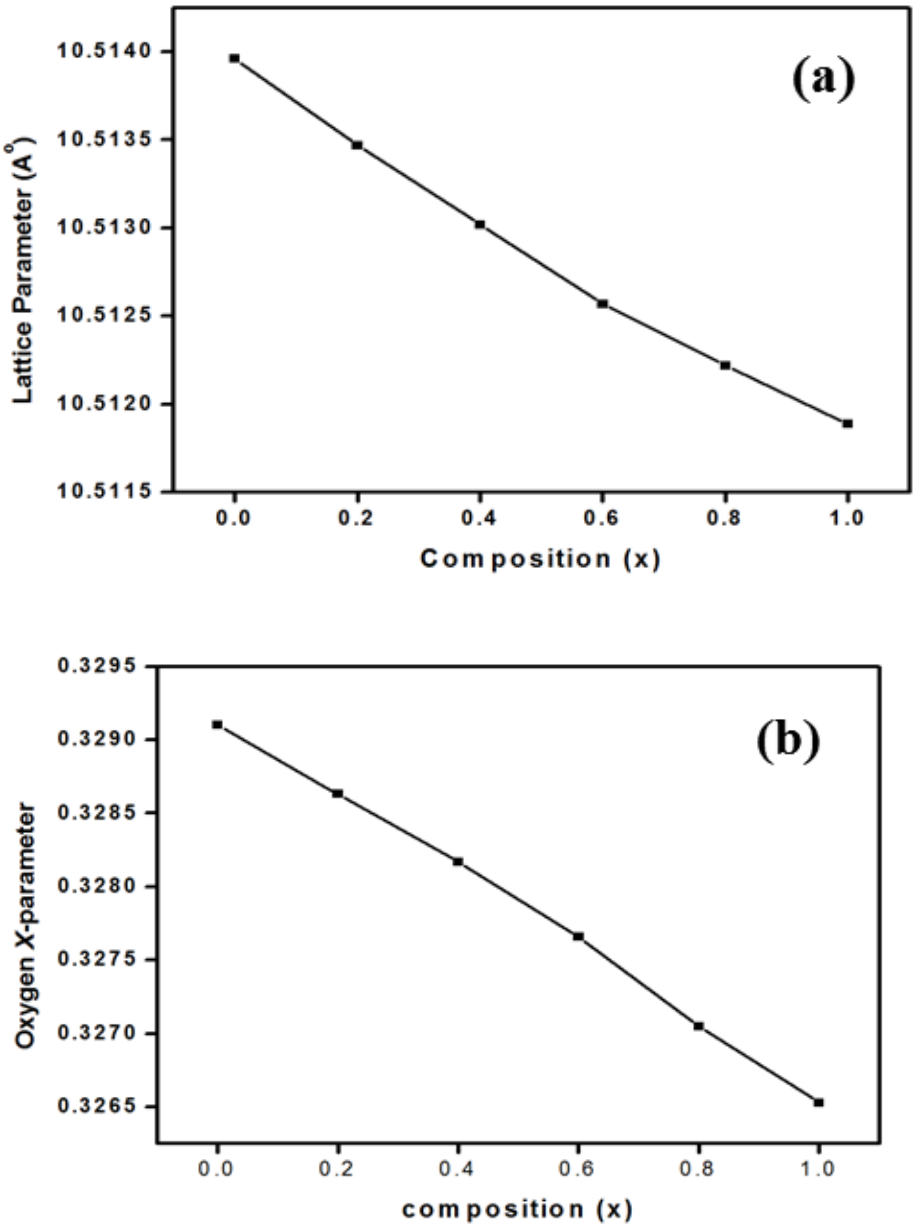

Fig 6.3 Variation of (a) lattice parameter and (b) oxygen *x* parameter with composition

6.3.2 Raman Spectroscopic Studies

Cubic pyrochlores, $A_2B_2O(1)_6O(2)$, belong to the space group $Fd\bar{3}m$ (No. 227), where Z = 8. The number of molecular units per primitive unit cell is two. The corresponding factor group for the cubic pyrochlore is O_h. The site symmetry is D_{3d} for A and B cations, C_{2v} for the O(1) anions and T_d for the O(2) anion (McCauley 1980). Factor group analysis based on above assumptions predicted twenty six

vibrational normal modes and out of which only six are Raman active (Rousseau, *et al.* 1981). The irreducible representations of the six Raman active modes are given below:

$$\Gamma \text{ (Raman)} = A_{1g} + E_g + 4F_{2g} \quad (6.2)$$

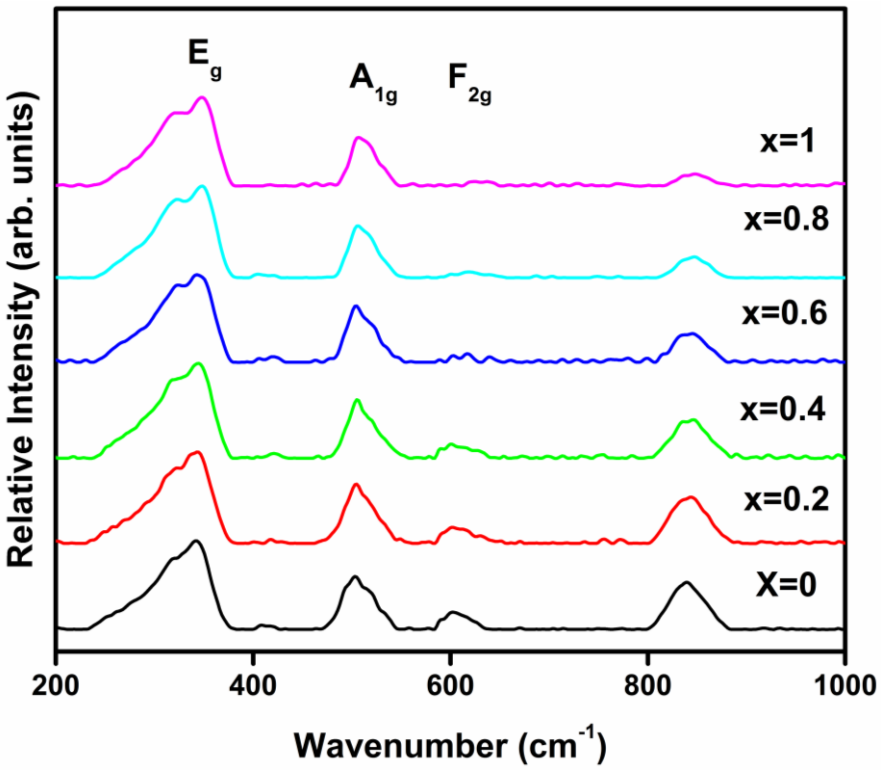

Fig 6.4 Fourier Transform Raman spectra of CaGdZrNb$_{1-x}$Ta$_x$O$_7$ (*x* = 0, 0.2, 0.4, 0.6, 0.8, 1) samples

Fig 6.4 shows the Fourier Transform Raman spectra of CaGdZrNb1$_{-x}$Ta$_x$O7 (*x* = 0, 0.2, 0.4, 0.6, 0.8, 1) samples sintered at 1550 ºC. Only three modes having high intensity are marked in the figure as other modes are very weak in intensity and these modes can be assigned to vibrations of BO_6 octahedra in accordance with Vandenbores work on pyrochlores (Vandenborre, *et al.* 1983). E_g mode appeared around ~ 350 cm^{-1} is the most prominent mode of pyrochlore and appears to be very broad because of the presence of two different cations at B site. This broadening is not due to smaller particle size because the samples are prepared by solid state high temperature route and the XRD patterns are reasonably sharp which confirms the fact

that size of the particles are in micro regime. A_{1g} mode appears around ~ 545 cm^{-1} can be assigned to O-B-O bending. Both E_g and A_{1g} does not have any change in intensity with respect to Ta doping. The four F_{2g} modes of the pyrochlore are usually observed around 300 cm^{-1}, 400 cm^{-1}, 510 cm^{-1} and 610 cm^{-1} (Gupta and Brown 2003). The absence of F_{2g} modes around 300 cm^{-1} and 510 cm^{-1} in the Raman spectra is due the overlap produced by broadening of E_g and A_{1g} modes. F_{2g} mode appearing around 400 cm^{-1} is very weak in intensity and according to group factor analysis; 8*b* site oxygen is related to this mode (Scheetz and White 1979). F_{2g} appears around ~ 600 cm^{-1} has considerable intensity and intensity decreases steadily with Ta substitution for Nb. This mode is linked with 48*f* oxygen (Michel, *et al.* 1974) and a decrease in intensity with Ta doping may be due to the restricted vibration of B-O bond due to high bond strength and subsequent shrinkage of the BO_6 induced by Ta doping. This is evident from the decrease in oxygen *x* parameter with doping as shown in Fig. 3(b) and its explanation in the text. Mode appears around 830 cm^{-1} is reported in the literature as a combination band and arises due to the distortion of BO_6 octahedra and subsequent relaxation of selection rules (Arenas *et al.* 2010). The intensity of this mode also found to decrease with increase in Ta doping and this may be due to the fact that Ta substitution reduces the symmetry distortion of the BO_6 octahedra. These effects are not due to the ionic size induced distortion, but due to the change in the shape of the octahedra induced by chemical bonding.

6.3.3 Transmission Electron Microscopy Studies

Transmission electron microscopy is the best tool to explore the structure of the compounds at its atomic levels. Fig 6.5 shows the high resolution images of the two representative samples along with histograms of a few lattice planes. Pyrochlore superlattice plane (111) is observed in both cases and the corresponding lattice spacing is marked in the figure which corroborates the XRD results. Histograms of the planes show the presence of an intermediate plane of atoms between the (111) approximately at a half distance between them. This plane is (222) plane with exactly half the lattice spacing and it is the most intense plane in X-ray diffraction pattern. Fig 6.6 shows the selected area electron diffraction (SAED) patterns of two samples. Major planes of the pyrochlores were indexed using ratio method and it is compared with corresponding XRD profiles. Super lattice planes of the pyrochlores appear only

as few scattered spots instead of rings which is typical of polycrystalline materials. (111) plane is merged into the high intensity transmitted beam at the centre.

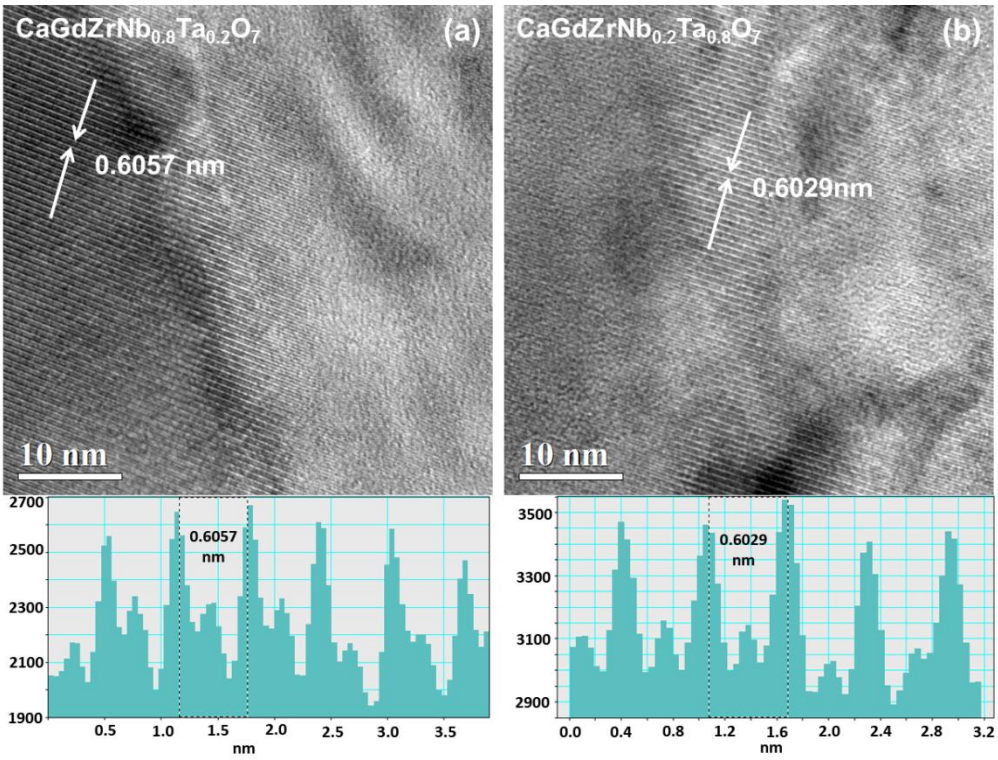

Fig 6.5 High resolution images and the corresponding histogram profiles of a few lattice planes of (a) $CaGdZrNb_{0.8}Ta_{0.2}O_7$ and (b) $CaGdZrNb_{0.2}Ta_{0.8}O_7$ samples

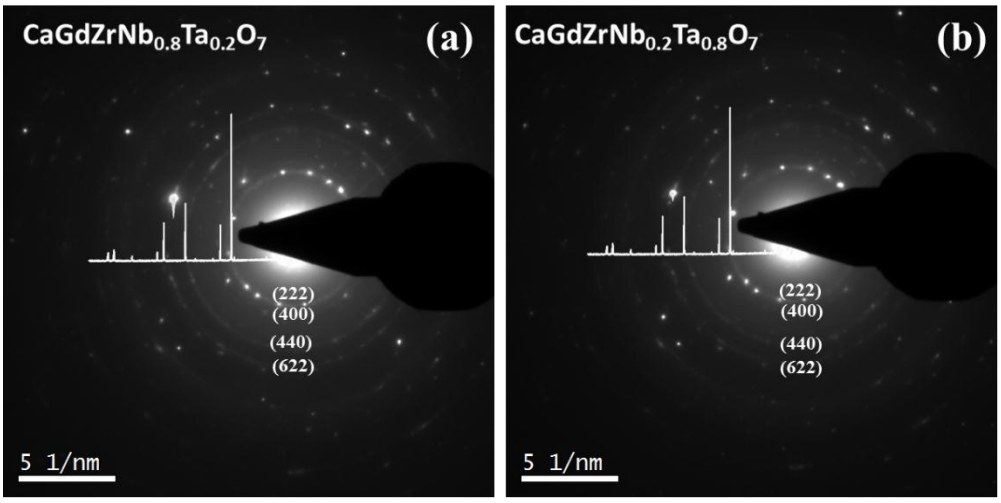

Fig 6.6 Selected Area Electron Diffraction (SAED) patterns of (a) $CaGdZrNb_{0.8}Ta_{0.2}O_7$ and (b) $CaGdZrNb_{0.2}Ta_{0.8}O_7$ samples

6.3.4 High Temperature XRD Studies

For high temperature applications of functional materials, the structural stability with temperature is a key factor to be investigated. The lattice thermal expansion coefficient is best estimate of structural stability with temperature and can be easily determined using High Temperature XRD. Lattice thermal expansion coefficient is calculated using the equation:

$$\alpha_a = \frac{1}{a_{298}} \left(\frac{da}{dT}\right) \quad K^{-1} \qquad (6.3)$$

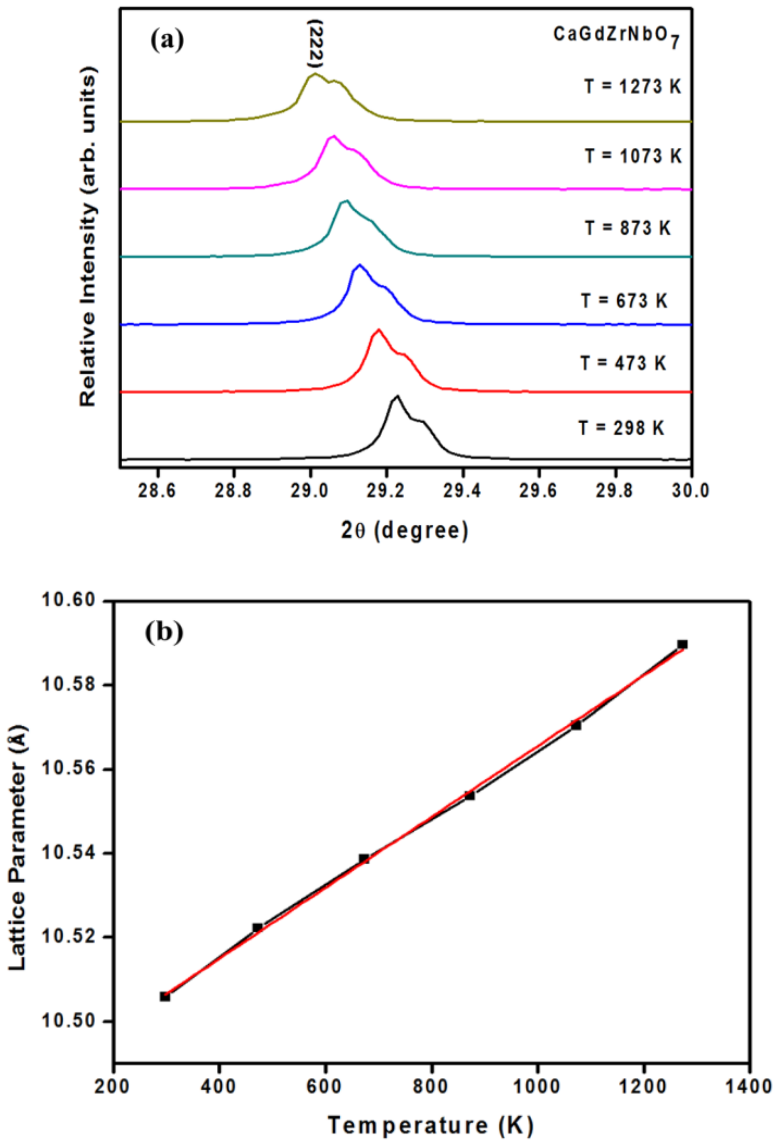

Fig 6.7 (a) High temperature XRD patterns of $CaGdZrNbO_7$ at different temperatures and (b) the corresponding lattice parameter vs. temperature plot

The XRD patterns were recorded for each sample at different temperatures and the patterns are fitted by Lebail fitting method using X'pert High Score Plus software. For each sample, plots are made with lattice parameter as a function of absolute temperature. The slope of the graph $\left(\frac{da}{dT}\right)$ is calculated by a linear fit of the graph and lattice thermal expansion coefficient is calculated using the above equation. High temperature XRD patterns of $CaGdZrNbO_7$ at different temperatures and the corresponding lattice parameter vs. temperature plots are shown in Fig 6.7. In high temperature XRD pattern, only (222) peak is shown and shift of the peak to the lower angle as temperature increases indicates the expansion of the lattice.

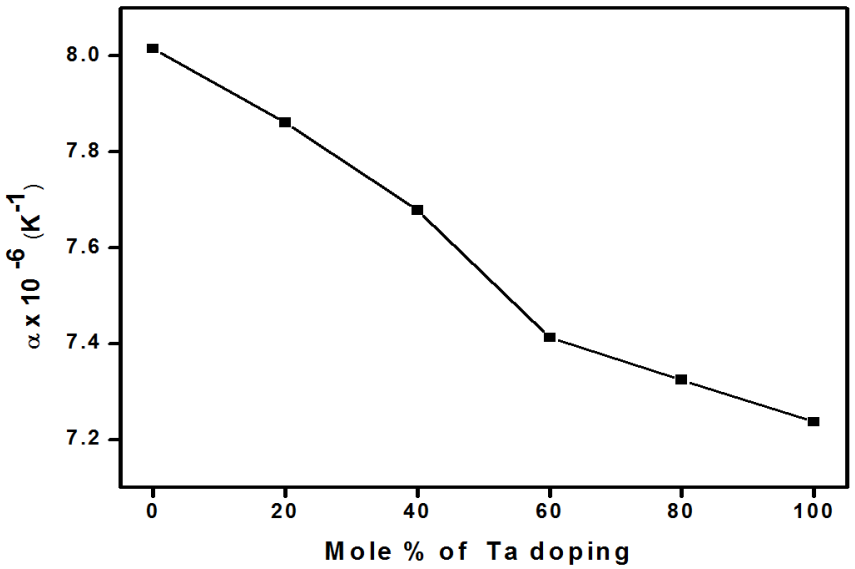

Fig 6.8 Variation of lattice thermal expansion coefficient with different compositions, CaGdZrNb$_{1-x}$Ta$_x$O$_7$ (x = 0, 0.2, 0.4, 0.6, 0.8, 1)

The variation of lattice thermal expansion coefficient with different compositions, $CaGdZrNb_{1-x}Ta_xO_7$ (x = 0, 0.2, 0.4, 0.6, 0.8, 1) is shown in Fig 6.8. In pyrochlore type compositions, the thermal expansion coefficient decreases with increase in substitution of Ta. The thermal expansion of zirconate pyrochlores depends on the Madelung binding energy and as Madelung binding energy increases, thermal expansion decreases (Shimamura, *et al.* 2007). The Madelung binding energy of zirconate pyrochlores depends on 48*f* oxygen x parameter and as x parameter decreases, Madelung energy increases (Subramanian, *et al.* 1983). The experimental

results of our high temperature XRD studies were in good agreement with the above trend. The decrease in thermal expansion coefficient with increase in substitution of Ta in place of Nb can also be correlated with the B-O bond strength. This can be theoretically proved using Renormalization group method based on the ionization energy theory developed by Arulsamy (Arulsamy 2011). The theory treats solid as chain of vibrating harmonic oscillators and used second order time-independent perturbation theory with the heavier effective mass condition, as required by the electron-electron screened Coulomb potential. Arulsamy also proved that the mathematical structure of the ionization-energy dressed electron-electron screened Coulomb potential is exactly the same as the ionization-energy dressed electron-phonon interaction potential. According to this theory, the square of the phonon frequency is directly proportional to exponential of ionization energy of the ions bonding electrons, which is responsible for the bond. The diatomic bond energy of Ta-O bond (799.1 ±12.6 KJ/mol) is greater than that of Nb-O bond (771.5 ±25.1 KJ/mol) (Lide 1994) and hence the diatomic bonding strength between Ta-O is greater than that for Nb-O. The stronger bond between Ta and O implies larger ionization energy of the bonding electrons, and therefore, the increase in phonon frequency. Consequently, increasing phonon frequency implies increasing rigidity of the system which ultimately leads to smaller thermal expansion.

6.3.5 Scanning Electron Microscopy Studies

The SEM microstructures of the thermally etched polished surfaces of the sintered pellets are given in Fig 6.9. It is seen that all the compounds are well-sintered with grains ranging from 1-8 μm in size. The average grain sizes for all compositions were measured from SEM images using linear intercept method and the data is shown in Table 6.3. The mean lineal intercept length is determined by laying a number of randomly placed test lines on the image and counting the number of times that grain boundaries are intercepted. It can be seen that average grain size of Nb rich compounds are high compared to that of Ta rich compounds. The micrographs further evidence the densification of the sintered pellets with less porosity. It was further observed that the $CaGdZrNbO_7$ micrograph shows uniform grain morphology, good packing and sharp grain boundaries.

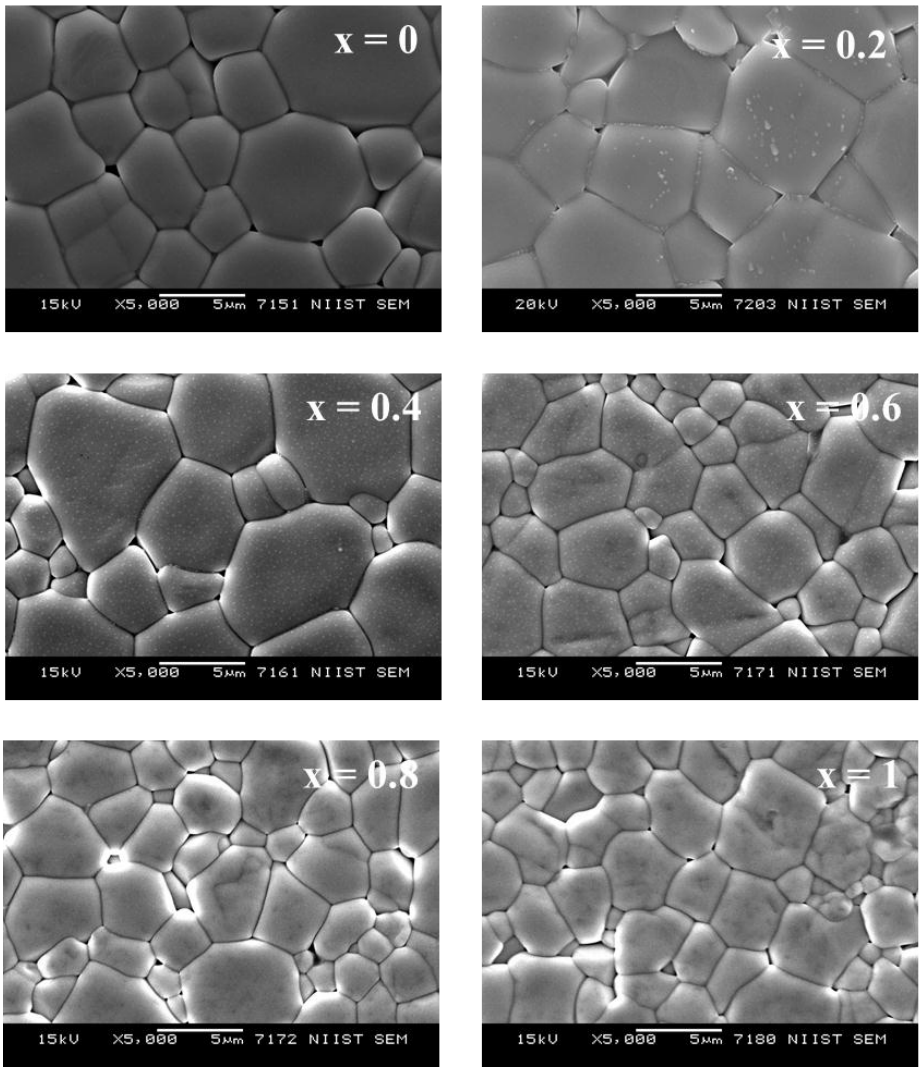

Fig 6.9 SEM images of polished, thermally etched surfaces of CaGdZrNb$_{1-x}$Ta$_x$O$_7$ (*x*= 0.1, 0.2, 0.3, 0.4, 0.5) samples sintered at 1550 ºC for 36 h

Table 6.3 Average grain size of CaGdZrNb$_{1-x}$Ta$_x$ O$_7$ (*x* = 0.1, 0.2, 0.3, 0.4, 0.5) samples measured from SEM images by linear intercept method

Compound	Average grain size (μm)
CaGdZrNbO$_7$	4.74±0.76
CaGdZrNb$_{0.8}$Ta$_{0.2}$O$_7$	4.91±0.70
CaGdZrNb$_{0.6}$Ta$_{0.4}$O$_7$	4.77±0.79
CaGdZrNb$_{0.4}$Ta$_{0.6}$O$_7$	3.98±0.33
CaGdZrNb$_{0.2}$Ta$_{0.8}$O$_7$	3.83±0.30
CaGdZrTaO$_7$	3.69±0.30

6.3.6 Impedance Spectroscopic Studies

The ionic conductivity of $CaGdZrNb_{1-x}Ta_xO_7$ (x = 0, 0.2, 0.4, 0.6, 0.8, 1) samples was measured by a two-probe complex impedance spectroscopy. In general, the ac impedance of an ionic conductor measured by a two-probe method contains contributions from the bulk, grain boundaries and electrode/electrolyte interface, which can be reflected in a complex plane by three successive arcs,(Kumar *et al.* 2004) as shown in Fig 6.10(b). The frequency increases from the right to the left across the plot. The arc at the high frequency end of the spectrum represents the bulk resistivity; the arc at the middle of the spectrum is a consequence of the grain boundary effect; the low-frequency arc is assigned to the electrode response. An idealized equivalent circuit for ceramic oxides corresponding to the impedance plot is shown in Fig 6.10(a). In a practical case, however, not all these arcs can be observed, depending on the nature of the samples and testing conditions (Kumar, *et al.* 2008).

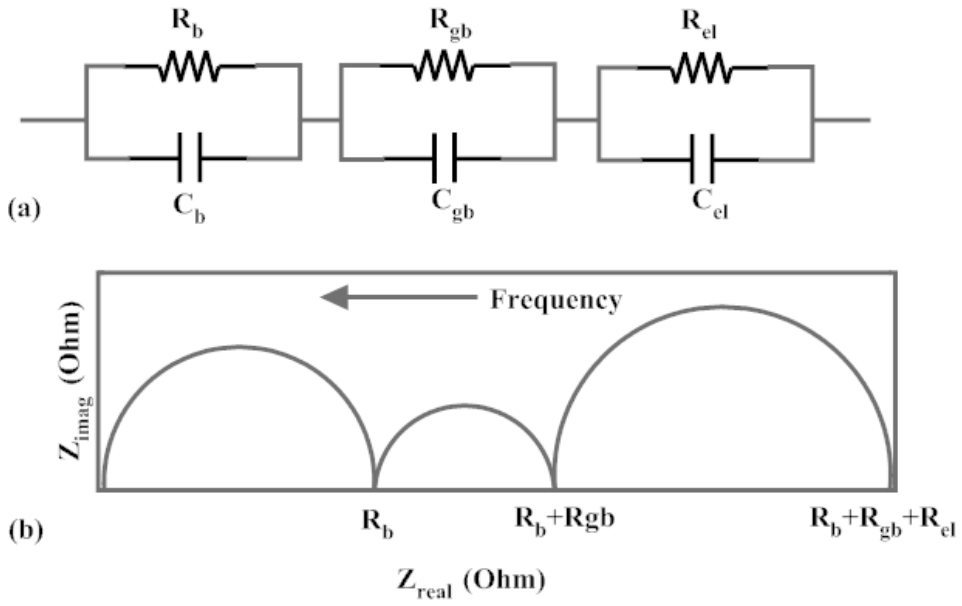

Fig 6.10 (a) An idealized equivalent circuit (b) and its corresponding impedance plot (a) *C*b, *R*b; *C*gb, *R*gb; and *C*el, *R*el represent resistance and capacitance for bulk, grain boundary, and electrode process, respectively. The frequency increases from the right to the left across the plot.

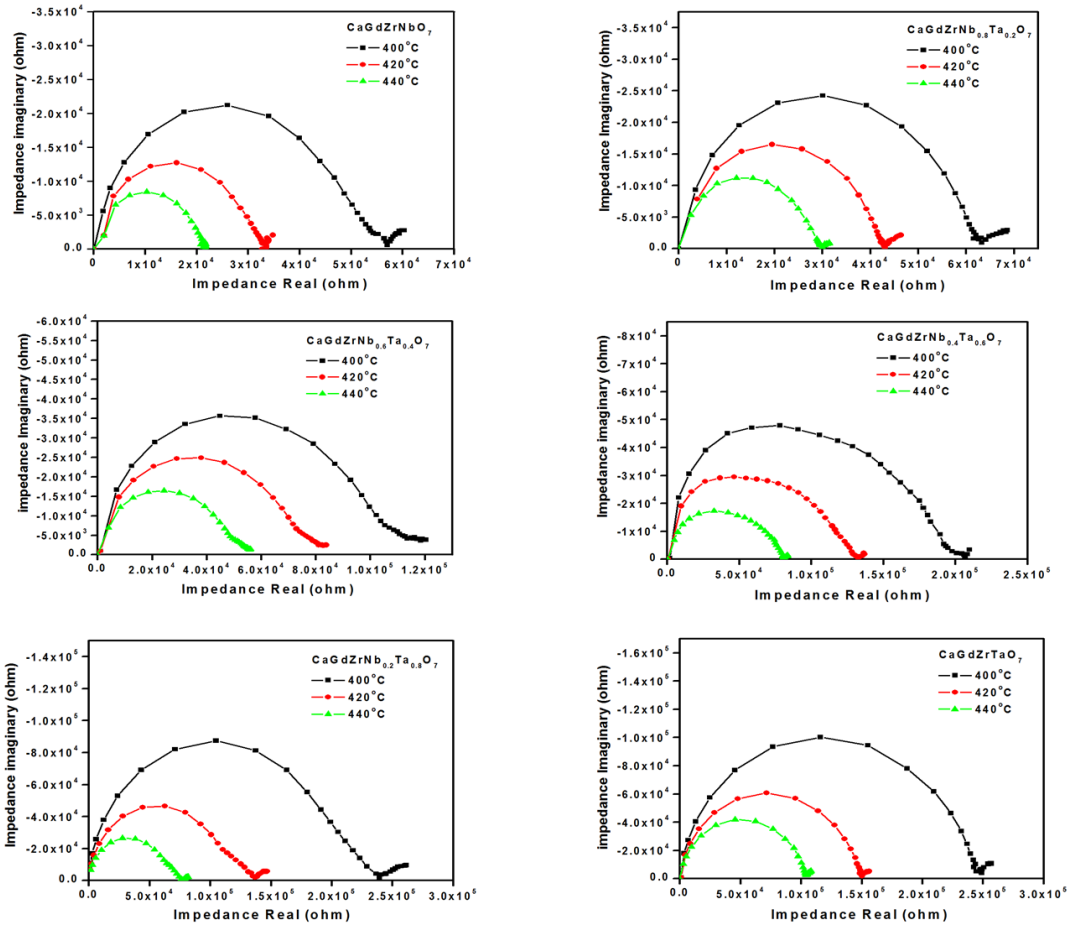

Fig 6.11 Cole – Cole plots of CaGdZrNb$_{1-x}$Ta$_x$ O$_7$ (x = 0.1, 0.2, 0.3, 0.4, 0.5) samples during impedance measurements for three different temperatures 400^{o}C, 420^{o}C and 440^{o}C

Fig 6.11 shows the Nyquist plots or Cole-Cole plots obtained for different compositions during impedance measurements for three different temperatures 400 ºC, 420 ºC and 440 ºC. It is obvious from the figure that impedance of the samples decreases with increase in temperature and this can be attributed to the fact that conduction process is thermally activated. One semicircle was observed in the measured temperature range followed by a low frequency inclined spike either due to the diffusion of ions in the electrode or the electrode polarization (Abram *et al.* 2001). Such a spike is characteristic of a blocking double-layer capacitance produced by the blocking of ionic charge carriers at the electrode sample interface. This also proves that charge carriers are oxide ions rather than electrons (Sibi, *et al.* 2009). All compositions CaGdZrNb$_{1-x}$Ta$_x$O$_7$ (x = 0, 0.2, 0.4, 0.6, 0.8, 1) have negligible

electronic conductivity as there are no free electrons available for conduction when the structure is stabilized with Ca (2+) and Nb/Ta (5+) . If Nb/Ta gets reduced, free electron will be created and electronic conductivity will be observed. But even at high temperature the structure is highly stable with relatively low thermal expansion indicates that such Nb/Ta are still in +5 states. Activation energy of conduction calculated from Arrhenius plot (discussed in the latter part of the text) is in the range 0.8 - 0.9 eV which is a typical value for oxide ion conduction in pyrochlores (Feighery *et al.* 1997, Kramer and Tuller 1995).

The conductivity measurements of the samples were carried out from 400 -750 ºC in the frequency range 1 MHz to 10 Hz. For conductivity calculation, the resistance of the sample is read at the intersection of the semicircle with the real axis at low frequency. The conductivity (σ) is then calculated by the relation:

$$\sigma = \frac{l}{RA} \qquad \textbf{(6.4)}$$

where ℓ/A is the geometrical factor, ℓ is the thickness and A is the area of the electrode.

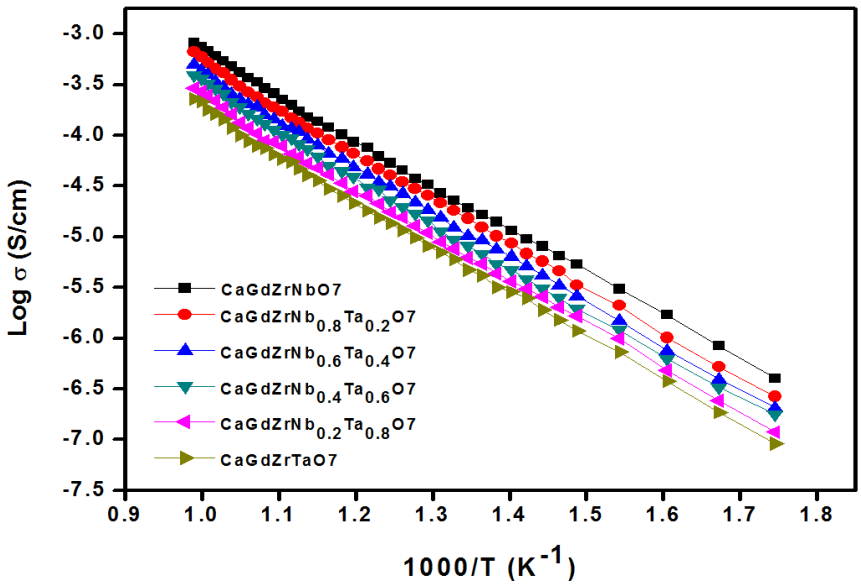

Fig 6.12 Arrhenius Plots of $CaGdZrNb_{1-x}Ta_x$ O_7 (x = 0.1, 0.2, 0.3, 0.4, 0.5) samples

The temperature dependence of the total conductivity of $CaGdZrNb_{1-x}Ta_x$ O_7 (x = 0, 0.2, 0.4, 0.6, 0.8, 1) samples are shown in Fig 6.12. The conduction is predominantly ionic and found to follow Arrhenius behavior given by the equation:

$$\sigma(T) = \sigma_0 \exp(-E_a/K_BT) \quad (6.5)$$

where σ_0 is pre-exponential factor, which is measure of effective number of oxide mobile ions, E_a denotes the activation energy for conduction process, K_B is the Boltzmann constant, and T is the absolute temperature. Total conductivity at 750^oC and the activation energy for the thermally activated conduction are given in Table 4. It is clear from the Arrhenius plot that total conductivity decreases with substitution of Ta in place of Nb. Both Ta and Nb have the same ionic radius (0.64 Å), but differs in their nuclear charge and electron cloud density. Due to the high electron cloud around the Ta, the Ta-O bond is stronger compared to Nb-O bond. Therefore as the Ta substitution increases, BO_6 octahedra will shrink and forms a more rigid network of atoms. This makes diffusion of oxide ions difficult in two ways: by reducing the pathway for oxygen migration and because of the high activation energy required for breaking the metal oxygen bond. It is evident from the Table 4 that activation energy required for oxide ion conduction increases with substitution of Ta. It is also obvious that the decrease in conductivity with substitution of Ta has a little dependence on morphological evolution of the samples with respect to doping as seen from SEM images. In general, as average size of the grains decreases, the grain boundary area increases and consequently, the conductivity decreases. The grain boundary acts as blocking layer to ionic motion due to its change in orientation from the grain interior. This may also cause a small change in total conductivity of the samples with respect to doping.

Oxygen ion conduction in pyrochlores, like in fluorites, proceeds via an oxygen vacancy mechanism. Ordered pyrochlore structure has an intrinsic oxygen vacancy at 8*a* site and the migration mechanism consists of jumps of 48*f* and 8*b* oxygen ions into these vacant sites leaving behind vacancies at their original sites (H.L Tuller 1994). In the pyrochlore lattice, contiguous pathways for oxygen ion migration are provided by jumps from a 48*f* site to a vacant 48*f* site along both <100> and <110> directions (van Dijk, *et al.* 1985, Wilde and Catlow 1998a). An alternate pathway is formed by a jump from a 48*f* to a vacant 8*b* site followed by a jump from an 8*b* to a vacant 48*f* site, but only along <110> directions (Pirzada, *et al.* 2001). Previous computational studies have found that 48*f* – 48*f* mechanism is more

energetically favourable pathway than the 48*f* – 8*b* mechanism (van Dijk, *et al.* 1983, Williford *et al.* 1999). Our experimental results also provides a clear indication that 48*f* – 48*f* mechanism is the dominant mechanism in oxide ion conduction process in pyrochlore oxides since B cation at 16*c* in pyrochlore is surrounded only by 48*f* oxygen atoms and a change in conductivity and activation energy with doping at B site is observed. When B-O bond strength increases with Ta doping, the 48*f* oxygen bonded to Ta cannot easily jump to the vacancy site to initiate oxygen migration and hence conductivity decreases.

6.4 Conclusions

$CaGdZrNb_{1-x}Ta_xO_7$ (x = 0, 0.2, 0.4, 0.6, 0.8, 1) pyrochlore oxide solid solutions were prepared by solid state route and sintered at 1550 ºC for 36 h to optimize its density. Powder X-ray diffraction and Raman spectroscopic studies were made to ensure the pyrochlore structure of the compositions. High resolution images and Selected Area Electron Diffraction (SAED) patterns further confirmed that samples are polycrystalline and single phase. High temperature X-ray diffraction measurement is used to calculate the thermal expansion coefficients of the samples. Thermal expansion is found to decrease with substitution of Ta in place of Nb and this can be attributed to high ionization energy of Ta and consequently to the high strength of Ta-O bond compared to Nb-O bond. Cole –Cole plots obtained by impedance measurements shows a single arc corresponding to both grain and grain boundary contributions followed by a small spike corresponding to electrode – electrolyte double layer capacitance. This double layer blocking capacitance is an evidence for oxide ion diffusion. Arrhenius plot shows that Nb rich compounds have high conductivity compared to Ta rich compounds and this can also be attributed to bond strength. It can be concluded that the oxide ion conduction in pyrochlore proceeds via 48*f* - 48*f* hoping mechanism and B – O bond strength plays an important role in deciding oxide ion conductivity of pyrochlore oxides. The above results would allow predicting the oxide ion conductivity and lattice thermal expansion of the pyrochlore type compounds depending on the nature of element substituted at the B site. Doping of an element with high ionization energy increases the bond strength, and consequently both oxide ion conductivity and thermal expansion coefficient decreases.

Chapter 7

Lattice Thermal Expansion and Oxide Ion Conductivity in $M_2Zr2_{-x}Ce_xO_7$ (M = Gd, Y and *x* = 0.1, 0.2, 0.3, 0.4, 0.5) system

$M_2Zr_{2-x}Ce_xO_7$ (M = Gd, Y and *x* = 0.1, 0.2, 0.3, 0.4, 0.5) system is prepared by high temperature with the intension that B site substitution can enhance oxide ion conductivity. All compounds adopted a defect fluorite structure due to the bigger Ce^{4+} at B site in place of relatively smaller Zr^{4+} ion and all the compositions falls below the phase boundary line in defect fluorite regime. The equivalence of disordered pyrochlore and defect fluorite is established through Rietveld refinement and structural properties are correlated with lattice thermal expansion and ionic conductivity. The lattice thermal expansion coefficient is found to increase with increase in Ce substitution at B site in both Y based and Gd based compounds. The oxide ion conductivity increases with Ce substitution and reaches a maximum and then decreases in both Gd as well as Y based systems. The prepared compounds have conductivity in the range 8 x 10^{-4} – 5 x 10^{-3} S/cm and can be improved by proper microstructural optimization.

7.1 Introduction

Stabilized zirconium oxide, especially YSZ is used as a key component in oxygen sensors and as electrolyte in solid oxide fuel cells for commercial applications because of its high conductivity (0.1 S/cm at 1000 ºC) coupled with an excellent stability with respect to reduction and oxidation over a wide operating range of temperature and pO2 which limits electronic conductivity to below 1 % (Vielstich 2003). Yttria stabilized zirconia cannot be used in intermediate temperature fuel cells due to its relatively low conductivity in the temperature range, 600 – 750 ºC and practical difficulty in making very thin films with reasonable mechanical strength to reduce electrolytic resistance (Brett, *et al.* 2008). Although materials like Gadolinium doped ceria and δ-Bi_2O_3 show very high ionic conductivities at intermediate temperature (600 – 750 ºC), their practical applications are limited by the reducibility at the operating condition and subsequent mechanical failure and enhanced electronic conductivity (Azad, *et al.* 1994, Tuller and Nowick 1975). Gadolinium zirconate based pyrochlore oxides are promising alternative to stabilized zirconium oxide due to their moderate oxide ion conductivity, high chemical and thermal stability and good mechanical strength.

Van Dijik et al. studied ionic conductivity of $Gd_xZr_{1-x}O_{2-x/2}$ and $Nd_xZr_{1-x}O_{2-x/2}$ solid solutions as a function of composition and highest bulk conductivity (5×10^{-3} at 720 ºC) and a minimum in activation energy (0.87 eV) is observed in for $GdO_{1.5}$ – ZrO_2 system with 50 mole % of $GdO_{1.5}$ which is equivalent to $Gd_2Zr_2O_7$. This nominal composition exists in a phase boundary region between pyrochlore and fluorite phases where small pyrochlore like phase can exists in fluorite type matrix or defect fluorite type phases in a pyrochlore matrix (van Dijk *et al.* 1980). Extensive study on $Gd_2(Zr_xTi_{1-x})_2O_7$ and $Y_2(Zr_xTi_{1-x})_2O_7$ by H.L Tuller and his group revealed that the ionic conductivity of titanium rich end members of the series were three orders of magnitude lower than that of zirconium rich end members and titanium rich members exhibit mixed ionic-electronic conductivity at elevated temperatures (Moon and Tuller 1988, Tuller, *et al.* 2000). Computational studies based on static energy minimization technique investigating defect structure of the pyrochlore oxides of the

formula $A_2B_2O_7$ (A = Gd, Y and B = Zr, Ti) by Wilde et al. proved that ionic motion in pyrochlore oxides proceeds predominantly by vacancy hoping mechanism between 48*f* sites (Wilde and Catlow 1998a). Molecular dynamics study by Wilde et al. established the crucial role of cation disorder on the vacancy migration of oxide ion in $Gd_2Zr_2O_7$ which undergoes an order-disorder transformation to defect fluorite type structure where both cations and anions get disordered (Wilde and Catlow 1998b). To the best of our knowledge, the effect of doping of a bigger rare earth cation like Ce^{4+} at B site in $Gd_2Zr_2O_7$ and $Y_2Zr_2O_7$ were not studied so far. In the present study, the structure, microstructure, lattice thermal expansion and oxide ion conducting properties of cerium doped gadolinium and yttrium zirconates are investigated.

7.2 Experimental

$Gd_2Zr_{2-x}Ce_xO_7$ and $Y_2Zr_{2-x}Ce_xO_7$ (x = 0.1, 0.2, 0.3, 0.4, 0.5) samples were prepared by the conventional ceramic route using the starting materials: Gd_2O_3, Y_2O_3, ZrO_2, and CeO_2 (SIGMA - ALDRICH, 99.99%). For easy understanding, $Gd_2Zr_{2-x}Ce_xO_7$ (x = 0.1, 0.2, 0.3, 0.4, 0.5) are designated as GZC1, GZC2, GZC3, GZC4 and GZC5 respectively and $Y_2Zr_{2-x}Ce_xO_7$ (x = 0.1, 0.2, 0.3, 0.4, 0.5) as YZC1, YZC2, YZC3, YZC4 and YZC5 respectively. The raw materials were weighed according to the stoichiometry of the samples and then mixed thoroughly in an agate mortar. Acetone was added to the powdered mixture for proper mixing. Then, the mixture was dried in an air oven at 100 ^oC for 1 h. This procedure of mixing and subsequent drying was repeated thrice to get a homogeneous mixture. The powdered samples were calcined at 1300 ^oC for 6 h, followed by a second calcination at 1500 ^oC for 10 h.

The calcined product was ground into a fine powder and then mixed with 2 wt. % solution of polyvinyl alcohol (PVA) as the organic binder for strengthening and good compaction of the pellet. The dried powder was pressed into cylindrical pellets of 10 mm diameter and about 2 - 3 mm thickness using a hydraulic press. Pellets were initially heated to 600 ^oC and kept for 30 minutes to completely remove the organic binder and sintered for 10 h at 1700 ^oC to optimize the density of the samples. Powder X-ray diffraction patterns were recorded to identify the crystalline

phase of the sintered samples using a Ni filtered Cu Kα radiation by a Philip's X'pert diffractometer (Step size = 0.02, Scanning time per step = 20 seconds, Divergence slit = 0.5°, and exported by X'pert Pro software). The unit cell parameters were calculated by least square method and Rietveld analysis was also performed to refine the structure using Fullprof-2010. For lattice thermal expansion studies, the XRD pattern of sample was recorded from 2θ = 10 – 90°, in the temperature range 293 – 1273 K on a Philips X'pert Pro XRD unit equipped with Anton Paar HTK attachment, at a regular interval of 200 K, in static air. The sintered pellets were polished and thermally etched near the sintering temperature for about 30 min. The grain microstructure on the surface of the thermally etched samples was recorded using a scanning electron microscope (JEOL, JSM 5600 LV). For Impedance spectroscopic studies, a high temperature curing silver paste was applied on polished flat faces of the pellet and electroded with long silver wires. The electroded pellets were cured in a tube furnace for half an hour at 600 ºC. Impedance measurements of the pellets were carried out from 400 ºC to 750 ºC in the frequency range 10 Hz to 1 MHz using a computer controlled Impedance Analyzer (Solartron, SI 1260). The complex impedance plots were made with the SMART software supplied by M/s Solartron Schlumberger, U.K.

7.3 Results and Discussions

7.3.1 Powder X-ray Diffraction Studies

Powder X-ray diffraction patterns of $Gd_2Zr_{2-x}Ce_xO_7$ and $Y_2Zr_{2-x}Ce_xO_7$ (x = 0.1, 0.2, 0.3, 0.4, 0.5) samples sintered at 1700 ºC are shown in Fig 7.1 (a) and (b) respectively. The XRD patterns of all the compounds can be indexed with fluorite type unit cell belonging to $Fm\bar{3}m$. Pyrochlore to defect fluorite transformations are usually triggered by A cation to B cation radius ratio (r_A/r_B). When radius ration is less than 1.46, pyrochlore structure will transform into defect fluorite phase above a critical temperature. Both $Gd_2Zr_2O_7$ and $Y_2Zr_2O_7$ undergo order-disorder transformation from pyrochlore to defect fluorite structure above 1550 ºC (Subramanian, *et al.* 1983), but remains close to the phase boundary between the two phases as the radius ratio (r_A/r_B) is slightly less than or equal to 1.46, the critical

radius ratio for pyrochlore to fluorite transformation . The average radius ratio is calculated for all compositions using ionic radii (Gd^{3+} = 1.053 Å and Y^{3+}= 1.019 Å at

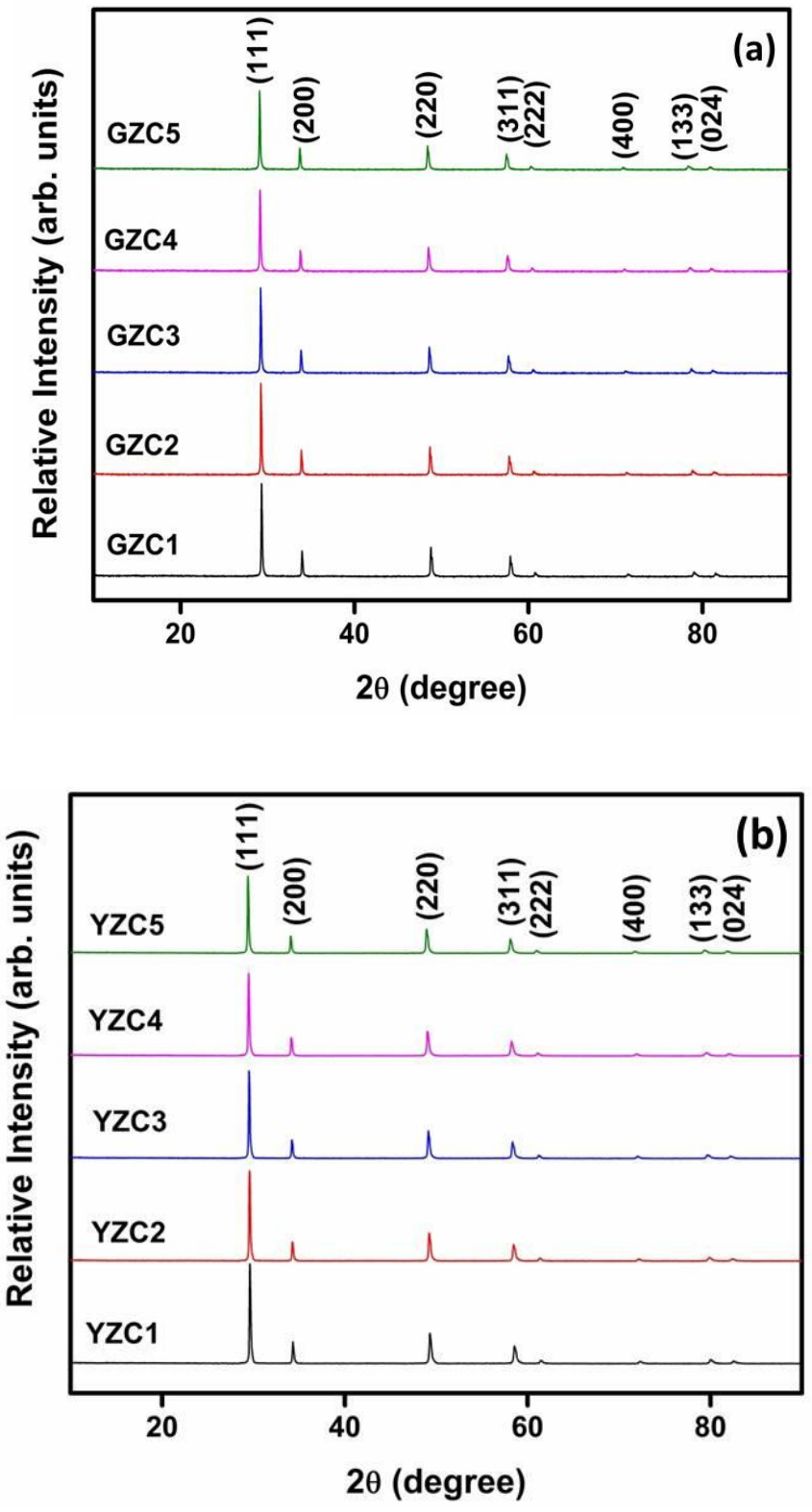

Fig 7.1 Powder X-ray diffraction patterns of (a) $Gd_2Zr_{2-x}Ce_xO_7$

and (b) $Y_2Zr_{2-x}Ce_xO_7$ (x = 0.1, 0.2, 0.3, 0.4, 0.5) samples

eight coordination, Zr^{4+} = 0.72 Å and Ce^{4+} = 0.87 Å at six coordination) taken from the work of R.D. Shannon (Shannon 1976). Fig. 7.2 shows the variation of radius ratio with the composition for $Gd_2Zr_{2-x}Ce_xO_7$ and $Y_2Zr_{2-x}Ce_xO_7$ (x = 0.1, 0.2, 0.3, 0.4, 0.5) samples. The progressive substitution of bigger Ce^{4+} cation in place of relatively smaller Zr^{4+} cation at B site, drives the transformation of pyrochlore structure completely to a defect fluorite domain well below the phase boundary where a complete mixing of A and B cations occur.

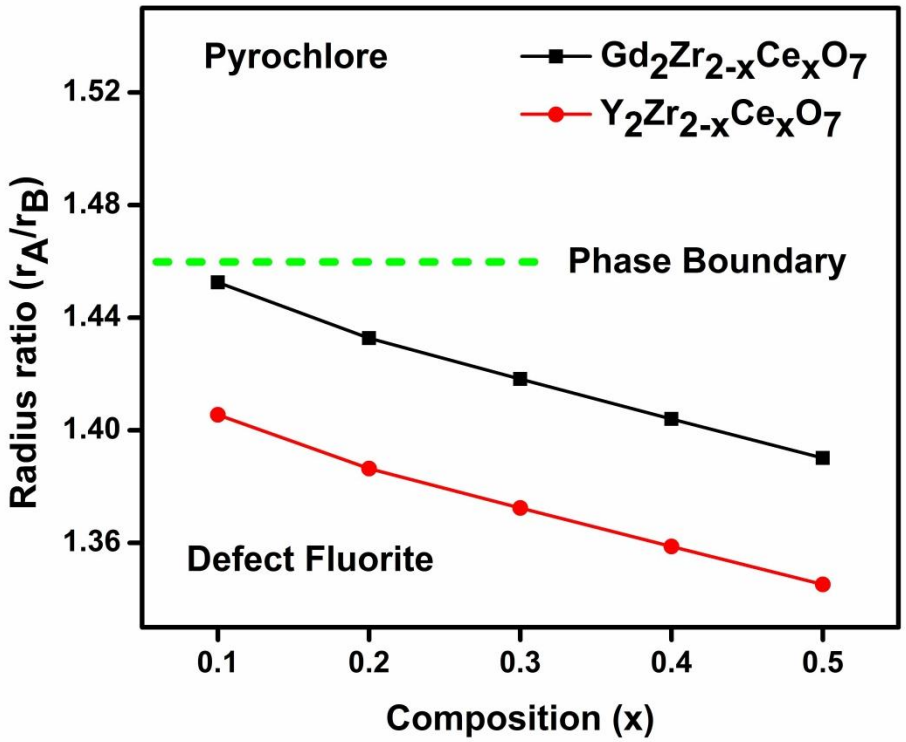

Fig 7.2 Variation of A cation to B cation radius ratio (r_A/r_B) with composition

The systematic structural analysis of samples is possible only by the intuitive assumption of a suitable structural model and subsequent Rietveld analysis of the structural model based on a weighted non-linear fit of theoretically generated pattern with the observed experimental XRD pattern to obtain accurate crystallographic parameters pertaining to the system. Two starting structural models can be assumed for all the samples since compositional stoichiometry allows a pyrochlore type structure and indexing of the observed pattern point toward a fluorite type structure. An ideal cubic pyrochlore structure belonging to $Fd\bar{3}m$ cannot be chosen as a starting

model since structure has undergone an order-disorder transformation to fluorite type structure. A disordered pyrochlore structure with a perfect mixing of A and B cation can be used as a starting model for Rietveld analysis. Anions mixing between three crystallographic sites: 48*f*, 8*b* and 8*a* are not considered for Rietveld analysis since oxygen sublattice is not sensitive to X-ray diffraction when compared to electron rich rare-earth cations. The starting model based on disordered pyrochlore structure is given in Table 7.1. When atoms from B site come to A site, its coordination changes from six to eight and as a result its ionic radii changes. The ionic radius of Zr^{4+} is 0.84 Å and that of Ce^{4+} is 0.97 Å when eight coordinated (Shannon 1976). Since ionic radius of Ce^{4+} is more close to that of Gd^{3+} or Y^{3+}, during structural disorder Ce^{4+} ions have high probability than Zr^{4+} ions to occupy A site so that the distortion of A cation polyhedra is minimum. Therefore in the starting model it is assumed that all the Ce atoms substituted are occupying A site in disordered pyrochlore structure. It is also assumed that mixing of A and B cation is perfect in the sense that 50% A cations go to B site and 50 % of B cations come to A site. The starting model based on disordered pyrochlore structure for GZC1 with respect to origin at B site atom is given in Table 7.1. The other starting model is based on fluorite type unit cell belonging to $Fm\bar{3}m$ space group with all cations occupying a common Wyckoff position and one eight of the anion sites are vacant. . The starting model based on anion deficient fluorite structure for GZC1 is given in Table 7.2

Table 7.1 Starting model for Rietveld refinement of GZC1 based on disordered pyrochlore unit cell with $Fd\bar{3}m$ space group

Atoms	Atom Label	Wyckoff position	X	Y	Z	Occupancy
Gd	Gd(1)	16*d*	0.500	0.500	0.500	1.0
Zr	Zr(1)	16*d*	0.500	0.500	0.500	0.9
Ce	Ce	16*d*	0.500	0.500	0.500	0.1
Gd	Gd(2)	16*c*	0.000	0.000	0.000	1.0
Zr	Zr(2)	16*c*	0.000	0.000	0.000	1.0
O	O(1)	48*f*	*x*	0.125	0.125	6.0
O	O(2)	8*b*	0.375	0.375	0.375	1.0
O	O(3)	8*a*	0.125	0.125	0.125	0.0

Table 7.2 Starting model for Rietveld refinement of GZC1 based on defect fluorite unit cell with $Fm\bar{3}m$ space group

Atoms	Atom Label	Wyckoff position	X	Y	Z	Occupancy
Gd	Gd	4*a*	0.000	0.000	0.000	0.500
Zr	Zr	4*a*	0.000	0.000	0.000	0.475
Ce	Ce	4*a*	0.000	0.000	0.000	0.025
O	O	8*c*	0.250	0.250	0.250	1.75

Table 7.3 Rietveld refined parameters of $Gd_2Zr_{2-x}Ce_xO_7$ (x = 0.1, 0.2, 0.3, 0.4, 0.5) based on disordered pyrochlore model

Sample		GZC1	GZC2	GZC3	GZC4	GZC5
Phase		Disordered pyrochlore	Disordered pyrochlore	Disordered pyrochlore	Disordered pyrochlore	Disordered pyrochlore
Unit Cell		Cubic	Cubic	Cubic	Cubic	Cubic
Space Group		$Fd\bar{3}m$	$Fd\bar{3}m$	$Fd\bar{3}m$	$Fd\bar{3}m$	$Fd\bar{3}m$
Total number of independent reflections		39	39	39	39	39
Lattice constant (Å)		10.5550(3)	10.5716 (4)	10.5883(3)	10.6066(2)	10.6232(5)
FWHM Parameters	U	0.0277(14)	0.0901(8)	0.2398(16)	0.1026(22)	0.2154(10)
	V	0.0277(15)	-0.0211(12)	-0.0833(13)	0.0283(15)	-0.0529(14)
	W	-0.0004(11)	0.0084(9)	0.0172(9)	-0.0018(18)	0.0115(9)
Zero		0.0250(14)	0.0032(6)	0.0172(17)	-0.0053(14)	-0.0123(7)
Asymmetry parameters		-0.0739(8)	-0.0652(8)	-0.0641(11)	-0.0788(8)	-0.0842(12)
		-0.0544(9)	-0.0505(7)	-0.0591(15)	-0.0556(12)	-0.0528(9)
Oxygen x-parameter		0.3666(4)	0.3682(5)	0.3697(2)	0.3716(6)	0.3736(5)
Overall B-factor		1.0491(7)	1.0930(9)	1.1287(11)	1.1650(13)	0.9705(23)
R-Factors	Rp	7.37	7.42	7.48	7.63	7.56
	Rwp	9.57	9.66	9.63	9.91	9.76
	Rexp	6.97	7.19	7.29	7.43	7.55
	χ^2	1.89	1.81	1.75	1.78	1.67
	GOF	1.4	1.3	1.3	1.3	1.3

Table 7.4 Rietveld refined parameters of $Y_2Zr_{2-x}Ce_xO_7$ (x = 0.1, 0.2, 0.3, 0.4, 0.5) based on disordered pyrochlore model

Sample		YZC1	YZC2	YZC3	YZC4	YZC5
Phase		Disordered pyrochlore	Disordered pyrochlore	Disordered pyrochlore	Disordered pyrochlore	Disordered pyrochlore
Unit Cell		Cubic	Cubic	Cubic	Cubic	Cubic
Space Group		$Fd\bar{3}m$	$Fd\bar{3}m$	$Fd\bar{3}m$	$Fd\bar{3}m$	$Fd\bar{3}m$
Total number of independent reflections		39	39	39	39	39
Lattice constant (Å)		10.4422(2)	10.4606(4)	10.4812(6)	10.4988(3)	10.5170(4)
FWHM	U	0.2757(10)	0.2993(13)	0.2542(11)	0.4563(19)	0.3628(13)
Parameters	V	-0.0349 (13)	-0.0760(17)	-0.0487(10)	-0.1386(14)	-0.1122(10)
	W	0.0092(17)	0.0184(11)	0.0131(13)	0.0271(16)	0.0228(11)
Zero		0.0005(12)	0.0145(16)	0.0234(15)	0.0156(12)	0.0031(14)
Asymmetry parameters		-0.0932(7)	-0.0823(9)	-0.0689(9)	-0.0979(10)	-0.0800(9)
		-0.0705(10)	-0.0708(12)	-0.0700(12)	-0.0707(9)	-0.0648(8)
Oxygen x-parameter		0.3714(6)	0.3723(4)	0.3731(3)	0.3739(5)	0.3746(4)
Overall B-factor		1.4256(16)	1.3538(19)	1.2674(14)	1.2880(11)	1.1733(20)
R-Factors	Rp	10.6	10.3	10.8	10.8	10.7
	Rwp	14.6	13.8	14.5	14.6	14.5
	Rexp	7.69	8.06	8.12	8.24	8.45
	χ^2	3.61	2.94	3.19	3.13	2.94
	GOF	1.9	1.7	1.8	1.8	1.7

Rietveld Analysis of powder XRD patterns was performed using Full proof - 2010 software with two different starting models. First of all scale factor and three background parameters were fitted. Diffraction peak profile was fitted with pseudo-Voigt profile function and Caglioti profile parameters were refined. Two peak profile asymmetric parameters were refined, but absorption and extinction coefficients were not considered during refinement. For pyrochlore based model, the variable 48*f* oxygen *x*-parameter was refined. Automatic occupancy refinement with crystallographic and stoichiometric constraint was not attempted because of the fact that Rietveld refinement is mathematical fitting method which will not guarantee a physically reasonable value if more refineable parameters and constraints are introduced in the starting model. The results after Rietveld refinement based on disordered pyrochlore model for $Gd_2Zr_{2-x}Ce_xO_7$ and $Y_2Zr_{2-x}Ce_xO_7$ (x = 0.1, 0.2, 0.3, 0.4, 0.5) is given as Table 7.3 and 7.4 respectively. The observed, calculated and

difference patterns of two representative samples are shown in Fig. 7.3 (a) and (b). It can be seen that observed and calculated pattern matched well except for very small difference in intensity and there is no additional peaks in the observed pattern. All R-factors are well below 20 % indicating good mathematical fit and goodness of fit is below three guarantees convergence to the global minimum value.

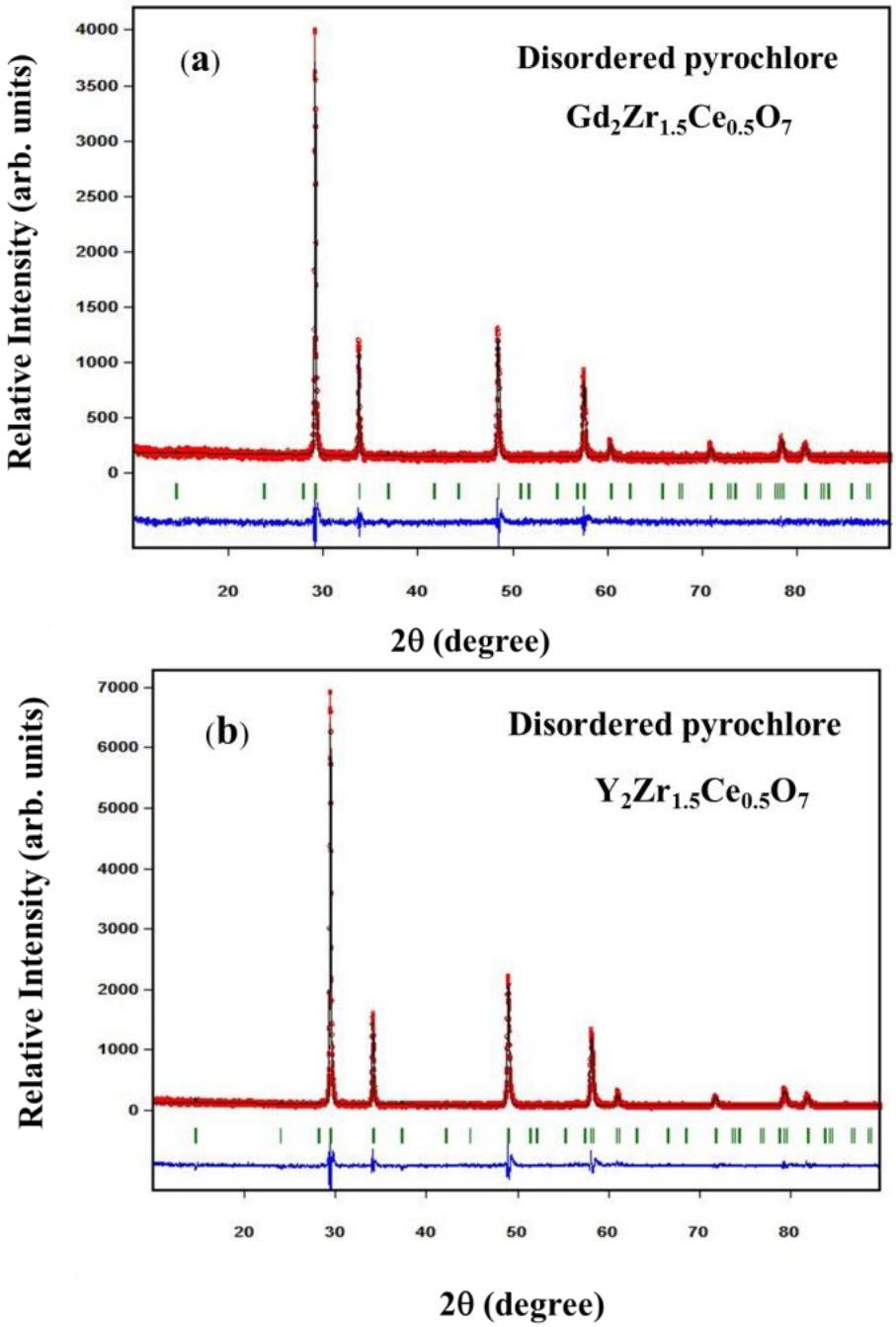

Fig. 7.3 Observed, calculated and difference XRD profiles of (a) GZC5 and (b) YZC5 after Rietveld refinement based on disordered pyrochlore model

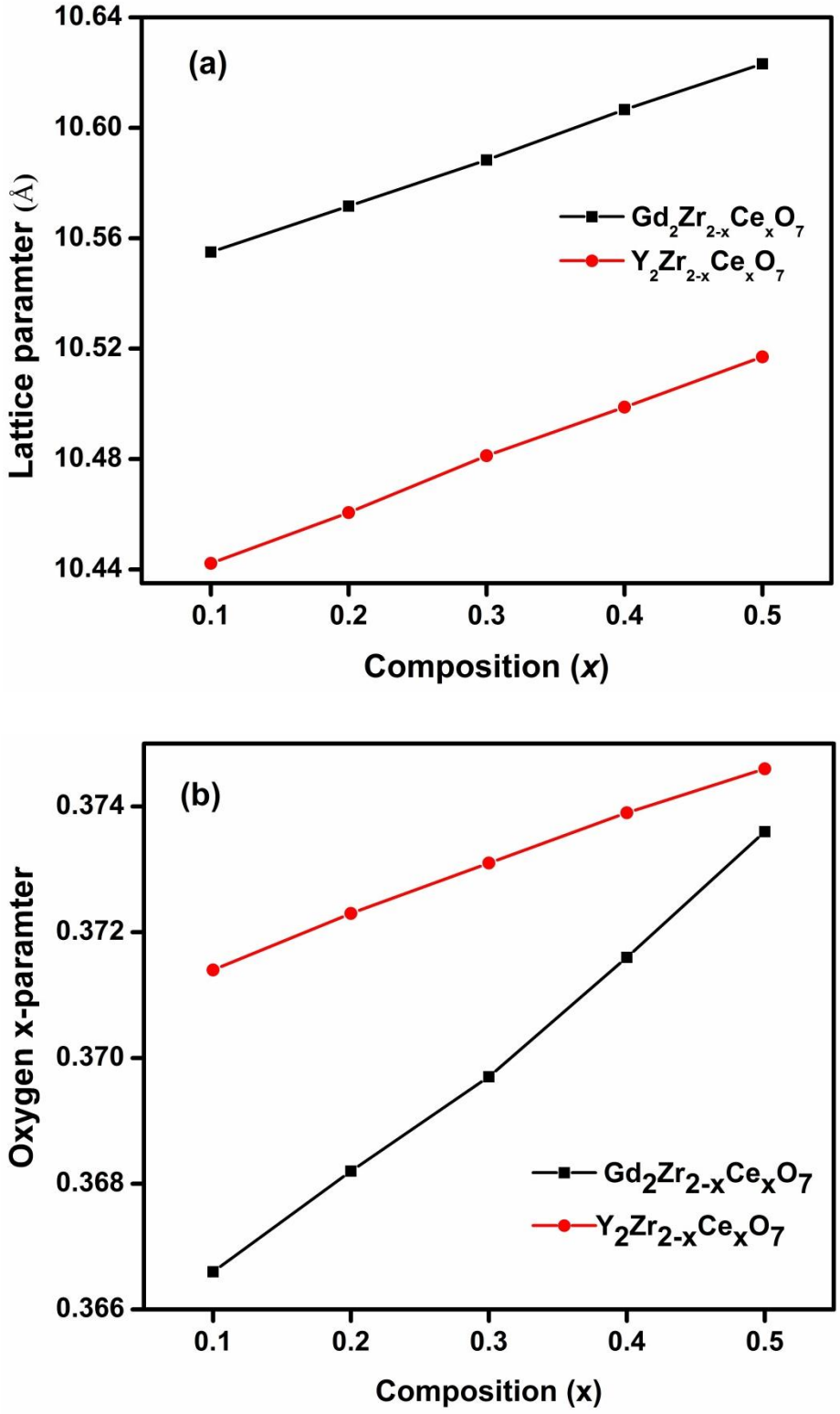

Fig.7.4 Variation of (a) lattice parameter and (b) oxygen *x*-parameter with composition

Table 7.5 Rietveld refined parameters of $Gd_2Zr_{2-x}Ce_xO_7$ (x = 0.1, 0.2, 0.3, 0.4, 0.5) based on defect fluorite model

Sample		GZC1	GZC2	GZC3	GZC4	GZC5
Phase		Defect fluorite	Defect fluorite	Defect fluorite	Defect fluorite	Defect fluorite
Unit Cell		Cubic	Cubic	Cubic	Cubic	Cubic
Space Group		$Fm\bar{3}m$	$Fm\bar{3}m$	$Fm\bar{3}m$	$Fm\bar{3}m$	$Fm\bar{3}m$
Total number of independent reflections		9	9	9	9	9
Lattice constant (Å)		5.2776(5)	5.2860(3)	5.2945(4)	5.3034(6)	5.3118(4)
FWHM Parameters	U	-0.0378(11)	0.0213(12)	0.0756(17)	-0.0323(19)	0.1484(14)
	V	0.0875(13)	0.0271(15)	0.0356(10)	0.1401(11)	-0.0031(12
	W	-0.0110 (16)	0.0002(10)	-0.0035(17)	-0.0208(18)	0.0028(10)
Zero		0.0263(10)	0.0046(13)	0.0198 (12)	0.0010(16)	-0.0110(13)
Asymmetry parameters		-0.0692(9)	-0.0621(8)	-0.0547(14)	-0.0759(10)	-0.0803(13)
		-0.0559(7)	-0.0518 (11)	-0.0594(15)	-0.0559(13)	-0.0530(9)
Overall B-factor		1.4189(18)	1.4821(16)	1.4475(21)	1.5246(17)	1.0543 (22)
R-Factors	Rp	7.80	7.93	7.32	8.02	7.91
	Rwp	10.2	10.3	9.45	10.4	10.2
	Rexp	6.77	6.94	7.29	7.28	7.40
	χ^2	2.28	2.20	1.68	2.05	1.91
	GOF	1.5	1.5	1.3	1.4	1.4

The variation of lattice parameter and oxygen x-parameter with composition is shown in Fig. 7.4 (a) and (b) respectively. Lattice parameters of both $Gd_2Zr_{2-x}Ce_xO_7$ and $Y_2Zr_{2-x}Ce_xO_7$ system varies in accordance with Vegard's law. The law states that the crystallographic parameters of a continuous substitutional solid solution vary linearly with concentration at constant temperature when the nature of the bonding is similar in the constituent phases (Vegard 1921). The lattice parameter is controlled by the relative size of the atoms or species exchanged and the law is valid for ionic salts and compounds in which the bonding is predominantly ionic in nature (Tilley 2006). Lattice parameter increases linearly with progressive substitution of Ce in place of Zr due to the higher ionic size of Ce compared to that of Zr. This also confirms the fact that Ce is completely occupying A site in our model since if Ce has a mixed occupancy at A and B sites, the variation of lattice parameter will be not be linear. Oxygen x-parameter also follows the same trend except for slight variation due to the

fact that since oxygen atoms diffract electrons weakly than electron rich rare earth atoms, the determination of oxygen *x*-parameter may not be as accurate as lattice parameter.

Table 7.6 Rietveld refined parameters of $Y_2Zr_{2-x}Ce_xO_7$ (x = 0.1, 0.2, 0.3, 0.4, 0.5) based on defect fluorite model

Sample		YZC1	YZC2	YZC3	YZC4	YZC5
Phase		Defect fluorite	Defect fluorite	Defect fluorite	Defect fluorite	Defect fluorite
Unit Cell		Cubic	Cubic	Cubic	Cubic	Cubic
Space Group		$Fm\bar{3}m$	$Fm\bar{3}m$	$Fm\bar{3}m$	$Fm\bar{3}m$	$Fm\bar{3}m$
Total number of independent reflections		9	9	9	9	9
Lattice constant (Å)		5.2212(7)	5.2304(4)	5.2407(5)	5.2495(3)	5.2587(6)
FWHM Parameters	U	0.1755(14)	0.2439(11)	0.1751 (13)	0.2927(16)	0.2089 (13)
	V	0.0489(10)	-0.0330(16)	0.0145(18)	-0.011(12)	0.0075(17)
	W	-0.0057(17)	0.0105(13)	0.0017(15)	0.0037(16)	0.0011(12)
Zero		0.0020(16)	0.0154(18)	0.0242(14)	0.0172(11)	0.0055(18)
Asymmetry parameters		-0.0897(11)	-0.0787(12)	-0.0648(10)	-0.0915(14)	-0.0695(11)
		-0.0714(9)	-0.0711(10)	-0.0703(11)	-0.0718(9)	-0.0657(8)
Overall B-factor		1.4907(15)	1.4132(19)	1.3334(17)	1.3790(21)	1.2761(16)
R-Factors	Rp	11.0	10.5	10.5	10.5	10.6
	Rwp	15.0	14.3	14.0	14.1	14.4
	Rexp	7.34	7.64	8.15	8.26	8.11
	χ^2	4.17	3.52	2.94	2.91	3.16
	GOF	2.0	1.9	1.7	1.7	1.8

The results after Rietveld refinement based on defect fluorite model for $Gd_2Zr_{2-x}Ce_xO_7$ and $Y_2Zr_{2-x}Ce_xO_7$ (x = 0.1, 0.2, 0.3, 0.4, 0.5) is given as Table 7.5 and 7.6 respectively. The observed, calculated and difference patterns of two representative samples are shown in Fig. 7.5 (a) and (b). This model is also proved to be valid for both the system of compounds since no additional peaks are observed in the pattern other than what is allowed by the space group. All R-factors and goodness of fit values are within acceptable range for structure determination using Rietveld analysis. The variation of lattice parameter with concentration of Ce is shown in Fig.7.6 and it is obvious from the figure that lattice parameter increases linearly with

Ce concentration in accordance with Vegard's law. Since all the cations occupy the same Wyckoff position, the replacement of Zr by bigger Ce atom will lead to an expansion of cation coordination polyhedra which in turn increases lattice parameter.

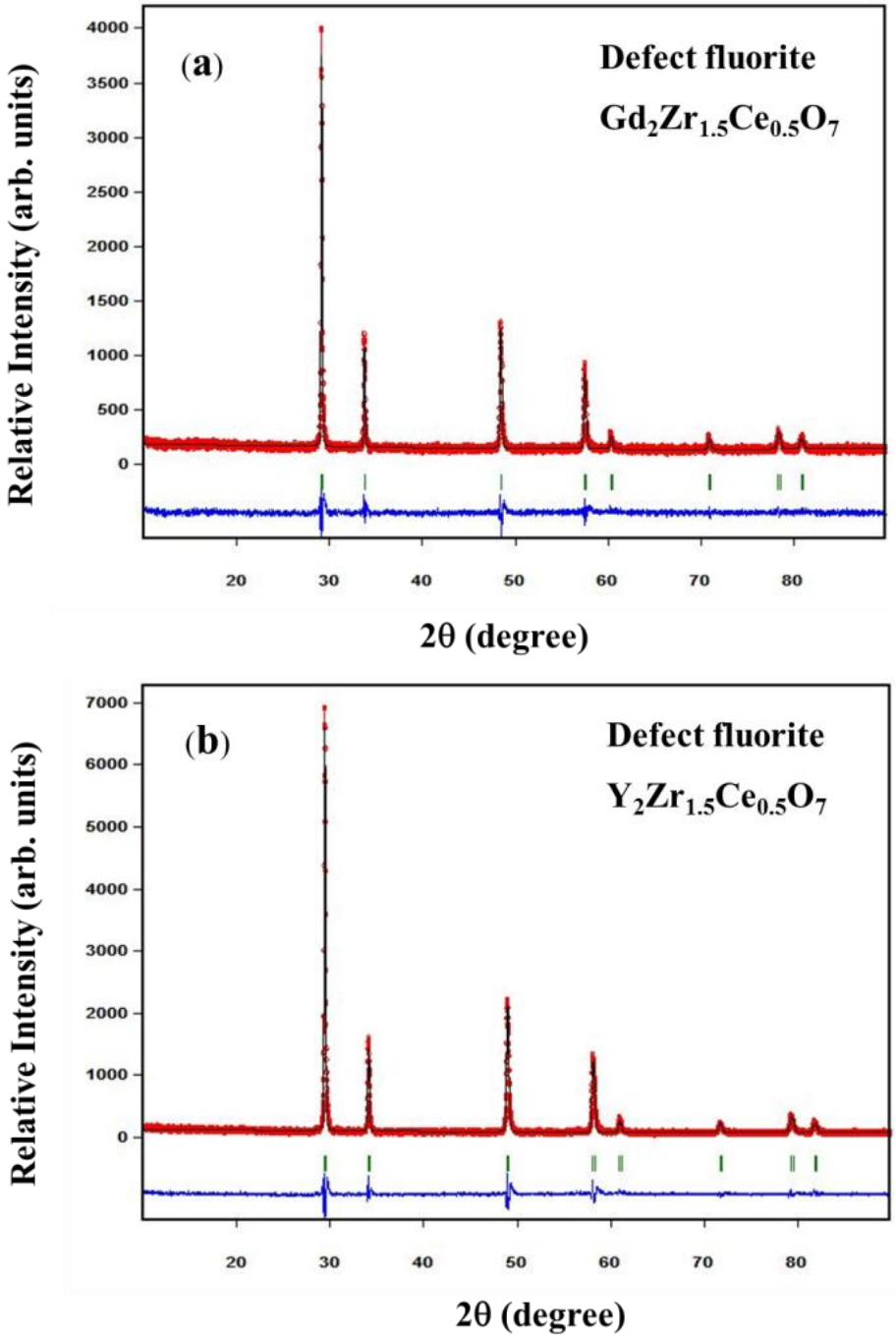

Fig. 7.5 Observed, calculated and difference XRD profiles of (a) GZC5 and (b) YZC5 after Rietveld refinement based on defect fluorite model

Both disordered pyrochlore model and defect fluorite model fit very well with experimental data obtained by powder X-ray diffraction technique. Hence Rietveld analysis unequivocally proved that disordered pyrochlore and defect fluorite are crystallographically equivalent even if they belong to different space group. The mixed occupancy of cations at A and B sites in disordered pyrochlore is equivalent to cations sharing a single crystallographic position in defect fluorite structure. Oxygen has two different sites (48*f*, 8*b*) in pyrochlore with one variable *x*- parameter, but fluorite structure allows only a single crystallographic position with fixed coordinates for oxygen. The fixed oxygen position in fluorite model is equivalent to x = 0.375 in pyrochlore structure and from Tables 7.3 and 7.4, it is clear that oxygen x-parameter is close to 0.375 and deviation is balanced by the presence of 8*b* oxygen. The vacant 8*a* site in pyrochlore is equivalent to deficiency of oxygen in the fluorite model. This close analogy between the structures can be exploited in tuning electrical and thermal properties of the compounds.

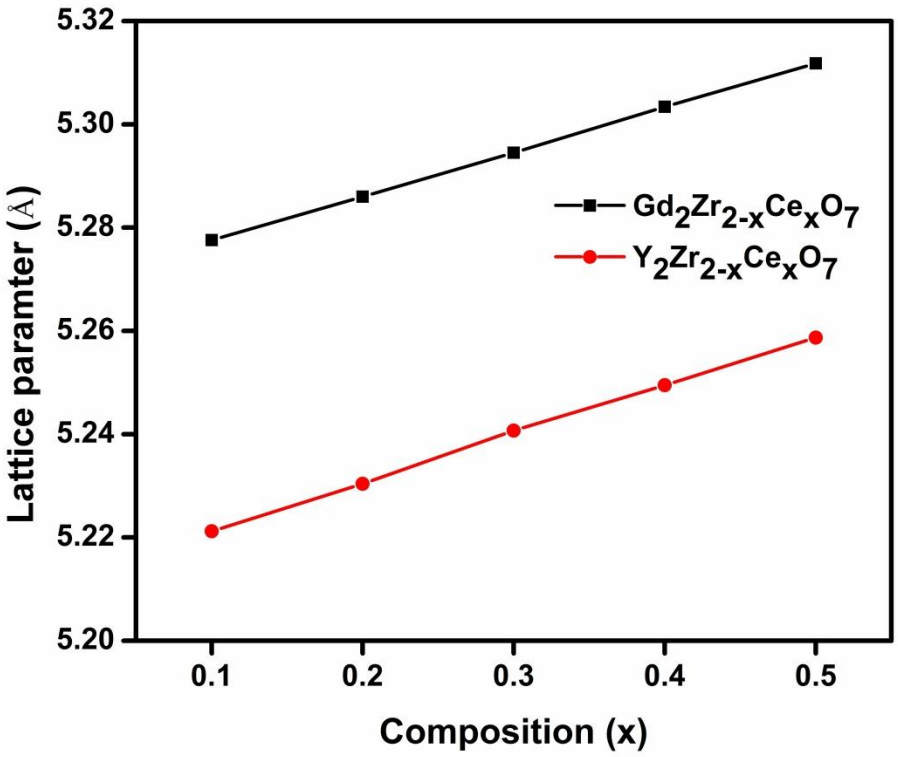

Fig.7.6 Variation of lattice parameter with composition for $Gd_2Zr_{2-x}Ce_xO_7$ and $Y_2Zr_{2-x}Ce_xO_7$ (x = 0.1, 0.2, 0.3, 0.4, 0.5) solid solutions

7.3.2 High temperature XRD studies

Determination of thermal expansion characteristics of a material is of importance in both basic and applied contexts. For technologically demanding applications, the availability of critically evaluated thermal expansion data is essential for developing functional materials with desirable properties. The structural stability and lattice thermal expansion coefficients can be determined accurately using high temperature powder X-ray diffraction technique. Since the structure under investigation belongs to cubic crystal system, the variation of lattice constant with temperature and the linear lattice thermal expansion coefficient given by equation 7.1 is a good estimate of thermal behavior of the material at high temperature.

$$\alpha_a = a_{298}\left(\frac{da}{dT}\right) \quad K^{-1} \qquad (7.1)$$

Powder XRD patterns were recorded for each sample at different temperatures from room temperature to 1273 K and the patterns were analyzed using X'pert High Score Plus software. The background for each pattern is defined manually and XRD profiles are fitted by Lebail fitting method based on $Fm\bar{3}m$ space group, allowing automatic refinement of lattice parameter. For each sample, plots are made with lattice parameter as a function of absolute temperature. The slope of the graph $\left(\frac{da}{dT}\right)$ is calculated by a linear fit of the graph and lattice thermal expansion coefficient is calculated using the equation (7.1). Powder XRD patterns of GDC5 and YDC5 at different temperatures from room temperature to 1273 K and the corresponding lattice parameter vs. temperature plots are shown in Fig. 7.7 and 7.8 respectively. The (111) and (200) peaks in high temperature XRD pattern of both GZC5 and YZC5 shift towards the lower angle as temperature increases, indicates the expansion of the lattice. The lattice parameter varies linearly with temperature for all compounds up to 1273 K and no lattice expansion anomaly is observed. This clearly proves that all compositions retained its structure up to 1273 K and Ce^{4+} is not reduced to Ce^{3+} even if it is occupying A site. The ionic radius of Ce^{4+} (0.87 Å when six coordinated and 0.97 Å when eight coordinated) is always less than that of Ce^{3+} (1.01 Å at six coordination and 1.143 Å at eight coordination). If Ce^{4+} reduces to Ce^{3+} at high

temperature, the lattice parameter will increase abruptly and this may lead to a lattice expansion anomaly. The high temperature XRD results confirmed that Ce reduction problem which is affecting conventional Ce-based electrolytes, can be eliminated by doping it in structurally stable pyrochlore type lattice even if it undergo order-disorder transformation.

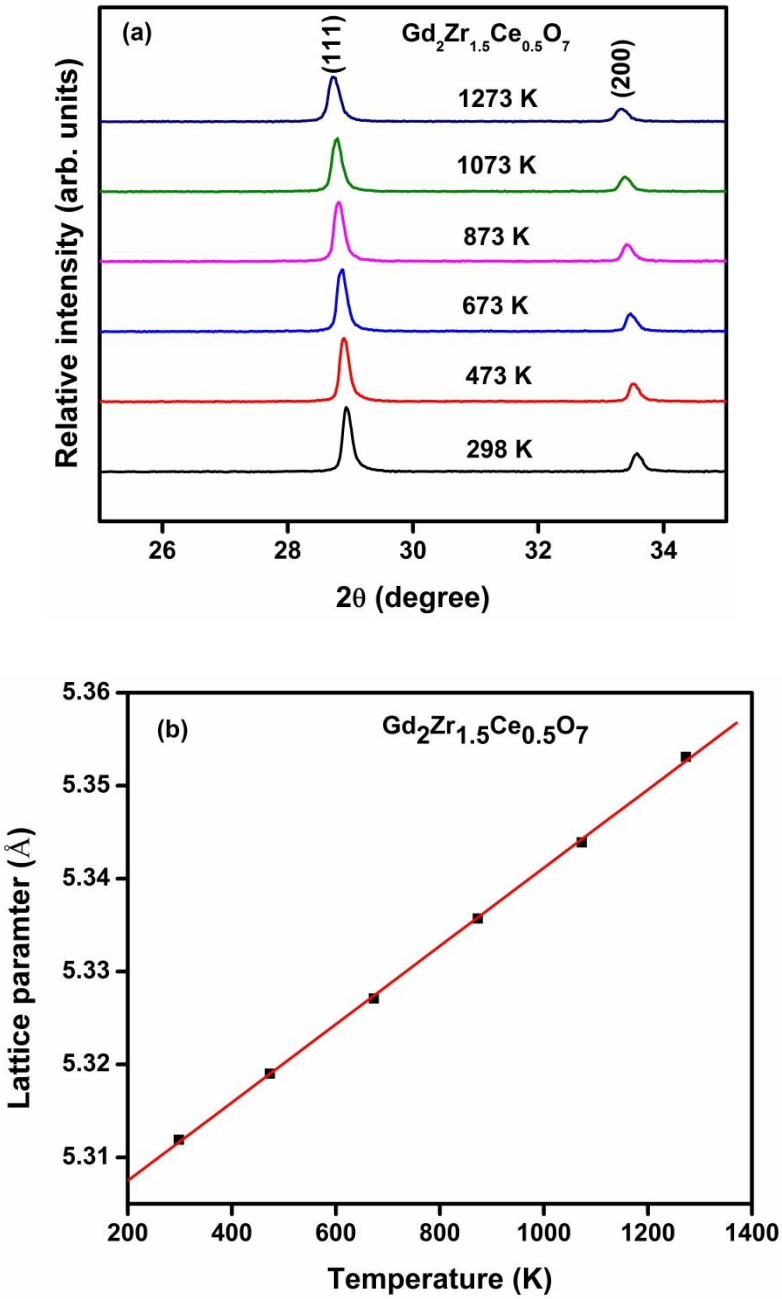

Fig 7.7 (a) Powder XRD patterns of GZC5 taken at different temperatures room temperature to 1273K (b) Linear fit of variation of lattice parameter with absolute temperature for GZC5

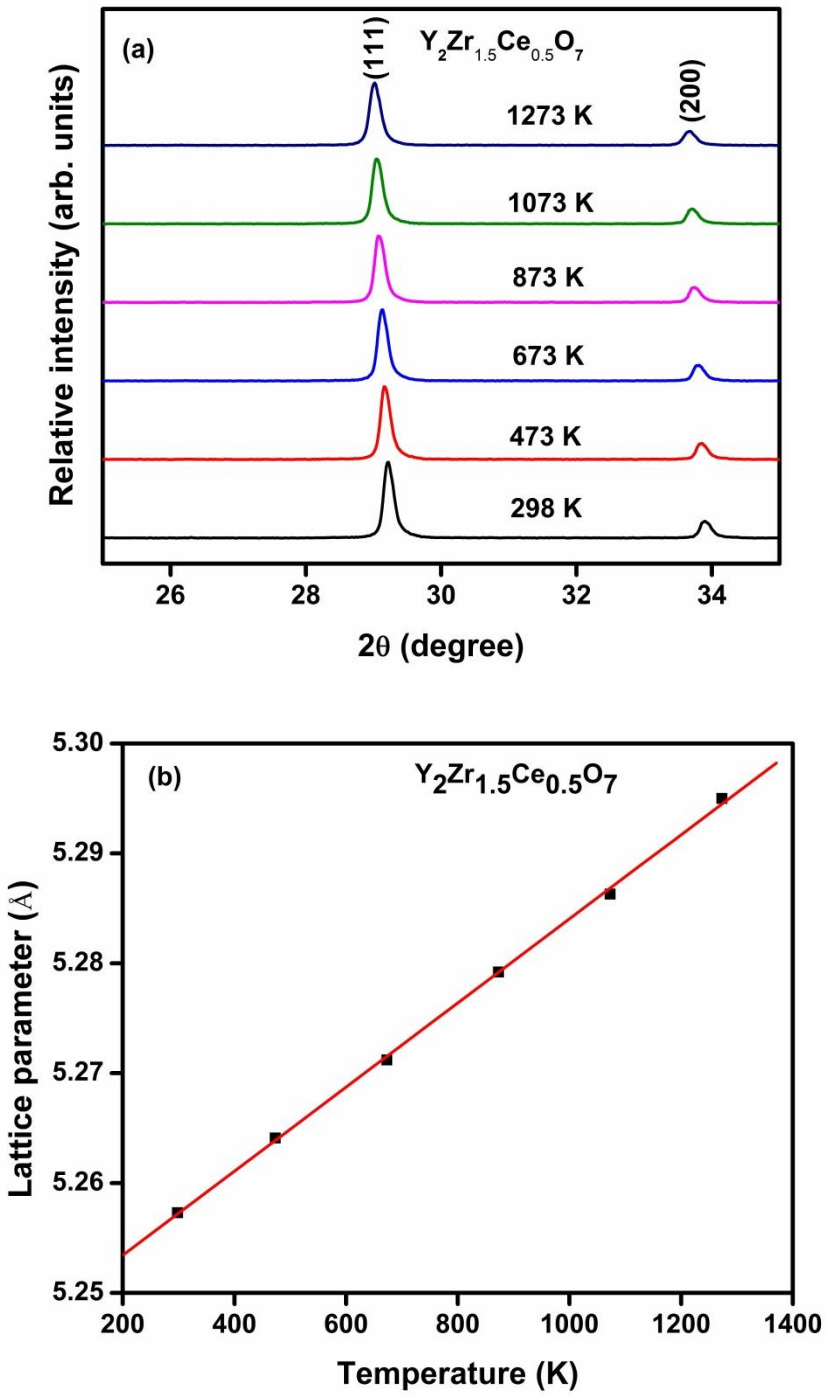

Fig 7.8 (a) Powder XRD patterns of YZC5 taken at different temperatures room temperature to 1273K (b) Linear fit of variation of lattice parameter with absolute temperature for YZC5

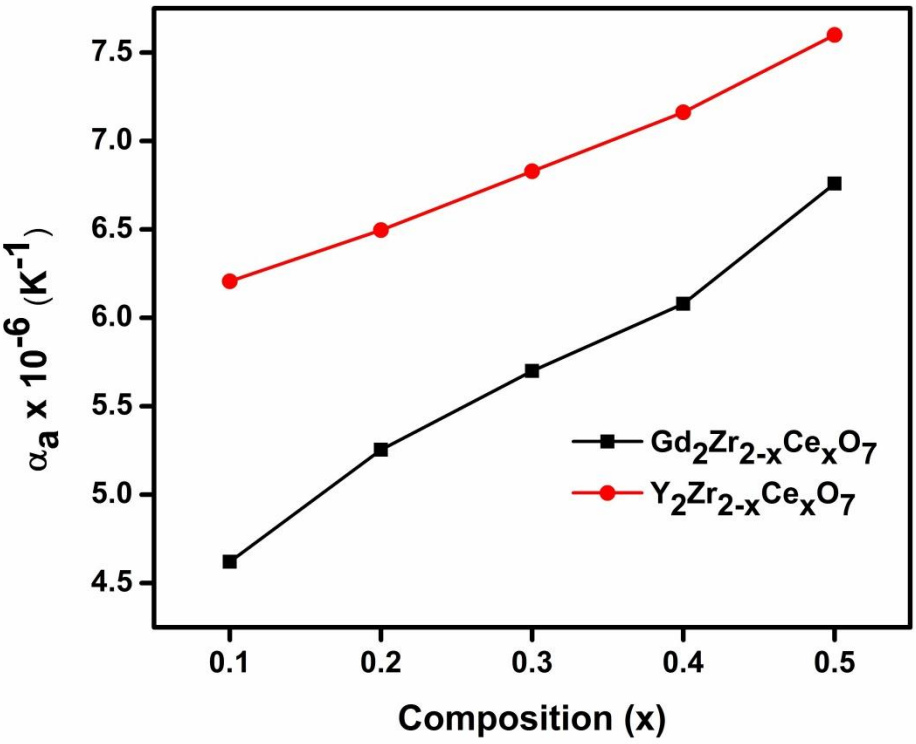

Fig 7.9 Variation of lattice thermal expansion coefficient with composition

Fig. 7.9 shows the variation of linear lattice thermal expansion coefficient with different compositions in $Gd_2Zr_{2-x}Ce_xO_7$ and $Y_2Zr_{2-x}Ce_xO_7$ (x = 0.1, 0.2, 0.3, 0.4, 0.5) solid solutions. For both the system of compounds, lattice thermal expansion coefficient increases with increase in doping concentration of Ce in place of Zr. Based on disordered pyrochlore model, the increase in lattice thermal expansion can be correlated to increasing disorder in the system with Ce doping. The Madelung energy and site potential calculations by Pannetier on various type of (3+, 4+) pyrochlores established average bond strength depends on oxygen *x*-parameter and as oxygen *x*-parameter increases, the Madelung energy of the lattice decreases and as a result, thermal expansion also increases (Pannetier 1973). It is clear from the Fig. 7.4 (b) that 48*f* oxygen *x*-parameter increases with increase in Ce substitution and hence the lattice thermal expansion also increases with Ce doping. Yttrium based system shows higher thermal expansion than Gadolinium based system which can also be correlated to comparably high oxygen x-parameter of yttrium based system. But Kutty et.al reported that thermal expansion coefficient increases with increases of atomic number of lanthanide element at A site in pyrozirconates (Kutty, *et al.* 1994). Our results show that even though atomic number of Yttrium is less than that of Gadolinium, the

lattice thermal expansion is relatively high for Yttrium based compounds. The major reason for this is the order-disorder transformation in the system which drives away the yttrium based compounds away from the phase boundary towards fluorite side. During pyrochlore to fluorite transformation, the average coordination of B site elements increases from 6 to 8. As the coordination number increases, the effective ionic radius of the cation increases and bond distance increases. In effect bond strength decreases with increase in coordination number. Therefore the average bond strength in fluorite phase is always less than that of pyrochlore phase and this difference will be more pronounced when the transformed phase is away from the phase boundary towards fluorite side. This is why yttrium based compounds show high thermal expansion than gadolinium based compounds.

7.3.3 Scanning Electron Microscopy Studies

SEM micrographs of $Gd_2Zr_{2-x}Ce_x O_7$ and $Y_2Zr_{2-x}Ce_x O_7$ (x = 0.1, 0.2, 0.3, 0.4, 0.5) samples sintered at 1700 ºC are shown in Fig 7.10 and 7.11 respectively. Average grain sizes of samples were calculated from SEM images by linear intercept method and results are presented in Table 7.7. For most of the samples, grain size is not observed to be uniform and doesn't show any dependence on the amount of Ce substituted in place of Zr.

Table 7.7 Average grain size of $M_2Zr_{2-x}Ce_x O_7$ (M = Gd, Y and *x* = 0.1, 0.2, 0.3, 0.4, 0.5) samples measured from SEM images by linear intercept method

Compound	Average grain size (μm)	Compound	Average grain size (μm)
$Gd_2Zr_{1.9}Ce_{0.1}O_7$	3.77±0.71	$Y_2Zr_{1.9}Ce_{0.1}O_7$	6.06±0.84
$Gd_2Zr_{1.8}Ce_{0.2}O_7$	4.06±1.06	$Y_2Zr_{1.8}Ce_{0.2}O_7$	2.43±0.38
$Gd_2Zr_{1.7}Ce_{0.3}O_7$	6.88±0.79	$Y_2Zr_{1.7}Ce_{0.3}O_7$	3.73±0.91
$Gd_2Zr_{1.6}Ce_{0.4}O_7$	4.48±1.18	$Y_2Zr_{1.6}Ce_{0.4}O_7$	3.45±0.38
$Gd_2Zr_{1.5}Ce_{0.5}O_7$	3.71±0.85	$Y_2Zr_{1.5}Ce_{0.5}O_7$	4.53±0.70

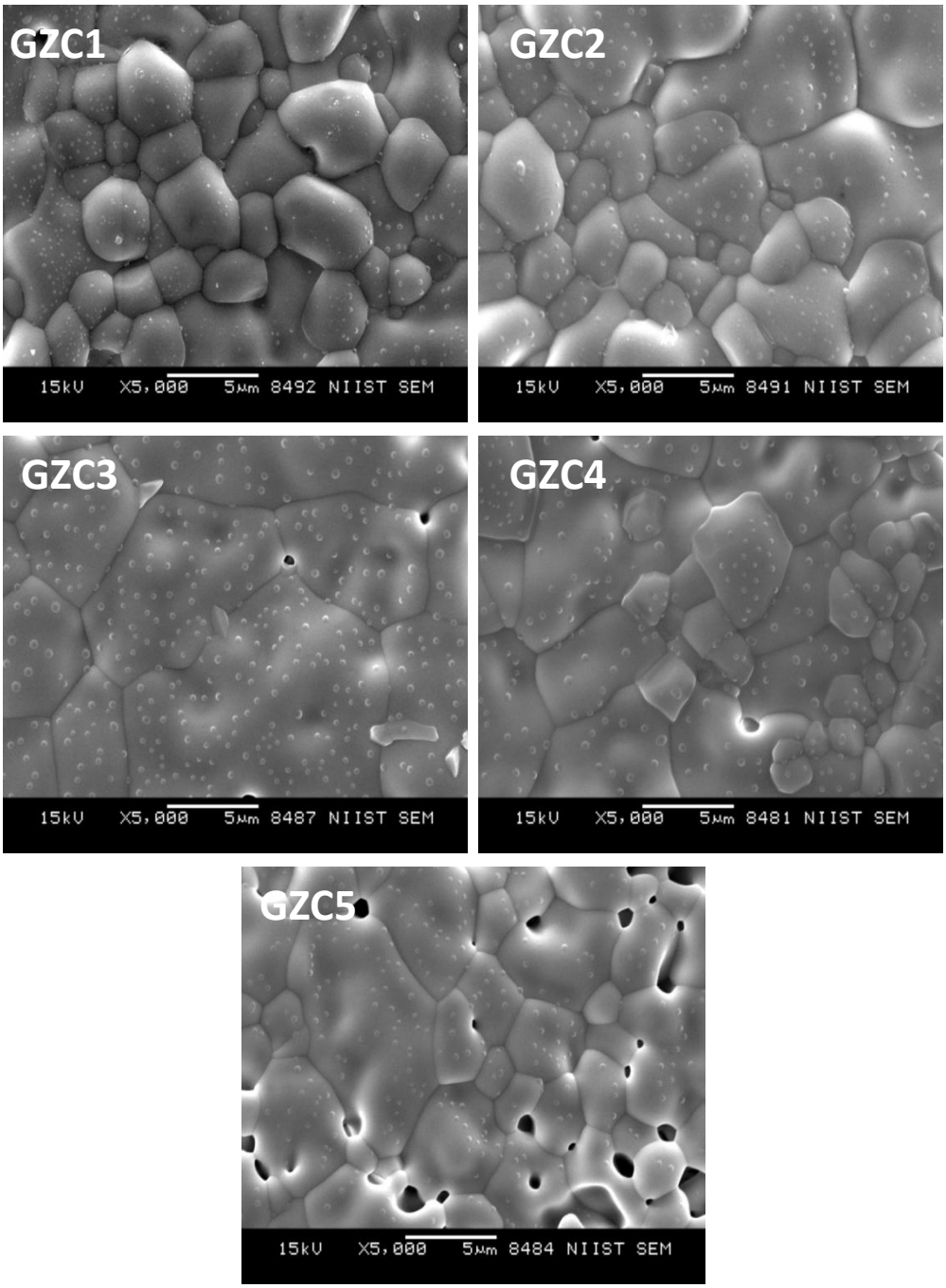

Fig 7.10 SEM images of $Gd_2Zr_{2-x}Ce_x O_7$ (x = 0.1, 0.2, 0.3, 0.4, 0.5) samples sintered at 1700 ^oC for 10 h

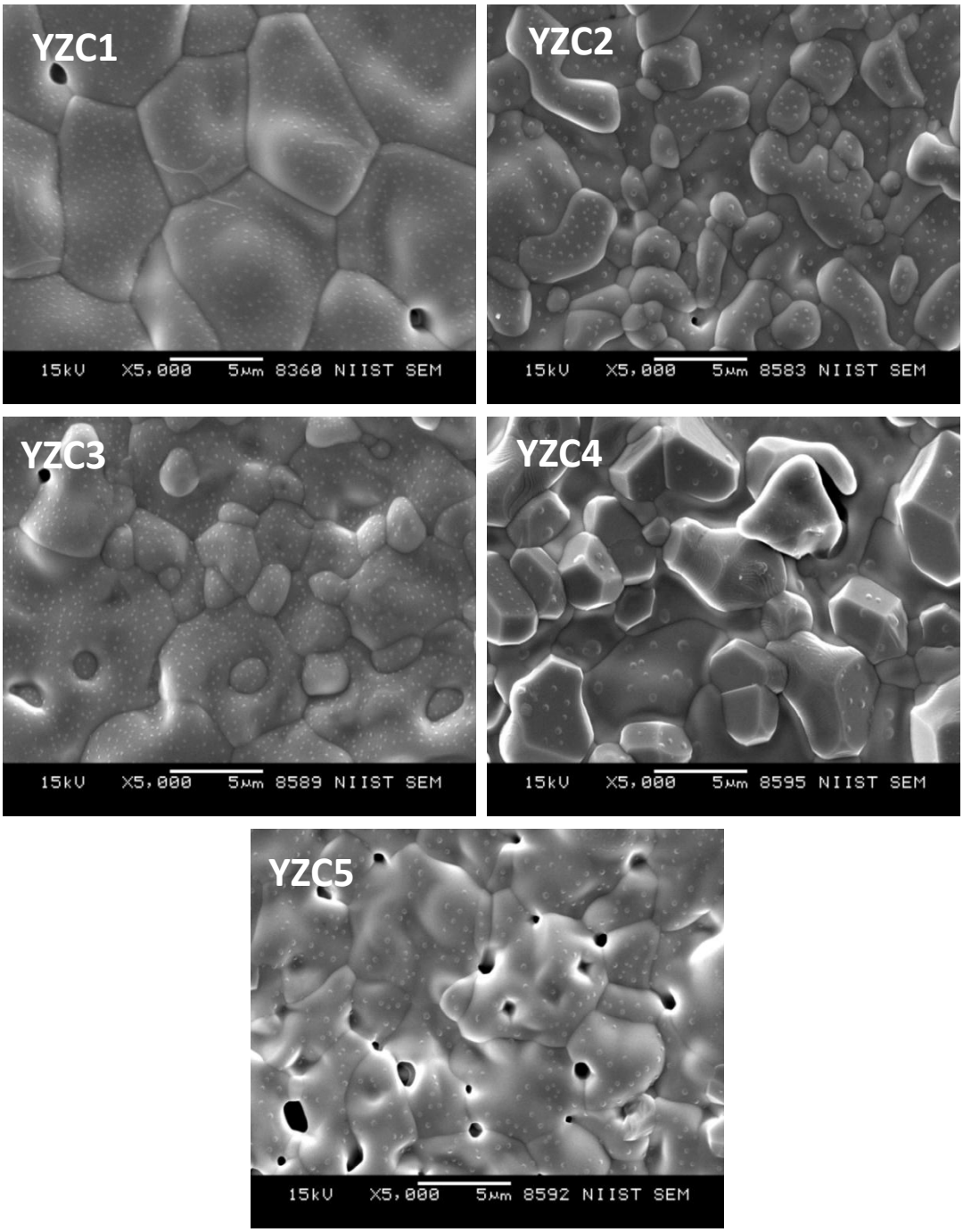

Fig 7.11 SEM images of $Y_2Zr_{2-x}Ce_x O_7$ (x = 0.1, 0.2, 0.3, 0.4, 0.5) samples sintered at 1700 ^oC for 10 h

The white dots observed in SEM images are not due to the presence of secondary phases or impurities since powder XRD patterns and Rietveld analysis clearly confirmed the single phase nature of the compounds. For better microstructure analysis, gold is coated over the surface of the sample to make it conductive. But non-uniform coating of gold over certain insulating ceramic materials may cause charging effect at certain points over the surface and such spots appear very bright in secondary electron images. It can be generally observed that as the crystal structure of the compounds becomes more disordered to form defect fluorite structure with the substitution of Ce, the microstructure becomes more porous and less dense. The sintering of the samples beyond 1700 ºCis practically difficult because platinum crucibles cannot withstand this temperature and alumina crucible can cause problems like reactivity with samples, diffusion of the samples into the crucible etc. The microstructural optimization may require sintering methods like microwave sintering; spark plasma sintering etc. or samples may be synthesized by alternate low temperature synthesis methods.

7.3.4 Impedance Spectroscopic Studies

Electrical properties of the prepared compounds were investigated by ac impedance spectroscopy. The cured silver coated pellets were attached with silver leads and high temperature sample holder is placed inside a temperature controlled furnace. The impedance spectrum at the room temperature is measure in the frequency range 1 MHz to 10 Hz with an input ac signal of 100 mV. Since oxide ion conduction is a temperature dependent process, appreciable conduction starts only after 400 ºC is reached. The furnace is allowed to dwell at 400 ºC and an impedance spectrum is measured. Thereafter temperature is raised in steps of 25 ºC up to 750 ºC and impedance spectra at each temperature is measured. Cole-Cole plot is convenient way of representing impedance data because it reveals electrical behavior of the compounds and its relation to the microstructural properties. The Cole –Cole plot of $Gd_2Zr_{2-x}Ce_xO_7$ and $Y_2Zr_{2-x}Ce_xO_7$ (x = 0.1, 0.2, 0.3, 0.4, 0.5) samples sintered at 1700 ^oC obtained from the impedance data measured at three different temperatures: 450 ^oC, 475 ^oC and 500 ^oC, are shown in Fig 7.12 and 7.13 respectively. For each sample, the intercept of the impedance arc at real axis decreases with increase in

temperature, indicating thermally activated process behind the conduction mechanism. In Fig 7. 12

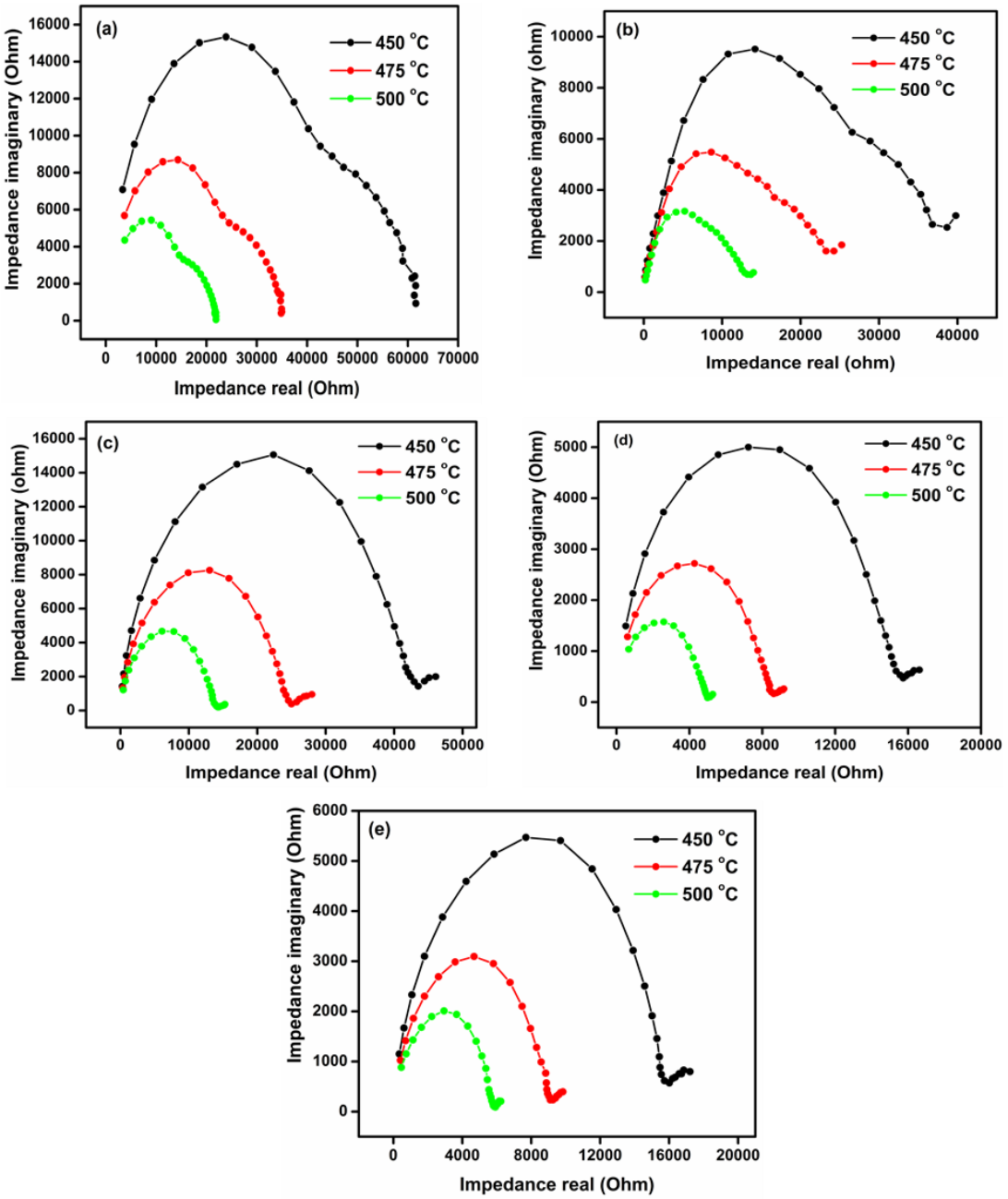

Fig 7.12 Cole – Cole plots of $Gd_2Zr_{2-x}Ce_xO_7$ (x = 0.1, 0.2, 0.3, 0.4, 0.5) samples

(a) and (b), three merged arcs are observed in the measured frequency domain, corresponding to contributions from grain interior at high frequency side, grain boundary at the middle and electrode-electrolyte interface at low frequency side. This

clearly indicates that there is a noticeable difference in relaxation times of oxide ions in grain interior and grain boundary within the measured frequency range. But for all

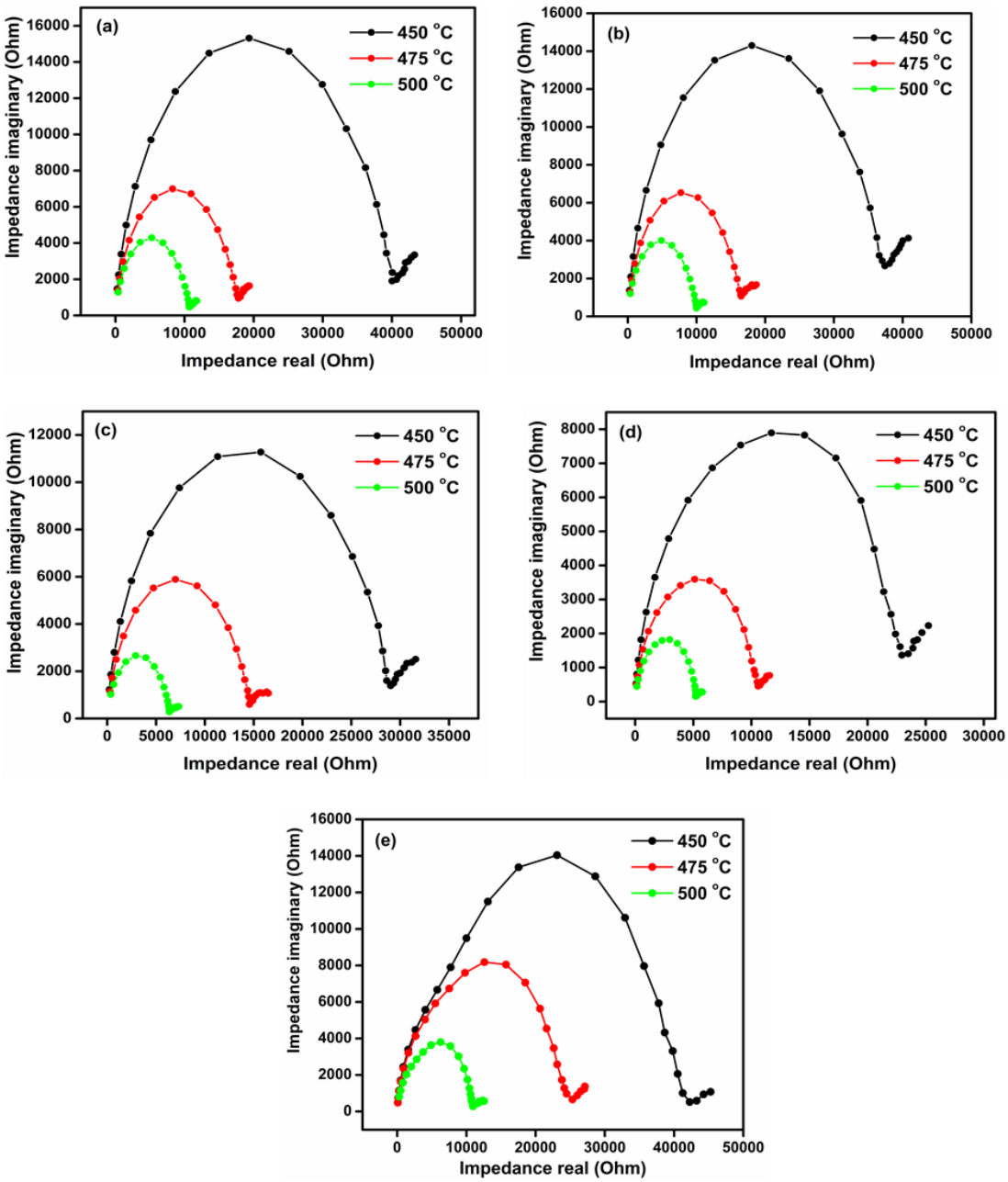

Fig 7.13 Cole – Cole plots of $Y_2Zr_{2-x}Ce_xO_7$ (x = 0.1, 0.2, 0.3, 0.4, 0.5) samples

other samples the Cole-Cole plot has only two distinct arcs; one corresponding to the contribution from both grain interior and grain boundary and the second from electrode-electrolyte interface. Here the difference in relaxation times of oxide ions in grain interior and grain boundary is small and this may be due to the fact that crystallographic dis-orientation in the grain boundary region is less with respect to

grain interior. The low frequency arc which is present in all Cole-Cole plots corresponding to the space charge layer formed at electrode-electrolyte interface due to the blocking of oxide ions at this interface since ions cannot flow through the silver electrode. The presence of low frequency arc is a direct evidence of predominant oxide ion conduction in the samples under investigation.

For conductivity calculations, the impedance of the sample at different temperature is read at the intercept of the impedance arc at the real axis which corresponds to total resistance with contributions from both grain interior and grain boundary. The total conductivity is calculated from the geometrical dimensions of the cylindrical pellets using the equation:

$$\boldsymbol{\sigma = \frac{l}{RA}} \qquad \textbf{(S/cm)} \qquad \textbf{(7.2)}$$

where R is the resistance of the sample, *l* is the thickness and A is the area of cross section of the samples. The logarithm of the product of the conductivity with corresponding temperature in Kelvin is plotted against inverse of the absolute temperature and the plots of $Gd_2Zr_{2-x}Ce_xO_7$ and $Y_2Zr_{2-x}Ce_xO_7$ (x = 0.1, 0.2, 0.3, 0.4, 0.5) samples are shown in Fig. 7.12 (a) and (b) respectively. For all the samples, the plot of log (σT) against 1000/T is a straight-line indicating that the conduction follows an Arrhenius behavior given by the exact form of Arrhenius equation for conductivity:

$$\boldsymbol{\sigma = \frac{A}{T}\ \exp(-E_a/KT)}\ \textbf{ S/cm} \qquad \textbf{(7.3)}$$

where σ is the total conductivity (grain + grain boundary), A is a constant, T is the absolute temperature, Ea is the activation energy of ionic conduction and K is the Boltzmann constant. The activation energy for the oxide ion conduction is calculated from the slope of the Arrhenius plot. The oxide ion conductivity at 750 ºC, the activation energy and the unit cell free volume calculated based on the results of Rietveld analysis based on defect fluorite unit cell are given in Table 7.5 for all compositions. The free volume in a unit cell is defined as the total volume of the unit cell minus the volume occupied by all the atoms in the unit cell. For Ce doped gadolinium system, the ionic conductivity increases with Ce content and reaches a

maximum for GZC4 and thereafter it decreases. Activation energy decreases with Ce doping reaches a minimum value for GZC4, there after it increases again slightly. For

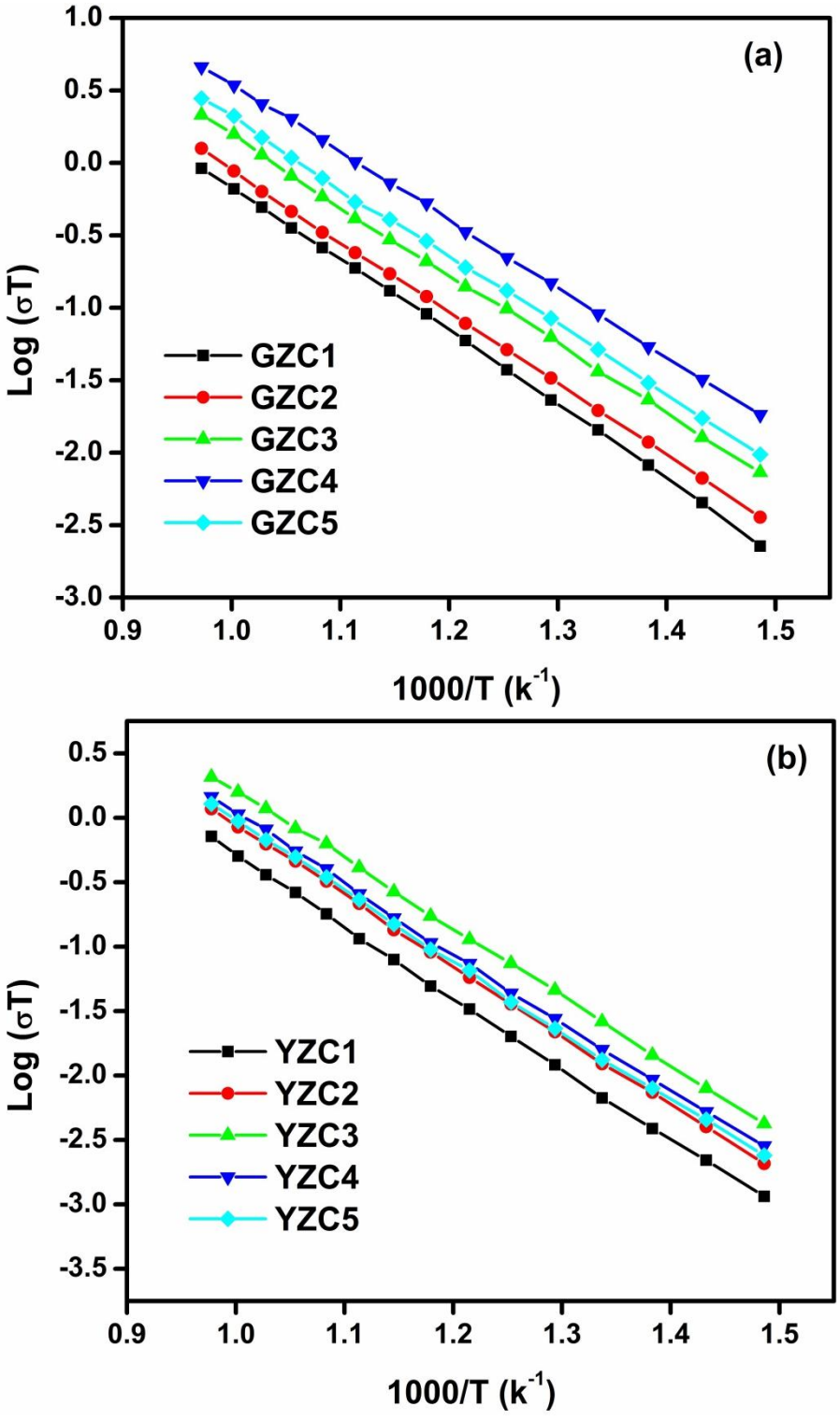

Fig 7.14 Arrhenius plots of (a) $Gd_2Zr_{2-x}Ce_xO_7$ (b) $Y_2Zr_{2-x}Ce_xO_7$ (x = 0.1, 0.2, 0.3, 0.4, 0.5) samples

Yttrium system also conductivity increases first with Ce content and reaches a maximum for YZC3 and thereafter it decreases. Activation energy follows the same trend as in the case of gadolinium system and minimum activation energy is observed for YZC3. When comparing yttrium and gadolinium systems, for the same doping level, gadolinium compounds have relatively high oxide ion conductivity and low activation energy. These observations clearly indicate that there is interplay of several crystallographic factors which can influence oxide ion conductivity and the order-disorder transformation adds a certain extent of complexity to the situation. With respect to disordered pyrochlore model, disorder in the cation and anion lattice increases with increase in Ce substitution and highest ionic conductivity is observed in partially ordered systems (Díaz-Guillén, *et al.* 2008, Pirzada, *et al.* 2001). The highest conductivity of GDC4 may be due to the fact that its disorder in the cation lattice is optimum to allow the diffusion of oxide ions and disorder in the anion lattice is optimum for creating ordered oxygen vacancies which allows conduction of oxide ions via vacancy hopping mechanism. The same is also true for yttrium system where maximum conductivity is observed for YZC3. Van Gool (Gool 1973) and Hagenmuller et al. (Hagenmuller and Gool 1978) proposed some conditions which will enhance ionic conductivity after analyzing ionic conductivity data for compounds with various crystal structures, available in the literature. From these conditions, Mongensen et al. extracted a few conditions which are most relevant to oxide ion conduction in fluorite and perovskite structure. High concentration of mobile oxide ions or oxide ion vacancies, open path between oxide ion sites and equal or slightly different energy of oxide ion sites are the major factor which promotes oxide ion conduction in fluorite type oxides (Mogensen, *et al.* 2004).

In pyrochlore structure, the vacancy of oxygen is at 8*a* site where the coordination is different from that of the occupied sites 48*f* and 8*b*. But in defect fluorite structure, the coordination environment around occupied and vacant oxygen sites (8*c*) is identical due to the mixing of cations at A and B sites. So the energy difference between the occupied and vacant sites is expected to diminish with transformation to fluorite type structure. But the presence of cations with different

oxidation state and ionic radius will lead to distortion of the coordination polyhedra which will reduce radius of the open pathway between the oxygen sites. This makes the diffusion of oxygen atoms difficult from an occupied site to a nearest unoccupied site. Moreover, the free volume available in the lattice is also a contributing factor to the oxide ion conduction via oxygen vacancy mechanism. These supporting and opposing factors certainly affect the oxide ion conducting behavior of the present systems.

Table 7.8 Oxide ion conductivity at 750 ºC, activation energy of oxide ion conduction and unit cell free volume of $M_2Zr_{2-x}Ce_xO_7$ (M = Gd, Y and *x* = 0.1, 0.2, 0.3, 0.4, 0.5) samples

Sample	Oxide Conductivity at 750 ºC (S/cm)	Activation energy (eV)	Unit cell Free volume (10^{-30} m^3)
$Gd_2Zr_{1.9}Ce_{0.1}O_7$	8.97×10^{-4}	0.9575	38.2053
$Gd_2Zr_{1.8}Ce_{0.2}O_7$	1.23×10^{-3}	0.9322	38.8043
$Gd_2Zr_{1.7}Ce_{0.3}O_7$	2.32×10^{-3}	0.9084	39.4140
$Gd_2Zr_{1.6}Ce_{0.4}O_7$	4.49×10^{-3}	0.8948	40.0597
$Gd_2Zr_{1.5}Ce_{0.5}O_7$	2.72×10^{-3}	0.9047	40.6656
$Y_2Zr_{1.9}Ce_{0.1}O_7$	7.02×10^{-4}	1.0484	34.0868
$Y_2Zr_{1.8}Ce_{0.2}O_7$	1.15×10^{-3}	1.0332	34.7365
$Y_2Zr_{1.7}Ce_{0.3}O_7$	2.03×10^{-3}	1.0131	35.4795
$Y_2Zr_{1.6}Ce_{0.4}O_7$	1.42×10^{-3}	1.0223	36.1018
$Y_2Zr_{1.5}Ce_{0.5}O_7$	1.25×10^{-3}	1.0287	36.7597

The increase in oxide ion conductivity with the substitution of the Ce observed in both Gd and Y systems is due to two major reasons. The increase of Ce at B site increases the mixing of A and B cations which lead to the cation sublattice disorder along with anion sublattice disorder. This disorder can produce more mobile oxide ions which can diffuse through the lattice and contribute to the conductivity of the samples. The increase of free volume within the lattice can also contribute to the enhanced conductivity of the defect fluorite samples. The study of effect of

microstructural factors like grain size, porosity etc. requires microstructural optimization by different synthesis methods and processing conditions since sintering of the samples at 1700 ºC for 10 h cannot produce highly dense samples.

7.4 Conclusions

$Gd_2Zr_{2-x}Ce_xO_7$ and $Gd_2Zr_{2-x}Ce_xO_7$ (x = 0.1, 0.2, 0.3, 0.4, 0.5) samples were synthesized by high temperature ceramic route. All compounds crystallizes with a defect fluorite structure due to the bigger Ce^{4+} at B site in place of relatively smaller Zr^{4+} ion and the disorder of cation sublattice increases with increase of substitution of Ce. Rietveld refinement of powder X-ray diffraction patterns were performed based on cation disordered pyrochlore model with space group $Fd\bar{3}m$ as well as anion deficient fluorite structure belonging to $Fm\bar{3}m$ space group. From the Rietveld analysis it is confirmed that the disorder in cation lattice drives the structural transformation from pyrochlore to defect fluorite structure. The lattice thermal expansion coefficient calculated from the high temperature xrd measurement is found to increase with increase in Ce substitution at B site in both Y based and Gd based compounds. This increase in lattice thermal expansion can be correlated to increased disorder in the lattice due to the substitution of bigger Ce^{4+} cation at B site. Cole – Cole plots obtained from the ac impedance measurements of the samples show contributions from both grain and grain boundary as single arc except for $Gd_2Zr_{1.9}Ce_{0.1}O_7$ and $Gd_2Zr_{1.8}Ce_{0.2}O_7$ samples. The oxide ion conductivity also found to increase with Ce substitution, reaches a maximum and then decreases. This is due to the combined effect of crystallographic factors like disorder, unit cell free volume, polyhedral distortion etc. and microstructural factors like grain size, porosity etc. A microstructural optimization by low temperature synthesis methods or sintering techniques like microwave sintering or spark plasma sintering is necessary for complete impedance analysis to reveal the effect of microstructural factors. Both Gd and Y based compounds have conductivity in the range $8 \times 10^{-4} - 5 \times 10^{-3}$ S/cm and for the same doping Gd based compounds have high conductivity and low activation energy. Hence these compounds can be promising candidates as solid electrolyte for IT-SOFC.

Chapter 8

Conclusions & Future Scope

This chapter presents the general conclusions derived from the study of structure, lattice thermal expansion and oxide ion conducting properties of rare earth based zirconate pyrochlore with different substituents at A and B sites. These conclusions can serve as a guideline for the designing of new oxide ion conductors in pyrochlore family. The future scope of the present work is also discussed, giving emphasis to the optimization and application of the developed oxide ion conductors as solid electrolyte in intermediate temperature fuel cells.

8.1 Conclusions

The present work on structure, lattice thermal expansion and oxide ion conducting properties of rare earth based zirconate pyrochlore is a fundamental study to formulate certain criteria for designing new oxide ion conductors belonging pyrochlore family of ceramic complex oxides. The conclusions drawn from the study can form a basis for understanding oxygen ion conduction in pyrochlore oxides and its correlation to the crystallography of the pyrochlore oxides and chemical nature of the substituting atoms. The major conclusions drawn from the study are presented below:

- The study of order disorder transformation in Ca-Y-Zr-Ta-O system, synthesized by high temperature ceramic route, as a solid solution of $CaTaO_{3.5}$ and $YZrO_{3.5}$ in different ratios (4:1 , 2:1, 1:1, 1:2, 1:4, 1:6) revealed the role of radius ratio (r_A/r_B) in controlling disorder of cation as well as anion sublattices in the pyrochlore structure. The introduction of multiple cations at both A and B sites in the pyrochlore structure to form quaternary pyrochlore oxides, allow more tunability to the pyrochlore structure, thereby adding more flexibility in tailoring the properties by adjusting composition. The radius ratio varies from 1.67 to 1.45 as the content of $YZrO_{3.5}$ increases and the structural transformation from pyrochlore to defect fluorite occurs when the ratio of $CaTaO_{3.5}$ and $YZrO_{3.5}$ in the solid solution is 1:4. The critical radius ratio observed for structural transformation in the present system is 1.48 and is close to reported critical radius ratio 1.46 for binary pyrochlore oxides.
- The decrease in intensity of superlattice peaks with increase of $YZrO_{3.5}$ content is a clear indication of disorder in the structure since additional planes produced by ordering in ideal pyrochlore structure is progressively disappearing. The complete disappearance of 1:4 and 1:6 compositions is indicating transformation of the pyrochlore structure to a defect fluorite structure.
- 48*f* oxygen *x*-parameter is a measure of distortion of A and B polyhedra in the pyrochlore structure. Oxygen x-parameter, calculated by the Rietveld analysis of the powder XRD pattern, is found to increase with increase in $YZrO_{3.5}$ content and approaches its upper limit 0.375. Thus the increase in

x-parameter can be considered as a measure of disorder in the pyrochlore structure.

- Raman spectra of the compounds confirms the structural transformation in Ca-Y-Zr-Ta-O system indicated by the decrease in intensity and increase in FWHM of pyrochlore Raman active modes A_{1g}, E_g and F_{2g} with increase in disorder and complete disappearance of such modes in defect fluorite structure. Selected area electron diffraction pattern and high resolution TEM images clearly establish the fact that transformation from pyrochlore to fluorite is accompanied by the absence of superlattice planes like (111).
- Oxide ion conductivity and lattice thermal expansion are found to near the phase boundary between pyrochlore and fluorite structure. Disordered pyrochlore structure which doesn't undergo complete transformation to defect fluorite has got highest conductivity among the compounds prepared in the Ca-Y-Zr-Ta-O system. This clearly establishes the role of disorder in enhancing the oxide conductivity in pyrochlore structured oxides.
- The microstructural studies shows that pyrochlore structured samples have good sintered density compared to defect fluorite structured samples. The porosity present in the defect fluorite structure samples can adversely affect the electrical properties, thereby lowering its oxide conductivity. Therefore it is difficult to predict whether disordered pyrochlores or defect fluorites exhibit high oxide ion conductivity when the microstructure and density are optimized. But it can be asserted that oxide ion conductivity is maximum near the phase boundary region and new compositions can be designed to be near the phase boundary by adjusting the radius ratio (r_A/r_B).
- $(Ca_xGd_{1-x})_2(Zr_{1-x}M_x)_2O_7$ (M = Nb, Ta) pyrochlore solid solutions were prepared by high temperature ceramic route and these compositions fall near to the phase boundary in pyrochlore domain. The disappearance of superlattice peaks in the powder XRD patterns of Nb substituted compounds is not only because of the disorder but also due to low X-ray scattering power of Nb. The compositions undergo disorder to order transition with increase of doping of Ca at A site and Nb/Ta at B site. Rietveld analysis of the powder XRD pattern,

Raman spectra and TEM studies confirms the disorder to order transitions in the present system.

- Lattice thermal expansion decreases with increase in ordering of the pyrochlore lattice and Nb substituted compounds have high thermal expansion coefficient compared to Ta substituted compounds due to low ionization energy of Nb compared to that of Ta. Thermal expansion in zirconate pyrochlores depend on Madelung binding energy
- Oxide ion conductivity shows a significant variation only when the pyrochlore lattice has sufficient disorder to allow the easy pathway for oxide ions to diffuse and maximum conductivity is observed for 10 mol % substituted Nb compound.
- In order to investigate the effect of bond strength at B site on oxide ion conductivity and lattice thermal expansion, $CaGdZrNb_{1-x}Ta_xO_7$ pyrochlore solid solutions were prepared by high temperature solid state reaction route and characterized to derive structure - property correlations. The specialty of the composition is that both Nb and Ta have the same ionic radius (0.64 Å) at six co-ordination and substitution of Nb by Ta doesn't produce any difference in radius ratio (r_A/r_B), the effect of which is already established.
- All compounds crystallize in ordered pyrochlore structure and there is a decrease in the intensity of superlattice peaks with the increase in substitution of Ta. This is mainly due to the high X-ray scattering power of Ta compared to that of Nb. Lattice parameter and oxygen *x*-parameter decreases with increase in substitution of Ta in place of Nb. The nuclear charge of Ta is higher than that of Nb which attracts the electron cloud around it more tightly causing the bond to shorten which in turn causes unit cell to shrink a little.
- Three major vibrational Raman active modes of the pyrochlore are observed for all compositions and with the increase in substitution of Ta, the intensity of F_{2g} mode increases considerably which implies the reduction in symmetry distortion of BO_6 octahedra due to the introduction of Ta at B site. Selected area electron diffraction pattern as well as high resolution images confirmed the presence of superlattice planes.

- Lattice thermal expansion coefficient decreases with increase in substitution of Ta in place of Nb. The diatomic bond energy of Ta-O bond is greater than that of Nb-O bond and hence the diatomic bonding strength between Ta-O is greater than that for Nb-O. The stronger bond between Ta and O implies larger ionization energy of the bonding electrons, and therefore, the increase in phonon frequency. According to group renormalization theory developed by Arulsamy, the phonon frequency of a solid is directly proportional to the ionization energy of the bonding electrons. Therefore, increasing phonon frequency implies increasing rigidity of the system which ultimately leads to smaller thermal expansion.
- Cole – Cole plots obtained by the impedance measurement of the samples reveals only one semicircular arc followed by a low frequency spike. The single semicircular arc corresponds to electrical responses from both grain and grain boundaries of the samples which indicates that relaxation frequencies in both contributions vary slightly so that two semicircles merged into one. The low frequency spike is due to the blocking of oxide ions at the electrode-electrolyte interface which is an evidence of predominant oxide ion conduction.
- Oxide ion conductivity is found to be maximum for Nb substituted compound due to the low bond strength of Nb-O bond compared to Ta-O bond which lowers activation energy to generate mobile oxide ions by breaking the bonds. The uniform and bigger grain sizes of Nb rich compositions evident from the SEM micrographs, also contributes to enhanced oxide ion conduction.
- Substitution of an element with same ionic radius but different nuclear charge at B site in pyrochlore has a considerable influence on oxide ion conducting properties of the samples. According to computer simulation studies, 48*f* – 48*f* oxygen vacancy mechanism is predominant in pyrochlore oxides rather than 48*f* – 8*b* mechanism. Since B site is surrounded only by 48*f* oxygen atoms, the influence of B site substitution on oxide ion conductivity observed in our studies confirms the predominance of 48*f* - 48*f* oxygen vacancy mechanism. Hence, in pyrochlore oxides, B site substitutions are more effective to improve the oxide ion conductivity.

- $M_2Zr_{2-x}Ce_xO_7$ (M = Gd, Y and x = 0.1 - 0.5) system was prepared by high temperature ceramic route and characterized to study the effect of substitution of bigger Ce^{4+} ion at B site in the pyrochlore on structure, lattice thermal expansion coefficient and oxide ion conductivity. All compounds are found to crystallize in defect fluorite structure with complete absence of superlattice peaks.
- Rietveld analysis performed based two different models: disordered pyrochlore model belonging to $Fd\bar{3}m$ space group and defect fluorite belonging to $Fm\bar{3}m$, clearly established the fact that both models are equivalent to each other and the structural transformation is a progressive transformation rather than an abrupt change.
- Lattice thermal expansion coefficient is found to increase with increase of Ce substitution in both Y and Gd based systems. This is due to the increase in disorder in cation sublattice due to the introduction of bigger Ce^{4+} ions at B site.
- Oxide ion conductivity increases with increase in Ce substitution up to certain substitution level depending upon the rare earth cation at A site and then decreases. But oxide ion conductivity depends on various crystallographic factors like disorder in the lattice, free volume in the unit cell, distortion of cation polyhedra etc. as well as on microstructural parameters like grain size, grain boundary effects, porosity etc. A conclusive statement on the dependence of oxide ion conductivity on substitution is possible only by a proper microstructural optimization by different synthesis methods or sintering techniques.

In the former part of this chapter, conclusions specific to different rare earth based zirconate pyrochlores are presented. Some general rules regarding the crystallography and chemical nature of the elements substituted in pyrochlore oxides, for designing new compositions to develop oxide ion conductors with high oxide ion conductivity and suitable lattice thermal expansion coefficient, can be derived from the present study.

- Disorder in pyrochlore oxides can be controlled by adjusting the ratio of average radius of A cation to that of B cation.
- The critical radius ratio for pyrochlore to defect fluorite transformation is approximately 1.46.
- For Good oxide ion conduction, the composition must be near to the phase boundary region between pyrochlore and defect fluorite.
- Oxide ion conduction will be enhanced by disorder only up to a certain extent which depends on different crystallographic factors and chemistry of the elements.
- Lattice thermal expansion increases with increase of disorder in pyrochlore oxides.
- Apart from radius ratio, bond strength plays a role in deciding the oxide ion conductivity and lattice thermal expansion.
- Substitution of elements with low ionization energy at B site can enhance oxide ion conductivity due to reduced metal oxygen bond strength, but at the same time, lattice thermal expansion increases. Therefore there should be a compromise between oxide ion conductivity and lattice thermal expansion coefficient to develop a thermally stable solid electrolyte for SOFC.
- Oxide ion conduction in pyrochlore proceeds via 48*f* - 48*f* oxygen vacancy mechanism and hence B site is more sensitive than A site when other elements are substituted

8.2 Future Scope

The major challenge of the 21st century is the generation of efficient and environment friendly energy technologies to meet the needs of ever growing human population. Presently, about 70 % of the total energy demand is being satisfied by the fossil fuel based energy sources which will be depleted within 40 – 50 years from now. Moreover, the combustion of these fossil fuels is considered to be the largest contributing factor to the release of greenhouse gases into the atmosphere and subsequent global warming. In this context, for large scale energy production solid oxide fuel cell is a good alternative. The heart of the fuel cell is its solid electrolyte and efficiency of the fuel cell is decided mostly by the oxide ion conductivity of the

electrolyte. Our ultimate goal is to develop an electrolyte with high conductivity at intermediate temperature range (600 – 750 ^{o}C) and matching thermal expansion coefficient with electrodes. The present study is only the first phase of work to achieve the goal and there is a good scope for the future work including improvement and optimization of the investigated systems as well as the design of new oxide ion conductors belonging to pyrochlore family based on the results obtained from the present study.

The present study concentrated much on the relation between the structural features and thermal and electrical properties of the zirconate pyrochlores. The calcination as well as sintering temperatures was chosen in such a way that the final product after processing must be a highly crystalline, single phase material. The microstructural optimization was not able to properly carry out due to the very high sintering temperature usually above 1600 ^{o}C for zirconate pyrochlores. The defect fluorite structured samples requires still high sintering temperature in the range 1700 – 1800 ^{o}C for getting a highly dense cylindrical pellets. Platinum crucibles cannot withstand such a high temperature and samples diffuse in to the crucible if alumina crucible is used for sintering. Moreover, for practical applications in SOFC sintering temperature must be reduced at least to 1500 ^{o}C so that electrodes and electrolytes prepared as thin layers can be sintered together to form an SOFC single cell. Very high sintering temperature in such cases may cause evaporation of volatile elements from electrode materials or chemical reaction between electrolyte and the electrodes. Therefore microstructural optimization requires low temperature soft chemical methods to prepare the compounds and sinter the pellets at sufficiently low temperature to get high density and uniformly packed big grains. The impedance spectra of the compounds can be measured up to 1000 ^{o}C using platinum electrodes and impedance data can be fitted to suitable equivalent circuit models to find the contribution of grain, grain boundary and electrodes. This can give a clear insight into the effect of microstructure on oxide ion conductivity of the samples. The microstructural optimization and impedance analysis can be the second phase of the work to achieve the goal of developing new electrolytes for IT-SOFC.

The third phase of the work must include the study of effect of oxygen partial pressure on the oxide ion conductivity of the prepared electrolyte and calculation of transference number which is the ratio of pure oxide ion conductivity to the total conductivity of the prepared electrolyte. The chemical stability of the electrolyte in oxidizing and reducing environment can be tested by measuring the impedance response of the samples in different atmospheres like oxygen, nitrogen, hydrogen etc. The compatibility of the electrolyte with different electrode materials can be tested using an SOFC test unit. This compatibility study must consider matching of the lattice thermal expansion between electrodes and the electrolyte as well as possible chemical reaction between the electrodes and electrolyte in both reducing and oxidizing environments. When a matching electrode - electrolyte combination is discovered, an SOFC unit can be fabricated and its total performance analysis can be done under no load condition as well as load condition. Fabrication of such a functional, high efficiency SOFC unit requires a lot of engineering works starting from the deposition of thin layers of electrodes and electrolytes to a fuel stack with suitable supporting components to form an SOFC stack either in flat plate or tubular configuration.

In summary, the work presented in this Ph.D thesis is the beginning of a big research program to develop a non - conventional energy source (IT - SOFC) to meet the energy requirement of the future generation. The realization of the ultimate goal to fabricate an IT – SOFC requires concerted efforts of material scientists working on different areas like development of electrolytes, cathodes, anodes and interconnect materials and engineers making different SOFC configurations depending upon its applications.

LIST OF PUBLICATIONS IN SCI JOURNALS

1. **A. N. Radhakrishnan**, P. Prabhakar Rao, S. K. Mahesh, D. S. Vaisakhan Thampi and Peter Koshy, "Role of Bond Strength on the Lattice Thermal Expansion and Oxide Ion Conductivity in Quaternary Pyrochlore Solid Solutions" **Inorganic Chemistry**, 2012, 51 (4), 2409–2419

2. **A.N. Radhakrishnan**, P. Prabhakar Rao, K.S. Mary Linsa, M. Deepa and Peter Koshy, "Influence of disorder-to-order transition on lattice thermal expansion and oxide ion conductivity in $(Ca_xGd_{1-x})_2(Zr_{1-x}M_x)_2O_7$ pyrochlore solid solutions" **Dalton Transactions**, 2011 , 40 (15), 3839-3848 .

3. **A.N. Radhakrishnan,** P. Prabhakar Rao, K.S. Sibi, M. Deepa and Peter Koshy, "Order–disorder phase transformations in quaternary pyrochlore oxide system: Investigated by X-ray diffraction, transmission electron microscopy and Raman spectroscopic techniques" **Journal of Solid State Chemistry**, 2009, 82 (8), 2312-2318.

4. K.S. Sibi, **A.N. Radhakrishnan**, M. Deepa, P. Prabhakar Rao and Peter Koshy, "Oxide ion conductivity and relaxation in $CaREZrNbO_7$ (RE = La, Nd, Sm, Gd, and Y) system", **Solid State Ionics**, 2009, 180 (20-22), 1164-1172.

5. M. Deepa, P. Prabhakar Rao∗, S. Sumi, **A.N. Radhakrishnan**, M.R. Chandran and Peter Koshy, "Structural and electrical properties of nonstoichiometric semiconducting pyrochlores in Ca–Ce–Ti–Nb–O system", **Materials Chemistry and physics**, 2011, 127 (1-2), 162-169

6. M. Deepa, P. Prabhakar Rao, Sumi S, **A.N. Radhakrishnan**, and Peter Koshy, "New negative temperature coefficient ceramics in Ca-Ce-Nb-M-O (M=Mo or W) system**" Journal of the American Ceramic Society**, 2010, 93 (6) , 1576-1579.

7. M. Deepa, P. Prabhakar Rao, **A.N. Radhakrishnan**, K.S. Sibi and Peter Koshy, "Pyrochlore type semiconducting ceramic oxides in Ca–Ce–Ti–M–O system (M = Nb or Ta)—Structure, microstructure and electrical properties", **Materials Research Bulletin**, 2009, 44 (7), 1481-1488.

8. S. K. Mahesh, P. Prabhakar Rao, Mariyam Thomas , **A. N. Radhakrishnan** and Peter Koshy, "Photoluminescence characteristics of new stannate pyrochlore based red phosphors: CaLaSnNbO7: Eu^{3+} ", **Journal of Materials Science: Materials for Electronics**, 2012, DOI: 10.1007/s10854-012-0636-6.

LIST OF PAPERS PRESENTED IN CONFERENCES

1. **A. N. Radhakrishnan**, P. Prabhakar Rao, S. K. Mahesh, D. S. Vaisakhan Thampi and Peter Koshy, "Oxide Ion Conductivity and Lattice Thermal Expansion Studies in $CaGdZrNb_{1-x}Ta_xO_7$ Pyrochlore Solid Solutions", **7th National Symposium and Conference on Solid State Chemistry and Allied Areas (ISCAS), November 2011, Jamia Millia Islamia, New Delhi.**

2. **A.N. Radhakrishnan**, P. Prabhakar Rao, K.S. Sibi and Peter Koshy, " Investigation of Structural disorder in pyrochlore oxide system: $(Ca_xGd_{1-x})_2(Zr_{1-x}Nb_x)_2O_7$ (x = 0, 1, 2, 3, 4, 5) using Powder X-ray Diffraction techniques and Raman Spectroscopy", **International Conference on Advanced Functional Materials- ICAFM, December 2009, Thiruvananthapuram.**

3. **A.N. Radhakrishnan**, P. Prabhakar Rao, K.S. Sibi and Peter Koshy, "Investigation of structural, microstructural and electrical properties of sintered $Gd_2Zr_2O_7$ Nano – powders prepared by citrate route", **Electron Microscope Society of India – National Conference (EMSI - NC), January 2009, Jhansi.**

REFERENCES

Abraham F., Debreuille-Gresse M. F., Mairesse G. and Nowogrocki G., "Phase transitions and ionic conductivity in $Bi_4V_2O_{11}$ an oxide with a layered structure" *Solid State Ionics*, 28-30, Part 1 (**1988**) 529-532.

Abram E. J., Sinclair D. C. and West A. R., "Electrode-Contact Spreading Resistance Phenomena in Doped-Lanthanum Gallate Ceramics" *Journal of Electroceramics*, 7, 3 (**2001**) 179-188.

Arenas D. J., Gasparov L. V., Qiu W., Nino J. C., Patterson C. H. and Tanner D. B., "Raman study of phonon modes in bismuth pyrochlores" *Physical Review B*, 82, 21 (**2010**) 214302 1-8.

Arévalo-López A. M. and Alario-Franco M. A., "On the structure and microstructure of $PbCrO_3$" *Journal of Solid State Chemistry*, 180, 11 (**2007**) 3271-3279.

Arulsamy A. D., "Renormalization group method based on the ionization energy theory" *Annals of Physics*, 326, 3 (**2011**) 541-565.

Azad A. M., Larose S. and Akbar S. A., "Bismuth oxide-based solid electrolytes for fuel cells" *Journal of Materials Science*, 29, 16 (**1994**) 4135-4151.

Bagockii V. S., "*Fuel cells problems and solutions"* Wiley: Hoboken, NJ (**2009**)

Bagotzky V. S., "*Fundamentals of electrochemistry"* Plenum Press: New York (**1993**)

Barsoukov E. and Macdonald J. R., "*Impedance spectroscopy : theory, experiment, and applications"* Wiley-Interscience: Hoboken, N.J. (**2005**)

Basu S., "*Recent trends in fuel cell science and technology"* Springer: New York (**2007**)

Begg B. D., Hess N. J., McCready D. E., Thevuthasan S. and Weber W. J., "Heavy-ion irradiation effects in $Gd_2(Ti_{2-x}Zr_x)O_7$ pyrochlores" *Journal of Nuclear Materials*, 289, 1-2 (**2001**) 188-193.

Belyaev I. N., Sholokhovich M. L. and Kkhan N., "Preparation of New Compounds $CaErBB'O_7$ with the Pyrochlore Structure" *Russian Journal of Inorganic Chemistry (Translation of Zhurnal Neorganicheskoi Khimii)*, 23, (**1978**) 1112–1114.

Binner J. G., "*Advanced ceramic processing and technology"* (Vol. 1) Noyes Publication: Park Ridge, NJ (**1990**)

Blomen L. J. M. J. and Mugerwa M. N., "*Fuel cell systems"* Plenum Press: New York (**1993**)

Boivin J. C. and Mairesse G., "Recent Material Developments in Fast Oxide Ion Conductors" *Chemistry of Materials*, 10, 10 (**1998**) 2870-2888.

Bosch K. J., Woudstra N. and Van Der Nat K. V., "*Designing solid oxide fuel cell gas turbine hybrid systems using exergy analysis"* ASME 4th International Conference on Fuel Cell Science, Engineering and Technology: Irvine, California, USA (**2006**)

Bouwmeester H. J. M. and Burggraaf A. J., " Dense ceramic membranes for oxygen separation" In A. J. Burggraaf & L. Cot (Eds.), *Membrane Science and Technology* (Vol. Volume 4, pp. 435-528) Elsevier: Amsterdam: (**1996**)

Boyce M. P., "*Handbook for cogeneration and combined cycle power plants"* ASME Press: New York (**2002**)

Brett D. J. L., Atkinson A., Brandon N. P. and Skinner S. J., "Intermediate temperature solid oxide fuel cells" *Chemical Society Reviews*, 37, 8 (**2008**) 1568-1578.

Brown J. T., Westinghouse Electric Corp P. P. A., Conference: 13. annual energy technology c. and exposition W. D. C. U. S. A. M., "Solid oxide fuel cells: technology and application" *Energy Technol. (Wash., D.C.)*, 13, (**1986**) Pages: 1526-1539.

Bruce P. G., "*Solid state electrochemistry"* Cambridge University Press: Cambridge; New York, NY, USA (**1995**)

Burggraaf A. J., van Dijk T. and Verkerk M. J., "Structure and conductivity of pyrochlore and fluorite type solid solutions" *Solid State Ionics*, 5, (**1981**) 519-522.

Busby R. L., "*Hydrogen and fuel cells : a comprehensive guide"* Penn Well Corporation: Tulsa, Oklahoma (**2005**)

Buydos J. F., "*Batteries, supercapacitors, and fuel cells"* Science Reference Section, Science, Technology, and Business Division, Library of Congress: Washington, D.C. (**2007**)

Chakoumakos B. C., "Systematics of the pyrochlore structure type, ideal $A_2B_2X_6Y$" *Journal of Solid State Chemistry*, 53, 1 (**1984**) 120-129.

Chambers A., "*Renewable energy in nontechnical language"* PennWell Corporation: Tulsa, Okla (**2004**)

Champion J. D. M., Wills A. S., Fennell T., Bramwell S. T., Gardner J. S. and Green M. A., "Order in the Heisenberg pyrochlore: The magnetic structure of $Gd_2Ti_2O_7$" *Physical Review B: Condensed Matter and Materials Physics*, 64, 14 (**2001**) 1404071-1404074.

Chandra S., "*Superionic solids : principles and applications"* Elsevier North-Holland, Amsterdam (**1981**)

Chaplot S. L., Mittal R. and Choudhury N., "*Thermodynamic properties of solids : experiment and modeling"* Wiley-VCH: Weinheim (**2010**)

Cheng D. K., "*Field and wave electromagnetics"* Addison Wesley: Reading, Mass. (**1983**)

Chowdari B. V. R., "*Proceedings of the 3rd Asian Conference on Solid State Ionics : materials and applications "* 3rd Asian Conference on Solid State Ionics : materials and applications: Varanasi, India (**1992**)

Corbel G., Laligant Y., Goutenoire F., Suard E. and Lacorre P., "Effects of partial substitution of Mo^{6+} by Cr^{6+} and W^{6+} on the crystal structure of the fast oxide-ion conductor structural effects of W^{6+}" *Chemistry of Materials*, 17, 18 (**2005**) 4678-4684.

Deepa M., Prabhakar Rao P., Sumi S., Radhakrishnan A. N., Chandran M. R. and Koshy P., "Structural and electrical properties of nonstoichiometric semiconducting pyrochlores in Ca-Ce-Ti-Nb-O system" *Materials Chemistry and Physics*, 127, 1-2 (**2011**) 162-169.

Diaz-Guillen J. A., Fuentes A. F., Diaz-Guillen M. R., Almanza J. M., Santamaria J. and Leon C., "The effect of homovalent A-site substitutions on the ionic conductivity of pyrochlore-type $Gd_2Zr_2O_7$" *Journal of Power Sources*, 186, 2 (**2009**) 349-352.

Díaz-Guillén M. R., Moreno K. J., Díaz-Guillén J. A., Fuentes A. F., Ngai K. L., Garcia-Barriocanal J., Santamaria J. and Leon C., "Cation size effects in oxygen ion dynamics of highly disordered pyrochlore-type ionic conductors" *Physical Review B*, 78, 10 (**2008**) 104304 1-7.

Djurado E. and Labeau M., "Second phases in doped lanthanum gallate perovskites" *Journal of the European Ceramic Society*, 18, 10 (**1998**) 1397-1404.

Du H. and Yao X., "Structural trends and dielectric properties of Bi-based pyrochlores" *Journal of Materials Science: Materials in Electronics*, 15, 9 (**2004**) 613-616.

E&G Services, "*Fuel cell handbook"* U.S. Dept. of Energy, Office of Fossil Energy, National Energy Technology Laboratory: Morgantown, WV (**2004**)

Eguchi K., Setoguchi T., Inoue T. and Arai H., "Electrical properties of ceria-based oxides and their application to solid oxide fuel cells" *Solid State Ionics*, 52, 1-3 (**1992**) 165-172.

Ehrenreich H. and Turnbull D., "*Solid state physics : advances in research and applications"* Academic Press: Orlando (**1987**)

Erickson E. E., Gray D., Taylor K., Macaluso R. T., LeTard L. A., Lee G. S. and Chan J. Y., "Synthesis, structure and dielectric characterization of $Ln_2Ti_{2-2x}M_{2x}O_7$(Ln = Gd, Er; M = Zr, Sn, Si)" *Materials Research Bulletin*, 37, 13 (**2002**) 2077-2083.

Etsell T. H. and Flengas S. N., "The electrical properties of solid oxide electrolytes" *Chemical Reviews (Washington, DC, United States)*, 70, 3 (**1970**) 339-376.

Ewing R. C., Weber W. J. and Lian J., "Nuclear waste disposal---pyrochlore ($A_2B_2O_7$): Nuclear waste form for the immobilization of plutonium and ``minor'' actinides" *Journal of Applied Physics*, 95, 11 (**2004**) 5949-5971.

Feighery A. J., Irvine J. T. S. and Zheng C., "High oxide ion conductivity in non-stoichiometric pyrochlores and fluorites in the ternary system ZrO_2 - Gd_2O_3 - TiO_2" *Ionics*, 3, 1-2 (**1997**) 30-35.

Gao W. and Sammes N. M., "*An introduction to electronic and ionic materials"* World Scientific: Singapore; River Edge, NJ (**1999**)

García-Adeva A. J. and Huber D. L., "Application of the generalized constant coupling approximation to the geometrically frustrated antiferromagnets $ZnCr_2O_4$ and $ZnCr_{2-2x}Ga_{2x}O_4$" *Physica B: Condensed Matter*, 320, 1-4 (**2002**) 18-22.

Gardner J. S., Gaulin B. D., Lee S. H., Broholm C., Raju N. P. and Greedan J. E., "Glassy Statics and Dynamics in the Chemically Ordered Pyrochlore Antiferromagnet $Y_2Mo_2O_7$" *Physical Review Letters*, 83, 1 (**1999**) 211-214.

Georges S., Goutenoire F., Bohnke O., Steil M. C., Skinner S. J., Wiemhöfer H. D. and Lacorre P., "The LAMOX Family of Fast Oxide-Ion Conductors: Overview and Recent Results" *Journal of New Materials for Electrochemical Systems*, 7, 1 (**2004**) 51-57.

Glerup M., Nielsen O. F. and Poulsen F. W., "The structural transformation from the pyrochlore structure, $A_2B_2O_7$, to the fluorite structure, AO_2, studied by Raman

spectroscopy and defect chemistry modeling" *Journal of Solid State Chemistry*, 160, 1 (**2001**) 25-32.

Goldstein J. I., Newbury D. E., Echlin P., Joy D. C., Fiori C. and Lifshin E., "*Scanning Electron Microscopy and X-ray Microanalysis: a text for Biologists, Materials Scientists, and Geologists"* Plenum Press: New York (**1981**)

Goodenough J. B., "Ceramic technology: Oxide-ion conductors by design" *Nature*, 404, 6780 (**2000**) 821-823.

Goodenough J. B., "Oxide Ion Electrolytes" *Annual Review of Materials Research*, 33, 1 (**2003**) 91-128.

Goodenough J. B., Ruiz-Diaz J. E. and Zhen Y. S., "Oxide-ion conduction in $Ba_2In_2O_5$ and $Ba_3In_2MO_8$ (M=Ce, Hf, or Zr)" *Solid State Ionics*, 44, 1-2 (**1990**) 21-31.

Gool W. V., "*Fast ion transport in solids"* North-Holland ; American Elsevier: Amsterdam (**1973**)

Grove W. R., "On Voltaic Series and the Combination of Gases by Platinum" *London and Edinburgh Philosophical Magazine and Journal of Science, Series 3*, 14, (**1839**) 127-130.

Grove W. R., "On a Gaseous Voltaic Battery" *London and Edinburgh Philosophical Magazine and Journal of Science, Series 3*, 21, (**1842**) 417-420.

Gupta H. C. and Brown S., "An analytical expression for Eg and Ag modes of pyrochlores" *Journal of Physics and Chemistry of Solids*, 64, 11 (**2003**) 2205-2207.

Gupta H. C., Brown S., Rani N. and Gohel V. B., "A lattice dynamical investigation of the Raman and the infrared frequencies of the cubic $A_2Sn_2O_7$ pyrochlores" *International Journal of Inorganic Materials*, 3, 7 (**2001**) 983-986.

H.L Tuller, "Atomic Transport in Heavily Defective Materials: Crystals and Glasses" In C. R. A. Catlow (Ed.), *Defects and disorder in crystalline and amorphous solids* Kluwer Academic Publishers: Dordrecht; Boston: (**1994**)

Hagenmuller P. and Gool W. V., "*Solid electrolytes : general principles, characterization, materials, applications"* Academic Press: New York (**1978**)

Harper G. D. J., "*Fuel cell projects for the evil genius"* McGraw-Hill: New York (**2008**)

Hashim S. S., Mohamed A. R. and Bhatia S., "Oxygen separation from air using ceramic-based membrane technology for sustainable fuel production and power generation" *Renewable and Sustainable Energy Reviews*, 15, 2 (**2011**) 1284-1293.

Hassan A. K., Lévy L. P., Darie C. and Strobel P., "Macroscopic anisotropy and symmetry breaking in the pyrochlore antiferromagnet $Gd_2Ti_2O_7$" *Physical Review B*, 67, 21 (**2003**) 214432 1-5.

Hayashi H., Inaba H., Matsuyama M., Lan N. G., Dokiya M. and Tagawa H., "Structural consideration on the ionic conductivity of perovskite-type oxides" *Solid State Ionics*, 122, 1-4 (**1999**) 1-15.

Heremans C., Wuensch B. J., Stalick J. K. and Prince E., "Fast-Ion Conducting $Y_2(Zr_yTi_{1-y})_2O_7$ Pyrochlores: Neutron Rietveld Analysis of Disorder Induced by Zr Substitution" *Journal of Solid State Chemistry*, 117, 1 (**1995**) 108-121.

Hess N. J., Begg B. D., Conradson S. D., McCready D. E., Gassman P. L. and Weber W. J., "Spectroscopic investigations of the structural phase transition in $Gd_2(Ti_{1-y}Zr_y)_2O_7$ pyrochlores" *Journal of Physical Chemistry B*, 106, 18 (**2002**) 4663-4677.

Hess N. J., Begg B. D., Conradson S. D., McCready D. E., Gassman P. L. and Weber W. J., "Spectroscopic investigations of the structural phase transition in $Gd_2(Ti_{1-y}Z_y)_2O_7$ pyrochlores" *Journal of Physical Chemistry B*, 106, 18 (**2002**) 4663-4677.

Hibino T., Ushiki K. and Kuwahara Y., "Electrochemical oxygen pump using CeO_2-based solid electrolyte for NO_x detection independent of O_2 concentration" *Solid State Ionics*, 93, 3-4 (**1997**) 309-314.

Hirayama M., Sonoyama N., Yamada A. and Kanno R., "Relationship between structural characteristics and photoluminescent properties of $(La_{1-x}Eu_x)_2M_2O_7$ (M=Zr, Hf, Sn) pyrochlores" *Journal of Luminescence*, 128, 11 (**2008**) 1819-1825.

Hiroi Z., Yamaura J. I., Yonezawa S. and Harima H., "Chemical trends of superconducting properties in pyrochlore oxides" *Physica C: Superconductivity and Its Applications*, 460, (**2007**) 20-27.

Inaba H. and Tagawa H., "Ceria-based solid electrolytes" *Solid State Ionics*, 83, 1-2 (**1996**) 1-16.

Ishihara T., "*Perovskite oxide for solid oxide fuel cells"* Springer: New York; London (**2008**)

Ishihara T., Akbay T., Furutani H. and Takita Y., "Improved oxide ion conductivity of Co doped $La_{0.8}Sr_{0.2}Ga_{0.8}Mg_{0.2}O_3$ perovskite type oxide" *Solid State Ionics*, 113-115, (**1998**) 585-591.

Ishihara T., Matsuda H. and Takita Y., "Doped $LaGaO_3$ perovskite type oxide as a new oxide ionic conductor" *Journal of the American Chemical Society*, 116, 9 (**1994**) 3801-3803.

Ishihara T., Matsuda H. and Takita Y., "Effects of rare earth cations doped for La site on the oxide ionic conductivity of $LaGaO_3$-based perovskite type oxide" *Solid State Ionics*, 79, C (**1995**) 147-151.

Jacobson A. J., "Materials for solid oxide fuel cells" *Chemistry of Materials*, 22, 3 (**2010**) 660-674.

Kalogirou S., "*Solar energy engineering : processes and systems"* Elsevier/Academic Press: Amsterdam; Boston (**2009**)

Kendall K. R., Navas C., Thomas J. K. and Loye H. C. z., "Recent developments in oxide ion conductors: Aurivillius phases" *Chemistry of Materials*, 8, 3 (**1996**) 642-649.

Kendrick E., Islam M. S. and Slater P. R., "Developing apatites for solid oxide fuel cells: Insight into structural, transport and doping properties" *Journal of Materials Chemistry*, 17, 30 (**2007**) 3104-3111.

Kennedy B. J., Hunter B. A. and Howard C. J., "Structural and bonding trends in tin pyrochlore oxides" *Journal of Solid State Chemistry*, 130, 1 (**1997**) 58-65.

Keramidas V. G. and White W. B., "Raman spectra of oxides with the fluorite structure" *Journal of Chemical Physics*, 59, 3 (**1973**) 1561-1562.

Kharton V. V., Figueiredo F. M., Navarro L., Naumovich E. N., Kovalevsky A. V., Yaremchenko A. A., Viskup A. P., Carneiro A., Marques F. M. B. and Frade J. R., "Ceria-based materials for solid oxide fuel cells" *Journal of Materials Science*, 36, 5 (**2001**) 1105-1117.

Kharton V. V., Marques F. M. B. and Atkinson A., "Transport properties of solid oxide electrolyte ceramics: A brief review" *Solid State Ionics*, 174, 1-4 (**2004**) 135-149.

Kharton V. V., Yaremchenko A. A., Viskup A. P., Patrakeev M. V., Leonidov I. A., Kozhevnikov V. L., Figueiredo F. M., Shaulo A. L., Naumovich E. N. and Marques F. M. B., "Oxygen permeability and ionic conductivity of perovskite-related $La_{0.3}Sr_{0.7}Fe(Ga)O_{3-\delta}$" *Journal of the Electrochemical Society*, 149, 4 (**2002**) E125-E135.

Kilner J. A. and Pena-Martinez J., "Workshop on SOFC: Materials and technology" *Fuel Cells*, 11, 1 (**2011**)

Kim J. H. and Yoo H. I., "Partial electronic conductivity and electrolytic domain of $La_{0.9}Sr_{0.1}Ga_{0.8}Mg_{0.2}O_{3-\delta}$" *Solid State Ionics*, 140, 1-2 (**2001**) 105-113.

Klee W. E. and Weitz G., "Infrared spectra of ordered and disordered pyrochlore-type compounds in the series $RE_2Ti_2O_7$, $RE_2Zr_2O_7$ and $RE_2Hf_2O_7$" *Journal of Inorganic and Nuclear Chemistry*, 31, 8 (**1969**) 2367-2372.

Kotomin E. A., Mastrikov Yu A., Heifets E., Merkle R., Maier J., Fleig J., Gordon A. and Felsteiner J., "First-principles modeling of $LaMnO_3$ SOFC cathode material" *ECS Transactions*, 13, 26 (**2008**) 301-306.

Kramer S. A. and Tuller H. L., "A novel titanate-based oxygen ion conductor: $Gd_2Ti_2O_7$" *Solid State Ionics*, 82, 1-2 (**1995**) 15-23.

Kumar M., Nesaraj A., Raj I. and Pattabiraman R., "Synthesis and characterization of $La_{0.9}Sr_{0.1}Ga_{0.8}Mg_{0.2}O_{3-\delta}$ electrolyte for intermediate temperature solid oxide fuel cells (ITSOFC)" *Ionics*, 10, 1 (**2004**) 93-98.

Kumar M., Raj I. A. and Pattabiraman R., "$Y_2Zr_2O_7$ (YZ)-pyrochlore based oxide as an electrolyte material for intermediate temperature solid oxide fuel cells (ITSOFCs)-Influence of Mn addition on YZ" *Materials Chemistry and Physics*, 108, 1 (**2008**) 102-108.

Kumar R. V., Iwahara H. and K.A. Gschneidner J. a. L. E., "Solid electrolytes" *Handbook on the Physics and Chemistry of Rare Earths* (Vol. Volume 28, pp. 131) Elsevier: (**2000**)

Kutty K. V. G., Rajagopalan S., Mathews C. K. and Varadaraju U. V., "Thermal expansion behaviour of some rare earth oxide pyrochlores" *Materials Research Bulletin*, 29, 7 (**1994**) 759-766.

Lacorre P., Goutenoire F., Bohnke O., Retoux R. and Lallgant Y., "Designing fast oxide-ion conductors based on $La_2Mo_2O_9$" *Nature*, 404, 6780 (**2000**) 856-858.

Lee Y. H., Chen J. M., Lee J. F. and Kao H. C. I., "XANES spectroscopic studies of the phase transition in $Gd_2Zr_2O_7$" *Journal of the Chinese Chemical Society*, 56, 3 (**2009**) 543-548.

Li P., Chen I. W. and Penner-Hahn J. E., "X-ray-absorption studies of zirconia polymorphs. II. Effect of Y_2O_3 dopant on ZrO_2 structure" *Physical Review B*, 48, 14 (**1993**) 10074-10081.

Li X., "*Principles of fuel cells"* Taylor & Francis: New York (**2006**)

Lian J., Wang L., Chen J., Sun K., Ewing R. C., Matt Farmer J. and Boatner L. A., "The order-disorder transition in ion-irradiated pyrochlore" *Acta Materialia*, 51, 5 (**2003**) 1493-1502.

Lian J., Wang L. M., Haire R. G., Helean K. B. and Ewing R. C., "Ion beam irradiation in $La_2Zr_2O_7$-$Ce_2Zr_2O_7$ pyrochlore" *Nuclear Instruments & Methods in Physics Research Section B-Beam Interactions with Materials and Atoms*, 218, (**2004**) 236-243.

Lian J., Wang L. M., Wang S. X., Chen J., Boatner L. A. and Ewing R. C., "Nanoscale manipulation of pyrochlore: New nanocomposite ionic conductors" *Physical Review Letters*, 87, 14 (**2001**) 145901 1-4.

Lian J., Zu X. T., Kutty K. V. G., Chen J., Wang L. M. and Ewing R. C., "Ion-irradiation-induced amorphization of $La_2Zr_2O_7$ pyrochlore" *Physical Review B*, 66, 5 (**2002**) 054108 1-5.

Lide D. R., "*CRC handbook of chemistry and physics : a ready-reference book of chemical and physical data"* CRC Press: Boca Raton, FL (**1994**)

Liu Y., Withers R. L. and Norén L., "The pyrochlore to 'defect fluorite' transition in the $Y_2(Zr_yTi_{1-y})_2O_7$ system and its underlying crystal chemistry" *Journal of Solid State Chemistry*, 177, 12 (**2004**) 4404-4412.

Liu Z.-G., Ouyang J.-H., Zhou Y. and Xia X.-L., "Electrical conductivity of samarium-ytterbium zirconate ceramics" *Electrochimica Acta*, 54, 15 (**2009**) 3968-3971.

Lutique S., Konings R. J. M., Rondinella V. V., Somers J. and Wiss T., "The thermal conductivity of $Nd_2Zr_2O_7$ pyrochlore and the thermal behaviour of pyrochlore-

based inert matrix fuel" *Journal of Alloys and Compounds*, 352, 1-2 (**2003**) 1-5.

Lutique S., Staicu D., Konings R. J. M., Rondinella V. V., Somers J. and Wiss T., "Zirconate pyrochlore as a transmutation target: Thermal behaviour and radiation resistance against fission fragment impact" *Journal of Nuclear Materials*, 319, (**2003**) 59-64.

Macdonald J. R., "Impedance spectroscopy" *Annals of Biomedical Engineering*, 20, 3 (**1992**) 289-305.

Mandal B. P., Banerji A., Sathe V., Deb S. K. and Tyagi A. K., "Order-disorder transition in $Nd_{2-y}Gd_yZr_2O_7$ pyrochlore solid solution: An X-ray diffraction and Raman spectroscopic study" *Journal of Solid State Chemistry*, 180, 10 (**2007**) 2643-2648.

Mandal B. P., Deshpande S. K. and Tyagi A. K., "Ionic conductivity enhancement in $Gd_2Zr_2O_7$ pyrochlore by Nd doping" *Journal of Materials Research*, 23, 4 (**2008**) 911-916.

Mandal B. P., Garg N., Sharma S. M. and Tyagi A. K., "Preparation, XRD and Raman spectroscopic studies on new compounds $RE_2Hf_2O_7$ (RE=Dy, Ho, Er, Tm, Lu, Y): Pyrochlores or defect-fluorite?" *Journal of Solid State Chemistry*, 179, 7 (**2006**) 1990-1994.

Mandal B. P., Krishna P. S. R. and Tyagi A. K., "Order-disorder transition in the $Nd_{2-y}Y_yZr_2O_7$ system: Probed by X-ray diffraction and Raman spectroscopy" *Journal of Solid State Chemistry*, 183, 1 (**2010**) 41-45.

Martin R. M., "*Electronic structure : basic theory and practical methods"* Cambridge University Press: Cambridge, UK; New York (**2004**)

McCauley R. A., "Structural characteristics of pyrochlore formation" *Journal of Applied Physics*, 51, 1 (**1980**) 290-294.

McCauley R. A., "Structural characteristics of pyrochlore formation" *Journal of Applied Physics*, 51, 1 (**1980**) 290.

McGeehin P. and Hooper A., "Fast ion conduction materials" *Journal of Materials Science*, 12, 1 (**1977**) 1-27.

Mehrer H., "Fast Ion Conductors" *Diffusion in Solids* (Vol. 155, pp. 475-490) Springer-Verlag Berlin Heidelberg: New York: (**2007**)

Meilicke S. and Halle S., "Order-Disorder Transitions in Gadolinium Zirconate: A Potential Electrolyte Material in Solid Oxide Fuel Cells" *Materials Research Society symposia proceedings.*, 393, (**1995**) 55-60.

Michel D., Perez y Jorba M. and Collongues R., "Study of order-disorder transformation of the fluorite structure has the pyrochlore structure for phases (1-x) ZrO_2 - x Ln_2O_3" *Materials Research Bulletin*, 9, 11 (**1974**) 1457-1468.

Michel D., y Jorba M. P. and Collongues R., "Study by Raman spectroscopy of order-disorder phenomena occurring in some binary oxides with fluorite-related structures" *Journal of Raman Spectroscopy*, 5, 2 (**1976**) 163-180.

Minervini L., Grimes R. W. and Sickafus K. E., "Disorder in pyrochlore oxides" *Journal of the American Ceramic Society*, 83, 8 (**2000**) 1873-1878.

Mitoseriu L., Ciomaga C. E., Dumitru I., Curecheriu L. P., Prihor F. and Guzu A., "Study of the frequency-dependence of the complex permittivity in Ba(Zr,Ti)O_3 ceramics: Evidences of the grain boundary phenomena" *Journal of Optoelectronics and Advanced Materials*, 10, 7 (**2008**) 1843-1846.

Mogensen M., Armstrong T., Gur T. and Yokokawa H., "*Ionic and Mixed Conducting Ceramics 6"* Curran Associates Inc: Red Hook, New York (**2009**)

Mogensen M., Lybye D., Bonanos N., Hendriksen P. V. and Poulsen F. W., "Factors controlling the oxide ion conductivity of fluorite and perovskite structured oxides" *Solid State Ionics*, 174, 1-4 (**2004**) 279-286.

Mogensen M., Sammes N. M. and Tompsett G. A., "Physical, chemical and electrochemical properties of pure and doped ceria" *Solid State Ionics*, 129, 1 (**2000**) 63-94.

Mond L. and Langer C., "A New Form of Gas Battery" *Proceedings of the Royal Society of London*, 46, 280-285 (**1889**) 296-304.

Moon P. K. and Tuller H. L., "Intrinsic Fast Oxygen Ionic Conductivity in the Gd2(ZrxTil.)2O7, and Y2 (ZrxTilx,)2O7, Pyrochlore Systems" *MRS Proc. MRS Proceedings*, 135, (**1988**)

Moon P. K. and Tuller H. L., "Ionic conduction in the $Gd_2Ti_2O_7$-$Gd_2Zr_2O_7$ system" *Solid State Ionics*, 28-30, Part 1 (**1988**) 470-474.

Moon P. K. and Tuller H. L., "Evaluation of the $Gd_2(Zr_xTi_{1-x})_2O_7$ pyrochlore system as an oxygen gas sensor" *Sensors and Actuators B: Chemical*, 1, 1-6 (**1990**) 199-202.

Mori M., Tompsett G. M., Sammes N. M., Suda E. and Takeda Y., "Compatibility of $Gd_xTi_2O_7$ pyrochlores ($1.72 \leq x \leq 2.0$) as electrolytes in high-temperature solid oxide fuel cells" *Solid State Ionics*, 158, 1-2 (**2003**) 79-90.

Moulson A. J. and Herbert J. M., "*Electroceramics : materials, properties, applications"* Chapman & Hall: London (**1992**)

Nachimuthu P., Thevuthasan S., Adams E. M., Weber W. J., Begg B. D., Mun B. S., Shun D. K., Lindle D. W., Gullikson E. M. and Perera R. C. C., "Near-edge X-ray absorption fine structure study of disordering in $Gd_2(Ti_{1-y}Zr_y)_2O_7$ pyrochlores" *Journal of Physical Chemistry B*, 109, 4 (**2005**) 1337-1339.

Nair K. R., Rao P. P., Raj A. V., Joseph S. K., Chandran M. R. and Koshy P., "New family of dielectric materials in Ca-Y-Ti-Nb-O system having pyrochlore type structure" *Journal of the American Ceramic Society*, 90, 11 (**2007**) 3656-3659.

Nakayama S., Kageyama T., Aono H. and Sadaoka Y., "Ionic conductivity of lanthanoid silicates, $Ln_{10}(SiO_4)_6O_3$ (Ln=La, Nd, Sm, Gd, Dy, Y, Ho, Er and Yb)" *Journal of Materials Chemistry*, 5, 11 (**1995**) 1801-1805.

Naumovich E. N., Kharton V. V., Samokhval V. V. and Kovalevsky A. V., "Oxygen separation using Bi_2O_3-based solid electrolytes" *Solid State Ionics*, 93, 1-2 (**1996**) 95-103.

Nernst W., "On Hydrogen" *Journal of Electrochemistry (Zeitschrift für Elektrochemie)*, 6, 2 (**1899**) 37-41.

Nikiforov L. G., "Possible method for estimating the parameter *x* in compounds of the pyrochlore type with general formula $A_2B_2O_7$" *Sov.Phys.Crystallogr.*, 17, (**1972**) 347-352.

Omar S., Belda A., Escardino A. and Bonanos N., "Ionic conductivity ageing investigation of 1Ce10ScSZ in different partial pressures of oxygen" *Solid State Ionics*, 184, 1 (**2011**) 2-5.

Ong E. T., Chung B. W., Doshi R., Guan J., Lear G. R., Montgomery K. and Minh N. Q., "Processing and Characterization of Solid Oxide Fuel Cells and Ceramic Oxygen Generators" *Ceramic transactions.*, 109, (**2000**) 77-86.

Orazem M. E. and Tribollet B., "*Electrochemical impedance spectroscopy"* Wiley: Hoboken, N.J. (**2008**)

Panero W. R., Stixrude L. and Ewing R. C., "First-principles calculation of defect-formation energies in the $Y_2(Ti,Sn,Zr)_2O_7$ pyrochlore" *Physical Review B*, 70, 5 (**2004**) 054110 1-11.

Pannetier J., "Electrostatic energy of pyrochlore networks" *Journal of Physics and Chemistry of Solids*, 34, 4 (**1973**) 583-589.

Petrowsky M. and Frech R., "Temperature Dependence of Ion Transport: The Compensated Arrhenius Equation" *The Journal of Physical Chemistry B*, 113, 17 (**2009**) 5996-6000.

Pirzada M., Grimes R. W., Minervini L., Maguire J. F. and Sickafus K. E., "Oxygen migration in $A_2B_2O_7$ pyrochlores" *Solid State Ionics*, 140, 3-4 (**2001**) 201-208.

Purton J. A. and Allan N. L., "Displacement cascades in $Gd_2Ti_2O_7$ and $Gd_2Zr_2O_7$: A molecular dynamics study" *Journal of Materials Chemistry*, 12, 10 (**2002**) 2923-2926.

Radhakrishnan A. N., Prabhakar Rao P., Sibi K. S., Deepa M. and Koshy P., "Order-disorder phase transformations in quaternary pyrochlore oxide system: Investigated by X-ray diffraction, transmission electron microscopy and Raman spectroscopic techniques" *Journal of Solid State Chemistry*, 182, 8 (**2009**) 2312-2318.

Radhakrishnan A. N., Rao P. P., Linsa K. S. M., Deepa M. and Koshy P., "Influence of disorder-to-order transition on lattice thermal expansion and oxide ion conductivity in $(Ca_xGd_{1-x})_2(Zr_{1-x}M_x)_2O_7$ pyrochlore solid solutions" *Dalton Transactions*, 40, 15 (**2011**) 3839-3848.

Rahaman M. N., "*Ceramic processing and sintering"* Dekker: New York (**2003**)

Ralph J. M., Kilner J. A. and Steele B. C., "Improving Gd-Doped Ceria Electrolytes for Low Temperature Solid Oxide Fuel Cells" *Materials Research Society symposia proceedings.*, 575, (**2000**) 309-314.

Rao C. N. R. and Subba Rao G. V., "Electrical conduction in metal oxides" *Phys. Stat. Sol. (a) Physica Status Solidi (a)*, 1, 4 (**1970**) 597-652.

Rao P. P., Nair K. R., Seema K. V., Koshy P. and Vaidyan V. K., "New pyrochlore type semiconducting ceramic oxides: $Ca_3Ce_{3-x}Bi_xTi_7Nb_2O_{26.5}$ (x = 0.5, 1.0, 2.0, or 3.0) structure, microstructure and electrical properties" *Journal of Materials Science*, 40, 15 (**2005**) 4085-4088.

Rodríguez J. A. and Garcia M. F., "*Synthesis, properties, and applications of oxide nanomaterials"* Wiley-Interscience: Hoboken, N.J. (**2007**)

Rousseau D. L., Bauman R. P. and Porto S. P. S., "Normal mode determination in crystals" *Journal of Raman Spectroscopy*, 10, 1 (**1981**) 253-290.

Sameera S., Prabhakar Rao P. and Chandran M. R., "Structure and dielectric properties of a new series of pyrochlores in the Ca-Sm-Ti-M-O (M = Nb and Ta) system" *Journal of Materials Science: Materials in Electronics*, 22, 11 (**2011**) 1631-1636.

Sammes N. M., Smirnova A. and Vasylyev O., "*Fuel cell technologies state and perspectives"* Springer: Dordrecht, UK (**2005**)

Sanjay Kumar N. R., Chandra Shekar N. V. and Sahu P. C., "Pressure induced structural transformation of pyrochlore $Gd_2Zr_2O_7$" *Solid State Communications*, 147, 9-10 (**2008**) 357-359.

Scheetz B. E. and White W. B., "Characterization of Anion Disorder in Zirconate $A_2B_2O_7$ Compounds by Raman Spectroscopy" *Journal of the American Ceramic Society*, 62, 9-10 (**1979**) 468-470.

Schelling P. K., Phillpot S. R. and Grimes R. W., "Optimum pyrochlore compositions for low thermal conductivity" *Philosophical Magazine Letters*, 84, 2 (**2004**) 127-137.

Schmidt M. C., "*Electric power research trends"* Nova Science Publishers: New York (**2007**)

Shannon R., "Revised effective ionic radii and systematic studies of interatomic distances in halides and chalcogenides" *Acta Crystallographica Section A: Foundations of Crystallography*, 32, 5 (**1976**) 751-767.

Shaula A. L., Kharton V. V. and Marques F. M. B., "Ionic and electronic conductivities, stability and thermal expansion of $La_{10-x}(Si,Al)_6O_{26 \pm \delta}$ solid electrolytes" *Solid State Ionics*, 177, 19-25 (**2006**) 1725-1728.

Shaula A. L., Yaremchenko A. A., Kharton V. V., Logvinovich D. I., Naumovich E. N., Kovalevsky A. V., Frade J. R. and Marques F. M. B., "Oxygen

permeability of $LaGaO_3$-based ceramic membranes" *Journal of Membrane Science*, 221, 1-2 (**2003**) 69-77.

Shimamura K., Arima T., Idemitsu K. and Inagaki Y., "Thermophysical Properties of Rare-Earth-Stabilized Zirconia and Zirconate Pyrochlores as Surrogates for Actinide-Doped Zirconia" *International Journal of Thermophysics*, 28, 3 (**2007**) 1074-1084.

Shimizu Y. and Maeda K., "Solid electrolyte NO_x sensor using pyrochlore-type oxide electrode" *Sensors and Actuators, B: Chemical*, 52, 1-2 (**1998**) 84-89.

Shinozaki K., Miyauchi M., Kuroda K., Sakurai O., Mizutani N. and Kato M., "Oxygen-Ion Conduction in the $Sm_2Zr_2O_7$ Pyrochlore Phase" *Journal of the American Ceramic Society*, 62, 9-10 (**1979**) 538-539.

Shlyakhtina A. V., Karyagina O. K. and Shcherbakova L. G., "Order-disorder transformations in $Ln_2Ti_2O_7$ (Ln = Lu, Yb, Tm, Gd)" *Inorganic Materials*, 40, 1 (**2004**) 59-65.

Shlyakhtina A. V., Knotko A. V., Boguslavskii M. V., Stefanovich S. Y., Peryshkov D. V., Kolbanev I. V. and Shcherbakova L. G., "Effects of the synthesis procedure, doping and non-stoichiometry on the order-disorder transformation in $Ln_2Ti_2O_7$ (Ln=Tm-Lu) oxygen-ion conductors" *Solid State Ionics*, 176, 29-30 (**2005**) 2297-2304.

Sibi K. S., Radhakrishnan A. N., Deepa M., Prabhakar Rao P. and Koshy P., "Oxide ion conductivity and relaxation in $CaREZrNbO_7$ (RE = La, Nd, Sm, Gd, and Y) system" *Solid State Ionics*, 180, 20-22 (**2009**) 1164-1172.

Sickafus K. E., Minervini L., Grimes R. W., Valdez J. A., Ishimaru M., Li F., McClellan K. J. and Hartmann T., "Radiation Tolerance of Complex Oxides" *Science*, 289, 5480 (**2000**) 748-751.

Singhal S. C., "Science and Technology of Solid-Oxide Fuel Cells" *MRS bulletin*, 25, 3 (**2000**) 16-21.

Singhal S. C. and Dokiya M., "*Solid oxide fuel cells : (SOFC VI) : proceedings of the Sixth International Symposium"* International Symposium on Solid Oxide Fuel, Cells: Pennington, NJ (**1999**)

Singhal S. C. and Kendall K., "*High temperature solid oxide fuel cells fundamentals, design, and applications"* Elsevier Oxford; New York (**2003**)

Slater P. R., Sansom J. E. H. and Tolchard J. R., "Development of apatite-type oxide ion conductors" *Chemical Record*, 4, 6 (**2004**) 373-384.

Spiegel C., "*PEM fuel cell modeling and simulation using Matlab"* Academic Press: Burlington, Mass. (**2008**)

Spiridinov F. M., Stepanov V. A., Komissarova L. N. and Spitsyn V. I., "The binary system HfO_2-Gd_2O_3" *Journal of The Less-Common Metals*, 14, 4 (**1968**) 435-443.

Srinivasan S., "*Fuel cells : from fundamentals to applications"* Springer: New York (**2006**)

Srinivasan S., Mosdale R., Stevens P. and Yang C., "Fuel Cells: Reaching the Era of Clean and Efficient Power Generation in the Twenty-First Century" *Annual Review of Energy and the Environment*, 24, 1 (**1999**) 281-328.

Stambouli A. B. and Traversa E., "Solid oxide fuel cells (SOFCs): a review of an environmentally clean and efficient source of energy" *Renewable and Sustainable Energy Reviews*, 6, 5 (**2002**) 433-455.

Stanek C. R., "*Atomic scale disorder in fluorite and fluorite related oxides"* Ph.D, University of London, London (**2003**)

Stanek C. R. and Grimes R. W., "Prediction of rare-earth $A_2Hf_2O_7$ pyrochlore phases" *Journal of the American Ceramic Society*, 85, 8 (**2002**) 2139-2141.

Stanek C. R., Minervini L. and Grimes R. W., "Nonstoichiometry in $A_2B_2O_7$ pyrochlores" *Journal of the American Ceramic Society*, 85, 11 (**2002**) 2792-2798.

Steele B. C. H., "Material science and engineering: The enabling technology for the commercialisation of fuel cell systems" *Journal of Materials Science*, 36, 5 (**2001**) 1053-1068.

Stevenson J. W., Armstrong T. R., McCready D. E., Pederson L. R. and Weber W. J., "Processing and electrical properties of alkaline earth-doped lanthanum gallate" *Journal of the Electrochemical Society*, 144, 10 (**1997**) 3613-3620.

Subbarao E. C., "A family of ferroelectric bismuth compounds" *Journal of Physics and Chemistry of Solids*, 23, 6 (**1962**) 665-676.

Subramanian M. A., Aravamudan G. and Subba Rao G. V., "Oxide pyrochlores: A review" *Progress in Solid State Chemistry*, 15, 2 (**1983**) 55.

Subramanian M. A., Ramirez A. P. and Kwei G. H., "Colossal magnetoresistance behavior in manganese oxides: pyrochlore versus perovskite" *Solid State Ionics*, 108, 1-4 (**1998**) 185-191.

Takahashi T., In M. Z. A. Munshi (Ed.), *Handbook of solid state batteries & capacitors* World Scientific Pub.: Singapore; River Edge, N.J.: (**1995**)

Takahashi T., Iwahara H. and Nagai Y., "High oxide ion conduction in sintered Bi_2O_3 containing SrO, CaO or La_2O_3" *Journal of Applied Electrochemistry*, 2, 2 (**1972**) 97-104.

Takamura H. and Tuller H. L., "Ionic conductivity of Gd_2GaSbO_7-$Gd_2Zr_2O_7$ solid solutions with structural disorder" *Solid State Ionics*, 134, 1-2 (**2000**) 67-73.

Tilley R. J. D., "*Understanding solids : the science of materials"* J. Wiley: Hoboken, NJ, USA (**2004**)

Tilley R. J. D., "*Crystals and crystal structures"* John Wiley: Hoboken, NJ (**2006**)

Tubant C., "*Handbook of Experimental Physics XII part I"* Akadem Verlag: Berlin (**1932**)

Tuller H. L., "Semiconduction and mixed ionic-electronic conduction in nonstoichiometric oxides: Impact and control" *Solid State Ionics*, 94, 1-4 (**1997**) 63-74.

Tuller H. L. and Nowick A. S., " Doped ceria as a solid oxide electrolyte" *Journal of the Electrochemical Society*, 122, 2 (**1975**) 255-259.

Tuller H. L., Schoonman J. and Riess I., "*Oxygen ion and mixed conductors and their technological applications"* Kluwer: Dordrecht (**2000**)

van Dijk M. P., Burggraaf A. J., Cormack A. N. and Catlow C. R. A., "Defect structures and migration mechanisms in oxide pyrochlores" *Solid State Ionics*, 17, 2 (**1985**) 159-167.

van Dijk M. P., de Vries K. J. and Burggraaf A. J., "Oxygen ion and mixed conductivity in compounds with the fluorite and pyrochlore structure" *Solid State Ionics*, 9-10, Part 2 (**1983**) 913-919.

van Dijk T., de Vries K. J. and Burggraaf A. J., "Electrical conductivity of fluorite and pyrochlore $Ln_xZr_{1-x}O_{2-x/2}$ (Ln = Gd, Nd) solid solutions" *physica status solidi (a)*, 58, 1 (**1980**) 115-125.

Van Gool W., "*Fast ion transport in solids"* American Elsevier: New York (**1973**)

Vandenborre M. T., Husson E., Chatry J. P. and Michel D., "Rare-earth titanates and stannates of pyrochlore structure; vibrational spectra and force fields" *Journal of Raman Spectroscopy*, 14, 2 (**1983**) 63-71.

Vegard L., "The constitution of mixed crystals and the space filling of the atoms" *Journal of Physics A: Hadrons and Nuclei*, 5, 1 (**1921**) 17-26.

Vielstich W., "*Handbook of fuel cells : fundamentals, technology and applications"* Wiley: Chichester (**2003**)

Vielstich W., Lamm A., Gasteiger H. A. and Yokokawa H., "*Handbook of fuel cells : fundamentals, technology, and applications"* Wiley: Hoboken, NJ, USA (**2003**)

Wang J., Nakamura A. and Takeda M., "Structural properties of the fluorite- and pyrochlore-type compounds in the Gd_2O_3-ZrO_2 system x $GdO_{1.5}$ - (1-x) ZrO_2 with $0.18 \leq x \leq 0.62$" *Solid State Ionics*, 164, 3-4 (**2003**) 185-191.

Wang Q. A., Wang H. and Yao X., "Structure, dielectric and optical properties of $Bi_{1.5}ZnNb_{1.5-x}Ta_xO_7$ cubic pyrochlores" *Journal of Applied Physics*, 101, 10 (**2007**) 104116 1-5.

Wang S. X., Begg B. D., Wang L. M., Ewing R. C., Weber W. J. and Govidan Kutty K. V., "Radiation stability of gadolinium zirconate: A waste form for plutonium disposition" *Journal of Materials Research*, 14, 12 (**1999**) 4470-4473.

Wang S. X., Wang L. M., Ewing R. C., Was G. S. and Lumpkin G. R., "Ion irradiation-induced phase transformation of pyrochlore and zirconolite" *Nuclear Instruments and Methods in Physics Research, Section B: Beam Interactions with Materials and Atoms*, 148, 1-4 (**1999**) 704-709.

Weissbart J. and Ruka R., "A Solid Electrolyte Fuel Cell" *Journal of the Electrochemical Society*, 109, 8 (**1962**) 723-726.

West A. R., "*Solid state chemistry and its applications"* Wiley: Chichester; New York (**1984**)

Whittle K. R., Cranswick L. M. D., Redfern S. A. T., Swainson I. P. and Lumpkin G. R., "Lanthanum pyrochlores and the effect of yttrium addition in the systems $La_{2-x}Y_xZr_2O_7$ and $La_{2-x}Y_xHf_2O_7$" *Journal of Solid State Chemistry*, 182, 3 (**2009**) 442-450.

Wilde P. J. and Catlow C. R. A., "Defects and diffusion in pyrochlore structured oxides" *Solid State Ionics*, 112, 3-4 (**1998a**) 173-183.

Wilde P. J. and Catlow C. R. A., "Molecular dynamics study of the effect of doping and disorder on diffusion in gadolinium zirconate" *Solid State Ionics*, 112, 3-4 (**1998b**) 185-195.

Williams D. B. and Carter C. B., "*Transmission electron microscopy: a textbook for materials science"* Plenum Press: New York (**1996**)

Williford R. E., Weber W. J., Devanathan R. and Gale J. D., "Effects of cation disorder on oxygen vacancy migration in $Gd_2Ti_2O_7$" *Journal of Electroceramics*, 3, 4 (**1999**) 409-424.

Wood J., "*Local energy : distributed generation of heat and power"* Institution of Engineering and Technology: London (**2008**)

Wuensch B. and Eberman K., "Order-disorder phenomena in $A_2B_2O_7$ pyrochlore oxides" *Journal of the Minerals, Metals and Materials Society*, 52, 7 (**2000**) 19-21.

Wuensch B. J. and Eberman K. W., "Order-disorder phenomena in $A_2B_2O_7$ pyrochlore oxides" *Journal of the Minerals, Metals and Materials Society*, 52, 7 (**2000**) 19-21.

Wuensch B. J., Eberman K. W., Heremans C., Ku E. M., Onnerud P., Yeo E. M. E., Haile S. M., Stalick J. K. and Jorgensen J. D., "Connection between oxygen-ion conductivity of pyrochlore fuel-cell materials and structural change with composition and temperature" *Solid State Ionics*, 129, 1-4 (**2000**) 111-133.

Yamaji K., Horita T., Ishikawa M., Sakai N. and Yokokawa H., "Chemical stability of the $La_{0.9}Sr_{0.1}Ga_{0.8}Mg_{0.2}O_{2.85}$ electrolyte in a reducing atmosphere" *Solid State Ionics*, 121, 1 (**1999**) 217-224.

Yamamoto O., Arati Y., Takeda Y., Imanishi N., Mizutani Y., Kawai M. and Nakamura Y., "Electrical conductivity of stabilized zirconia with ytterbia and scandia" *Solid State Ionics*, 79, C (**1995**) 137-142.

Yamamura H., Nishino H., Kakinuma K. and Nomura K., "Electrical conductivity anomaly around fluorite-pyrochlore phase boundary" *Solid State Ionics*, 158, 3 (**2003**) 359-365.

Yashima M., Kakihana M. and Yoshimura M., "Metastable-stable phase diagrams in the zirconia-containing systems utilized in solid-oxide fuel cell application" *Solid State Ionics*, 86-88, Part 2 (**1996**) 1131-1149.

Yasuda I., Matsuzaki Y., Yamakawa T. and Koyama T., "Electrical conductivity and mechanical properties of alumina-dispersed doped lanthanum gallates" *Solid State Ionics*, 135, 1-4 (**2000**) 381-388.

Yoshimura K., Sakai H., Ohno H., Kambe S. and Walstedt R. E., "Physical properties of new superconductor $Cd_2Re_2O_7$ with pyrochlore-type structure" *Physica B: Condensed Matter*, 329, (**2003**) 1319-1320.

Zhang F. X., Lian J., Becker U., Ewing R. C., Hu J. and Saxena S. K., "High-pressure structural changes in the $Gd_2Zr_2O_7$ pyrochlore" *Physical Review B: Condensed Matter and Materials Physics*, 76, 21 (**2007**) 214104 1-5.

Zhang F. X., Manoun B. and Saxena S. K., "Pressure-induced order-disorder transitions in pyrochlore $RE_2Ti_2O_7$ (RE = Y, Gd)" *Materials Letters*, 60, 21-22 (**2006**) 2773-2776.